NASA Technical Paper 1865

Design and Experimental Results for a Flapped Natural-Laminar-Flow Airfoil for General Aviation Applications

Dan M. Somers

JUNE 1981

NASA

NASA Technical Paper 1865

Design and Experimental Results for a Flapped Natural-Laminar-Flow Airfoil for General Aviation Applications

Dan M. Somers
Langley Research Center
Hampton, Virginia

National Aeronautics
and Space Administration

**Scientific and Technical
Information Branch**

1981

INTRODUCTION

Research on advanced-technology airfoils for general aviation applications has received considerable attention over the past decade at the NASA Langley Research Center. The initial emphasis in this research program was on the design and testing of turbulent-flow airfoils with the basic objective of producing a series of airfoils which could achieve higher maximum lift coefficients than the airfoils in use on general aviation airplanes at that time. For this series of airfoils, it was assumed that the flow over the entire airfoil would be turbulent, primarily because of the construction techniques in use (mostly riveted sheet metal). A summary of this work is presented in reference 1. While these new NASA low-speed airfoils did achieve higher maximum lift coefficients, the cruise drag coefficients were essentially no lower than the earlier NACA four- and five-digit airfoils. Accordingly, the emphasis in the research program has been shifted toward natural-laminar-flow (NLF) airfoils in an attempt to obtain lower cruise drag coefficients while retaining the high maximum lift coefficients of the new NASA airfoils. In this context, the term "natural-laminar-flow airfoil" refers to an airfoil which can achieve significant extents of laminar flow ($\geq$30-percent chord) solely through favorable pressure gradients (no boundary-layer suction or cooling).

Research on natural-laminar-flow airfoils dates back to the 1930's at the National Advisory Committee for Aeronautics (NACA). (See ref. 2.) The work at NACA was culminated with the 6-series airfoils (ref. 3). The 6-series airfoils were not generally successful as low-drag airfoils, however, because of the construction techniques available at the time.

The advent of composite structures has led to a resurgence in NLF research. The initial applications were sailplanes, but recently, a number of powered general aviation airplanes have been constructed of composites - most notably, the Bellanca Skyrocket II (ref. 4) and the Windecker Eagle (ref. 5). In Europe, powered composite airplanes have also been produced. One such aircraft, the LFU 205, used an NLF airfoil specifically tailored for its mission (ref. 6).

Thus, the introduction of composite construction has allowed aerodynamicists to design NLF airfoils which achieve, in flight, the low-drag characteristics measured in the wind tunnel (ref. 7). The goal of the present research on NLF airfoils at Langley Research Center is to combine the high maximum lift capability of the NASA low-speed airfoils with the low-drag characteristics of the NACA 6-series airfoils.

As part of the present research, an NLF airfoil, the NLF(1)-0416, was designed using the method of reference 8 and verified experimentally (ref. 9) in the Langley Low-Turbulence Pressure Tunnel (LTPT) (ref. 10). Based upon the success of this airfoil and the excellent agreement between the theoretical predictions and the experimental results, a second, more advanced, airfoil was designed using the method of reference 8. An experimental investigation was then conducted in the Low-Turbulence Pressure Tunnel to obtain the basic low-

speed, two-dimensional aerodynamic characteristics of the airfoil. The results have been compared with the predictions from the method of reference 8.

Use of trade names or names of manufacturers in this report does not constitute an official endorsement of such products or manufacturers, either expressed or implied, by the National Aeronautics and Space Administration.

SYMBOLS

Values are given in both SI and U.S. Customary Units. Measurements and calculations were made in U.S. Customary Units.

c_p pressure coefficient, $\dfrac{p_l - p_\infty}{q_\infty}$

c airfoil chord, cm (in.)

c_c section chord-force coefficient, $\oint c_p \, d\left(\frac{z}{c}\right)$

c_d section profile-drag coefficient, $\int_{\text{Wake}} c_d' \, d\left(\frac{h}{c}\right)$

c_d' point drag coefficient (ref. 11)

c_l section lift coefficient, $c_n \cos \alpha - c_c \sin \alpha$

c_m section pitching-moment coefficient about quarter-chord point, $-\oint c_p\left(\frac{x}{c} - 0.25\right) d\left(\frac{x}{c}\right) + \oint c_p\left(\frac{z}{c}\right) d\left(\frac{z}{c}\right)$

c_n section normal-force coefficient, $-\oint c_p \, d\left(\frac{x}{c}\right)$

h vertical height in wake profile, cm (in.)

M free-stream Mach number

p static pressure, Pa (lbf/ft^2)

q dynamic pressure, Pa (lbf/ft^2)

R Reynolds number based on free-stream conditions and airfoil chord

t airfoil thickness, cm (in.)

x airfoil abscissa, cm (in.)

z airfoil ordinate, cm (in.)

α angle of attack relative to chord line, deg

δ_f flap deflection, positive downward, deg

Subscripts:

l local point on airfoil

max maximum

min minimum

∞ free-stream conditions

Abbreviations:

ls lower surface

LTPT Langley Low-Turbulence Pressure Tunnel

NLF natural laminar flow

us upper surface

AIRFOIL DESIGN

OBJECTIVES AND CONSTRAINTS

The target application for this airfoil is a high-performance, single-engine, general aviation airplane. This application requires low section profile-drag coefficients c_d at a Reynolds number R of about 9×10^6 for the cruise section lift coefficient ($c_l = 0.2$) as well as for the climb section lift coefficients ($c_l = 0.5$ to 1.0).

Two primary objectives were identified for this airfoil. The first objective was to design an airfoil which would produce a maximum lift coefficient $c_{l,max}$ at $R = 3 \times 10^6$ comparable to those of the NASA low-speed series airfoils. (See ref. 1.) A requirement related to the first objective was that $c_{l,max}$ not decrease with transition fixed near the leading edge on both surfaces. This means that the maximum lift coefficient cannot depend on the achievement of laminar flow. Thus, if the leading edge of the wing is contaminated by insect remains, etc., the $c_{l,max}$ should not decrease. This requirement is set by safety considerations relating to stall and, therefore, to landing speeds. The second objective was to obtain low profile-drag coefficients c_d from the cruise lift coefficient c_l of 0.2 to about 1.

Three constraints were placed on this airfoil design in order to make it compatible with existing aircraft designs. First, the airfoil thickness t/c must be 15 percent. Second, the pitching-moment coefficient c_m should be no more negative than -0.05 at the cruise lift coefficient ($c_l = 0.2$). Third, the airfoil must incorporate a simple flap having a chord equal to 25 percent of the airfoil chord c.

PHILOSOPHY

Given the previously discussed objectives and constraints, certain characteristics of the design are evident. The following sketch illustrates the desired $c_l - c_d$ curve, which meets the goals for this design:

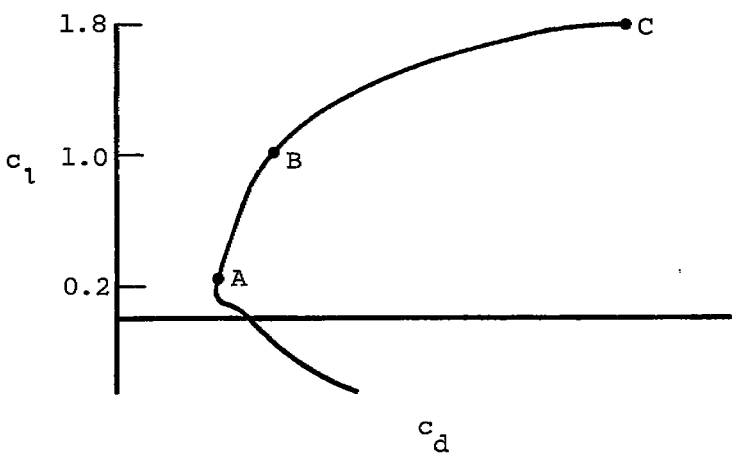

Sketch 1

The desired airfoil shape can be related to the pressure distributions which occur at the various lift coefficients shown in the sketch. Point A is the cruise condition ($c_l = 0.2$, $R = 9 \times 10^6$). The value of c_d for this point is determined by the extents of laminar flow on the upper and lower surfaces. There is little aerodynamic advantage in achieving low drag below $c_l = 0.2$. This is especially important if high maximum lift must be obtained (point C). However, in an attempt to insure a low-drag coefficient at the cruise lift coefficient ($c_l = 0.2$) despite contour deviations due to construction tolerances, the lower limit of the low-drag range was extended downward to $c_l = 0.1$. Notice that the drag at point B ($c_l = 1.0$) is not quite as low as at point A ($c_l = 0.2$). This feature is quite important because it shows that the transition point on the upper surface moves slowly and steadily toward the leading edge with increasing c_l, as opposed to the sudden forward jump characteristic of the NACA 6-series airfoils. This feature leads to an airfoil with a relatively blunt leading edge which, in turn, should produce a high maximum lift coefficient as well as good flap effectiveness.

This outline of the desired section characteristics is not sufficient to design the airfoil, however, primarily because of the variable introduced by

the flap and the unconstrained extents of laminar flow on the upper and lower surfaces. In order to evaluate the effects of these variables, it is helpful to examine the design goals with respect to overall aircraft performance. For this airfoil, the primary goal is a reduction in wing parasite drag. This goal can be achieved in a number of ways, two of which are discussed in this report. First, if a high maximum lift coefficient $c_{l,max}$ can be realized, the wing area can be reduced relative to a wing with a lower $c_{l,max}$. This conclusion is based on the assumption that both aircraft must achieve the same minimum speed. Second, if the amount of laminar flow on one or both surfaces can be extended, the minimum profile-drag coefficient $c_{d,min}$ will be reduced. Further analysis indicates that by maximizing $c_{l,max}/c_{d,min}$, the wing parasite drag is minimized. Unfortunately, a reduction in $c_{d,min}$ through the extension of the amount of laminar flow on the upper surface generally results in a reduction in $c_{l,max}$. (See ref. 3.) By trial and error, it was determined that $c_{l,max}/c_{d,min}$ would be maximized for this application if the extent of laminar flow was about 0.4c on the upper surface and about 0.6c on the lower surface.

The effect of the flap on the design can be evaluated by examining the constraint on the pitching-moment coefficient ($c_{m,cruise} \geq -0.05$). The objective of a high maximum lift coefficient is in conflict with the pitching-moment constraint. For this design, the flap can be used to alleviate this conflict by employing negative (up) flap deflections. This concept allows an airfoil to be designed which has a fairly large amount of camber (conducive to a high $c_{l,max}$) but retains the ability to achieve a low pitching-moment coefficient at the cruise lift coefficient ($c_l = 0.2$). This concept has the added advantage that, by deflecting the flap up or down, the low-drag range can be shifted to lower or higher lift coefficients, respectively. (See ref. 12.) Based upon experience with other airfoils, the negative flap deflection δ_f was limited to -10^o.

From the preceding discussion, the pressure distributions along the $c_l - c_d$ curve from points A to B in sketch 1 can be deduced. The pressure distribution for a flap deflection of 0^o at a lift coefficient of about 0.7 (i.e., between points A and B) should probably resemble sketch 2.

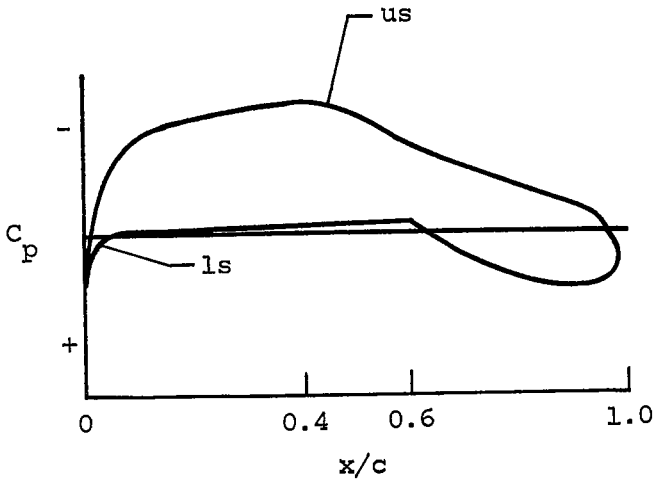

Sketch 2

For the reasons previously stated, a favorable pressure gradient on the upper surface is desirable up to $x/c = 0.4$. Aft of 0.4c on the upper surface, a short region of slightly adverse pressure gradient is desirable to promote the efficient transition from laminar to turbulent flow (ref. 13). Thus, the initial slope of the pressure recovery is relatively shallow. This short region is followed by a steeper concave pressure recovery which produces lower drag and has less tendency to separate than the corresponding linear or convex pressure recovery (ref. 13). The proposed pressure recovery, although concave, does not approach the extreme shape of a Stratford recovery (ref. 14). The Stratford recovery is not appropriate for an airfoil which must operate over a range of lift coefficients and Reynolds numbers (ref. 15).

For the reasons previously stated, a favorable pressure gradient on the lower surface is desirable up to $x/c = 0.6$. A rather abrupt and very steep concave pressure recovery is introduced aft of 0.6c, which results in a large amount of aft camber. This camber, although limited by the pitching-moment constraint ($c_{m,cruise} \geq -0.05$ with $\delta_f = -10^\circ$), helps produce a high maximum lift coefficient.

For point A ($c_l = 0.2$) in sketch 1, the pressure distribution should resemble sketch 3. For this lift coefficient, the flap is deflected up 10°. Along

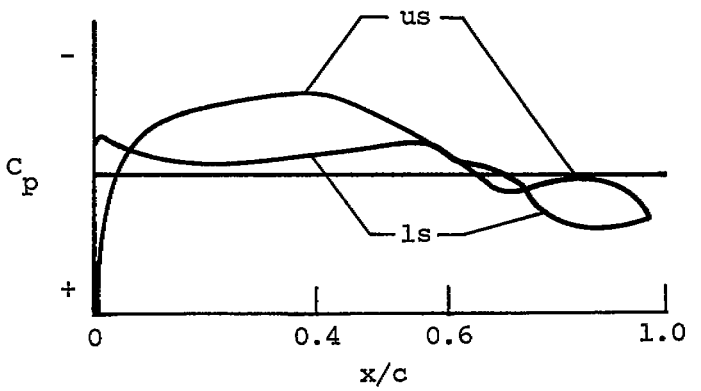

Sketch 3

the lower surface, the pressure gradient is initially adverse, then zero, and then increasingly favorable. Basically, this concept is to transition as the Stratford pressure recovery (ref. 14) is to separation. The concept was suggested by Richard Eppler of the University of Stuttgart, Stuttgart, West Germany.

For point B ($c_l = 1.0$) in sketch 1, the pressure distribution should resemble sketch 4. For this lift coefficient, the flap is deflected down 10°. A favorable pressure gradient on the upper surface to $x/c = 0.4$ and a zero pressure gradient on the lower surface to $x/c = 0.6$ is expected to result in low drag, albeit at the lower limit of the low-drag range for this flap deflection.

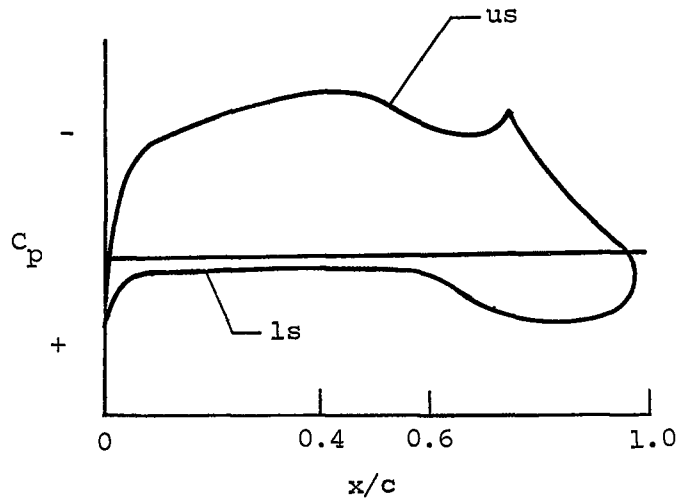

Sketch 4

It should be noted that the cruise-flap concept may not be optimum for all applications. If the construction tolerances at the flap hinge are not sufficiently tight, lift and drag penalties due to a disturbance to the turbulent boundary layer may be sufficient to offset the advantages of this concept. (See ref. 16.)

EXECUTION

Given the pressure distributions for $c_l = 0.2$, $c_l = 0.7$, and $c_l = 1.0$, the design of the airfoil is reduced to the inverse problem of transforming the pressure distributions into an airfoil shape. The method of reference 8 was used because it is ideal for handling multipoint designs, i.e., designs where more than one angle of attack must be considered. This method was also chosen because of its capability to analyze flap deflections and because of confidence gained during the design, analysis, and experimental verification of the NLF(1)-0416 airfoil (ref. 9).

The inviscid pressure distributions computed by the method of reference 8 for $c_l = 0.7$ ($\delta_f = 0^o$), $c_l = 0.2$ ($\delta_f = -10^o$), and $c_l = 1.0$ ($\delta_f = 10^o$) are shown in figures 1(a), 1(b), and 1(c), respectively. The resulting shapes are shown in figure 2 and the coordinates with 0^o flap deflection are presented in table I. The designation, NLF(1)-0215F, follows the form:

Application	Airfoil number	$c_{l,design}$	t/c
Natural Laminar Flow	1	0.2	0.15

The second "F" designates "flapped." For this airfoil, $c_{l,design}$ is defined as the cruise lift coefficient. It must be emphasized, however, that this in no way implies that this airfoil was designed at only one point, $c_{l,design}$; all of the objectives and constraints were considered.

EXPERIMENTAL PROCEDURE

WIND TUNNEL

The Langley Low-Turbulence Pressure Tunnel (LTPT) is a closed-throat, single-return tunnel which can be operated at stagnation pressures from 3 to 1000 kPa (0.03 to 10 atm). (See ref. 10.) The minimum unit Reynolds number is approximately 3.9×10^4 per meter (1.2×10^4 per foot) at a Mach number of 0.05, whereas the maximum unit Reynolds number is approximately 4.9×10^7 per meter (1.5×10^7 per foot) at a Mach number of 0.23. The maximum tunnel-empty test-section Mach number of 0.46 occurs at a stagnation pressure of about 100 kPa (1 atm).

The test section is 91.44 cm (36.00 in.) wide by 228.6 cm (90.00 in.) high. Hydraulically actuated circular plates provide positioning and attachment for the two-dimensional model. The plates, 101.6 cm (40.00 in.) in diameter, are flush with the tunnel sidewalls and rotate with the model. The model ends were mounted to rectangular model attachment plates, as shown in figure 3.

MODEL

The forward portion of the wind-tunnel model of the NLF(1)-0215F airfoil consisted of an aluminum spar surrounded by plastic filler with two thin layers of fiberglass forming the aerodynamic surface. The flap was constructed of aluminum and was attached to the forward portion of the model by aluminum brackets. These brackets were shaped so as to simulate 0°, -10°, and 10° deflections of a sealed, center-hinged, simple flap. (See fig. 4.) The location of the flap-hinge point was $x/c = 0.7500$, $z/c = 0.0328$. The model had a chord of 60.960 cm (24.000 in.) and a span of 91.44 cm (36.00 in.). Upper- and lower-surface orifices were located 7.62 cm (3.00 in.) to one side of the midspan at the chord stations listed in table II. Spanwise orifices were located in the upper surface only in order to monitor the two-dimensionality of the flow at high angles of attack. All the orifices were 1.0 mm (0.040 in.) in diameter with their axes perpendicular to the surface. The model surface was sanded with No. 600 dry silicon carbide paper to insure an aerodynamically smooth finish. The steps and gaps between the brackets and the forward portion of the model and between the brackets and the flap were eliminated by filling. The model contour accuracy was generally within ±0.05 mm (0.002 in.) as determined by measurement.

WAKE RAKE

A fixed wake rake (fig. 5) was cantilevered from the tunnel sidewall at the model midspan and 1.0 chord downstream from the trailing edge of the model. The wake rake employed 91 total-pressure tubes, 0.152 cm (0.060 in.) in diameter, and 5 static-pressure tubes, 0.318 cm (0.125 in.) in diameter. The total-pressure tubes were flattened to 0.102 cm (0.040 in.) for a length of 0.61 cm (0.24 in.) from the tips of the tubes. Each static-pressure tube had four flush orifices located 90° apart, 8 tube diameters from the tip of the tube in the measurement plane of the total-pressure tubes.

INSTRUMENTATION

Measurements of the static pressures on the model surfaces and of the wake-rake pressures were made by an automatic pressure-scanning system utilizing variable-capacitance precision transducers. Basic tunnel pressures were measured with precision quartz manometers. Geometric angle of attack was measured by a calibrated digital shaft encoder driven by a pinion gear and a rack attached to the circular plates. Data were obtained by a high-speed data-acquisition system and were recorded on magnetic tape.

TESTS AND METHODS

The model was tested at Reynolds numbers based on airfoil chord from approximately 2×10^6 to 9×10^6. The Mach number was varied from about 0.1 to 0.3. The model was tested both smooth (transition free) and with transition fixed by roughness at 0.05c on both surfaces. The roughness was sized for each Reynolds number by the method of reference 17. The granular roughness was sparsely distributed along the 3-mm (0.1-in.) wide strips which were applied to the model with lacquer.

For several test runs, the model upper surface was coated with oil to determine the location as well as the nature of the boundary-layer transition from laminar to turbulent flow (ref. 18).

The static-pressure measurements at the model surface were reduced to standard pressure coefficients and numerically integrated to obtain section normal-force and chord-force coefficients and section pitching-moment coefficients about the quarter-chord point. Section profile-drag coefficients were computed from the wake-rake total and static pressures by the method of reference 11.

Standard low-speed wind-tunnel boundary corrections (ref. 19), a maximum of approximately 3 percent of the measured section characteristics and 0.2° angle of attack, have been applied to the data. The wake-rake total-pressure-tube displacement correction (ref. 11), a maximum increase of approximately 2 percent of the measured profile-drag coefficients, has not been taken into account in order that the data be directly comparable to previously published airfoil data.

DISCUSSION OF RESULTS

EXPERIMENTAL RESULTS

Pressure Distributions

The pressure distributions for various angles of attack with a flap deflection δ_f of 0° at a Reynolds number of 6.0×10^6 and a Mach number of 0.10 are shown in figure 6. At $\alpha = -13.08^\circ$, -12.08°, and -11.08° (figs. 6(a) to 6(c)), the entire lower surface is separated. As the angle of attack is increased from -10.15° (fig. 6(d)), which corresponds to $c_{l,min}$, the lower-surface, leading-edge pressure peak decreases in magnitude until it has disappeared at $\alpha = 0.01^\circ$

(fig. 6(n)). At this angle of attack, the profile-drag coefficient is minimum, and favorable pressure gradients exist along the upper surface to about 0.40c and along the lower surface to about 0.60c. As the angle of attack is increased further, the pressure gradient along the upper surface becomes less favorable until, at $\alpha = 3.06^{\circ}$, it is essentially flat (fig. 6(q)). As the angle of attack is increased even further, the position of minimum pressure on the upper surface moves slowly forward while the magnitude of the minimum pressure increases (figs. 6(r) to 6(y)). This feature was one of the design goals discussed in "Philosophy" and represents an improvement over the sudden forward jump of $c_{p,min}$, typical of the NACA 6-series airfoils. At $\alpha = 12.20^{\circ}$ (fig. 6(z)), the minimum pressure on the upper surface occurs at $x/c = 0.0$, thus forming a leading-edge peak. At $\alpha = 13.21^{\circ}$ (fig. 6(aa)), the lift coefficient is maximum, and turbulent trailing-edge separation has occurred on the upper surface at about 0.85c. The leading-edge peak continues to increase in magnitude, even beyond $c_{l,max}$, indicating that leading-edge separation does not occur (figs. 6(bb) to 6(dd)).

The pressure distributions for various angles of attack with a flap deflection of -10° at a Reynolds number of 6.0×10^6 and a Mach number of 0.10 are shown in figure 7. At $\alpha = -11.09^{\circ}$, -10.10°, and -9.07° (figs. 7(a) to 7(c)), the entire lower surface is separated. As the angle of attack is increased from -8.17° (fig. 7(d)), which corresponds to $c_{l,min}$, the lower-surface, leading-edge pressure peak decreases in magnitude. It should be noted that the kink (depression) in the upper-surface pressure distribution which occurs at approximately 0.75c is the result of the corner formed in the upper surface by the negative flap deflection. (See fig. 4(b).) Further negative flap deflection increases the magnitude of this depression and, correspondingly, the possibility of separation in the corner. Thus, the negative flap deflection is limited by the requirement of low drag. The minimum profile-drag coefficient occurs at $\alpha = 1.52^{\circ}$ despite the persistence of the lower-surface, leading-edge peak which the laminar flow apparently survives (fig. 7(p)). At $\alpha = 2.51^{\circ}$ (fig. 7(r)), the peak has disappeared and favorable pressure gradients exist along the upper surface to about 0.35c and along the lower surface to about 0.60c. As the angle of attack is increased further, the pressure gradient along the upper surface becomes less favorable until, at $\alpha = 4.05^{\circ}$, it is essentially flat (fig. 7(t)). As the angle of attack is increased even further, the position of minimum pressure on the upper surface moves slowly forward until, at $\alpha = 14.20^{\circ}$ (fig. 7(dd)), a leading-edge peak is formed. The maximum lift coefficient occurs at $\alpha = 15.25^{\circ}$ (fig. 7(ee)). The leading-edge peak continues to increase in magnitude, even beyond $c_{l,max}$, indicating that leading-edge separation does not occur (figs. 7(ff) to 7(hh)).

The pressure distributions for various angles of attack with a flap deflection of 10° at a Reynolds number of 6.0×10^6 and a Mach number of 0.10 are shown in figure 8. The kink (spike) in the upper-surface pressure distribution at approximately 0.75c is caused by the radius formed in the upper surface by the positive flap deflection. (See fig. 4(c).) At $\alpha = -11.18^{\circ}$ (fig. 8(a)), a sharp peak is evident in the lower-surface pressure distribution. As the angle of attack is increased, this peak decreases in magnitude until it has disappeared at $\alpha = -3.04^{\circ}$ (fig. 8(i)). At this angle of attack, the profile-drag coefficient is minimum and a favorable pressure gradient exists along the upper surface to about 0.45c. As the angle of attack is increased further, the

pressure gradient along the upper surface becomes less favorable until, at $\alpha = 1.05^{\circ}$, it is essentially flat (fig. 8(m)). As the angle of attack is increased even further, turbulent trailing-edge separation occurs on the upper surface (figs. 8(o) to 8(aa)). The maximum lift coefficient occurs at $\alpha = 12.20^{\circ}$ with the flow over the entire flap separated (fig. 8(x)). The leading-edge peak continues to increase in magnitude, even beyond $c_{l,max}$, indicating that leading-edge separation does not occur (figs. 8(y) to 8(aa)).

Transition Location

For a flap deflection of 0° and a Reynolds number of 3.0×10^6, the mechanism of the boundary-layer transition from laminar to turbulent flow on the upper surface, at an angle of attack of 0.0°, was a laminar separation bubble which extends from laminar separation to turbulent reattachment as shown in figure 9(a). This bubble occurred at about 0.5c and was caused by the slight adverse pressure gradient immediately downstream of the minimum pressure on the upper surface. (See fig. 6(n).) This gradient was a design goal as discussed in "Philosophy." At $\alpha = 2.0^{\circ}$ (fig. 9(b)), the laminar separation bubble has decreased in length and moved forward. At $\alpha = 4.0^{\circ}$ (fig. 9(c)), the laminar separation bubble has disappeared and transition has moved further forward.

Section Characteristics

Reynolds number effects.- The section characteristics with a flap deflection of 0° at a Mach number of 0.10 are shown in figure 10. The effects of Reynolds number on the section characteristics with this flap deflection are summarized in figure 11. The angle of attack for zero lift coefficient, approximately -5.8°, was unaffected by Reynolds number. The lift-curve slope and pitching-moment coefficients were relatively insensitive to Reynolds number variation. The maximum lift coefficient increased substantially with increasing Reynolds number, whereas the minimum drag coefficient and the width of the low-drag range decreased significantly.

The section characteristics with a flap deflection of -10° at a Mach number of 0.10 are shown in figure 12. The effects of Reynolds number on the section characteristics with this flap deflection are summarized in figure 13. The angle of attack for zero lift coefficient, approximately -0.2°, was unaffected by Reynolds number. The lift-curve slope and pitching-moment coefficients were also unaffected by Reynolds number. The maximum lift coefficient increased moderately with increasing Reynolds number, whereas the minimum drag coefficient and the width of the low-drag range decreased significantly.

The section characteristics with a flap deflection of 10° at a Mach number of 0.10 are shown in figure 14. The effects of Reynolds number on the section characteristics with this flap deflection are summarized in figure 15. The abrupt change in lift-curve slope at a lift coefficient of about 1.4 was caused by a forward jump of the transition location on the upper surface. This jump was caused by a disturbance generated by the chordwise orifices (fig. 16). The premature transition led to premature, turbulent trailing-edge separation and,

thus, a reduction in lift-curve slope. Premature transition also occurred with a flap deflection of 0°, although it did not result in such a sudden trailing-edge separation (fig. 17). This phenomenon does, however, explain the change in lift-curve slope evident in figure 10(a).

Mach number effects.- The effects of Mach number on the section characteristics with a flap deflection of 0° for a Reynolds number of 6.0×10^6 are summarized in figure 18. The angle of attack for zero lift coefficient was unaffected by Mach number. The lift-curve slope increased moderately with increasing Mach number, whereas the pitching-moment coefficients decreased. The maximum lift coefficient decreased slightly with increasing Mach number (fig. 19), whereas the minimum drag coefficient was unaffected (fig. 20).

Effect of roughness.- The effect of roughness on the section characteristics with a flap deflection of 0° for various Reynolds numbers is shown in figure 21. The angle of attack for zero lift coefficient as well as the pitching-moment coefficients increased with transition fixed, whereas the lift-curve slope decreased. All these results are a consequence of the boundary-layer displacement effect which decambers the airfoil slightly; the displacement thickness is greater for the transition-fixed condition than for the transition-free condition. Increasing Reynolds number decreases the displacement thickness and, therefore, the displacement effect.

Of more importance, however, is the effect of roughness on the maximum lift coefficient and on the drag coefficients. The addition of roughness had essentially no effect on $c_{l,max}$ for any of the Reynolds numbers. Thus, one of the most important design requirements has been achieved. (See "Objectives and Constraints.") The drag coefficients were, of course, adversely affected by the roughness.

The effect of roughness on the section characteristics with flap deflections of -10° and 10° for various Reynolds numbers is shown in figures 22 and 23, respectively. All the previously mentioned effects are again apparent.

Effect of flap deflection.- The effect of flap deflection on the section characteristics for various Reynolds numbers with transition free is shown in figure 24. The effects of flap deflection and roughness on maximum lift coefficient and minimum drag coefficient are summarized in figures 25 and 26, respectively.

COMPARISON OF THEORETICAL AND EXPERIMENTAL RESULTS

Pressure Distributions

The comparison of theoretical and experimental pressure distributions is shown in figure 27. The pressure distributions predicted by the method of reference 8 are inviscid (potential-flow) and incompressible. The experimental pressure distributions were obtained for a Reynolds number of 6.0×10^6 and a Mach number of 0.10 and, thus, contain the same data presented in figures 6(n), 7(p), and 8(l). With a flap deflection of 0° at an angle of attack of 0.01° (fig. 27(a)), the theoretical predictions and the experimental data are in close

agreement. Although the values of the pressure coefficients do not match exactly, the pressure gradients agree well. With a flap deflection of -10° at an angle of attack of 1.52° (fig. 27(b)), the agreement between theory and experiment is very good. With a flap deflection of 10° at an angle of attack of 0.05° (fig. 27(c)), the decambering viscous effects have become more apparent and the disparities include small differences in the pressure gradients as well as larger differences in the values of the pressure coefficients.

Section Characteristics

The theoretical section characteristics were computed by the method of reference 8. A boundary layer is calculated using the potential-flow pressure distribution. However, no iteration between the boundary-layer displacement thickness and the pressure distribution is performed. The lift and pitching-moment coefficients are determined from the potential flow and then some simple viscous corrections are applied including a correction for boundary-layer separation. The profile-drag coefficients are obtained by applying a modified Squire-Young formula to the boundary-layer characteristics at the trailing edge.

The comparison of theoretical and experimental section characteristics with a flap deflection of 0° and transition free is shown in figure 28. The magnitudes of both the angle of attack for zero lift coefficient and the pitching-moment coefficients are overpredicted by the method of reference 8 (fig. 28(c)). These results are obtained because the theoretical method does not contain a boundary-layer displacement iteration. The agreement between theoretical and experimental lift-curve slopes is good. The maximum lift coefficients are overpredicted by the method of reference 8 although the agreement improves slightly with increasing Reynolds number. Past experience indicates that this overprediction is not typical of the method of reference 8. (For example, see ref. 9.) The calculated drag coefficients agree well with the experimental data and become increasingly conservative (high) with increasing Reynolds number.

The comparison of theoretical and experimental section characteristics with a flap deflection of -10° and transition free is shown in figure 29. Because the displacement effect with this flap deflection is small, the agreement between theoretical and experimental angles of zero lift coefficient, lift-curve slopes, and pitching-moment coefficients is very good. At the higher angles of attack, the theoretical method predicts separation in the corner formed in the upper surface by the negative flap deflection; therefore, a realistic estimate of the maximum lift coefficient is not possible. The calculated drag coefficients agree well with the experimental data and again become increasingly conservative (high) with increasing Reynolds number. The disparity in the lower limit of the low-drag range is attributed to the increased turbulence in the wind tunnel at the higher Reynolds numbers. (See ref. 10.)

The comparison of theoretical and experimental section characteristics with a flap deflection of 10° and transition free is shown in figure 30. The magnitudes of both the lift and pitching-moment coefficients are overpredicted by the method of reference 8. The agreement between theoretical and experimental lift-curve slopes is good up to the angle of attack at which separation occurs on the upper suface of the flap. The maximum lift coefficients are overpredicted

by the method of reference 8. The calculated drag coefficients agree well with the experimental data over the range of lift coefficients for which little separation occurs. The predicted drag coefficients become increasingly conservative (high) with increasing Reynolds number. At the lower angles of attack, the theoretical method predicts separation in the corner formed in the lower surface by the positive flap deflection; therefore, the calculated results are not realistic and, accordingly, have not been included. No comparison for $R = 2.0 \times 10^6$ has been made because the theoretical method predicts separation in the corner at all angles of attack for this Reynolds number.

The comparisons of theoretical and experimental section characteristics with transition fixed and flap deflections of 0°, -10°, and 10° are shown in figures 31, 32, and 33, respectively. The results are the same as for the transition-free condition except that the small differences between the theoretical and experimental drag coefficients do not increase with increasing Reynolds number.

CONCLUDING REMARKS

A flapped natural-laminar-flow airfoil for general aviation applications, the NLF(1)-0215F, has been designed and analyzed theoretically and verified experimentally in the Langley Low-Turbulence Pressure Tunnel. The basic objective of combining the high maximum lift of the NASA low-speed airfoils with the low cruise drag of the NACA 6-series airfoils has been achieved. The safety requirement that the maximum lift coefficient not be significantly affected with transition fixed near the leading edge has also been met. Comparisons of the theoretical and experimental results show generally good agreement.

The most important result is that the new natural-laminar-flow airfoil achieves maximum lift coefficients similar to those of the NASA low-speed airfoils even with transition fixed near the leading edge. At the same time, the new airfoil with transition fixed exhibits no higher cruise drag than comparable turbulent-flow airfoils. Thus, if the new airfoil is employed in an aircraft design and laminar flow is not achieved, nothing is lost relative to the NASA low-speed airfoils. If laminar flow is achieved, a very substantial profile-drag reduction results.

Finally, this airfoil demonstrates the unique and powerful capabilities of the theoretical method to design and analyze multipoint designs, including those which incorporate simple flaps.

Langley Research Center
National Aeronautics and Space Administration
Hampton, VA 23665
April 13, 1981

REFERENCES

1. McGhee, Robert J.; Beasley, William D.; and Whitcomb, Richard T.: NASA Low- and Medium-Speed Airfoil Development. NASA TM-78709, 1979.

2. Jacobs, Eastman N.: Preliminary Report on Laminar-Flow Airfoils and New Methods Adopted for Airfoil and Boundary-Layer Investigations. NACA WR L-345, 1939 (formerly, NACA ACR).

3. Abbott, Ira H.; Von Doenhoff, Albert E.; and Stivers, Louis S., Jr.: Summary of Airfoil Data. NACA Rep. 824, 1945. (Supersedes NACA WR L-560.)

4. Payne, Henry E.: Laminar Flow Rethink - Using Composite Structure. [Preprint] 760473, Soc. Automot. Eng., Apr. 1976.

5. Alther, G. A.: A Significant Role for Composites in Energy-Efficient Aircraft. Technical Sessions of the Thirty-Sixth Annual Conference - Reinforced Plastics/Composites Institute, Soc. Plast. Ind., Inc., Feb. 1981, Sess. 12-D, pg. 1 - Sess. 12-D, pg. 4.

6. Eppler, R. (Francesca Neffgen, transl.): Laminar Airfoils for Reynolds Numbers Greater Than 4×10^6. B-819-35, Apr. 1969. (Available from NTIS as N69-28178.)

7. Eppler, Richard: Some New Airfoils. Science and Technology of Low Speed and Motorless Flight, NASA CP-2085, Part I, 1979, pp. 131-153.

8. Eppler, Richard; and Somers, Dan M.: A Computer Program for the Design and Analysis of Low-Speed Airfoils. NASA TM-80210, 1980.

9. Somers, Dan M.: Design and Experimental Results for a Natural-Laminar-Flow Airfoil for General Aviation Applications. NASA TP-1861, 1981.

10. Von Doenhoff, Albert E.; and Abbott, Frank T., Jr.: The Langley Two-Dimensional Low-Turbulence Pressure Tunnel. NACA TN 1283, 1947.

11. Pankhurst, R. C.; and Holder, D. W.: Wind-Tunnel Technique. Sir Isaac Pitman & Sons, Ltd. (London), 1965.

12. Pfenninger, Werner: Investigations on Reductions of Friction on Wings, in Particular by Means of Boundary Layer Suction. NACA TM 1181, 1947.

13. Wortmann, F. X.: Experimental Investigations on New Laminar Profiles for Gliders and Helicopters. TIL/T.4906, British Minist. Aviat., Mar. 1960.

14. Stratford, B. S.: The Prediction of Separation of the Turbulent Boundary Layer. J. Fluid Mech., vol. 5, pt. 1, Jan. 1959, pp. 1-16.

15. Eppler, Richard; and Somers, Dan M.: Low Speed Airfoil Design and Analysis. Advanced Technology Airfoil Research - Volume I, NASA CP-2045, Part 1, 1979, pp. 73-99.

16. Eppler, Richard: The Effect of Disturbances on a Wing. Science and Technology of Low Speed and Motorless Flight, NASA CP-2085, Part 1, 1979, pp. 81-91.

17. Braslow, Albert L.; and Knox, Eugene C.: Simplified Method for Determination of Critical Height of Distributed Roughness Particles for Boundary-Layer Transition at Mach Numbers from 0 to 5. NACA TN 4363, 1958.

18. Loving, Donald L.; and Katzoff, S.: The Fluorescent-Oil Film Method and Other Techniques for Boundary-Layer Flow Visualization. NASA MEMO 3-17-59L, 1959.

19. Allen, H. Julian; and Vincenti, Walter G.: Wall Interference in a Two-Dimensional-Flow Wind Tunnel, With Consideration of the Effect of Compressibility. NACA Rep. 782, 1944. (Supersedes NACA WR A-63.)

TABLE I.- NLF(1)-0215F AIRFOIL COORDINATES ($\delta_f = 0^o$)

[c = 60.960 cm (24.000 in.)]

UPPER SURFACE		LOWER SURFACE	
X/C	Z/C	X/C	Z/C
.00240	.00917	.00000	-.00006
.00909	.01947	.00245	-.00704
.02004	.03027	.01099	-.01211
.03527	.04120	.02592	-.01656
.05469	.05201	.04653	-.02052
.07816	.06250	.07242	-.02399
.10546	.07247	.10324	-.02699
.13635	.08175	.13854	-.02954
.17050	.09019	.17788	-.03166
.20758	.09761	.22073	-.03334
.24720	.10389	.26654	-.03456
.28894	.10887	.31473	-.03531
.33237	.11240	.36468	-.03554
.37702	.11428	.41576	-.03519
.42253	.11427	.46731	-.03415
.46864	.11219	.51867	-.03225
.51524	.10784	.56920	-.02925
.56247	.10147	.61825	-.02441
.61010	.09373	.66662	-.01663
.65752	.08513	.71614	-.00705
.70408	.07603	.76645	.00167
.74914	.06673	.81565	.00804
.79206	.05746	.86198	.01155
.83222	.04844	.90359	.01198
.86902	.03983	.93862	.00990
.90193	.03175	.96588	.00655
.93044	.02428	.98504	.00323
.95409	.01737	.99630	.00086
.97285	.01082	1.00000	.00000
.98710	.00507		
.99658	.00126		
1.00000	.00000		

TABLE II.- MODEL ORIFICE LOCATIONS

[c = 60.960 cm (24.000 in.)]

UPPER SURFACE		LOWER SURFACE	
X/C	Z/C	X/C	Z/C
.000146	.000625	.000146	.000625
.005713	.015346	.004379	-.008742
.010538	.021233	.009975	-.011800
.015313	.026138	.014979	-.013642
.020421	.030596	.019983	-.015133
.025425	.034479	.024892	-.016396
.030733	.038267	.030021	-.017546
.040425	.044354	.040096	-.019488
.050333	.049808	.050096	-.021129
.060283	.054721	.059950	-.022500
.075242	.061313	.074850	-.024288
.100425	.070779	.099883	-.026733
.150950	.085604	.149996	-.030225
.200571	.096329	.200117	-.032592
.250650	.104325	.250071	-.034142
.300717	.109963	.299896	-.035092
.350792	.113358	.350188	-.035454
.400571	.114463	.400063	-.035317
.450671	.113167	.449963	-.034513
.500904	.109354	.499933	-.033013
.550633	.103158	.550167	-.030417
.600850	.095242	.600188	-.026417
.650742	.086363	.649913	-.019392
.700500	.076742	.699396	-.010138
.746638	.067304	.745754	-.001542
.802404	.055258	.800988	.006450
.851800	.044013	.851267	.011025
.901758	.031804	.899833	.012079
.950917	.018442	.948883	.008863
.974675	.010325	.974208	.005071

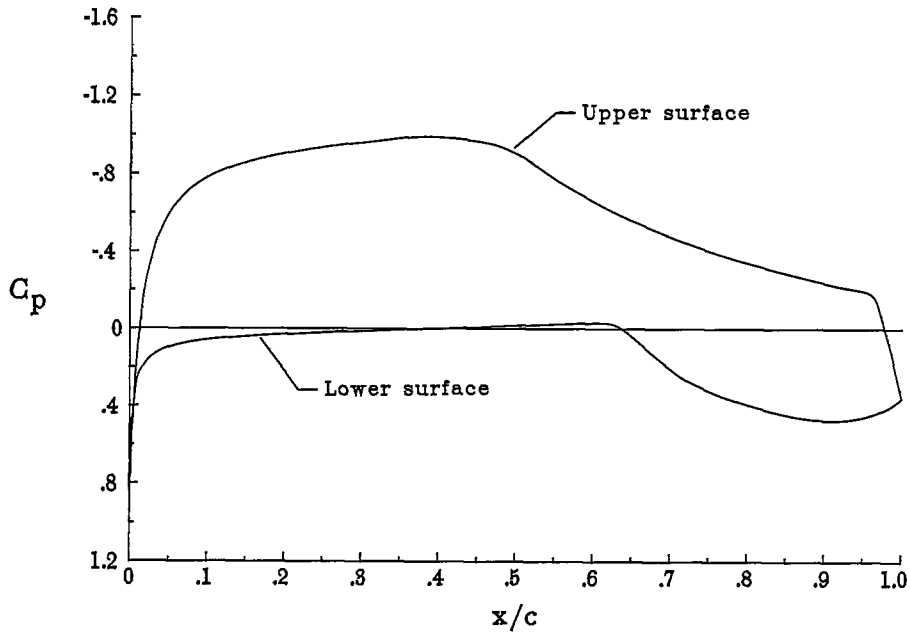

(a) $c_l = 0.7$; $\delta_f = 0^o$.

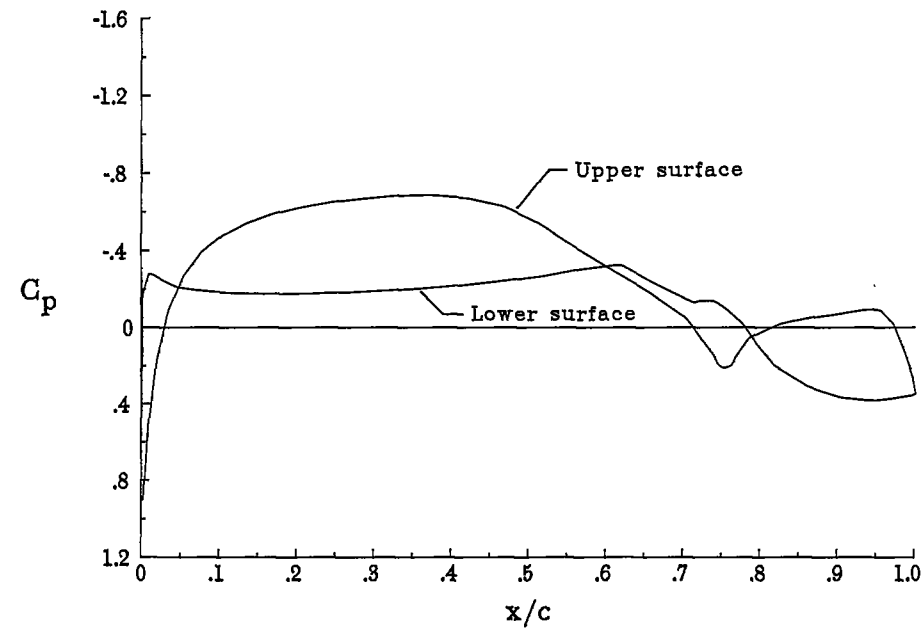

(b) $c_l = 0.2$; $\delta_f = -10^o$.

Figure 1.- Inviscid pressure distributions.

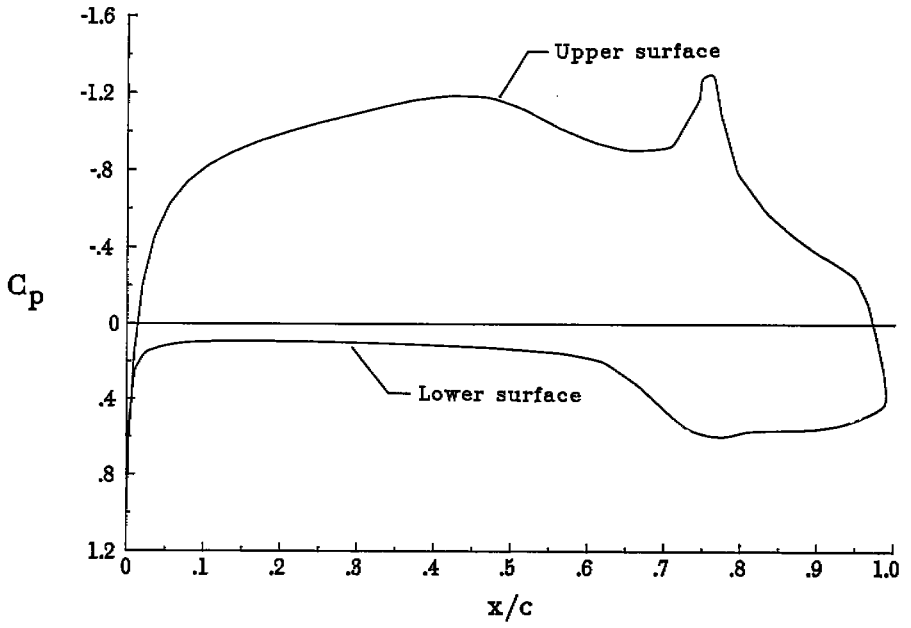

(c) $c_l = 1.0$; $\delta_f = 10^o$.

Figure 1.- Concluded.

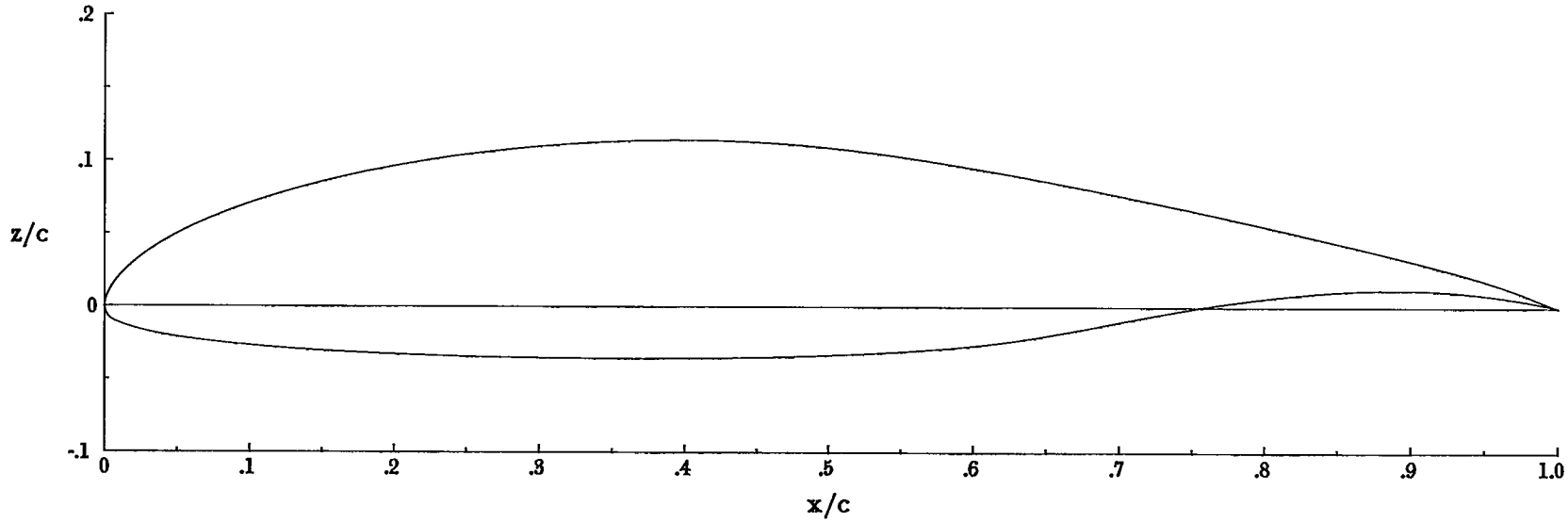

(a) $\delta_f = 0^o$.

Figure 2.- NLF(1)-0215F airfoil shape.

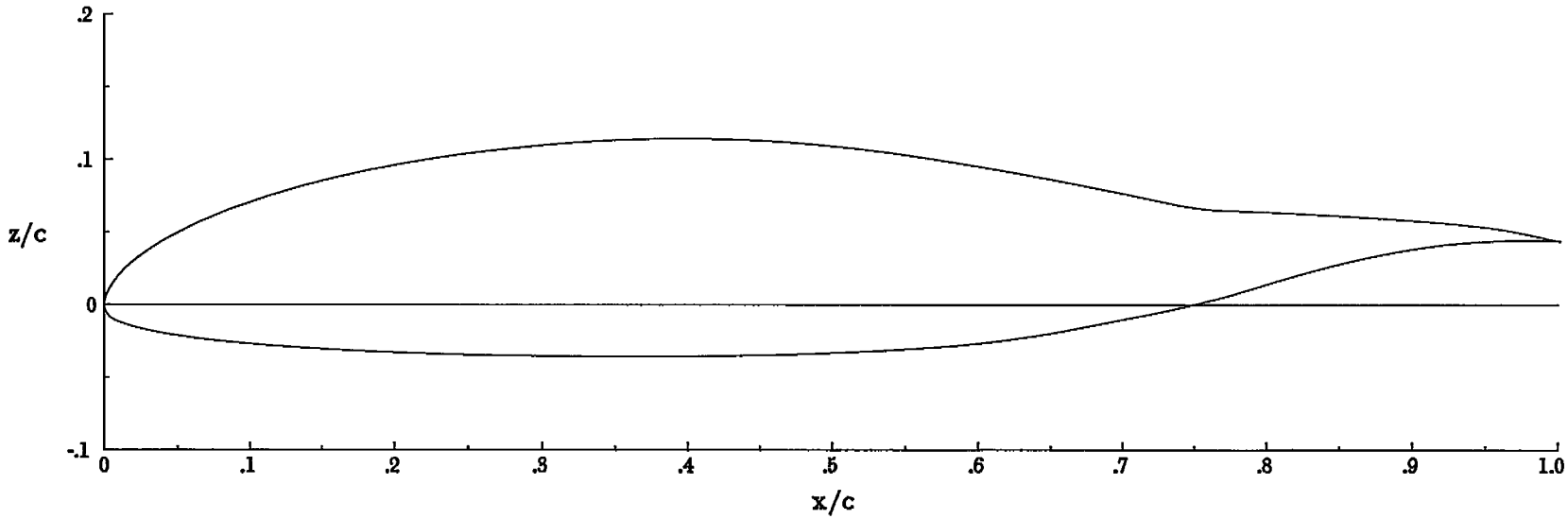

(b) $\delta_f = -10^o$.

Figure 2.- Continued.

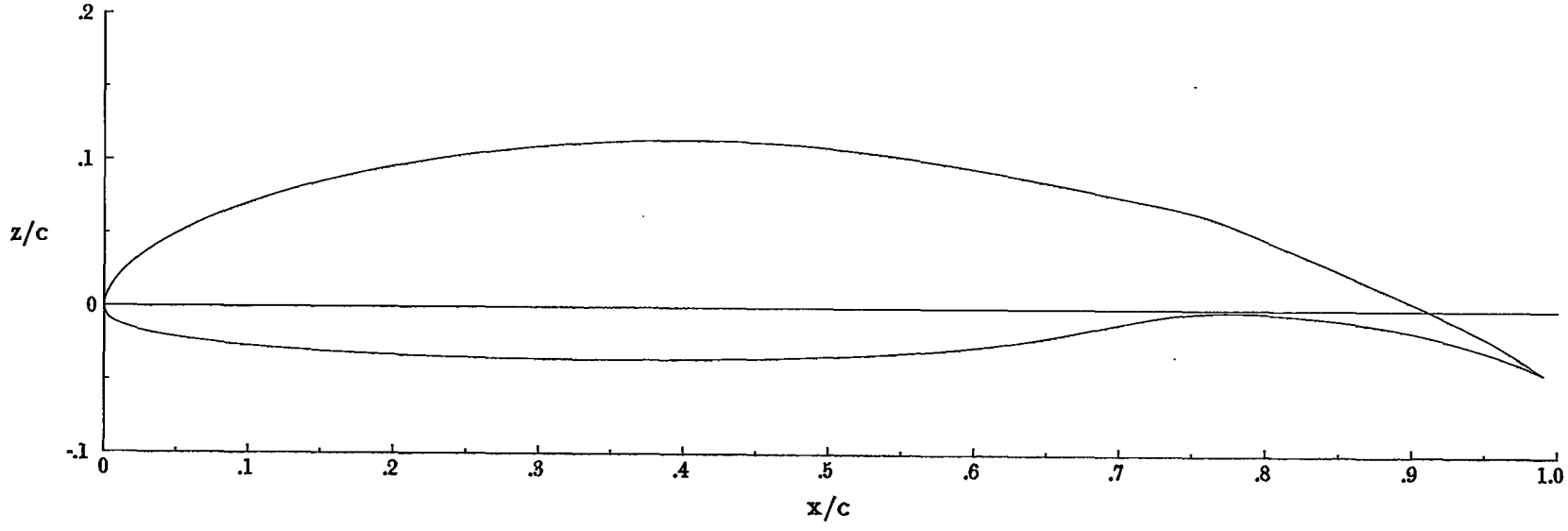

(c) $\delta_f = 10^o$.

Figure 2.- Concluded.

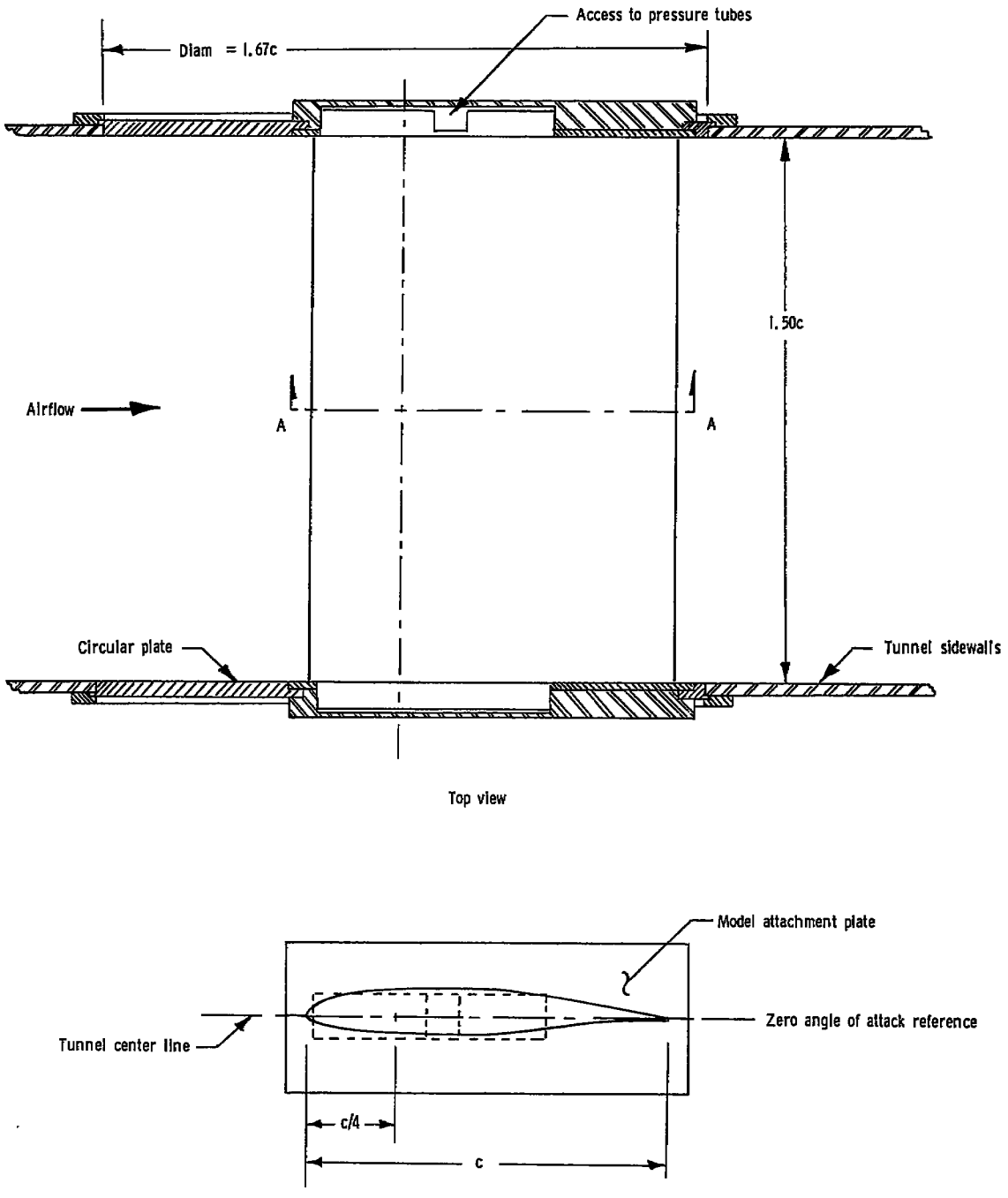

Figure 3.- Typical airfoil model mounted in wind tunnel. All dimensions are in terms of model chord, c = 61.0 cm (24.0 in.).

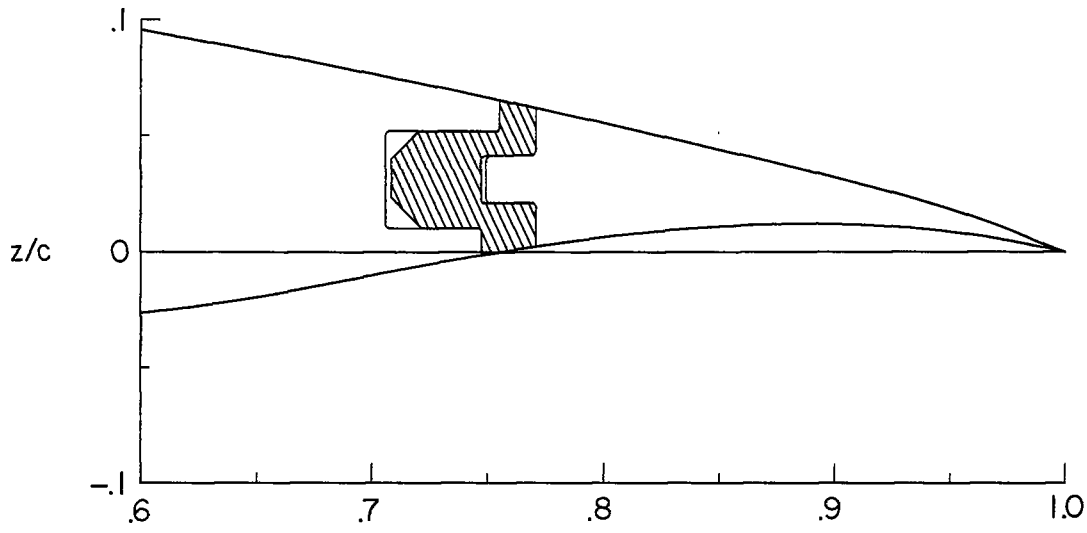

(a) $\delta_f = 0°$.

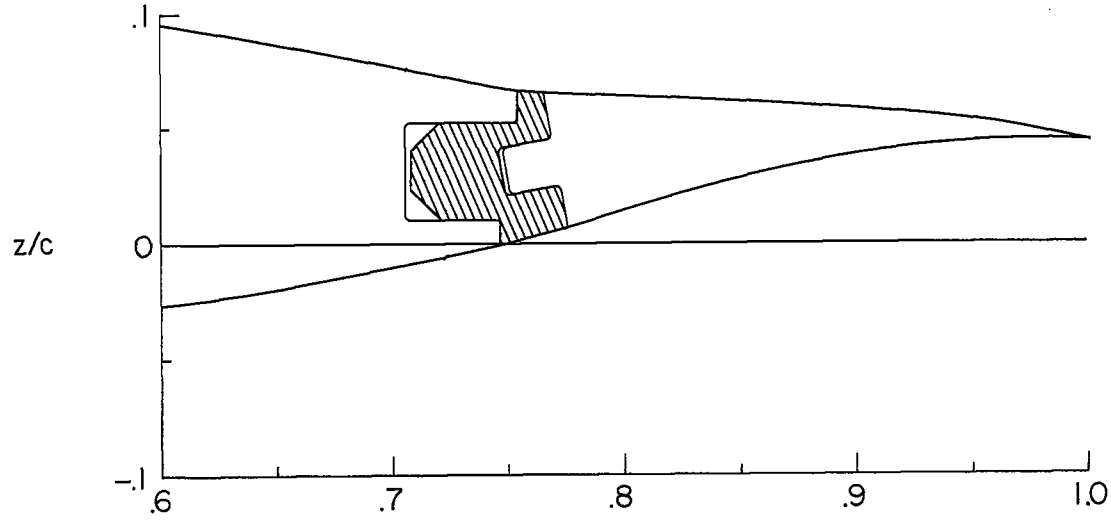

(b) $\delta_f = -10°$.

Figure 4.- Flap brackets.

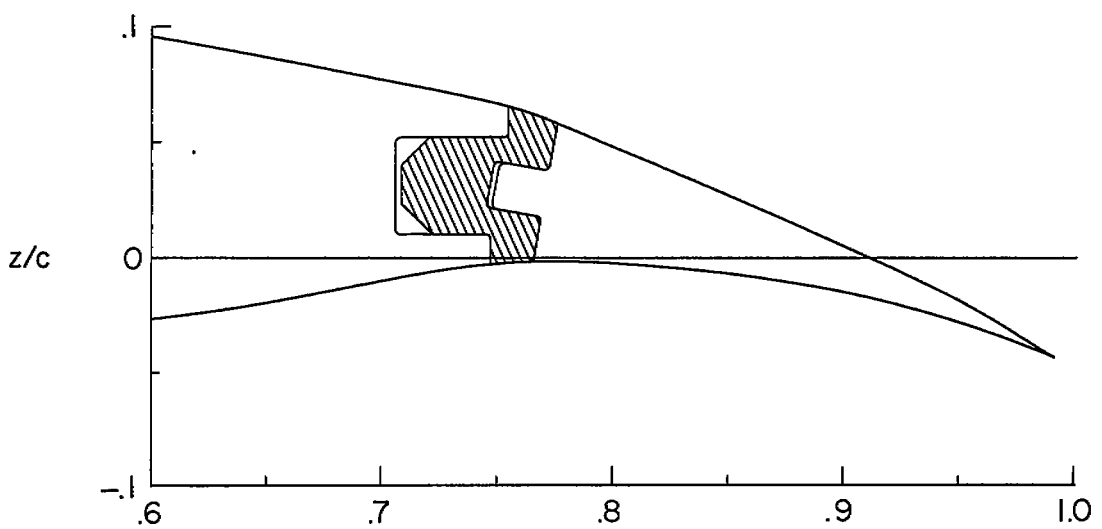

(c) $\delta_f = 10^o$.

Figure 4.- Concluded.

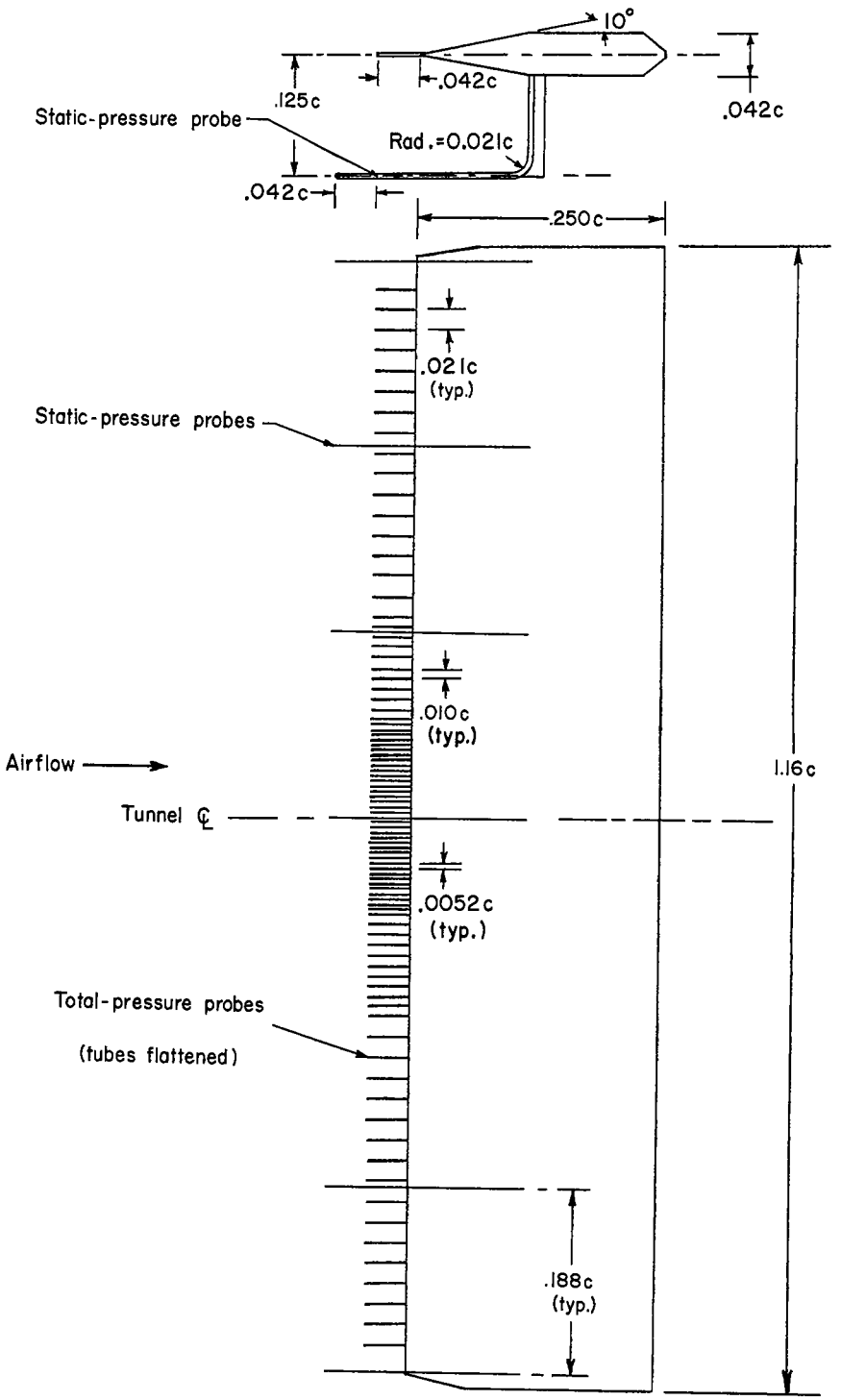

Figure 5.- Wake rake. All dimensions are in terms of model chord, c = 61.0 cm (24.0 in.).

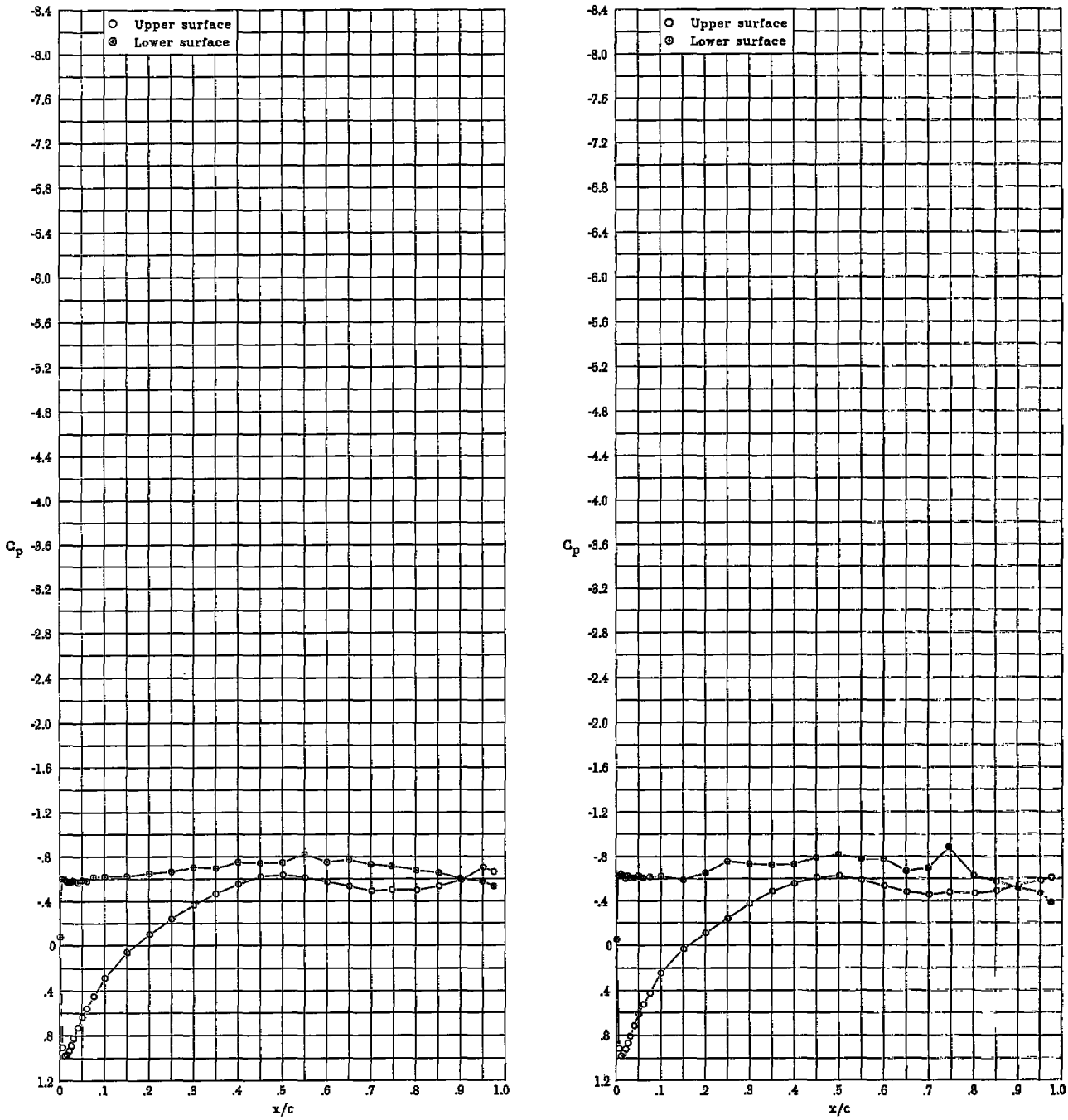

(a) $\alpha = -13.08^{\circ}$; $c_l = -0.288$; $c_d = 0.1781$; $c_m = 0.001$.

(b) $\alpha = -12.08^{\circ}$; $c_l = -0.299$; $c_d = 0.1758$; $c_m = 0.001$.

Figure 6.- Pressure distributions with $\delta_f = 0^{\circ}$ for $R = 6.0 \times 10^6$ and $M = 0.10$.

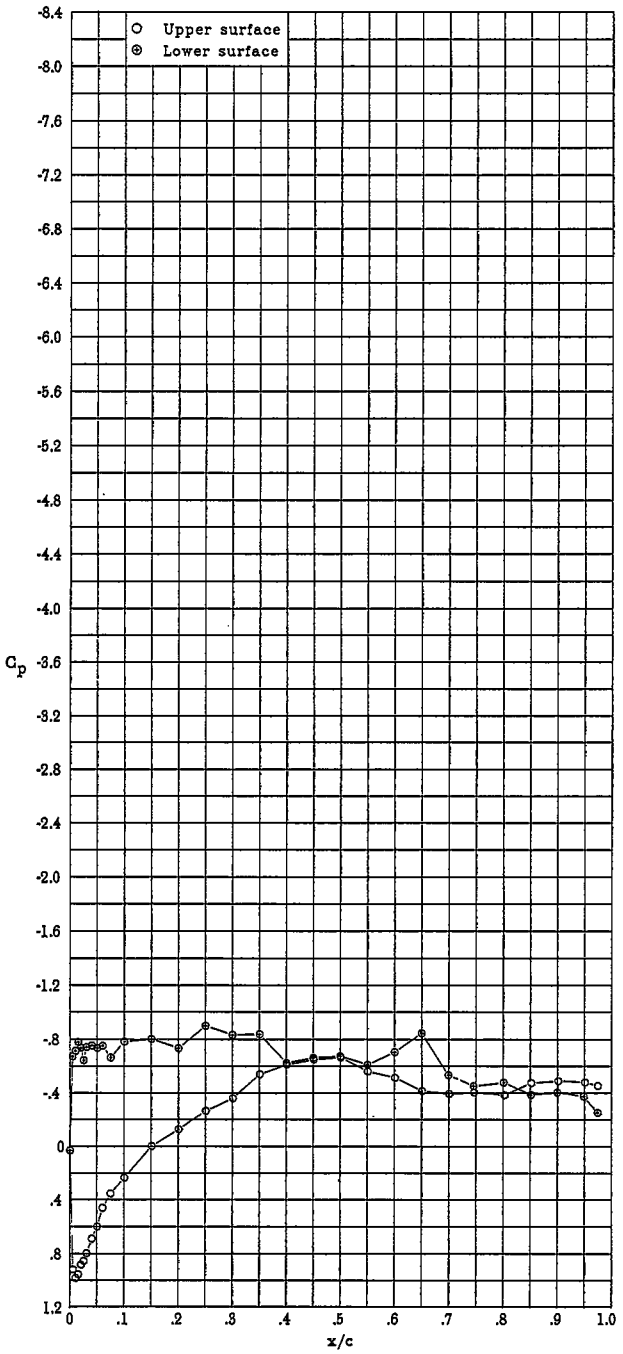

(c) $\alpha = -11.08^\circ$; $c_l = -0.287$; $c_d = 0.1544$; $c_m = -0.022$.

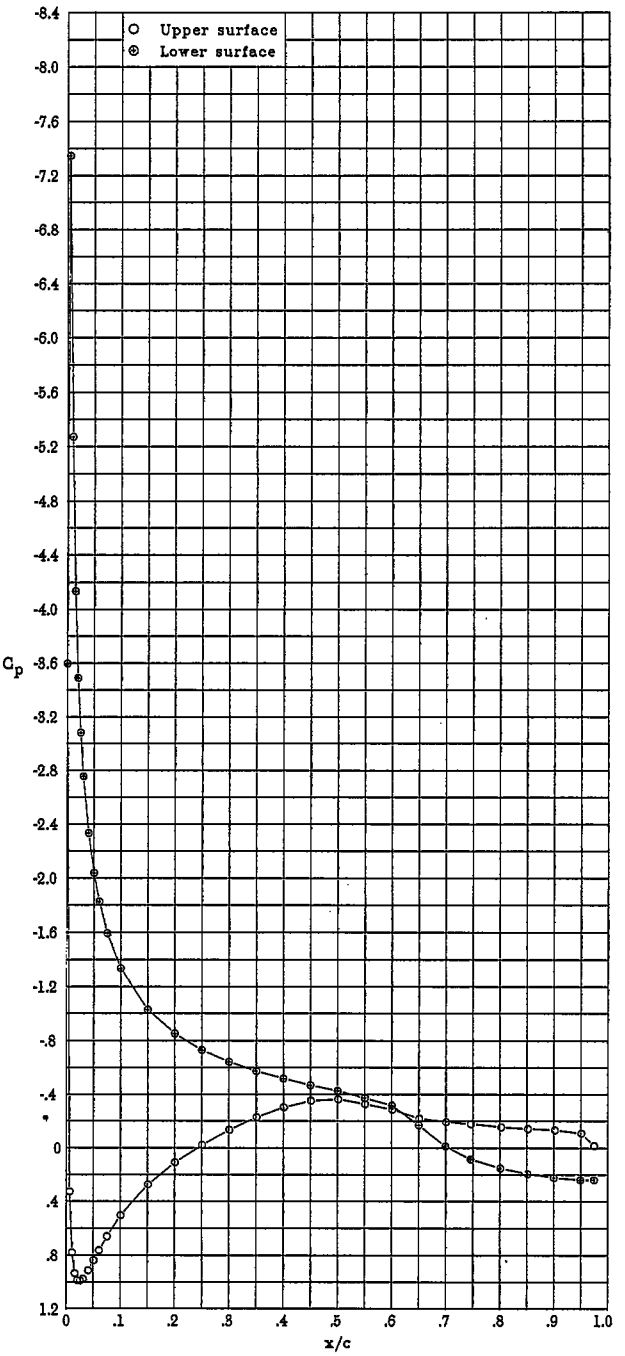

(d) $\alpha = -10.15^\circ$; $c_l = -0.482$; $c_d = 0.0121$; $c_m = -0.125$.

Figure 6.- Continued.

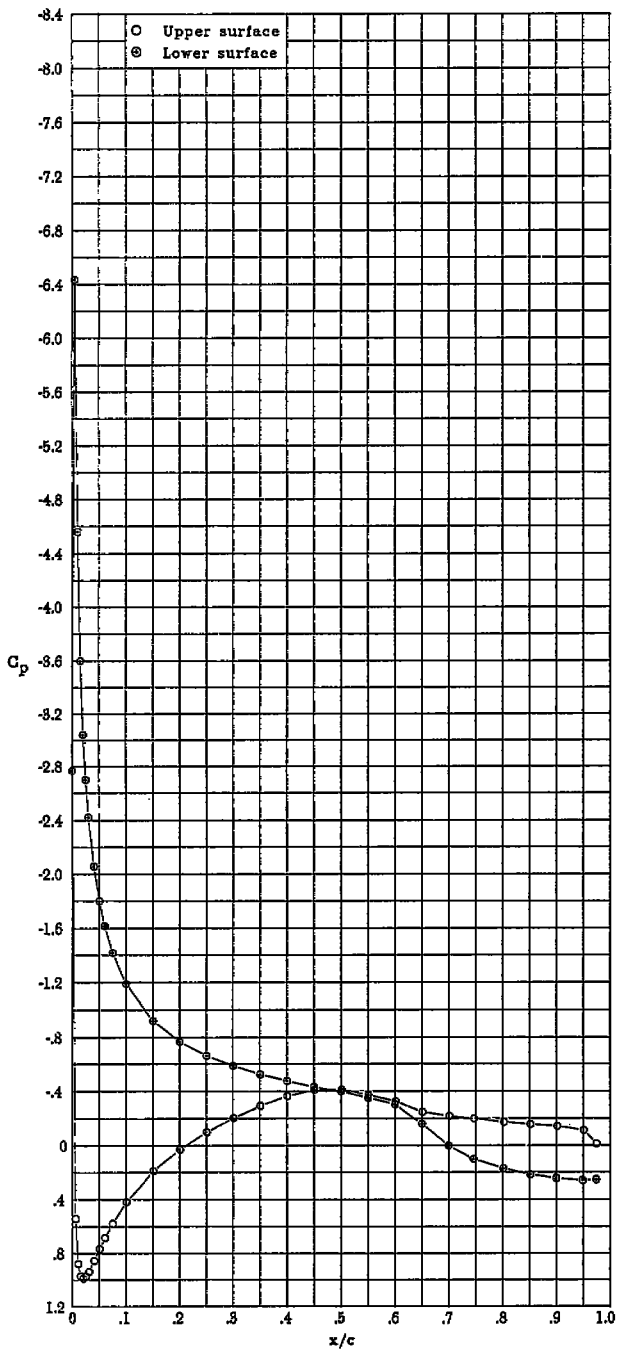

(e) $\alpha = -9.17^{\circ}$; $c_l = -0.375$; $c_d = 0.0105$; $c_m = -0.128$.

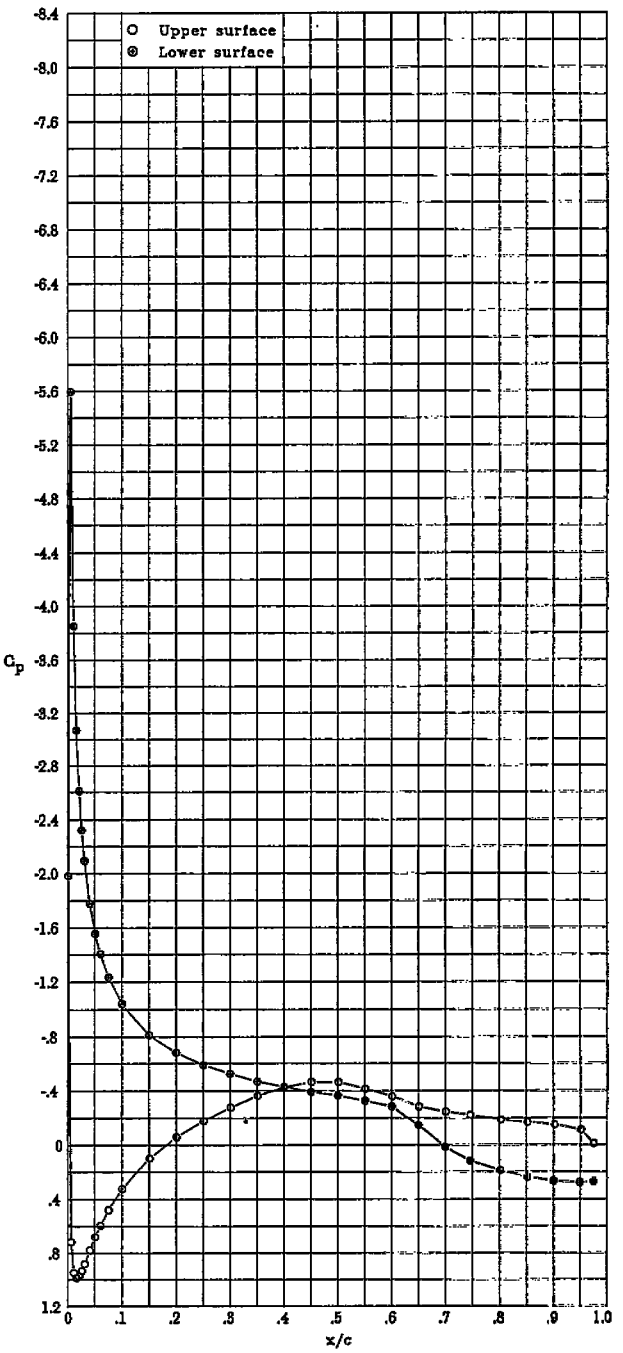

(f) $\alpha = -8.15^{\circ}$; $c_l = -0.264$; $c_d = 0.0090$; $c_m = -0.130$.

Figure 6.- Continued.

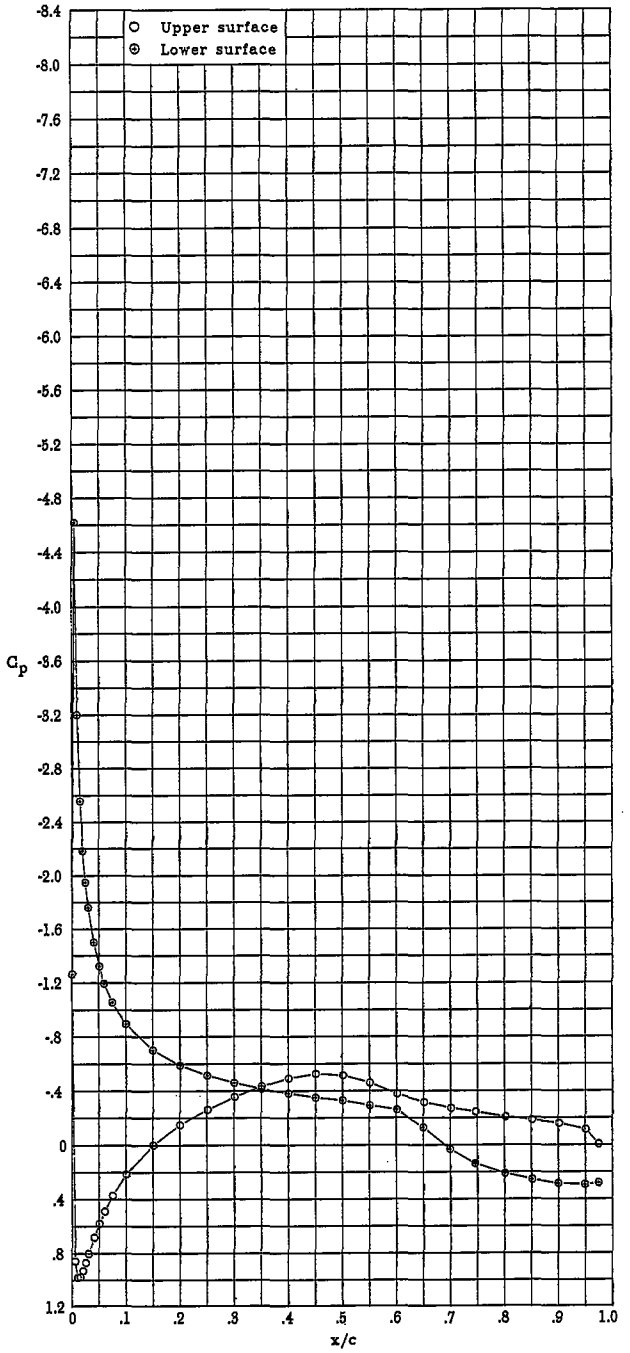

(g) $\alpha = -7.11^\circ$; $c_l = -0.149$; $c_d = 0.0078$; $c_m = -0.132$.

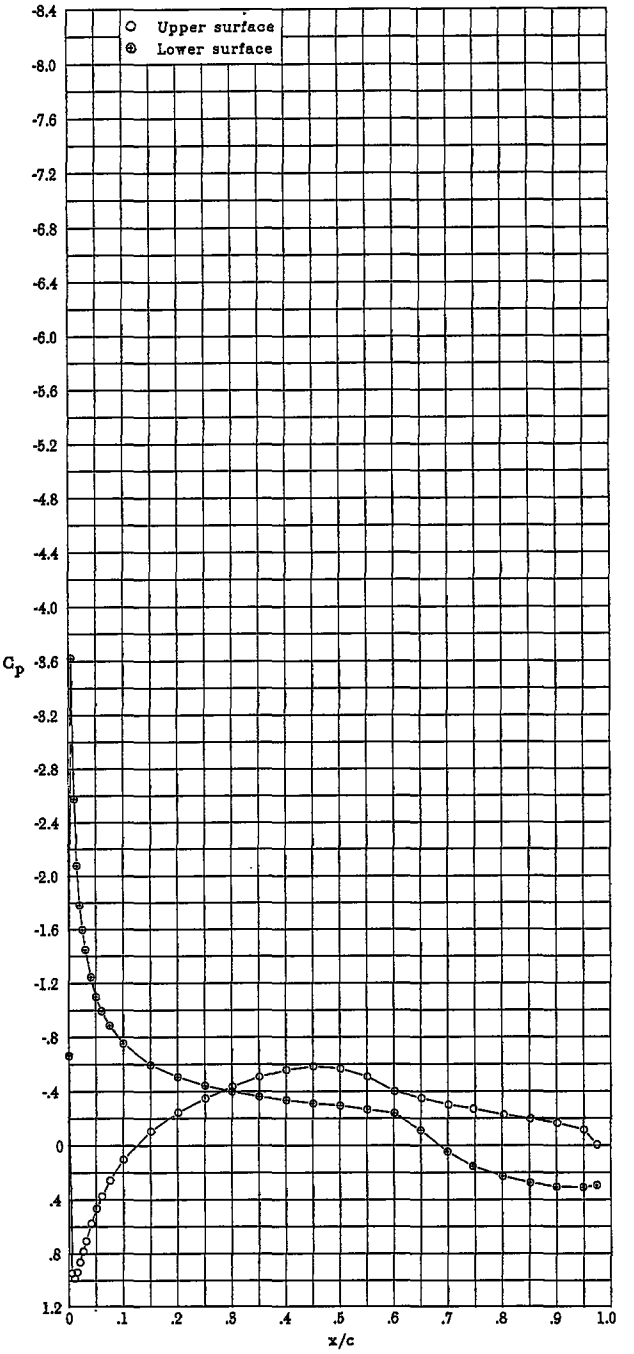

(h) $\alpha = -6.08^\circ$; $c_l = -0.034$; $c_d = 0.0075$; $c_m = -0.134$.

Figure 6.- Continued.

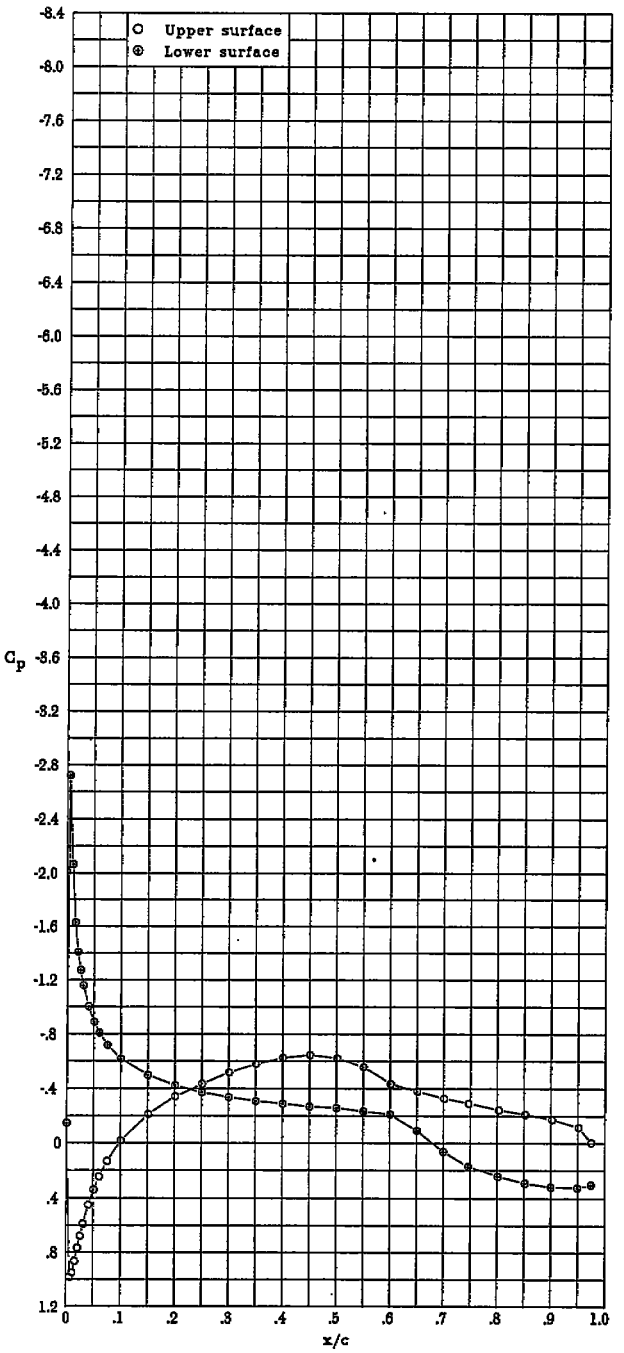

(i) $\alpha = -5.09^{\circ}$; $c_l = 0.081$; $c_d = 0.0074$; $c_m = -0.136$.

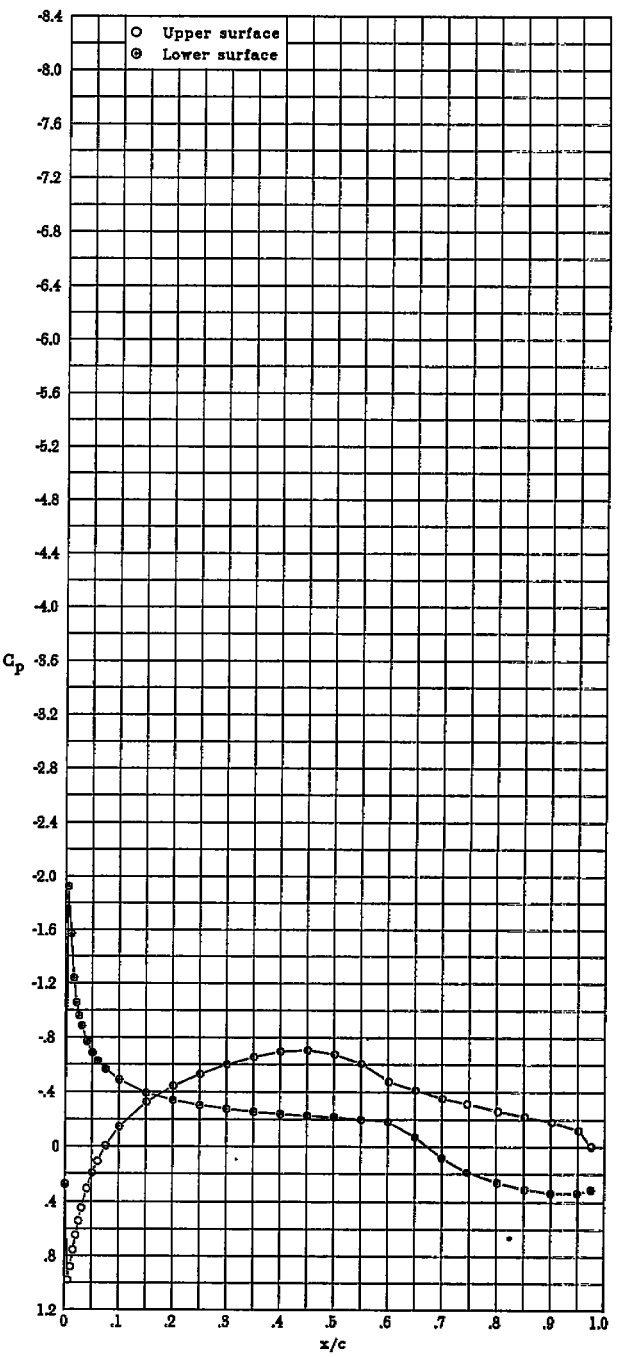

(j) $\alpha = -4.05^{\circ}$; $c_l = 0.198$; $c_d = 0.0071$; $c_m = -0.139$.

Figure 6.- Continued.

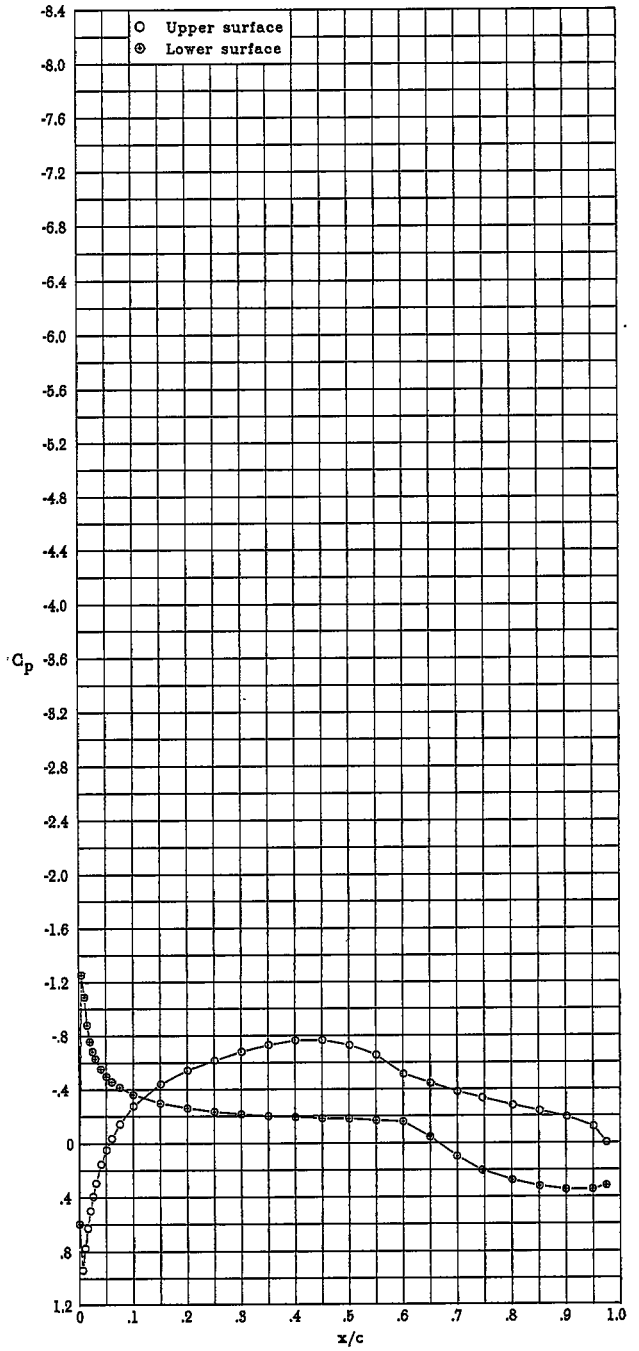

(k) $\alpha = -3.05^\circ$; $c_l = 0.312$; $c_d = 0.0068$; $c_m = -0.141$.

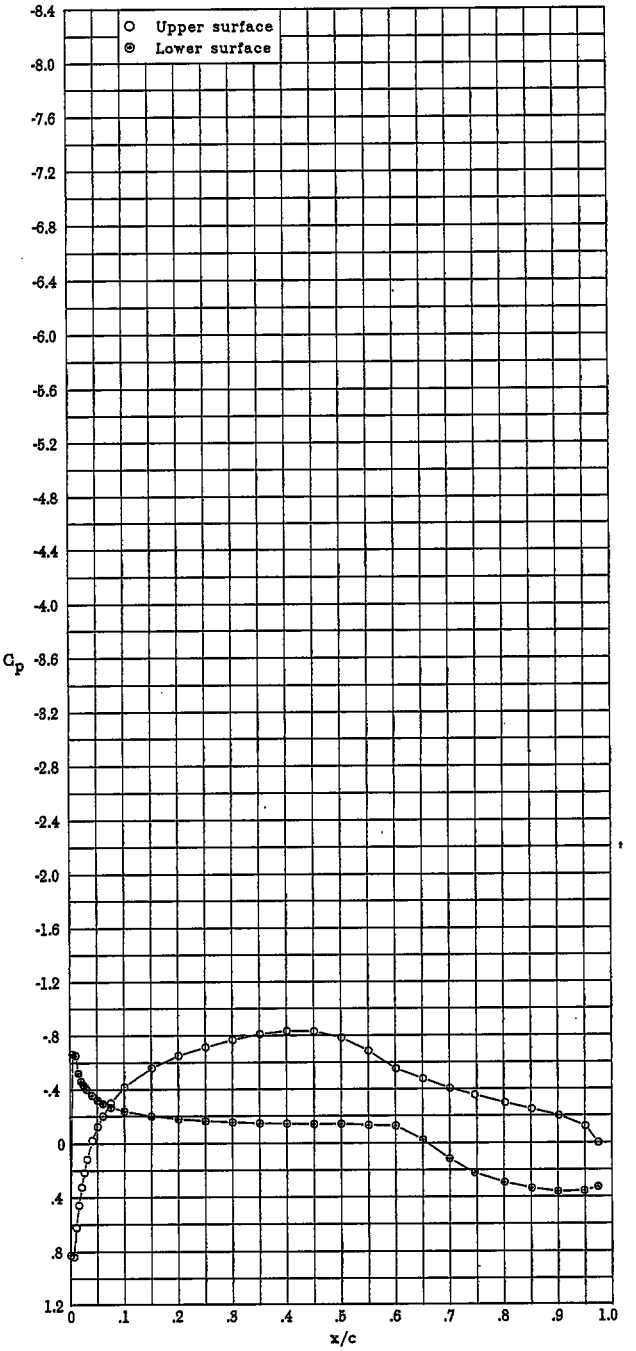

(l) $\alpha = -2.04^\circ$; $c_l = 0.428$; $c_d = 0.0062$; $c_m = -0.144$.

Figure 6.- Continued.

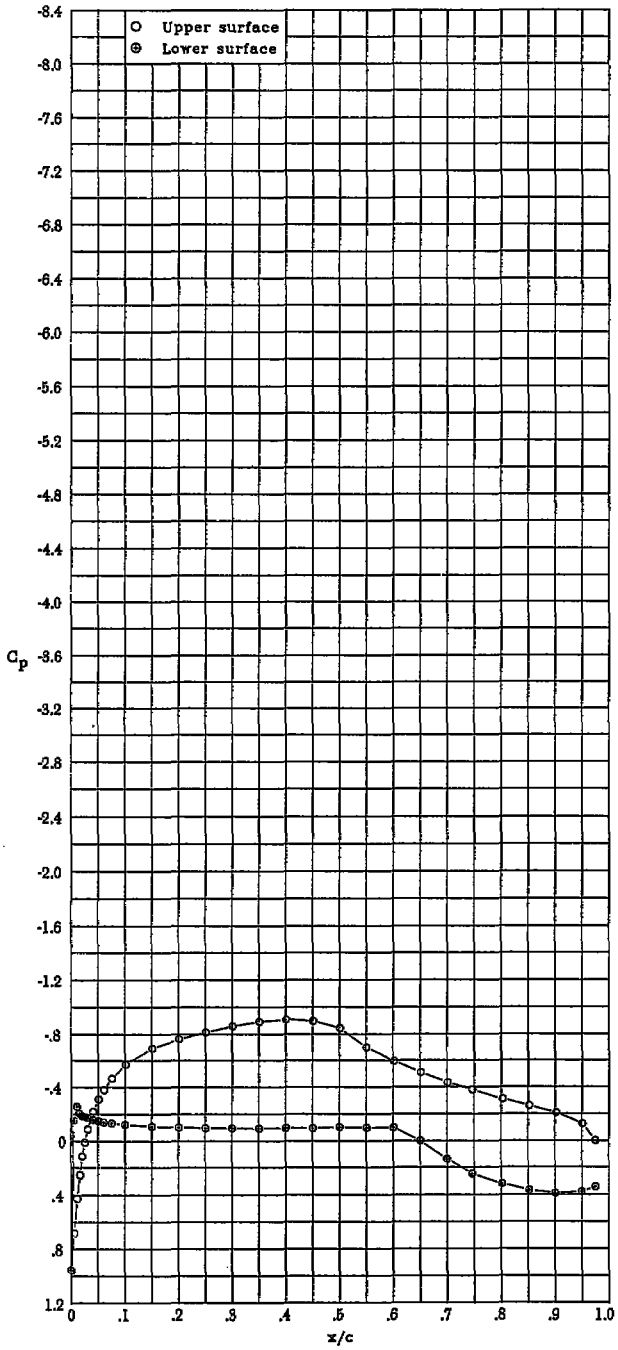

(m) $\alpha = -1.02^{\circ}$; $c_l = 0.550$; $c_d = 0.0049$; $c_m = -0.147$.

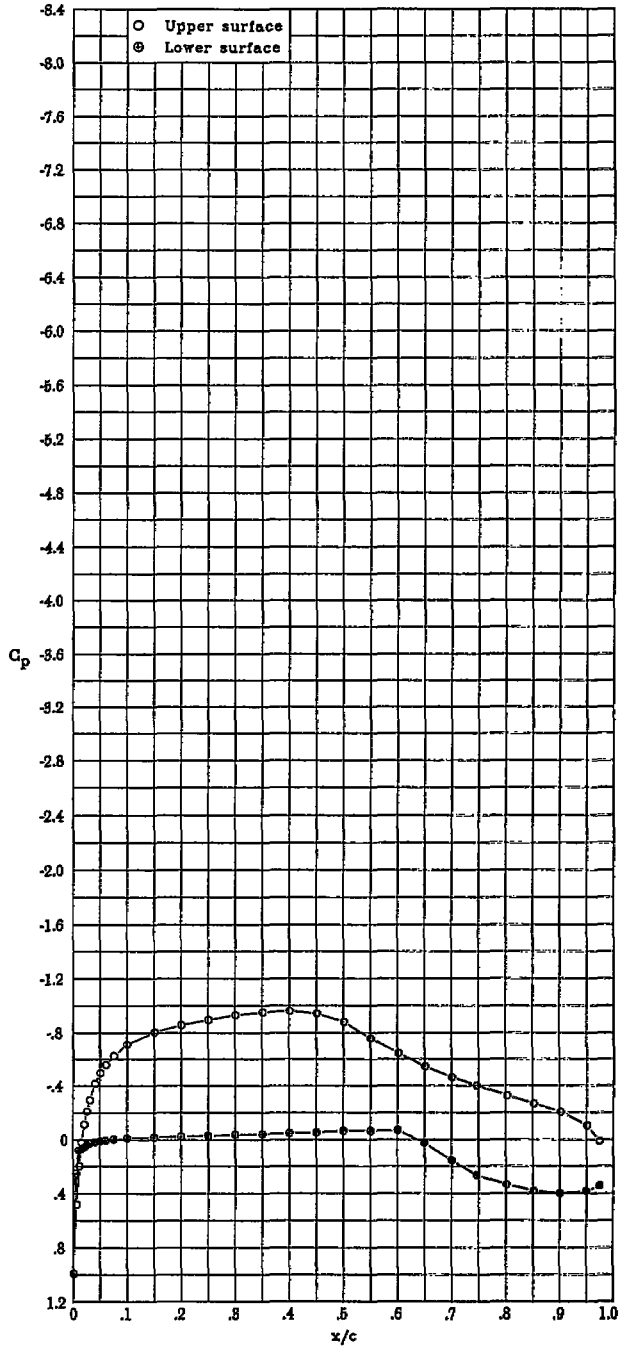

(n) $\alpha = 0.01^{\circ}$; $c_l = 0.657$; $c_d = 0.0045$; $c_m = -0.148$.

Figure 6.- Continued.

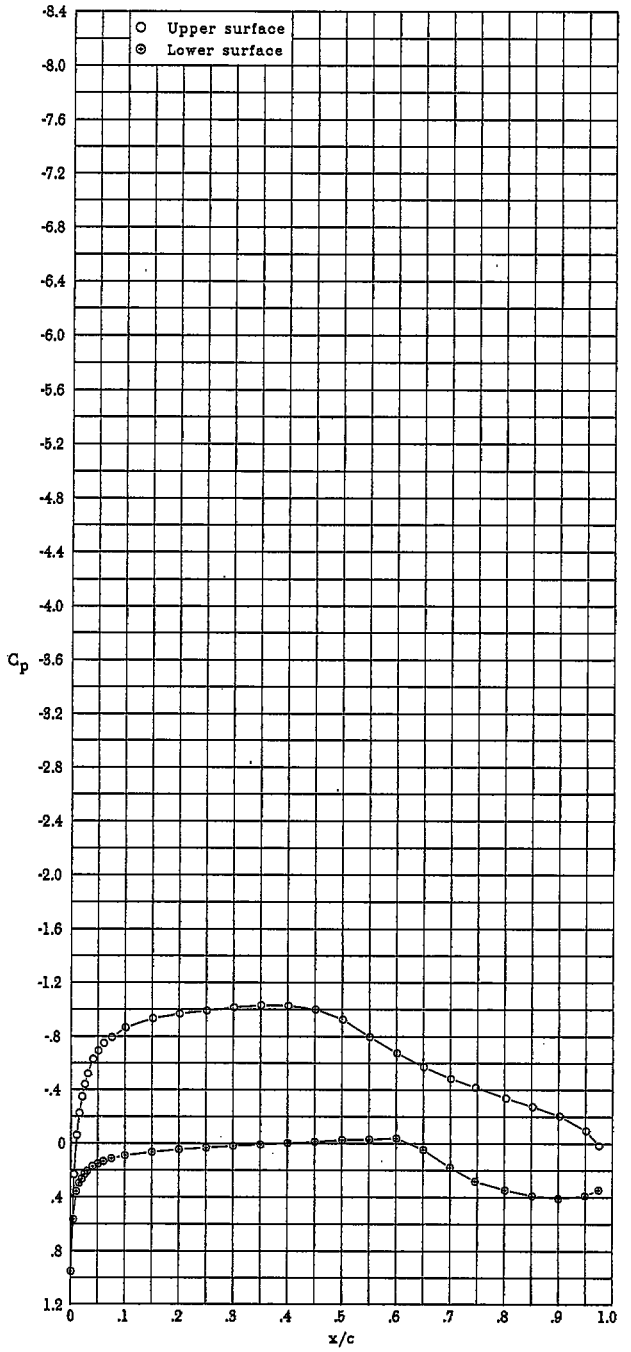

(o) $\alpha = 1.02^\circ$; $c_l = 0.767$; $c_d = 0.0048$; $c_m = -0.149$.

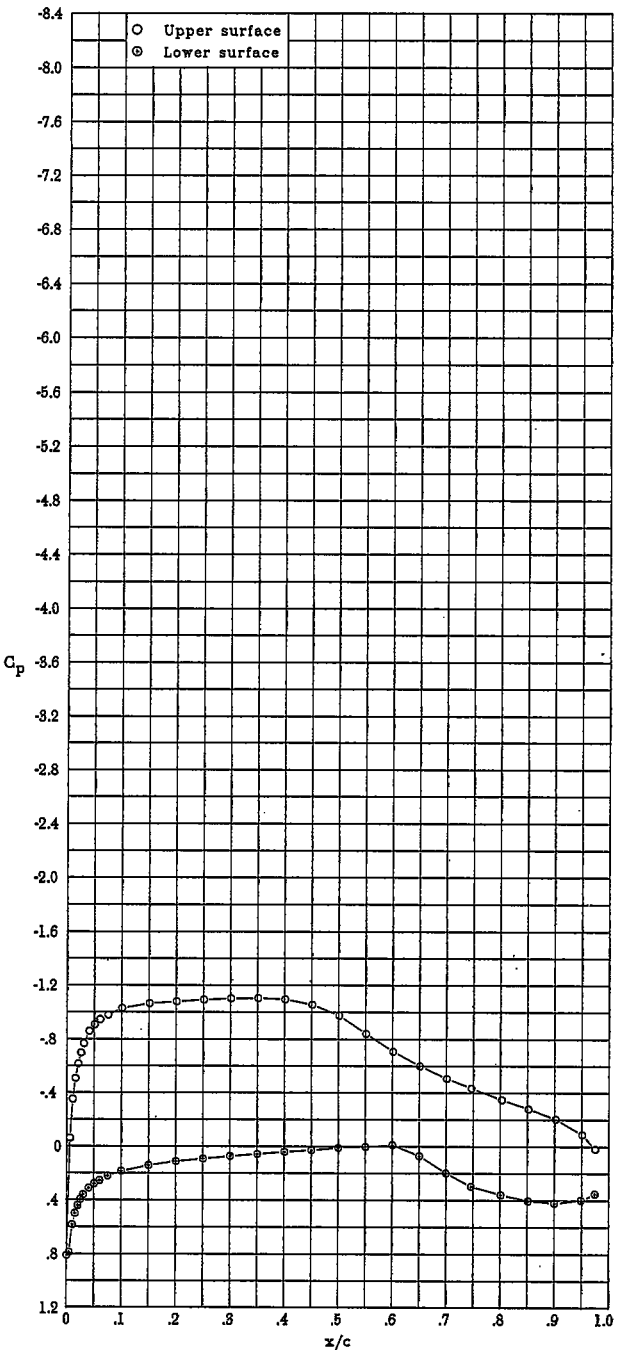

(p) $\alpha = 2.03^\circ$; $c_l = 0.876$; $c_d = 0.0052$; $c_m = -0.150$.

Figure 6.- Continued.

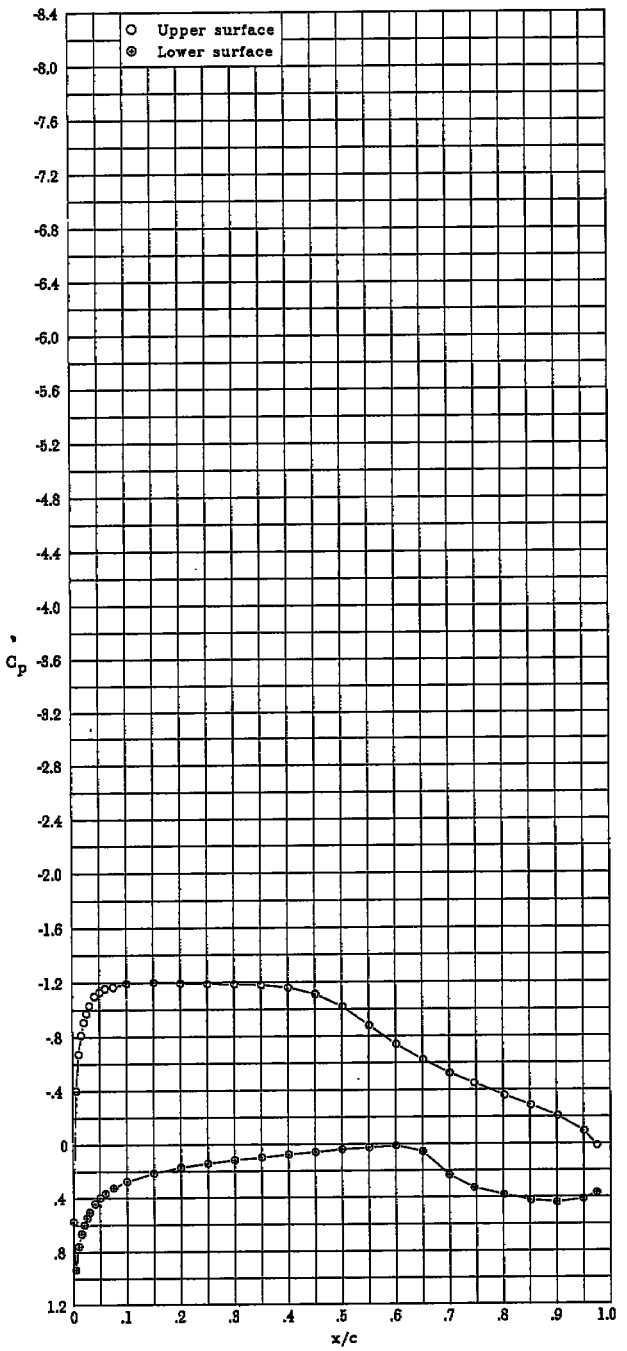

(q) $\alpha = 3.06^{\circ}$; $c_l = 0.981$; $c_d = 0.0057$; $c_m = -0.152$.

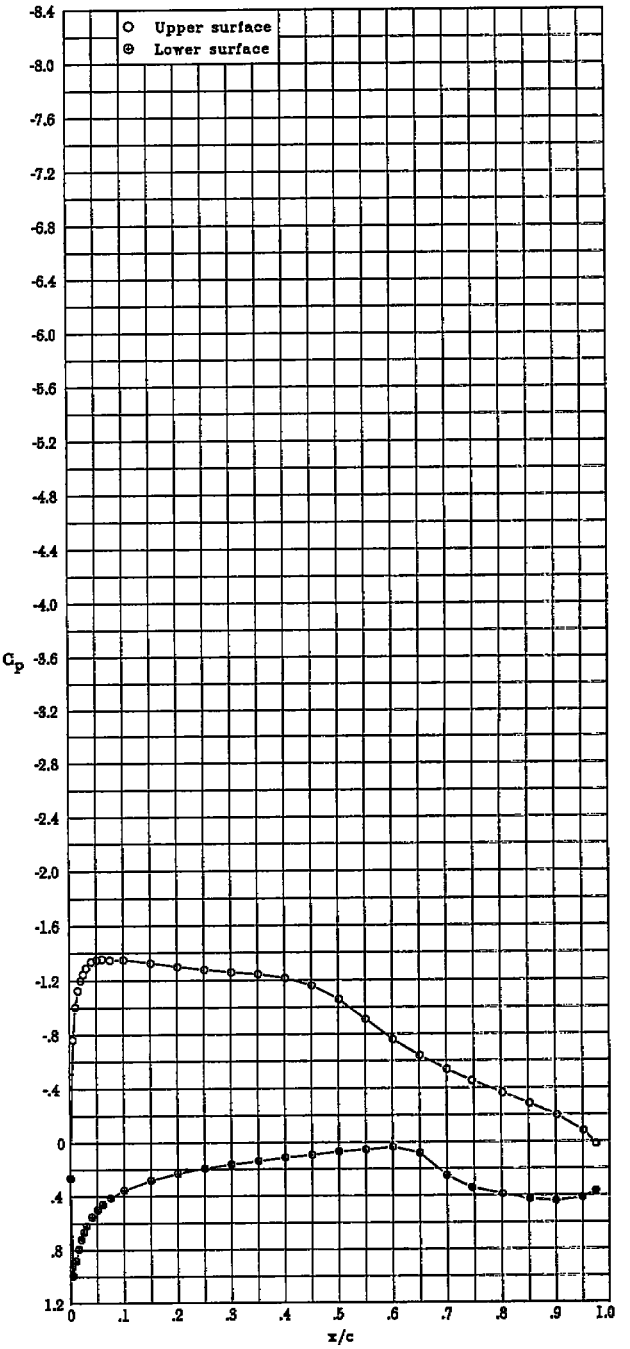

(r) $\alpha = 4.07^{\circ}$; $c_l = 1.075$; $c_d = 0.0072$; $c_m = -0.151$.

Figure 6.- Continued.

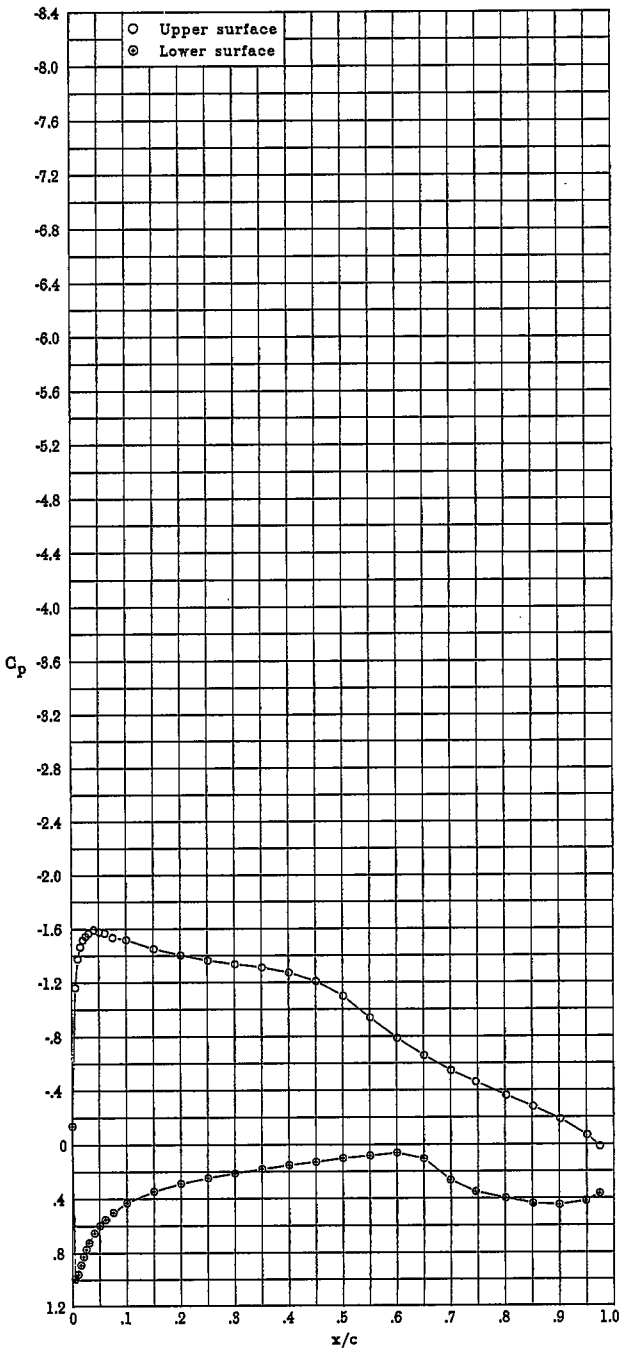

(s) $\alpha = 5.09°$; $c_l = 1.171$; $c_d = 0.0085$; $c_m = -0.149$.

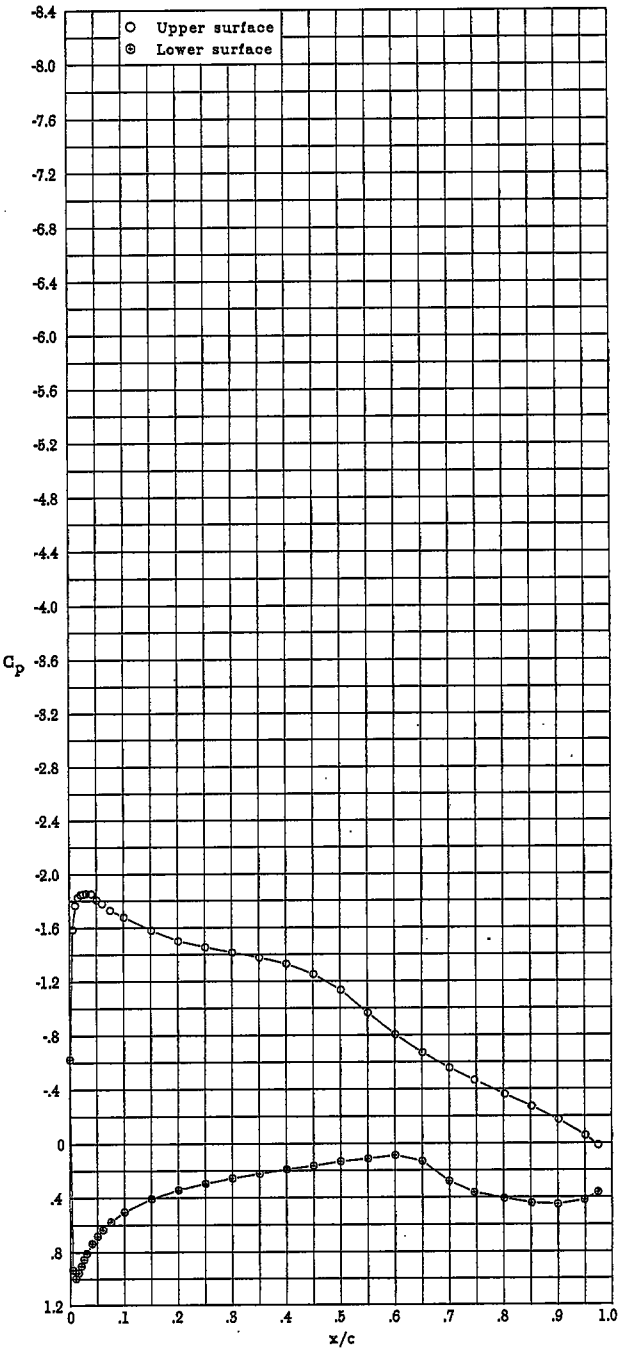

(t) $\alpha = 6.10°$; $c_l = 1.263$; $c_d = 0.0092$; $c_m = -0.147$.

Figure 6.- Continued.

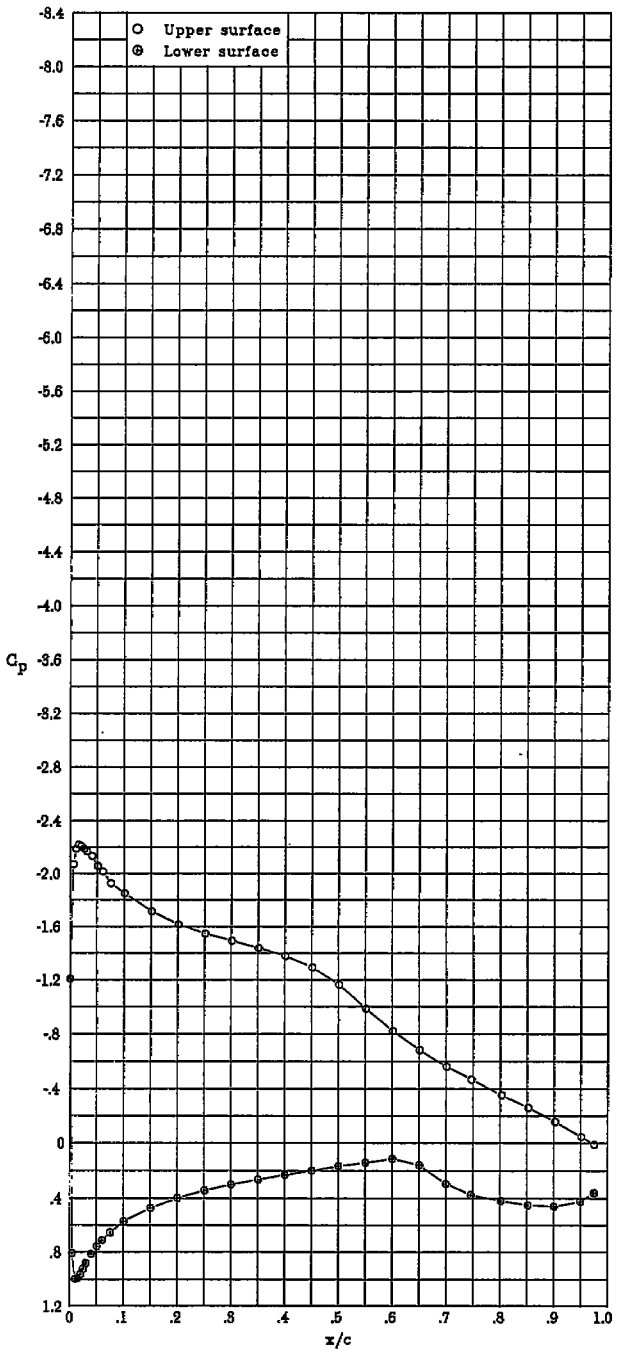

(u) $\alpha = 7.13^\circ$; $c_l = 1.364$; $c_d = 0.0107$; $c_m = -0.143$.

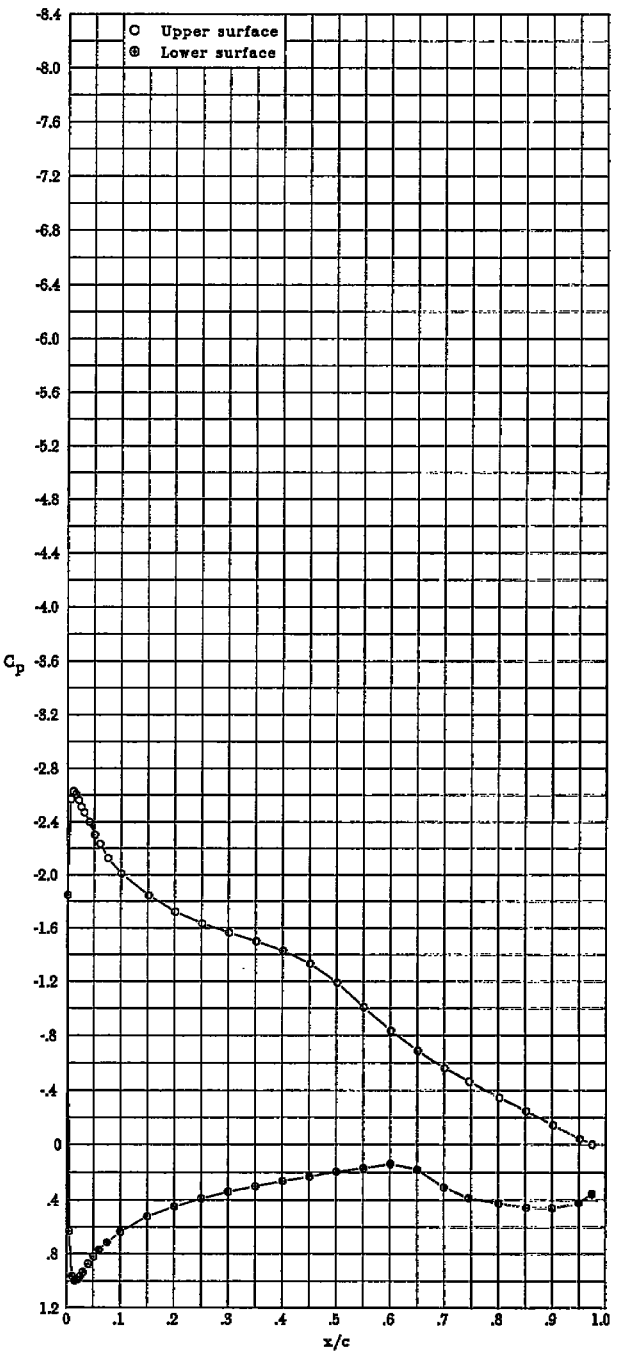

(v) $\alpha = 8.14^\circ$; $c_l = 1.443$; $c_d = 0.0124$; $c_m = -0.142$.

Figure 6.- Continued.

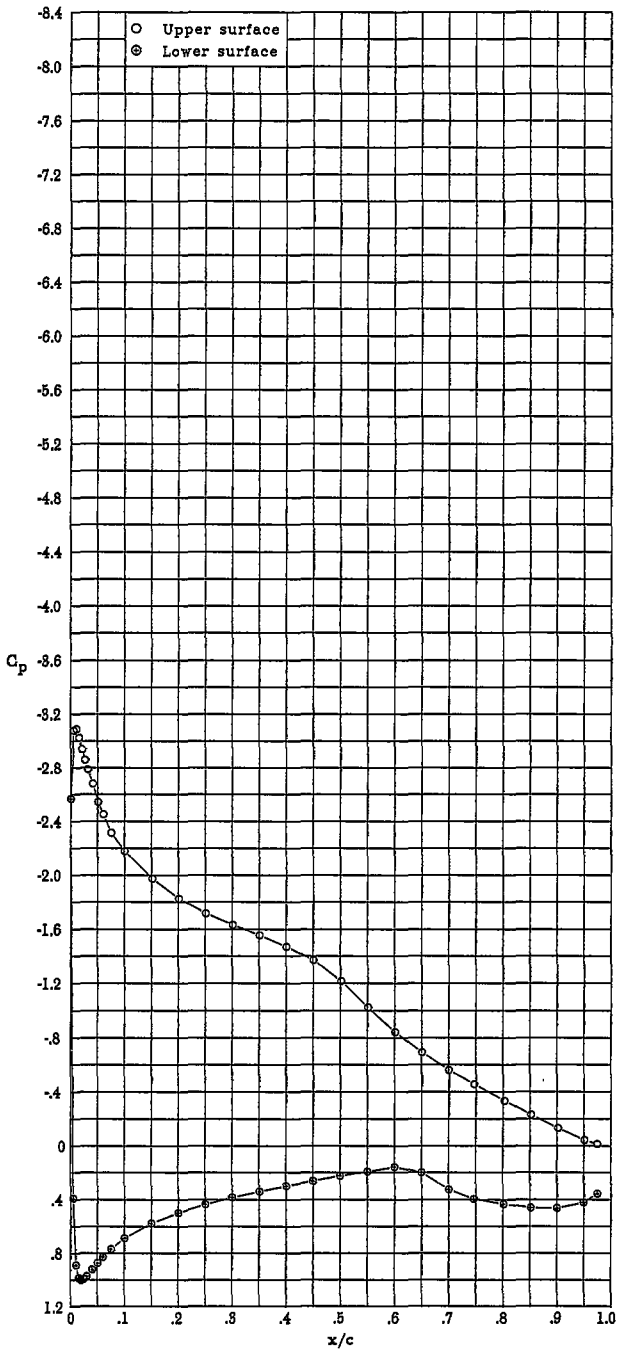

(w) α = 9.16°; c_l = 1.527; c_d = 0.0140; c_m = −0.138.

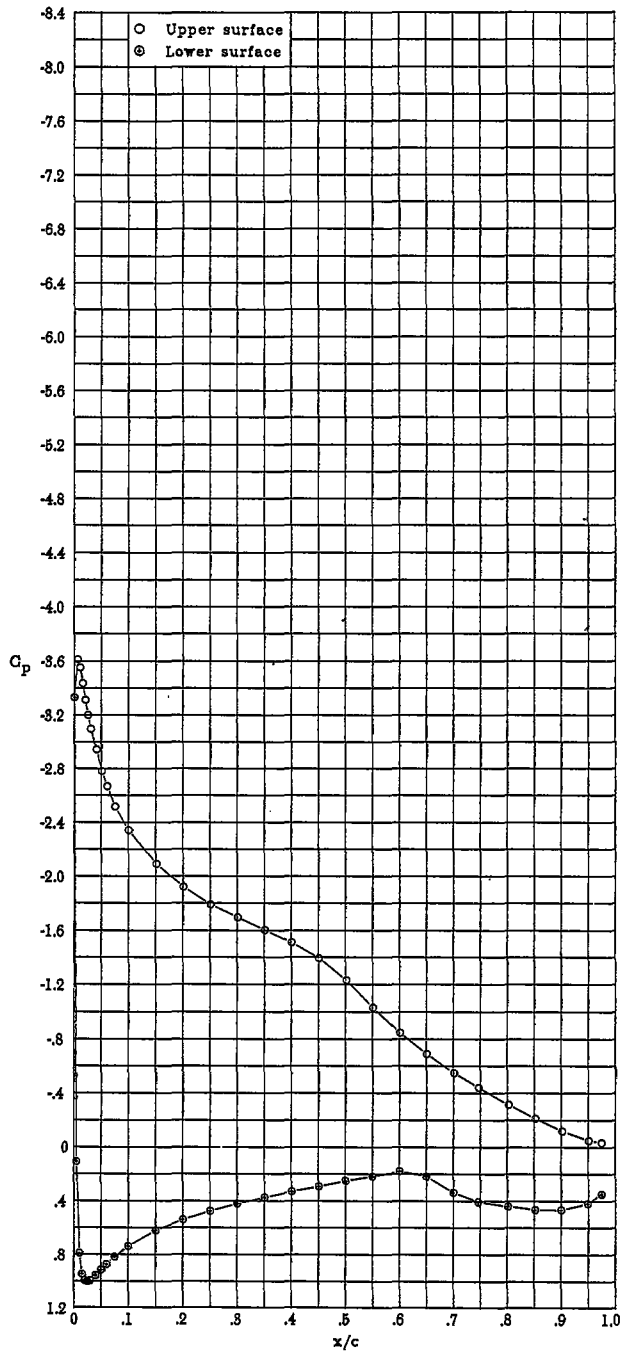

(x) α = 10.17°; c_l = 1.601; c_d = 0.0159; c_m = −0.134.

Figure 6.- Continued.

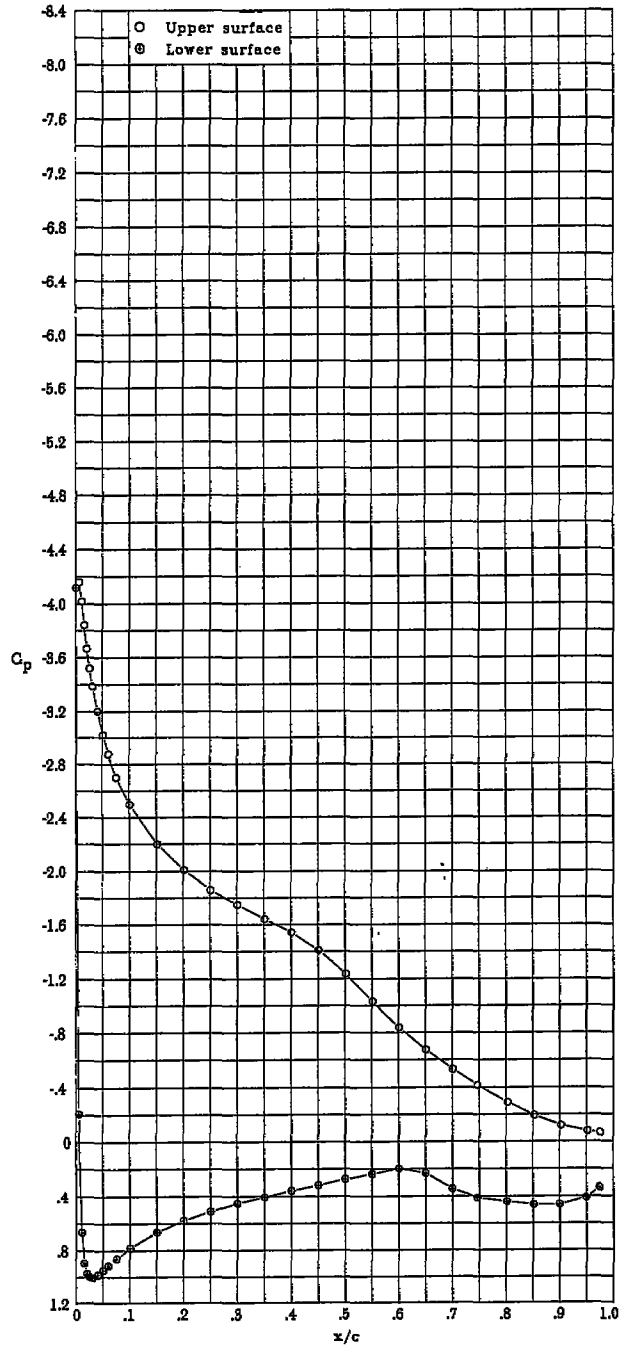

(y) α = 11.19°; c_l = 1.667; c_d = 0.0187; c_m = −0.129.

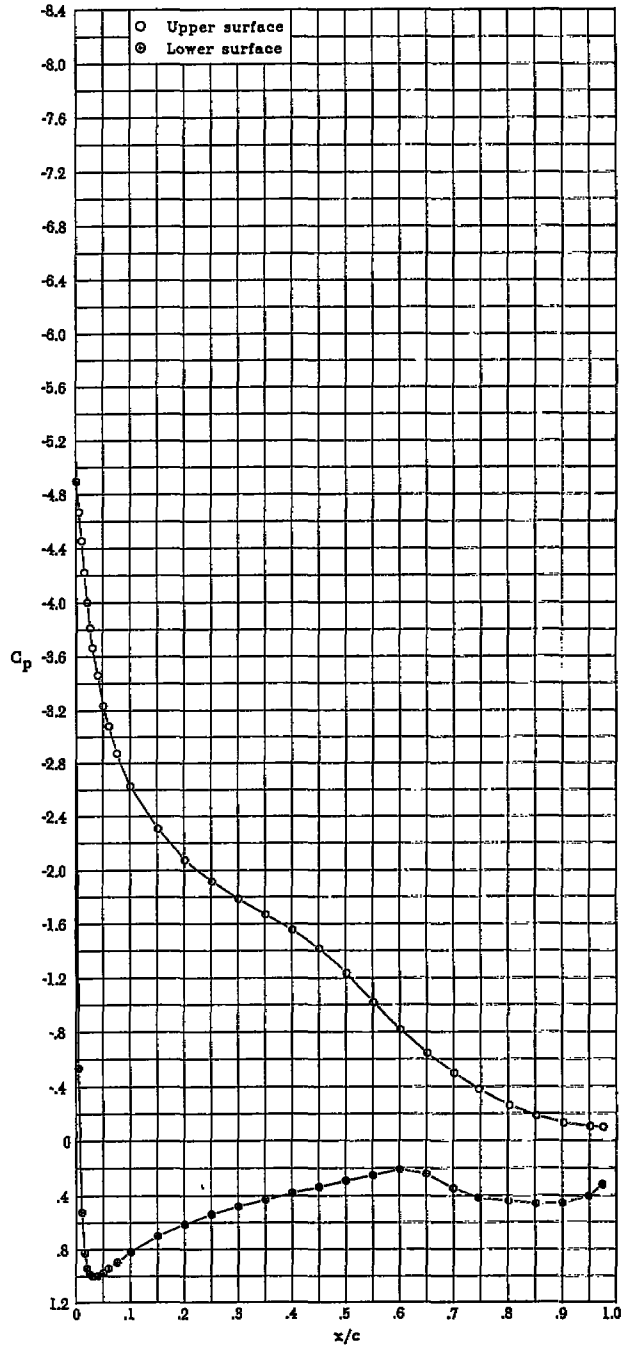

(z) α = 12.20°; c_l = 1.719; c_d = 0.0211; c_m = −0.123.

Figure 6.- Continued.

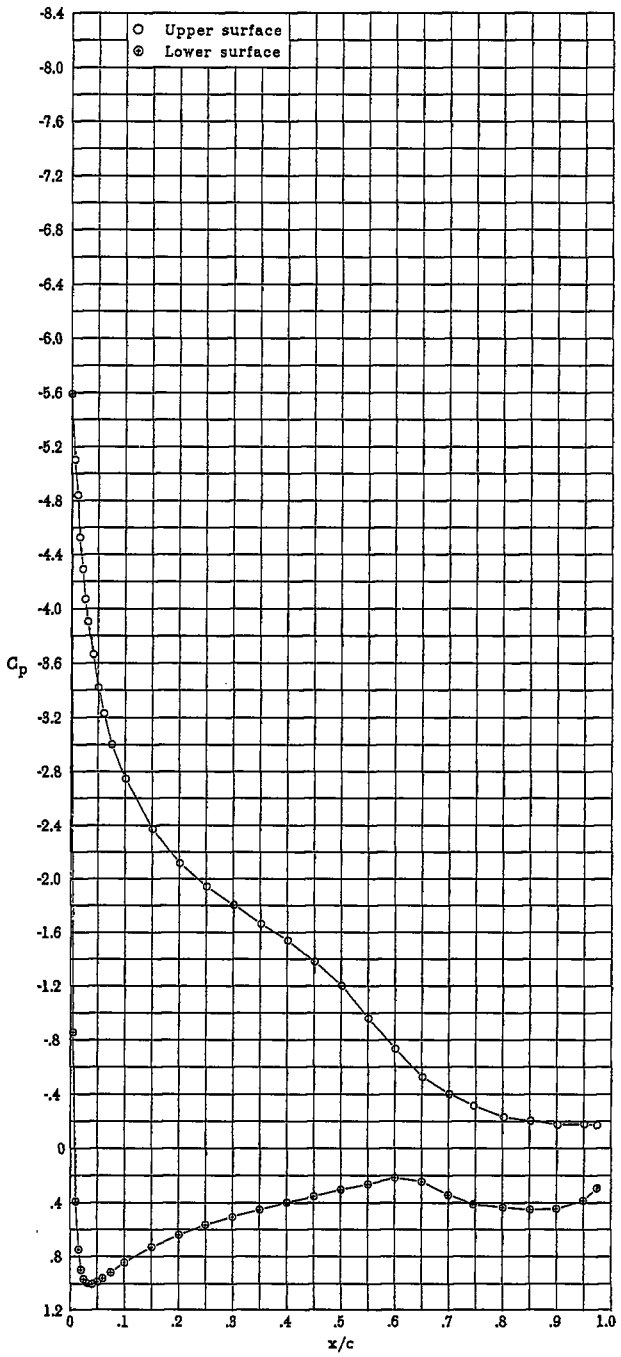

(aa) α = 13.21°; c_l = 1.738; c_d = 0.0272; c_m = −0.112.

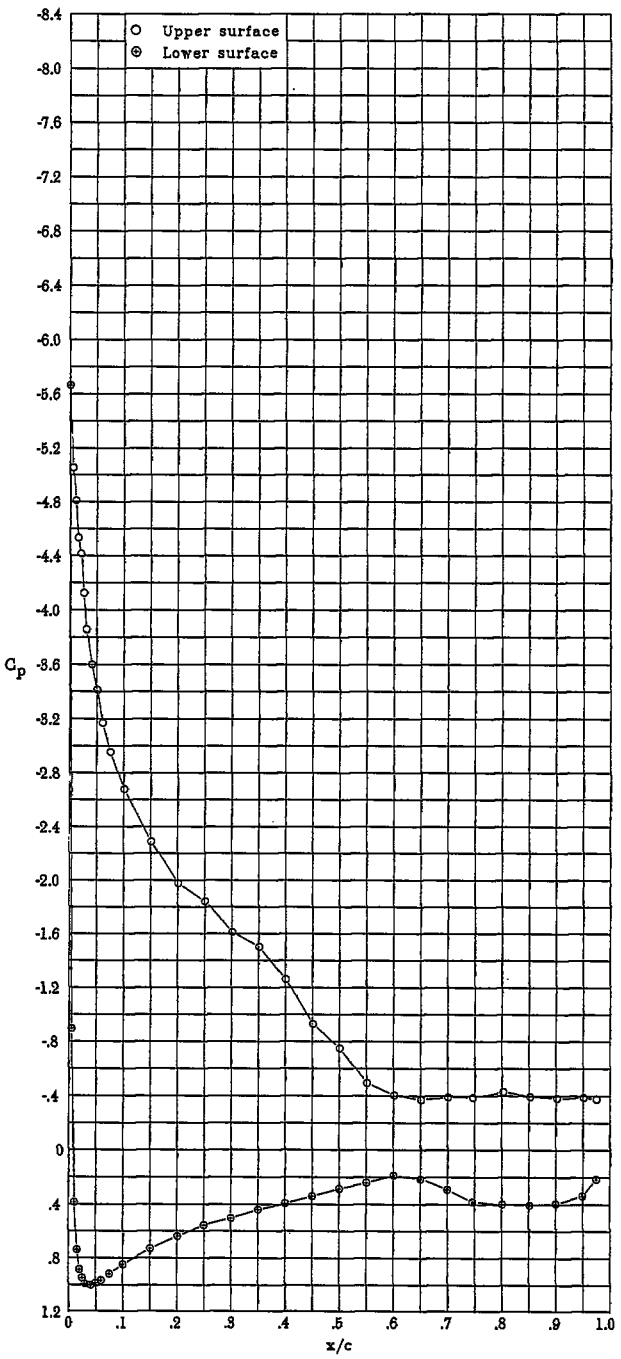

(bb) α = 14.20°; c_l = 1.601; c_d = 0.0826; c_m = −0.101.

Figure 6.- Continued.

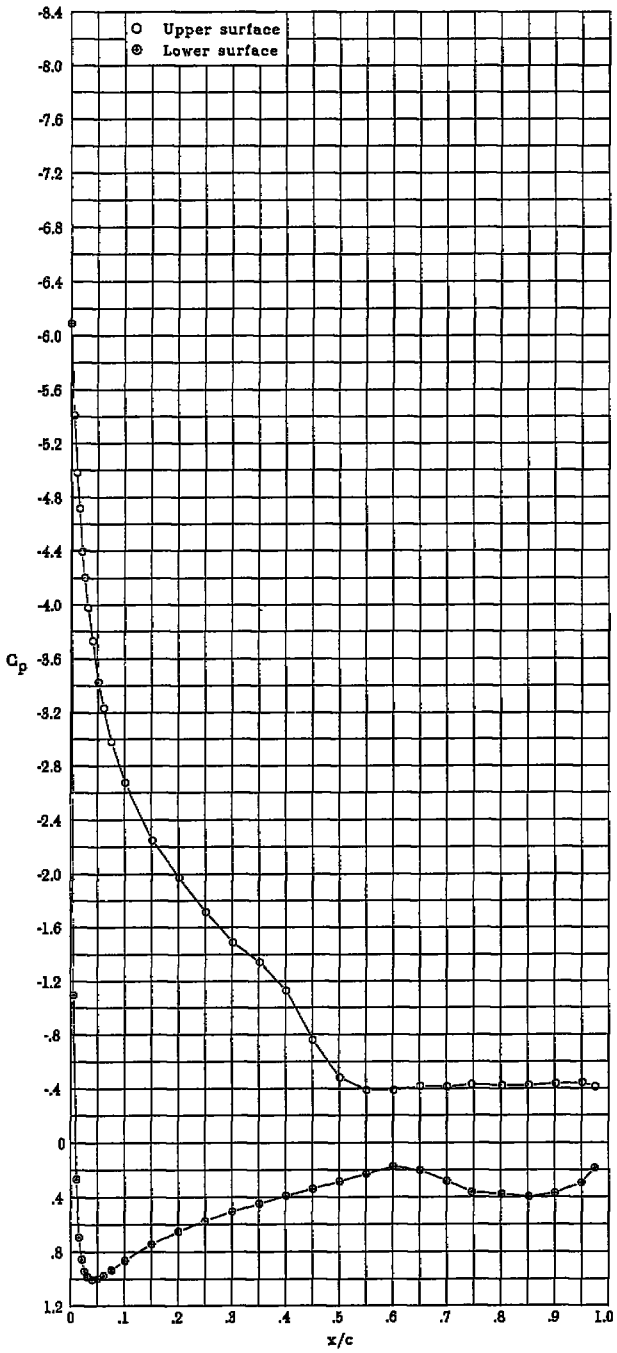

(cc) $\alpha = 15.21^{\circ}$; $c_l = 1.556$; $c_d = 0.1059$; $c_m = -0.093$.

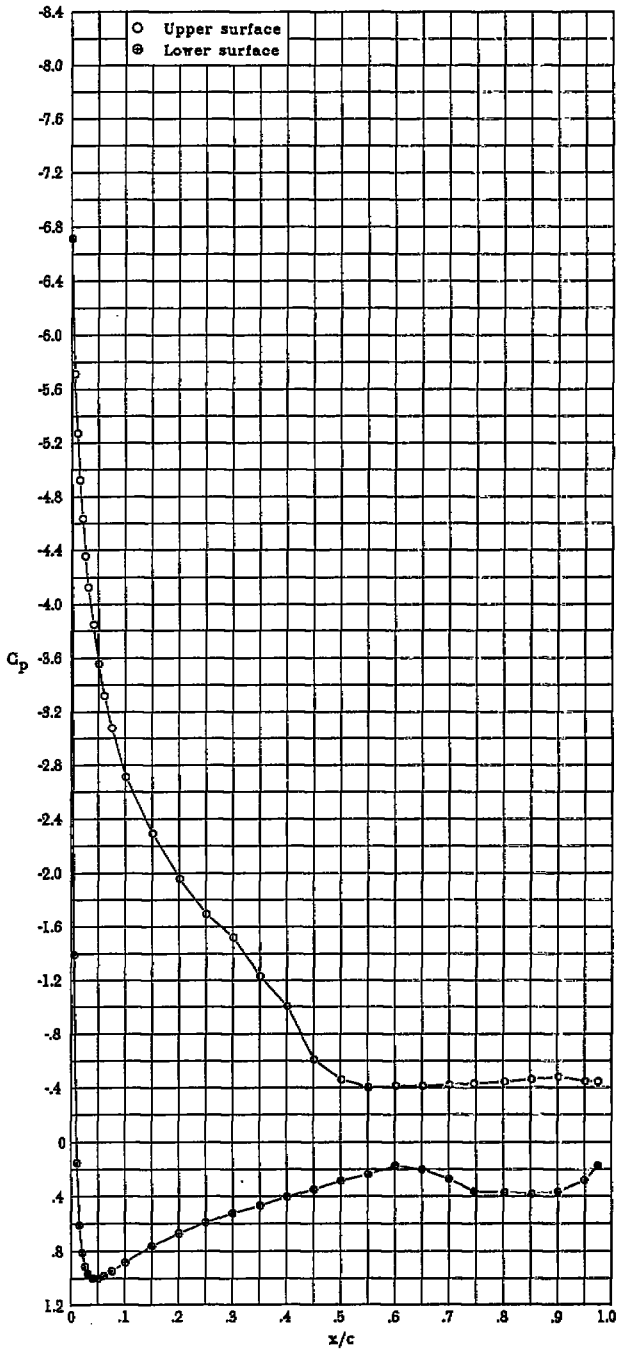

(dd) $\alpha = 16.21^{\circ}$; $c_l = 1.559$; $c_d = 0.1241$; $c_m = -0.091$.

Figure 6.- Concluded.

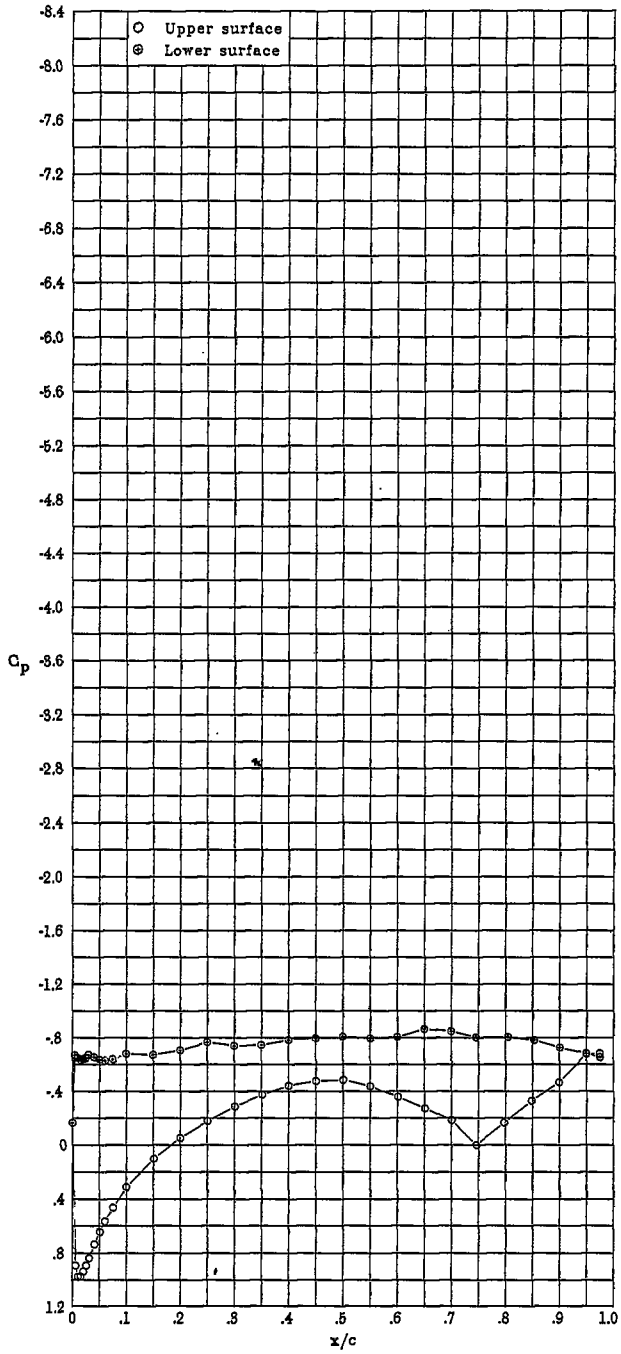

(a) $\alpha = -11.09^\circ$; $c_l = -0.497$; $c_d = 0.2128$; $c_m = 0.072$.

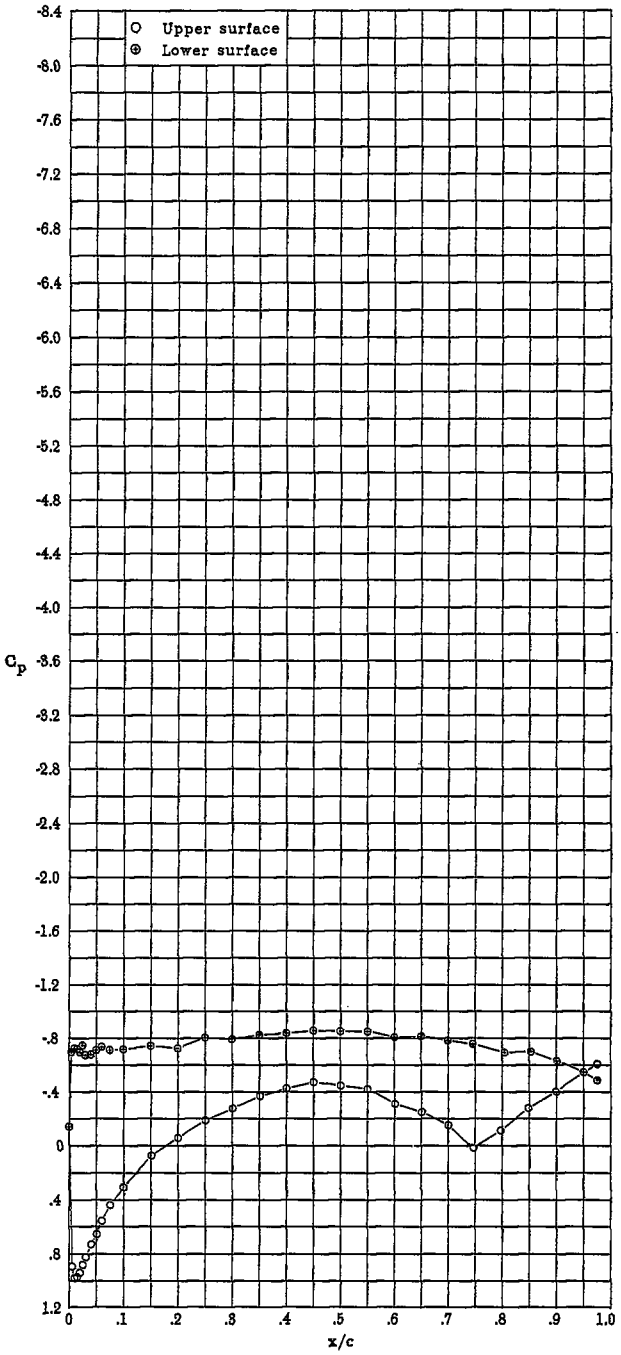

(b) $\alpha = -10.10^\circ$; $c_l = -0.522$; $c_d = 0.2036$; $c_m = 0.068$.

Figure 7.- Pressure distributions with $\delta_f = -10^\circ$ for $R = 6.0 \times 10^6$ and $M = 0.10$.

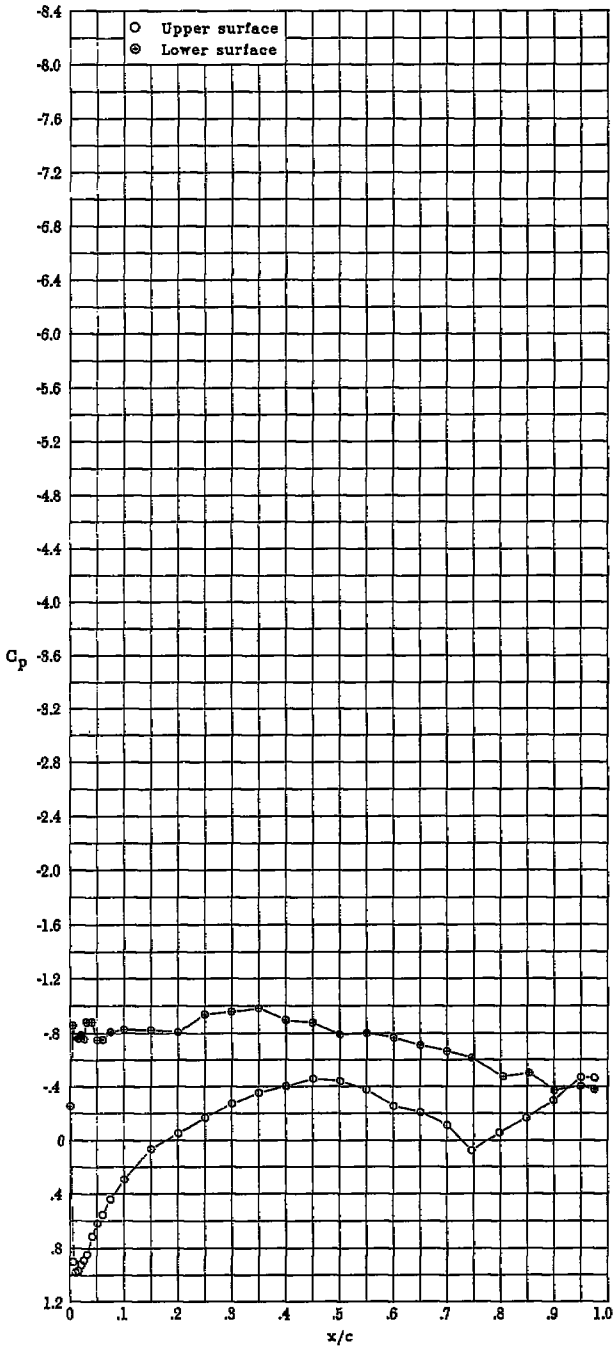

(c) $\alpha = -9.07^\circ$; $c_l = -0.542$; $c_d = 0.1820$; $c_m = 0.050$.

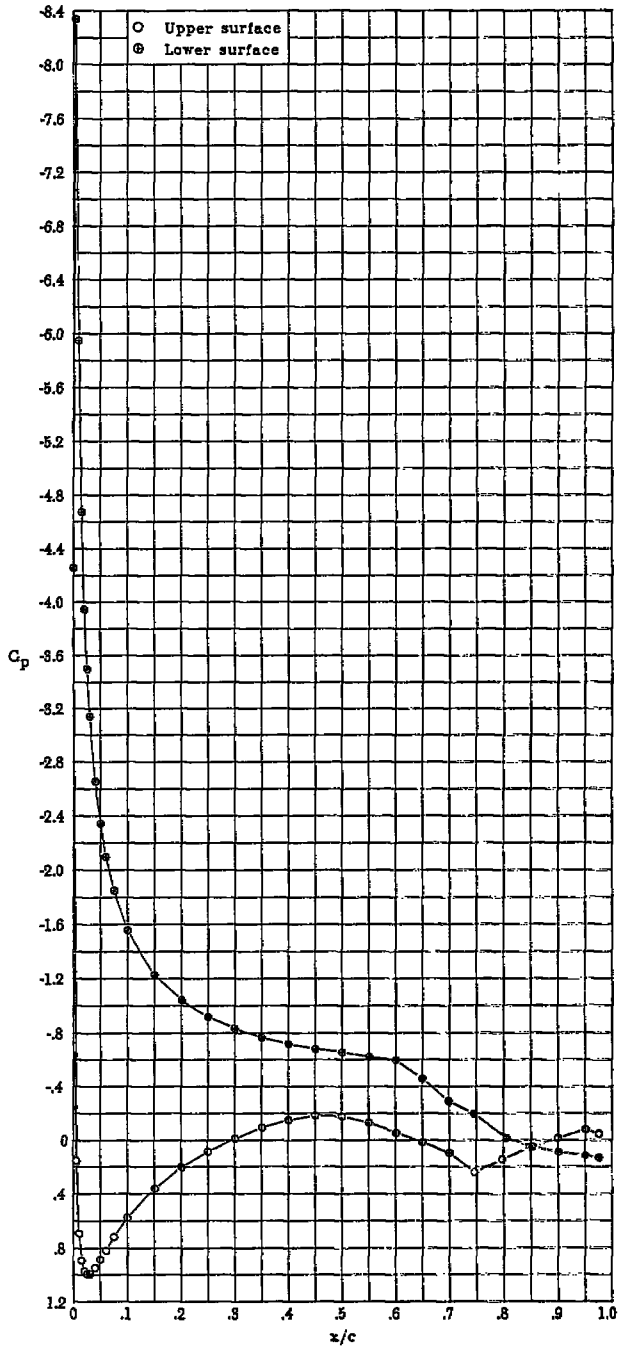

(d) $\alpha = -8.17^\circ$; $c_l = -0.849$; $c_d = 0.0148$; $c_m = -0.035$.

Figure 7.- Continued.

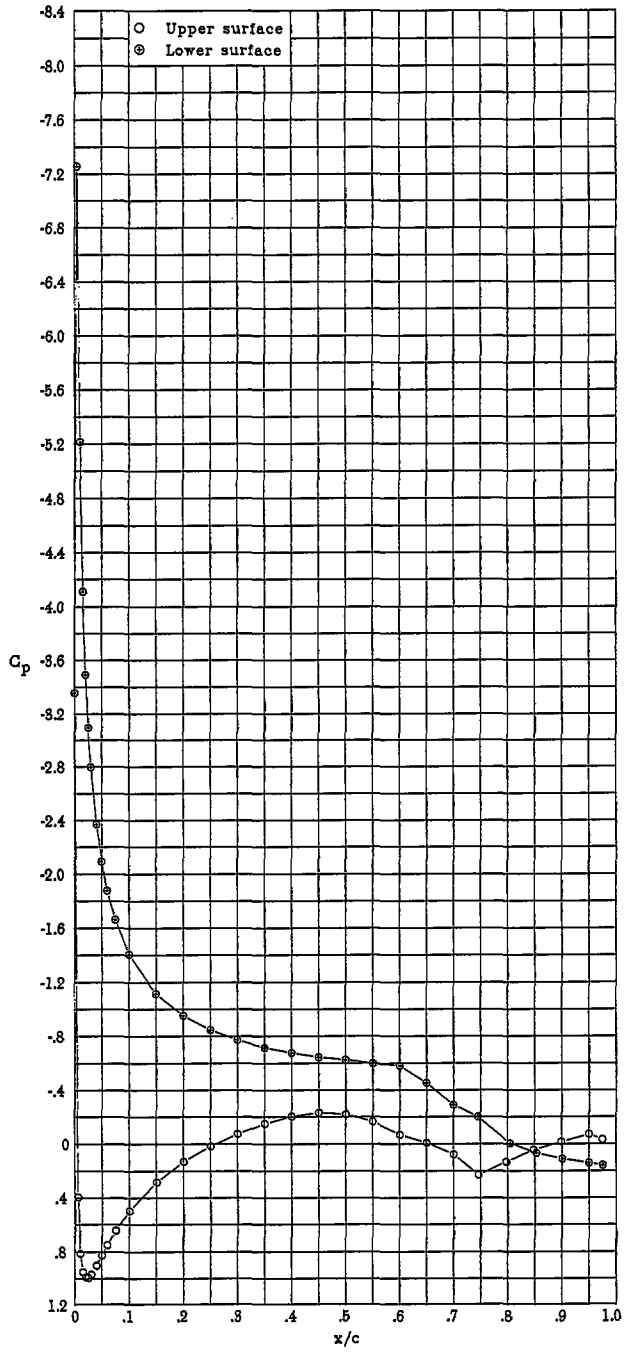

(e) $\alpha = -7.13°$; $c_l = -0.749$; $c_d = 0.0131$; $c_m = -0.035$.

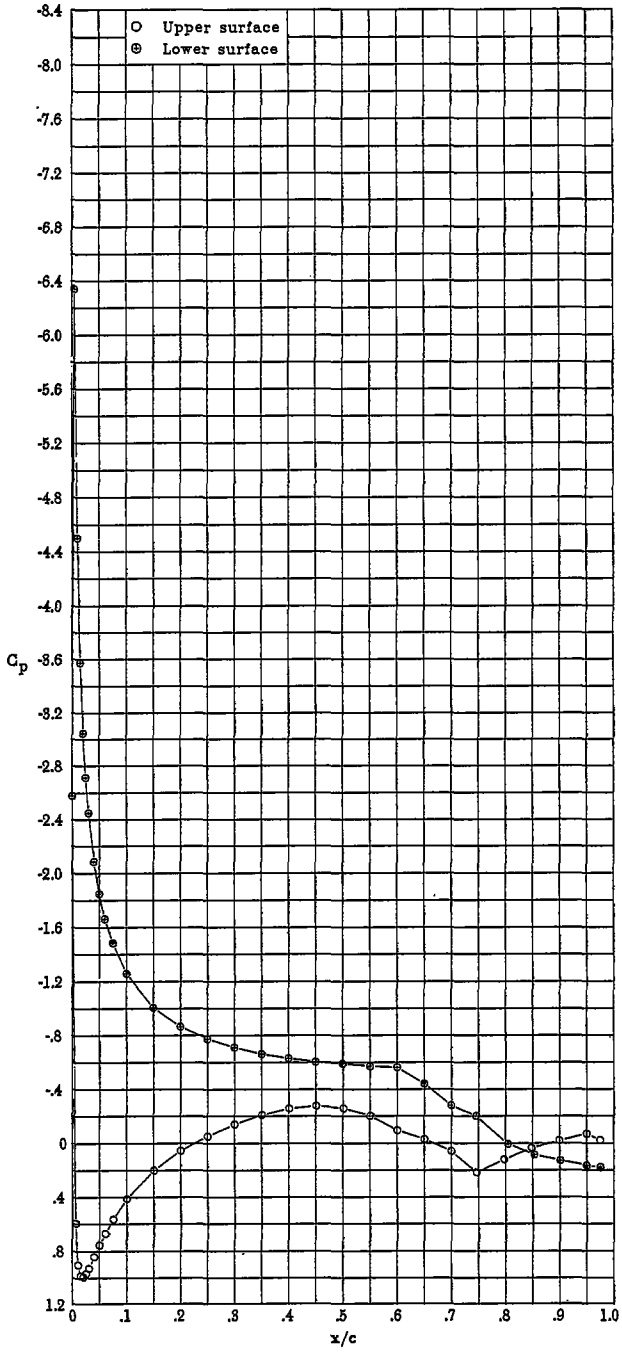

(f) $\alpha = -6.12°$; $c_l = -0.647$; $c_d = 0.0118$; $c_m = -0.035$.

Figure 7.- Continued.

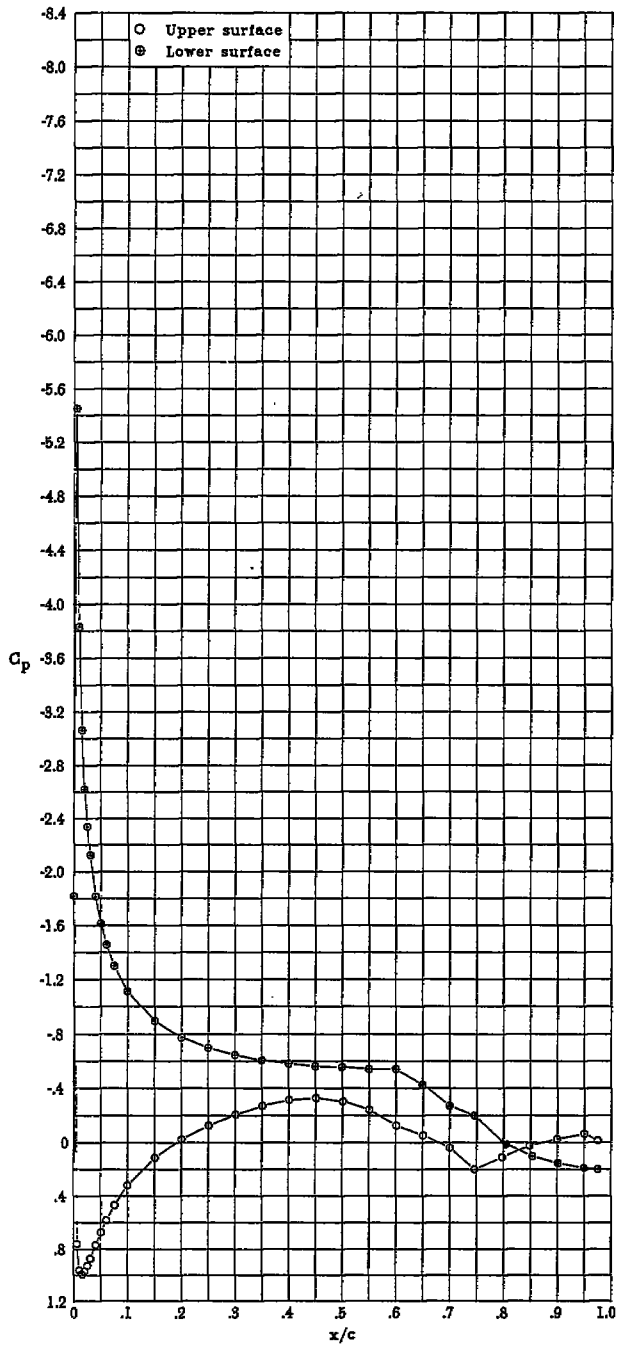

(g) $\alpha = -5.11^{\circ}$; $c_l = -0.541$; $c_d = 0.0104$; $c_m = -0.036$.

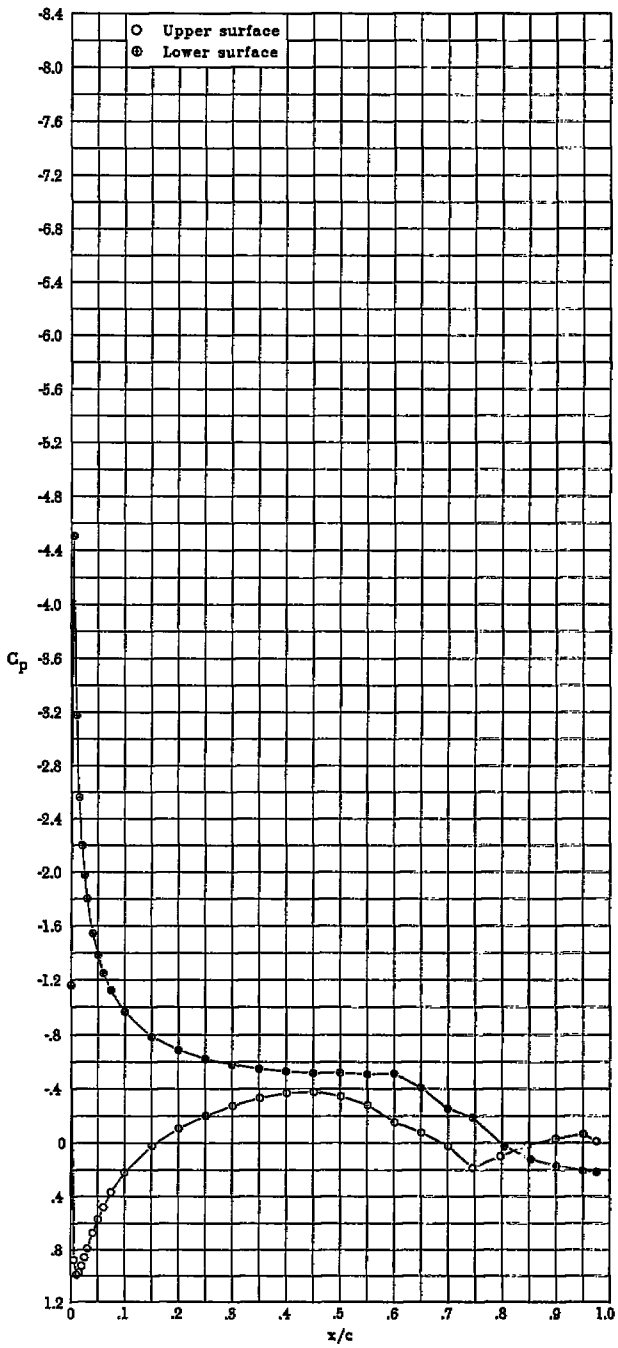

(h) $\alpha = -4.10^{\circ}$; $c_l = -0.431$; $c_d = 0.0091$; $c_m = -0.037$.

Figure 7.- Continued.

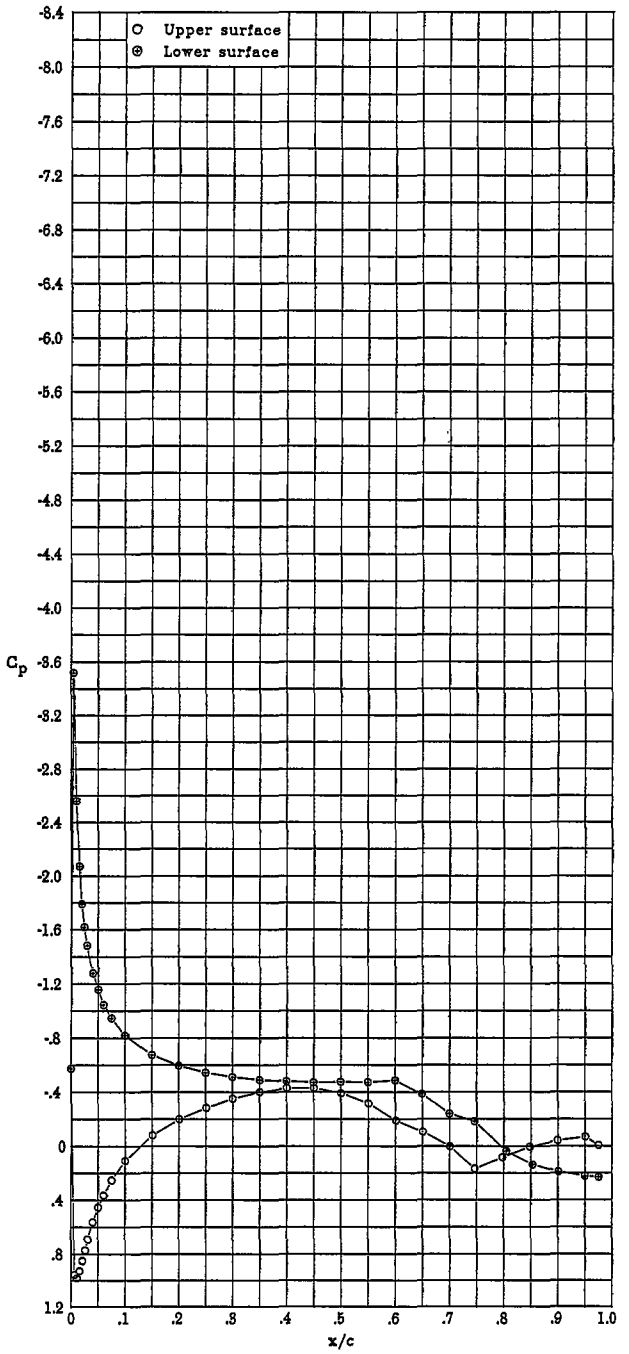

(i) $\alpha = -3.06°$; $c_l = -0.317$; $c_d = 0.0080$; $c_m = -0.038$.

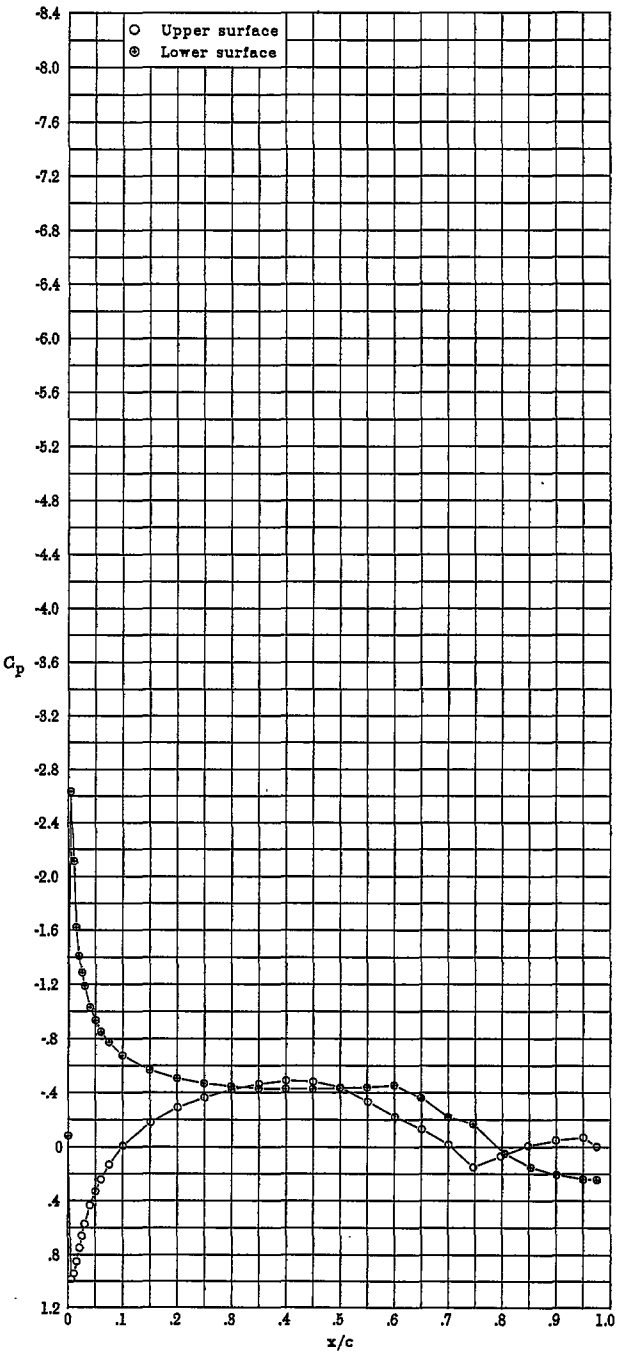

(j) $\alpha = -2.05°$; $c_l = -0.205$; $c_d = 0.0072$; $c_m = -0.039$.

Figure 7.- Continued.

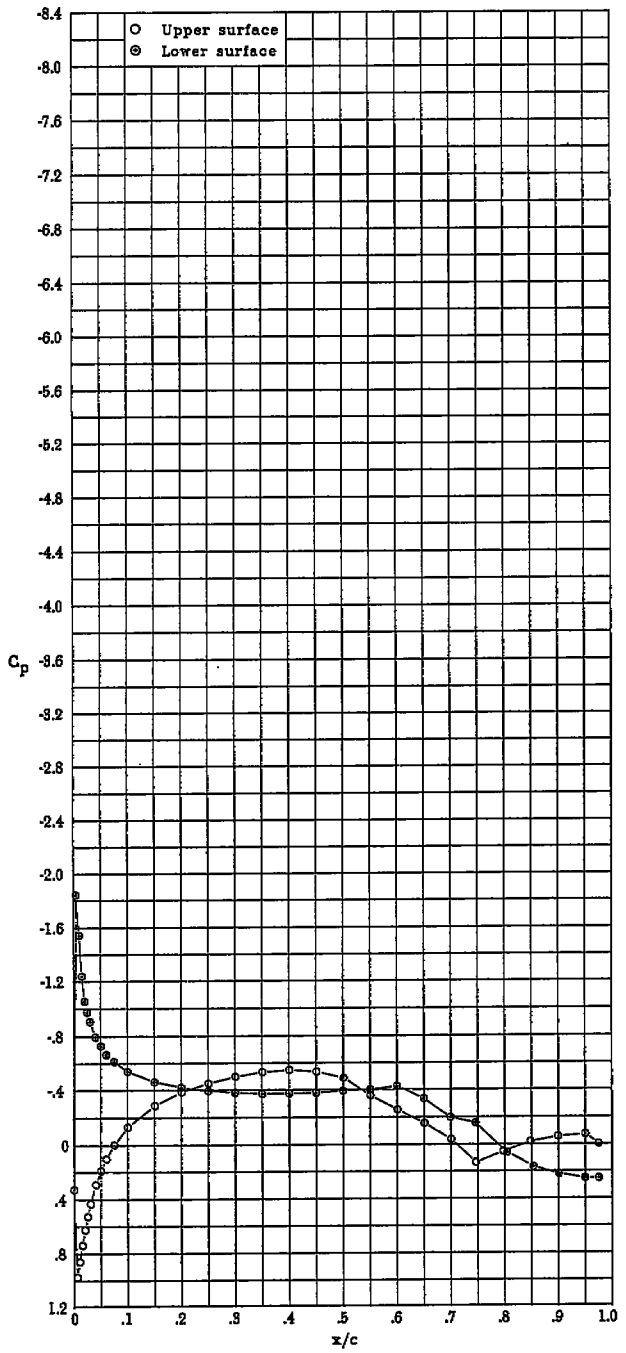

(k) $\alpha = -1.04^\circ$; $c_l = -0.090$; $c_d = 0.0070$; $c_m = -0.041$.

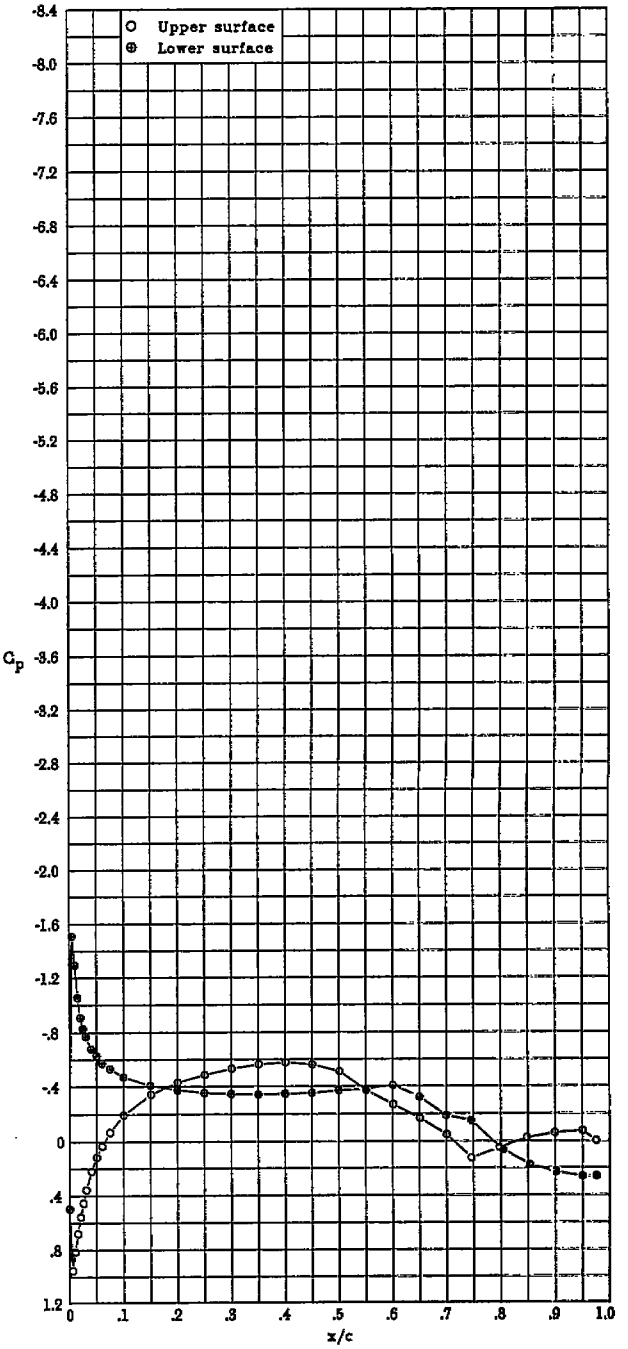

(l) $\alpha = -0.54^\circ$; $c_l = -0.032$; $c_d = 0.0069$; $c_m = -0.042$.

Figure 7.- Continued.

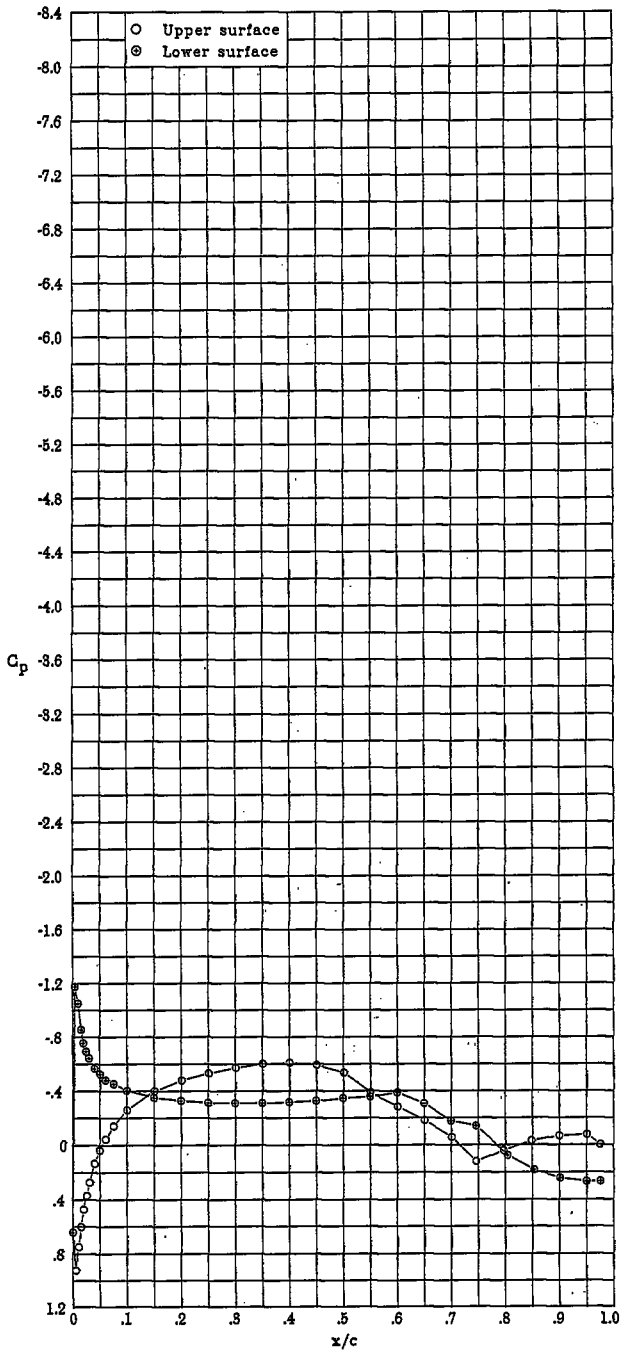

(m) $\alpha = -0.02^\circ$; $c_l = 0.027$; $c_d = 0.0069$; $c_m = -0.043$.

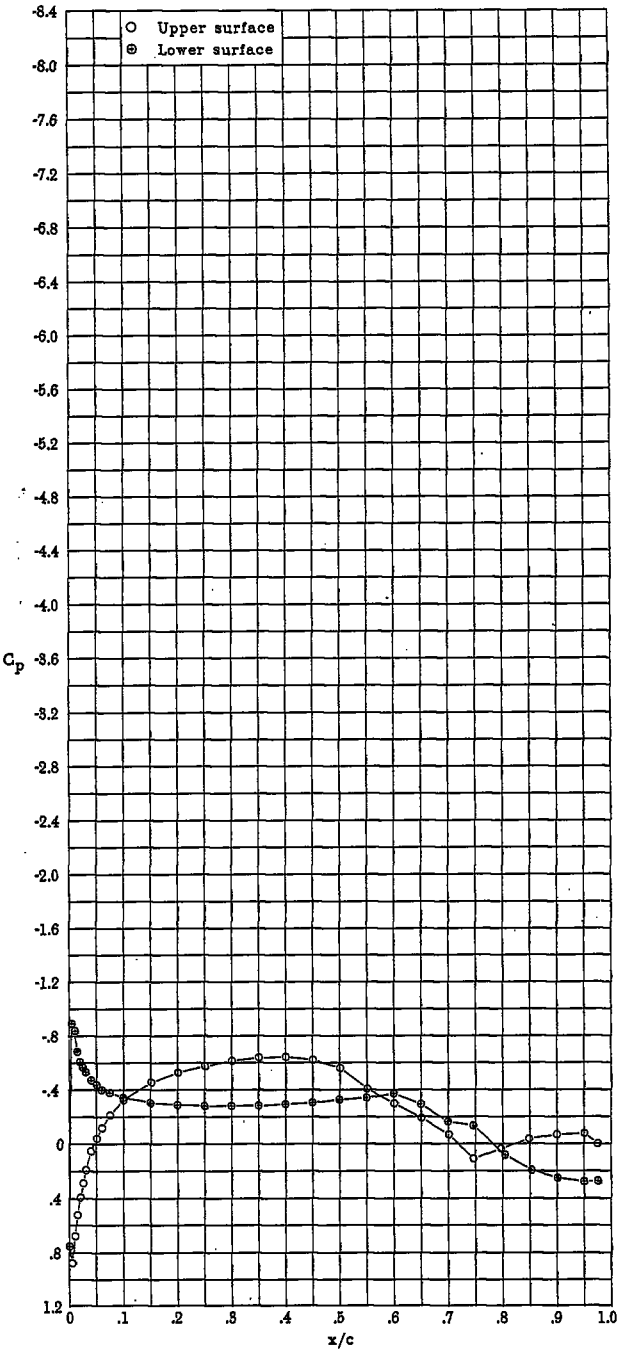

(n) $\alpha = 0.48^\circ$; $c_l = 0.082$; $c_d = 0.0066$; $c_m = -0.044$.

Figure 7.- Continued.

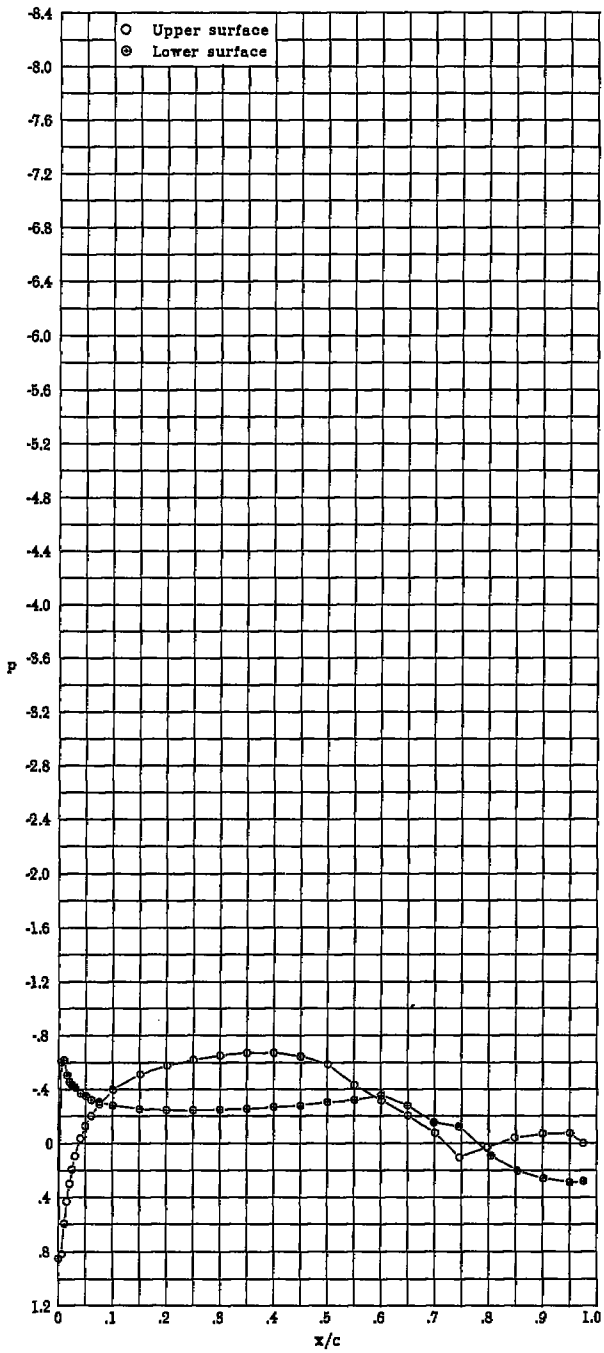

(o) $\alpha = 1.00^{\circ}$; $c_l = 0.142$; $c_d = 0.0064$; $c_m = -0.045$.

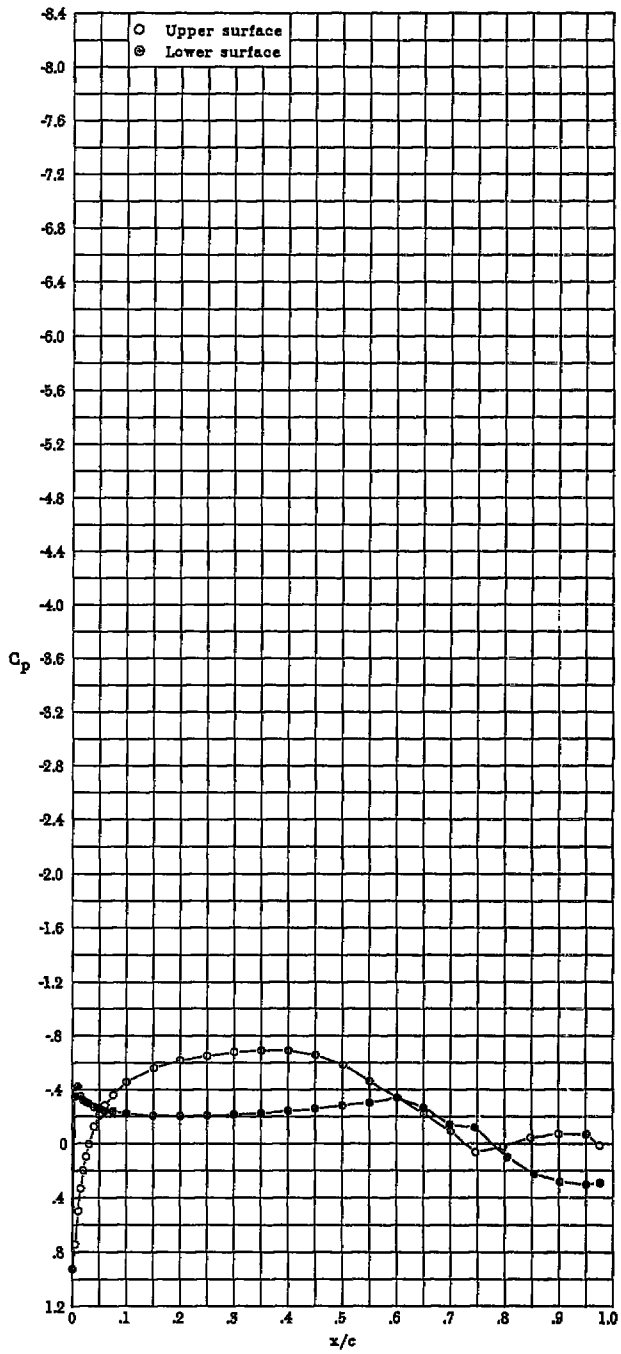

(p) $\alpha = 1.52^{\circ}$; $c_l = 0.197$; $c_d = 0.0043$; $c_m = -0.047$.

Figure 7.- Continued.

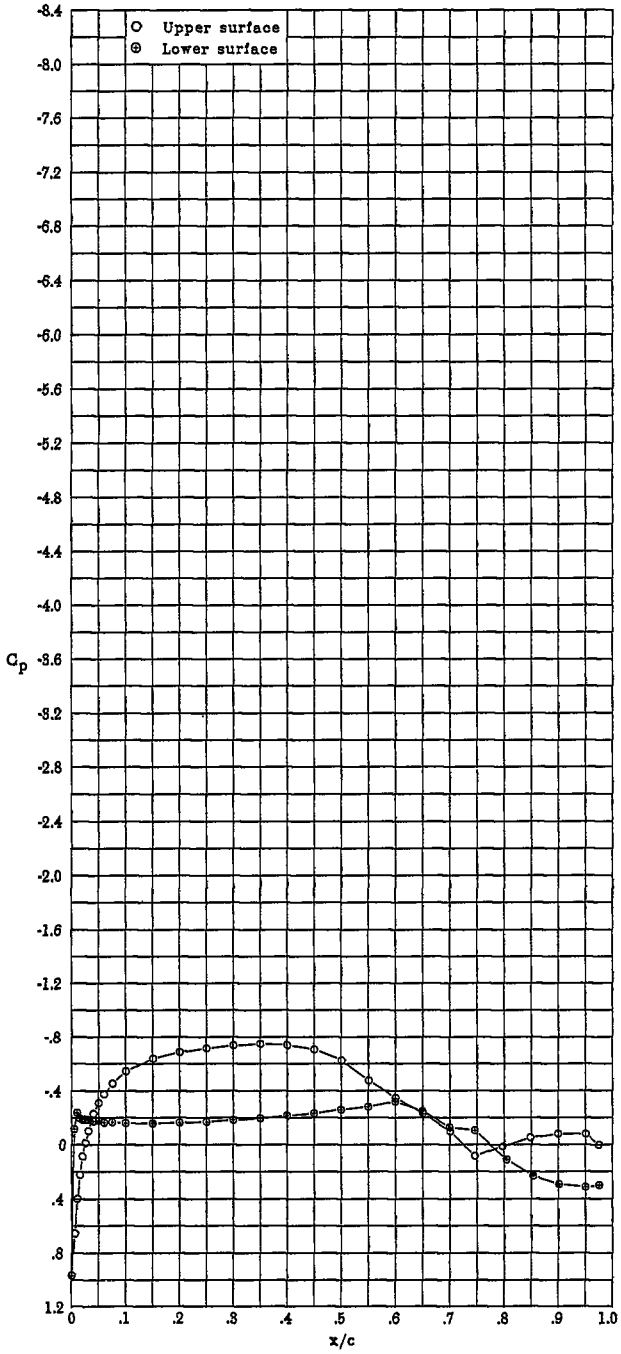

(q) $\alpha = 2.01^\circ$; $c_l = 0.262$; $c_d = 0.0044$; $c_m = -0.049$.

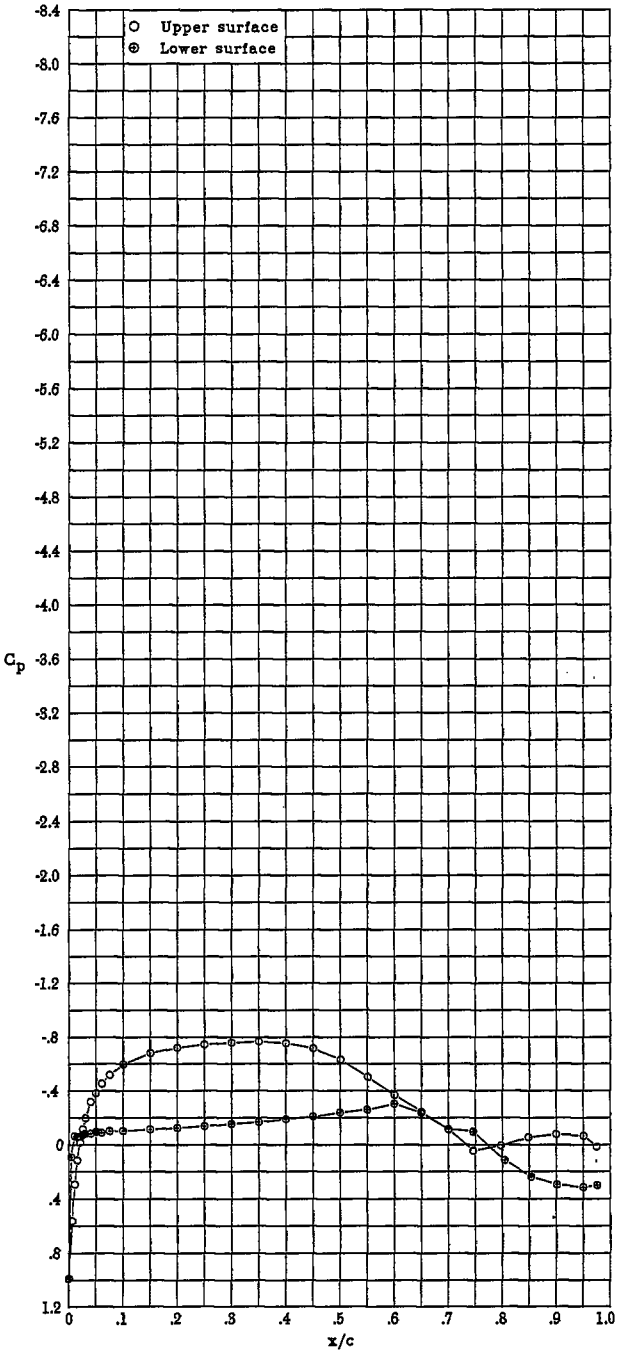

(r) $\alpha = 2.51^\circ$; $c_l = 0.311$; $c_d = 0.0043$; $c_m = -0.049$.

Figure 7.- Continued.

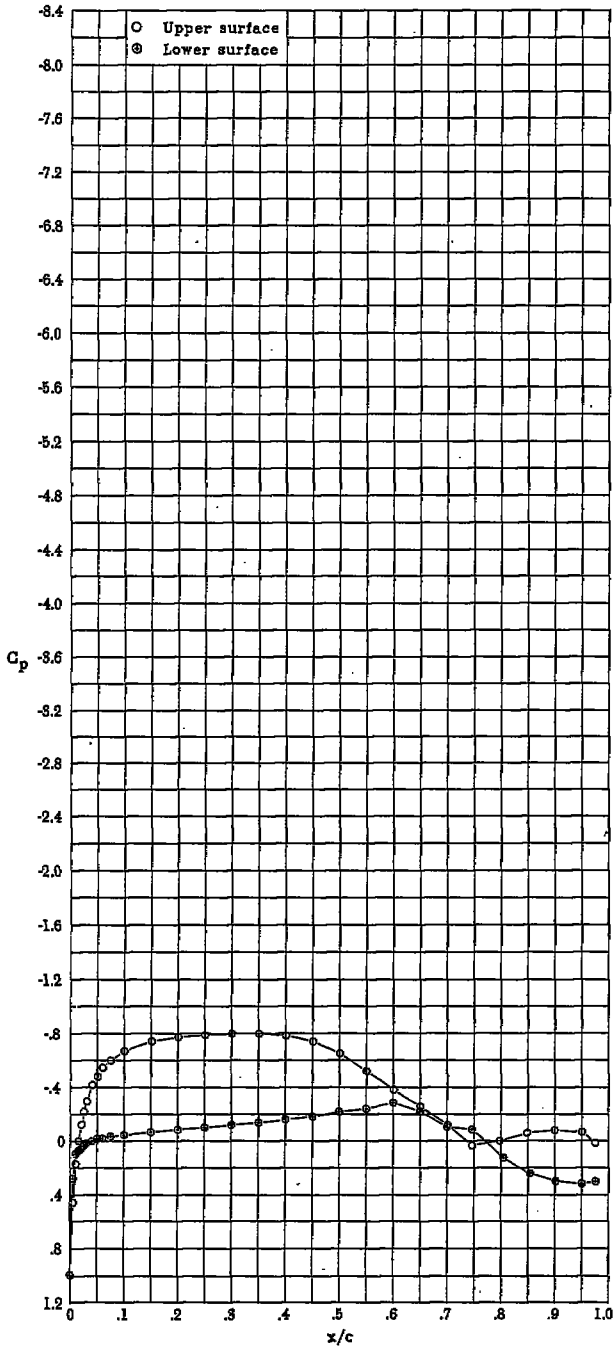

(s) $\alpha = 3.03^\circ$; $c_l = 0.368$; $c_d = 0.0043$; $c_m = -0.050$.

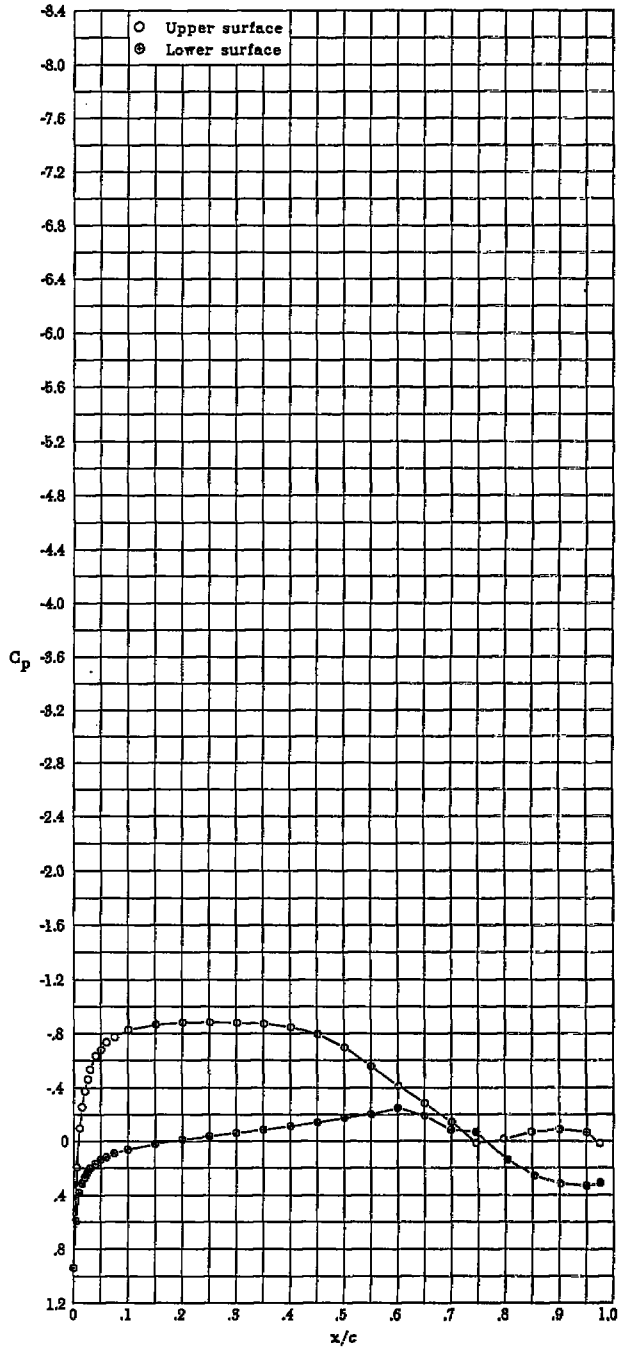

(t) $\alpha = 4.05^\circ$; $c_l = 0.483$; $c_d = 0.0045$; $c_m = -0.052$.

Figure 7.- Continued.

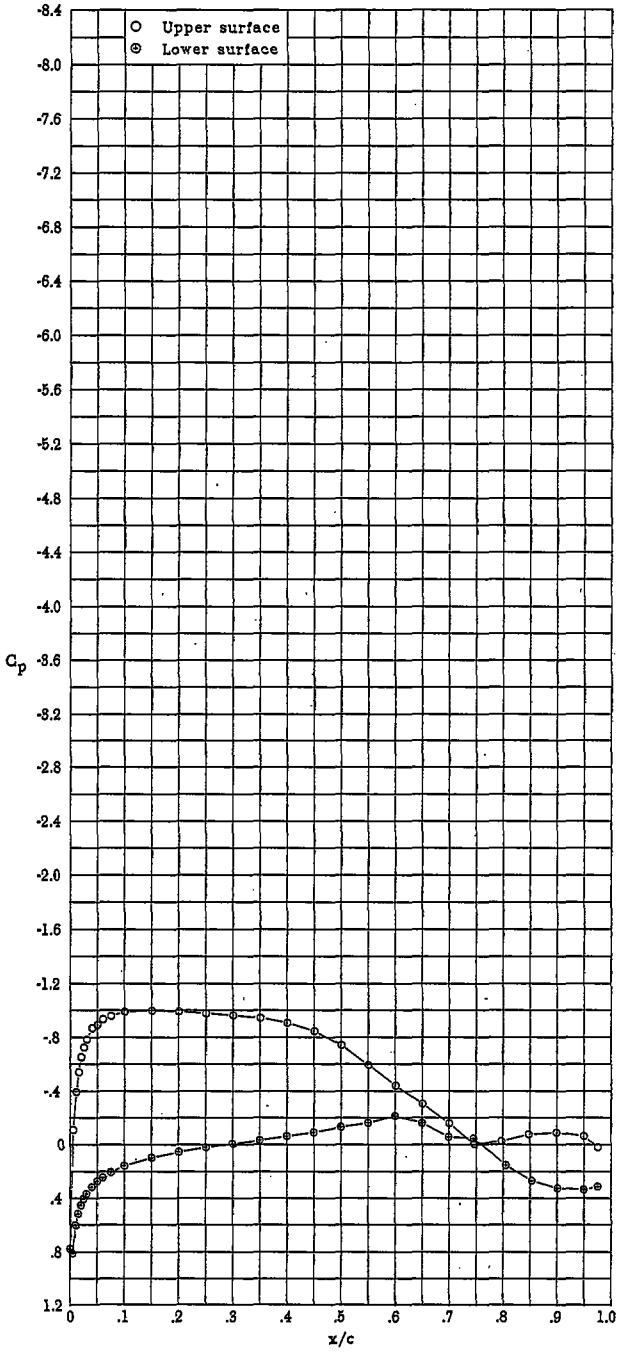

(u) $\alpha = 5.07°$; $c_l = 0.593$; $c_d = 0.0048$; $c_m = -0.054$.

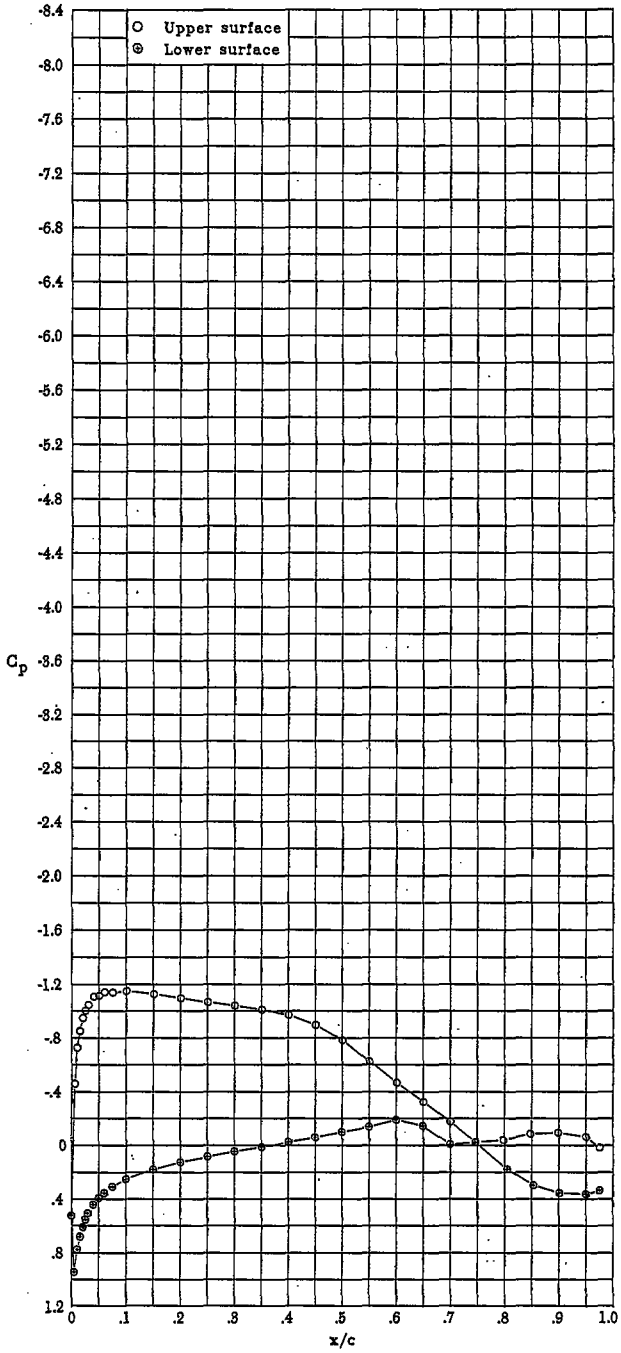

(v) $\alpha = 6.08°$; $c_l = 0.704$; $c_d = 0.0055$; $c_m = -0.058$.

Figure 7.- Continued.

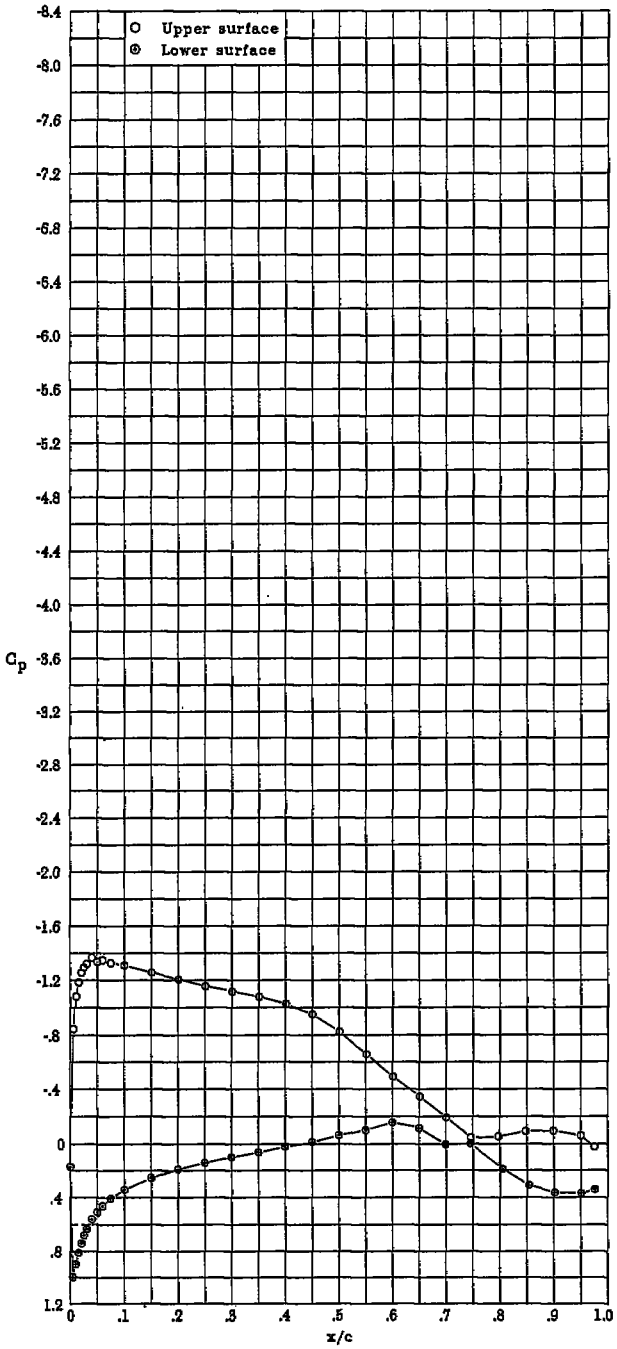

(w) α = 7.09°; c_l = 0.810; c_d = 0.0068; c_m = −0.058.

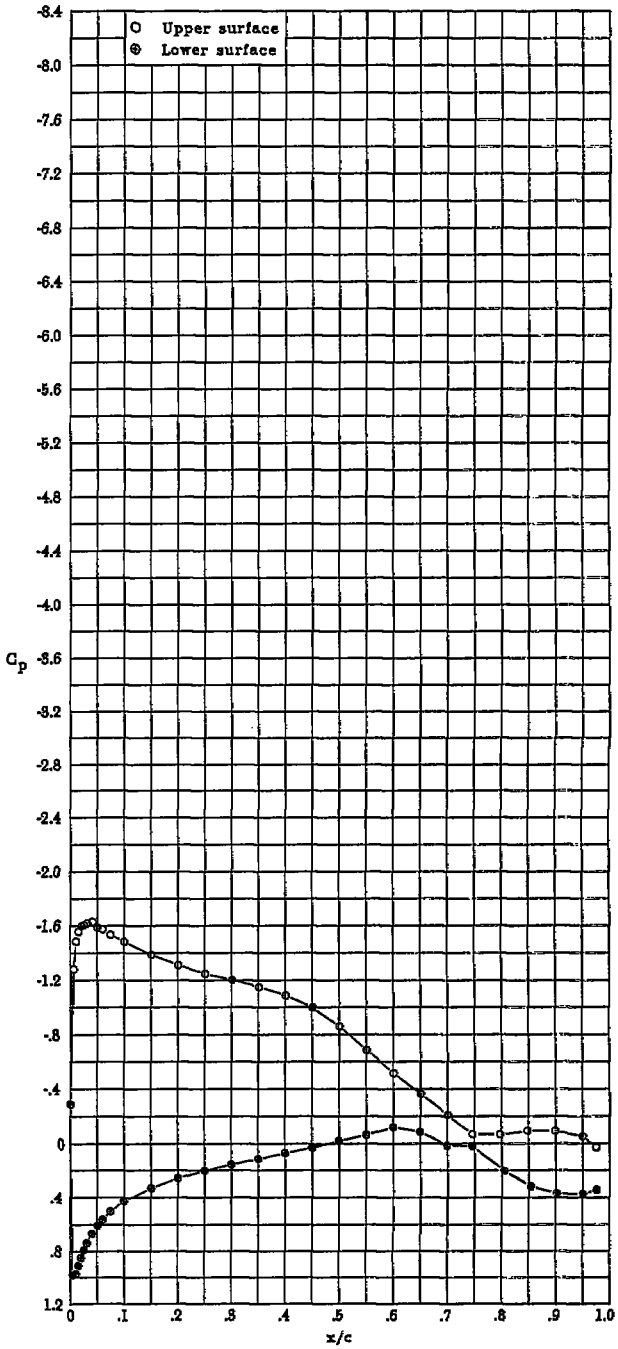

(x) α = 8.12°; c_l = 0.918; c_d = 0.0080; c_m = −0.059.

Figure 7.- Continued.

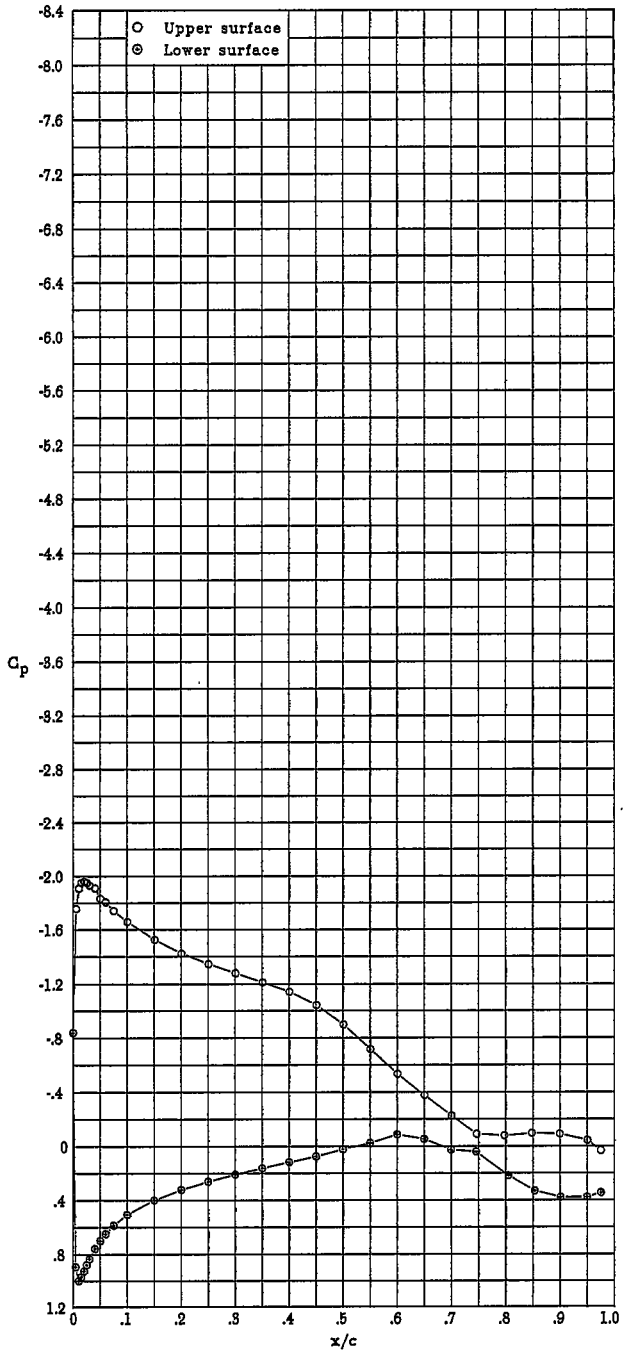

(y) $\alpha = 9.14^\circ$; $c_l = 1.024$; $c_d = 0.0091$; $c_m = -0.059$.

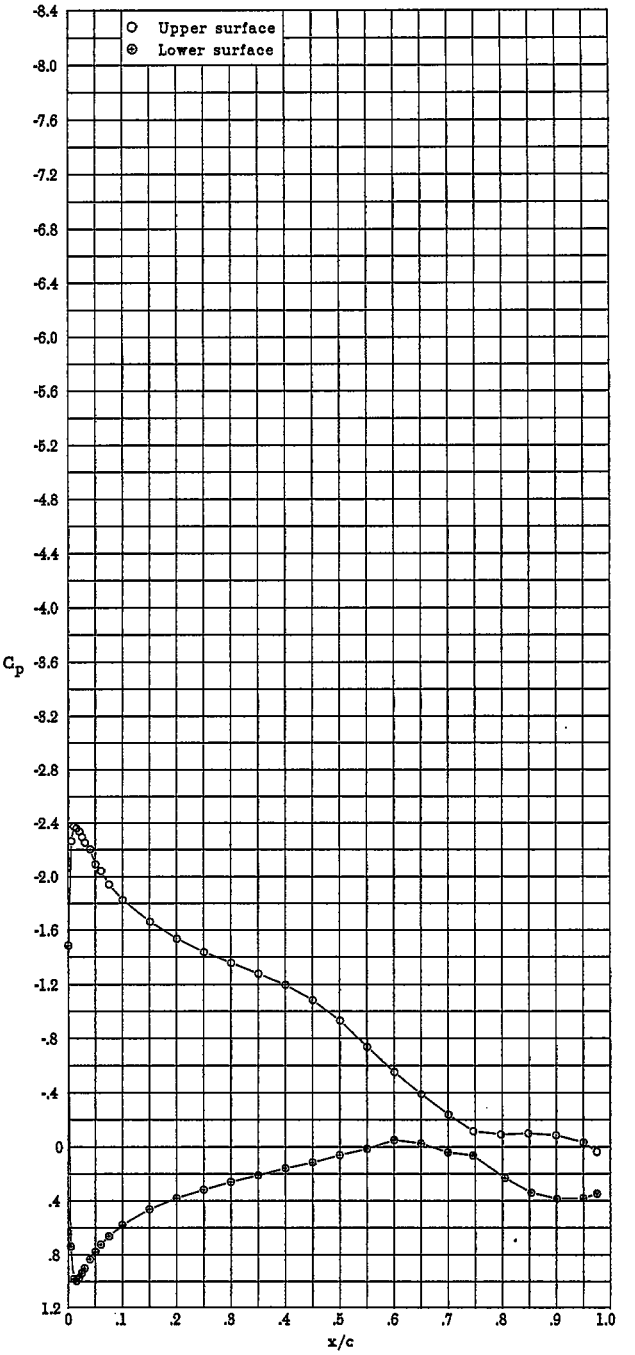

(z) $\alpha = 10.16^\circ$; $c_l = 1.127$; $c_d = 0.0099$; $c_m = -0.059$.

Figure 7.- Continued.

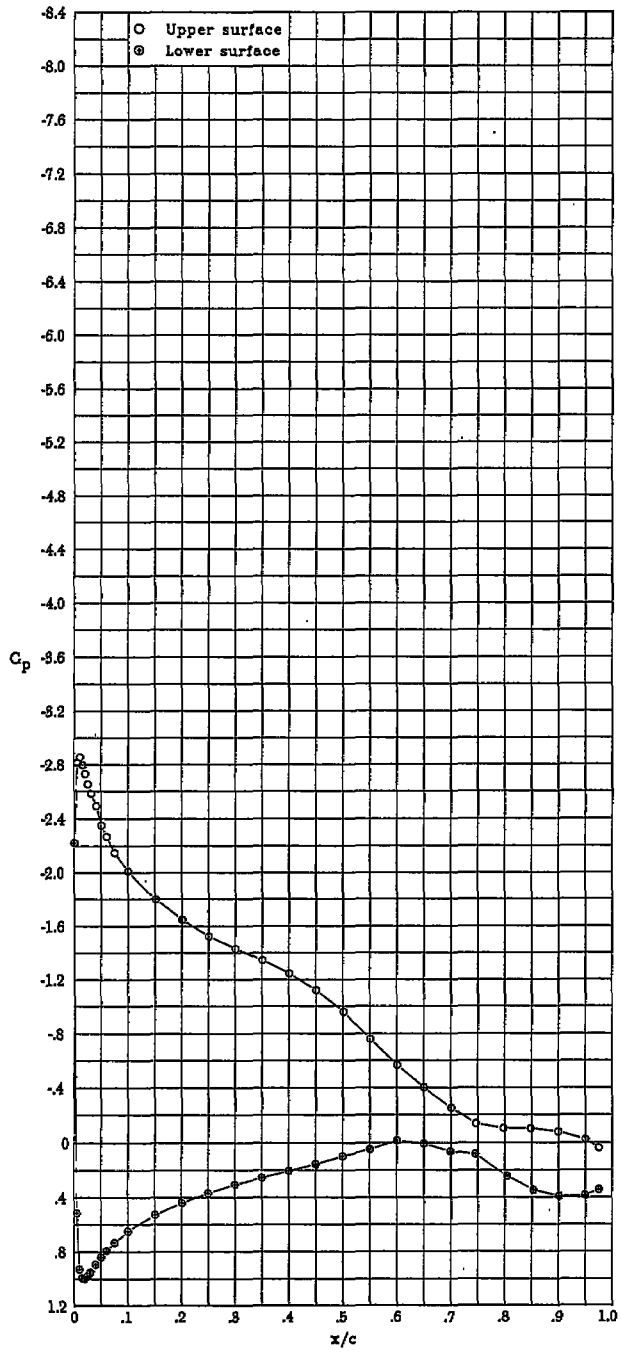

(aa) $\alpha = 11.17^\circ$; $c_l = 1.229$; $c_d = 0.0106$; $c_m = -0.059$.

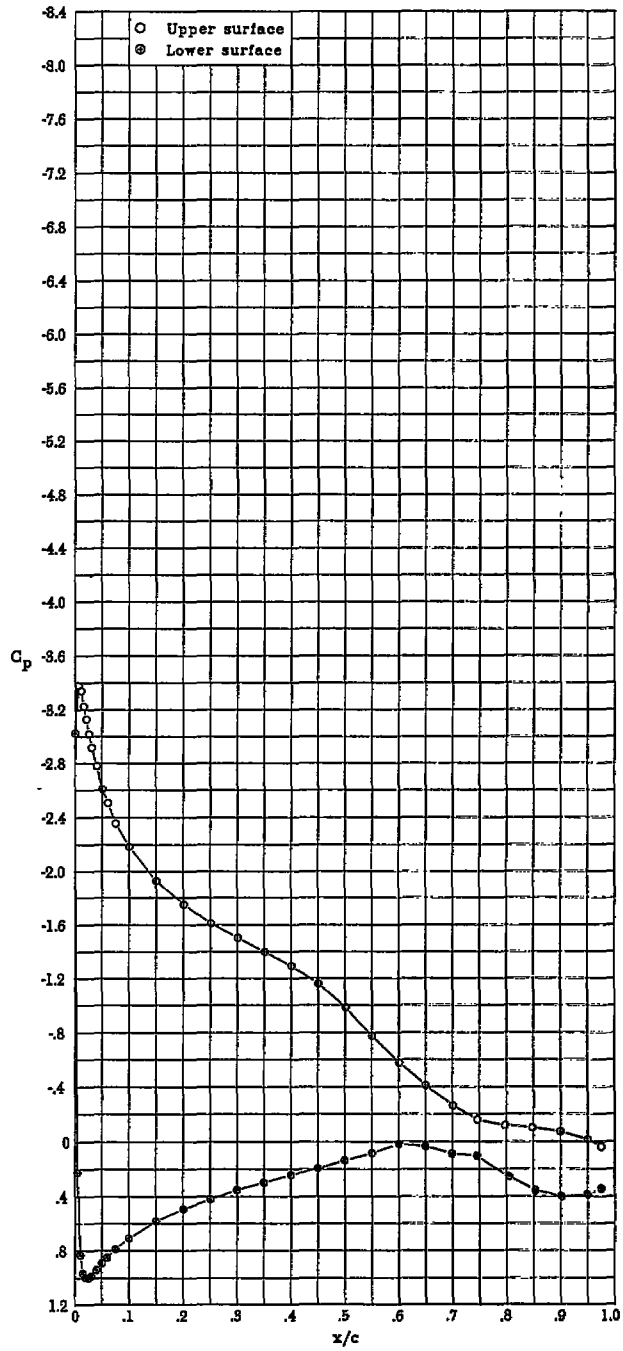

(bb) $\alpha = 12.16^\circ$; $c_l = 1.325$; $c_d = 0.0122$; $c_m = -0.059$.

Figure 7.- Continued.

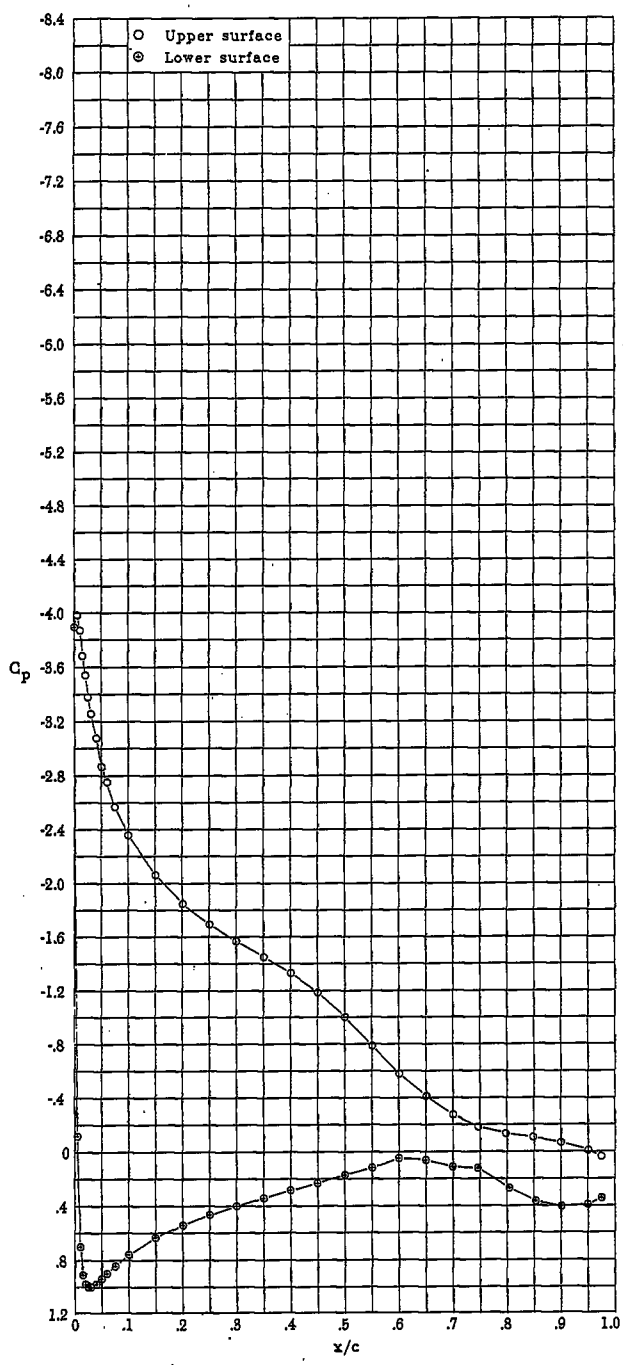

(cc) $\alpha = 13.18^\circ$; $c_l = 1.417$; $c_d = 0.0139$; $c_m = -0.059$.

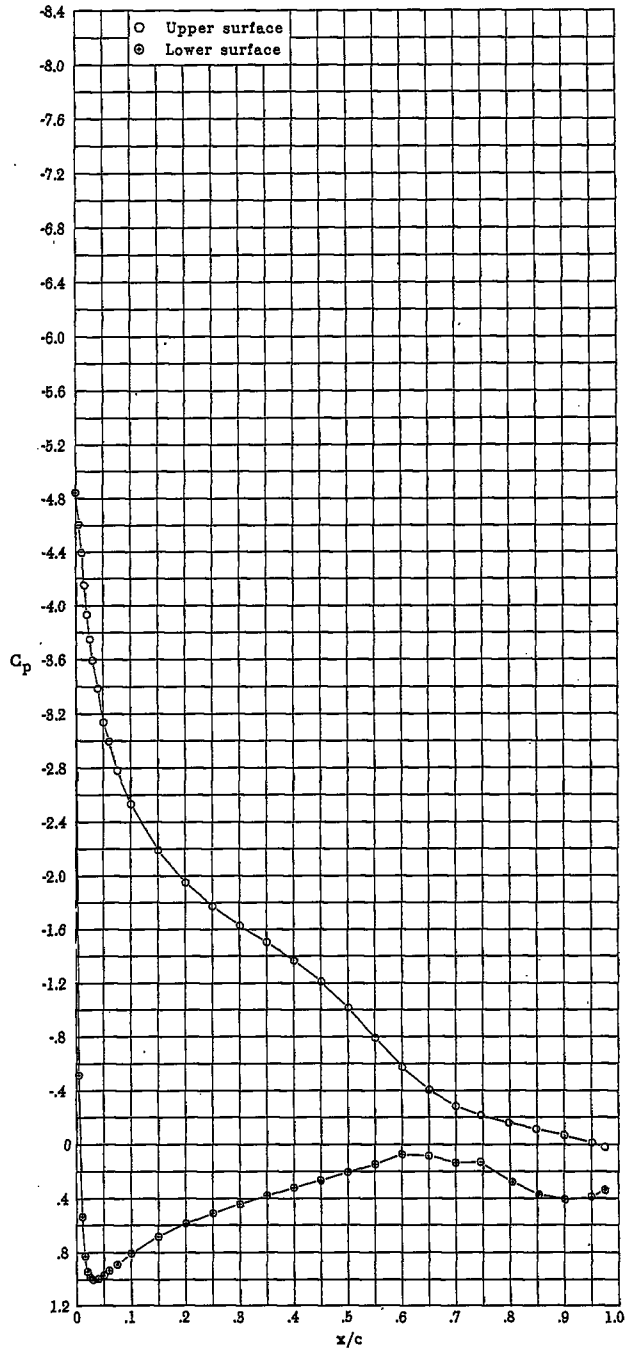

(dd) $\alpha = 14.20^\circ$; $c_l = 1.506$; $c_d = 0.0164$; $c_m = -0.059$.

Figure 7.- Continued.

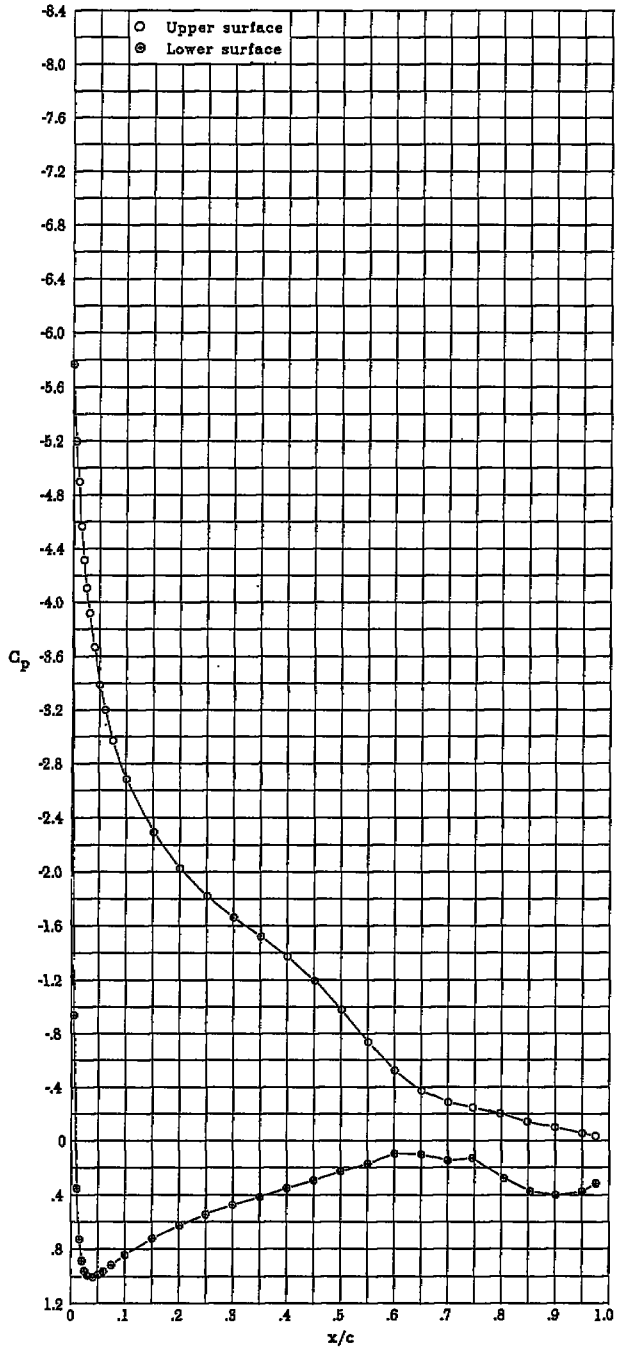

(ee) α = 15.25°; c_l = 1.568; c_d = 0.0214; c_m = −0.057.

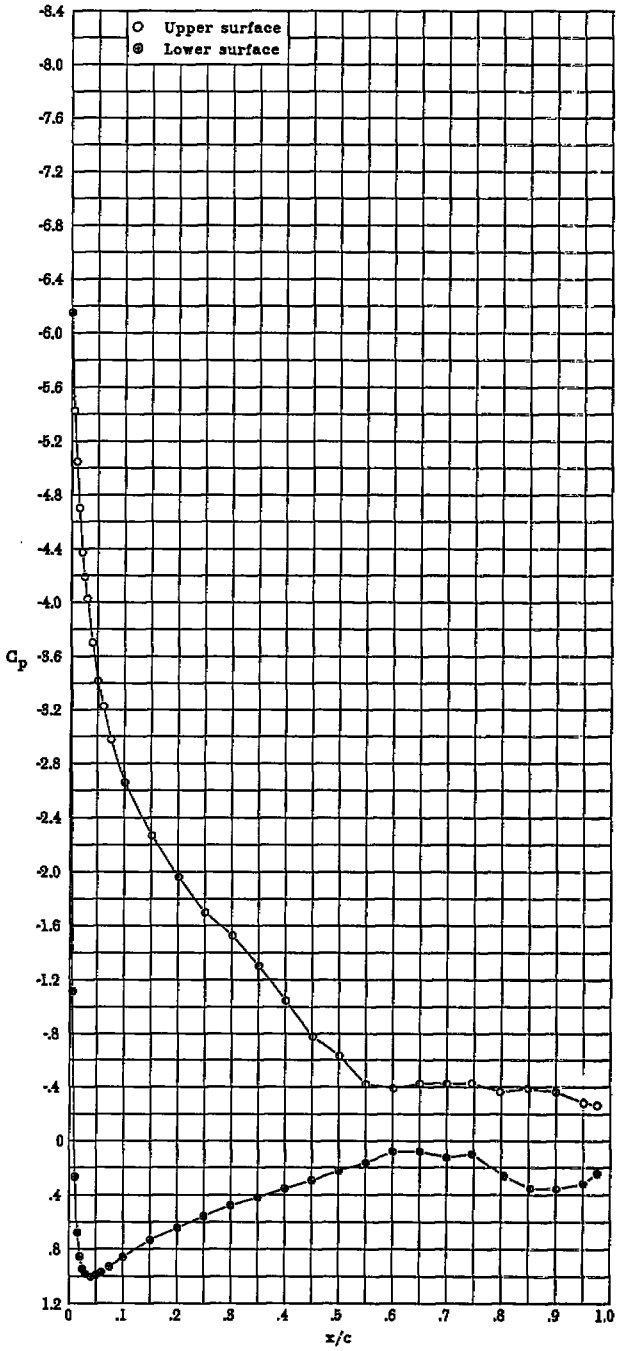

(ff) α = 16.21°; c_l = 1.505; c_d = 0.0694; c_m = −0.066.

Figure 7.- Continued.

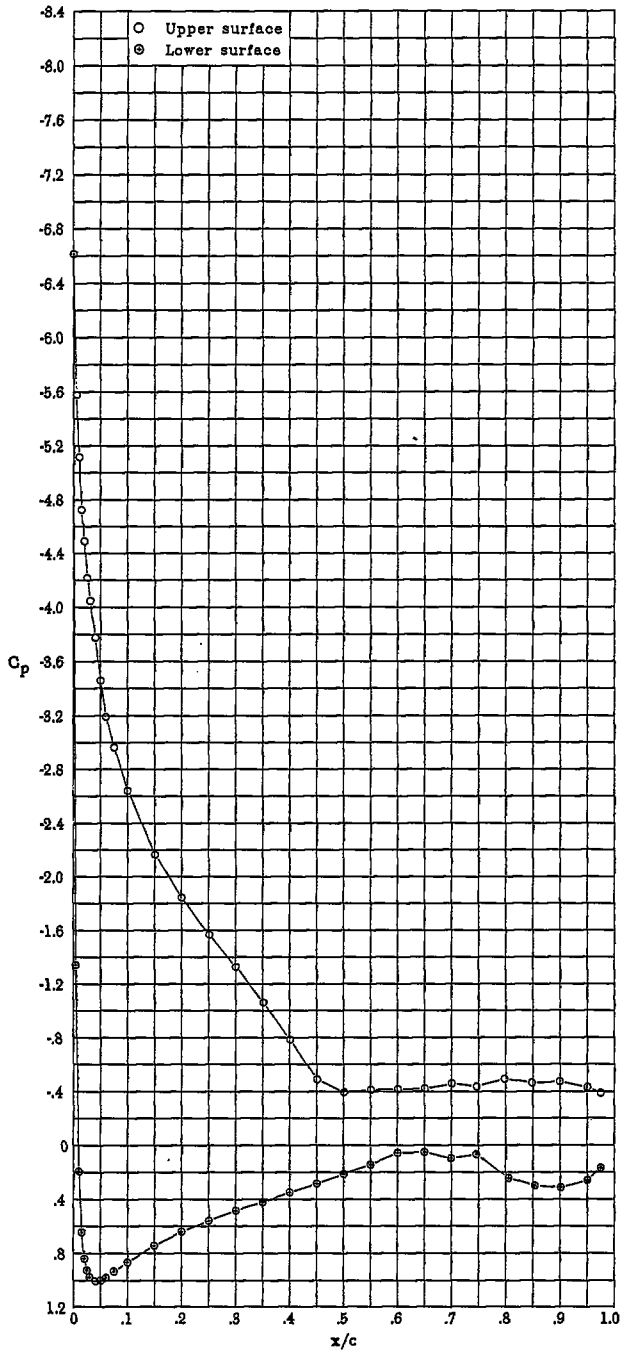

(gg) α = 17.22°; c_l = 1.429; c_d = 0.1089; c_m = −0.064.

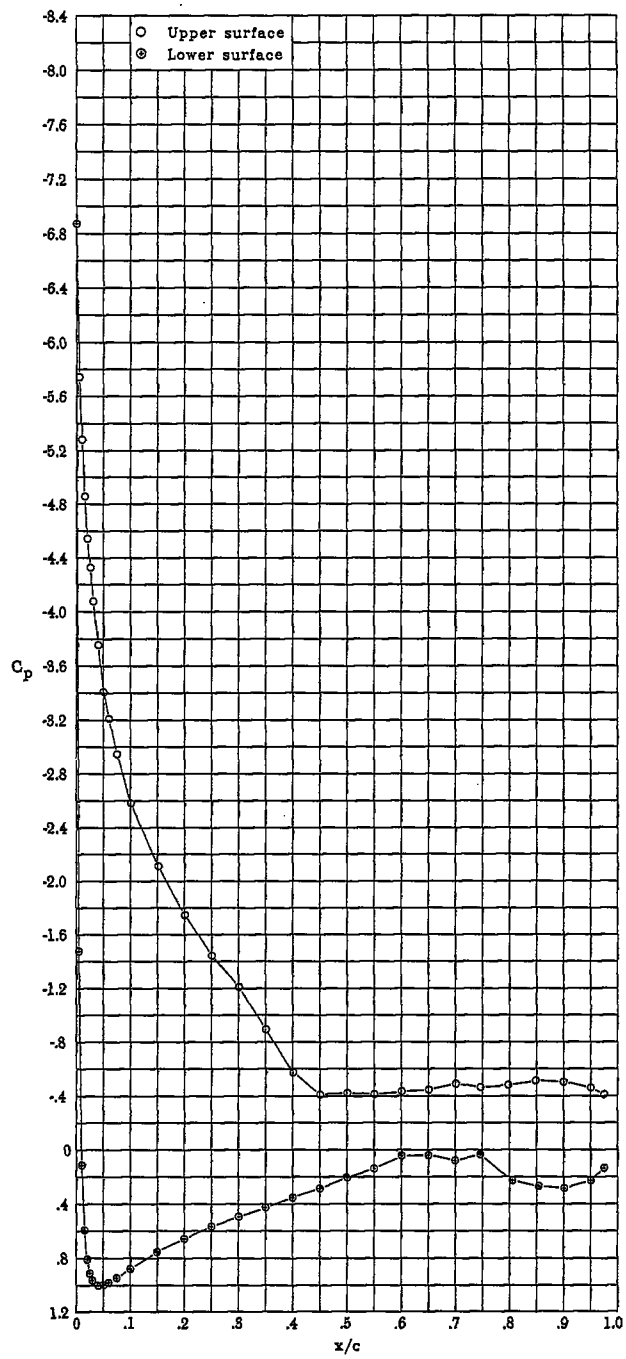

(hh) α = 18.21°; c_l = 1.388; c_d = 0.1250; c_m = −0.060.

Figure 7.- Concluded.

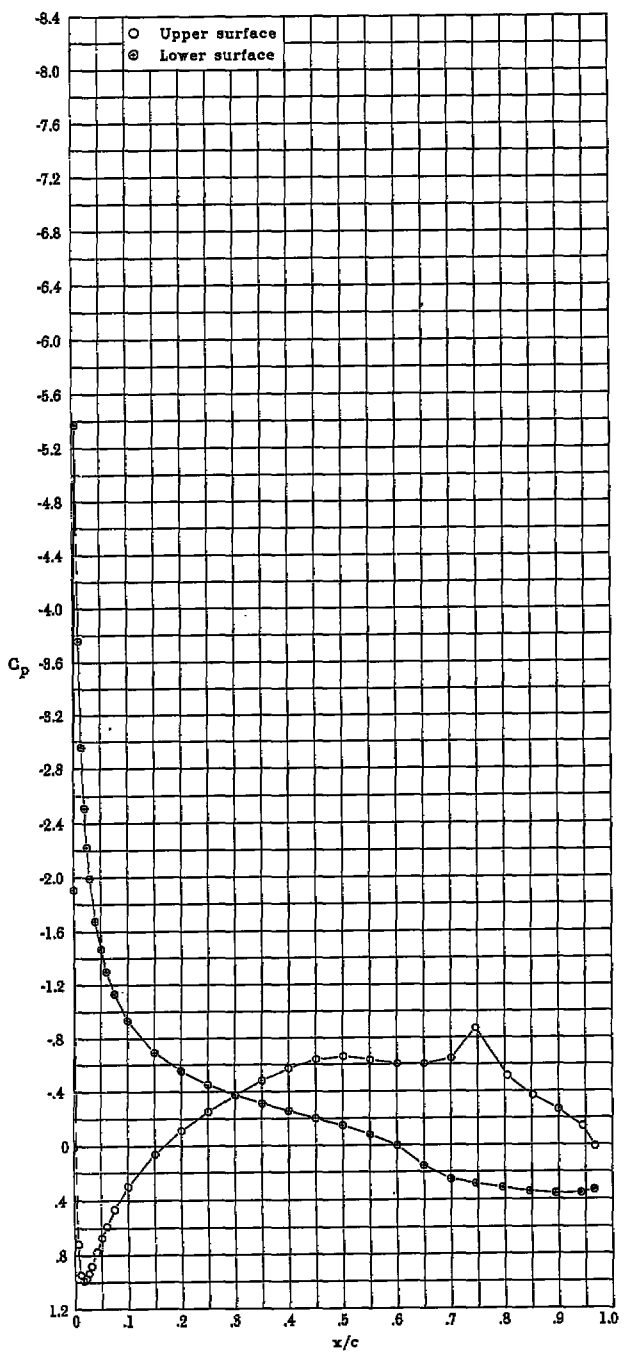

(a) $\alpha = -11.18^{\circ}$; $c_l = 0.059$; $c_d = 0.0084$; $c_m = -0.228$.

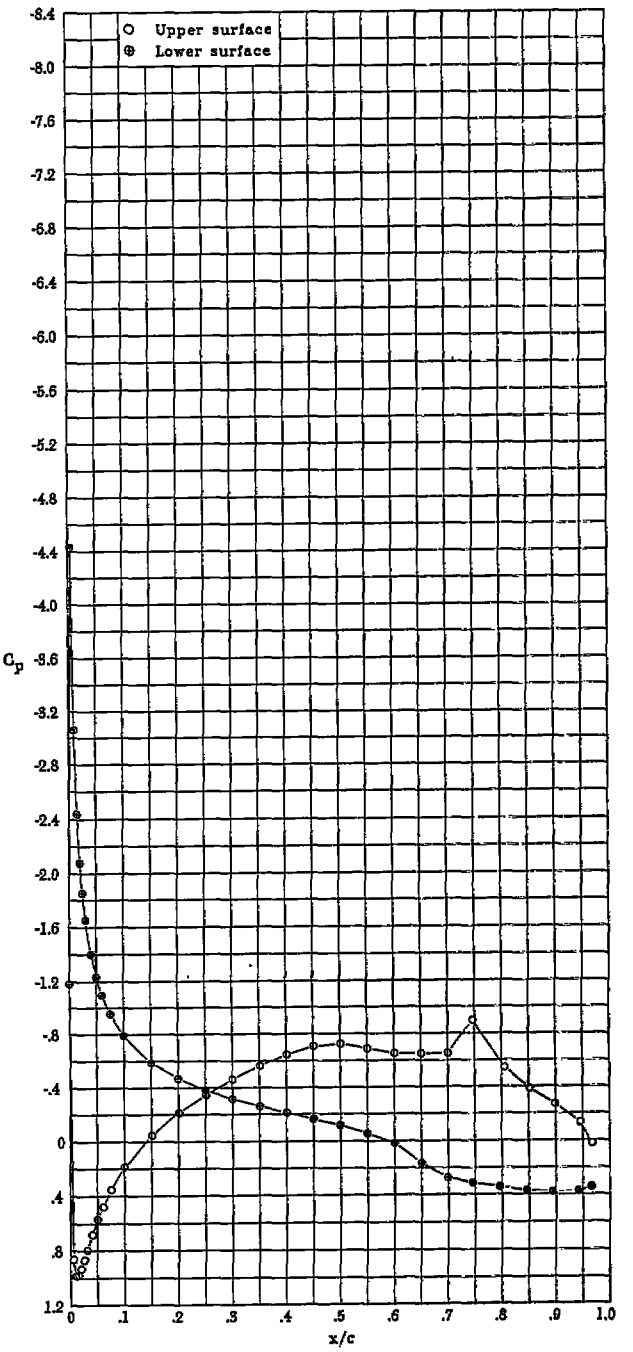

(b) $\alpha = -10.12^{\circ}$; $c_l = 0.180$; $c_d = 0.0083$; $c_m = -0.232$.

Figure 8.- Pressure distributions with $\delta_f = 10^{\circ}$ for $R = 6.0 \times 10^6$ and $M = 0.10$.

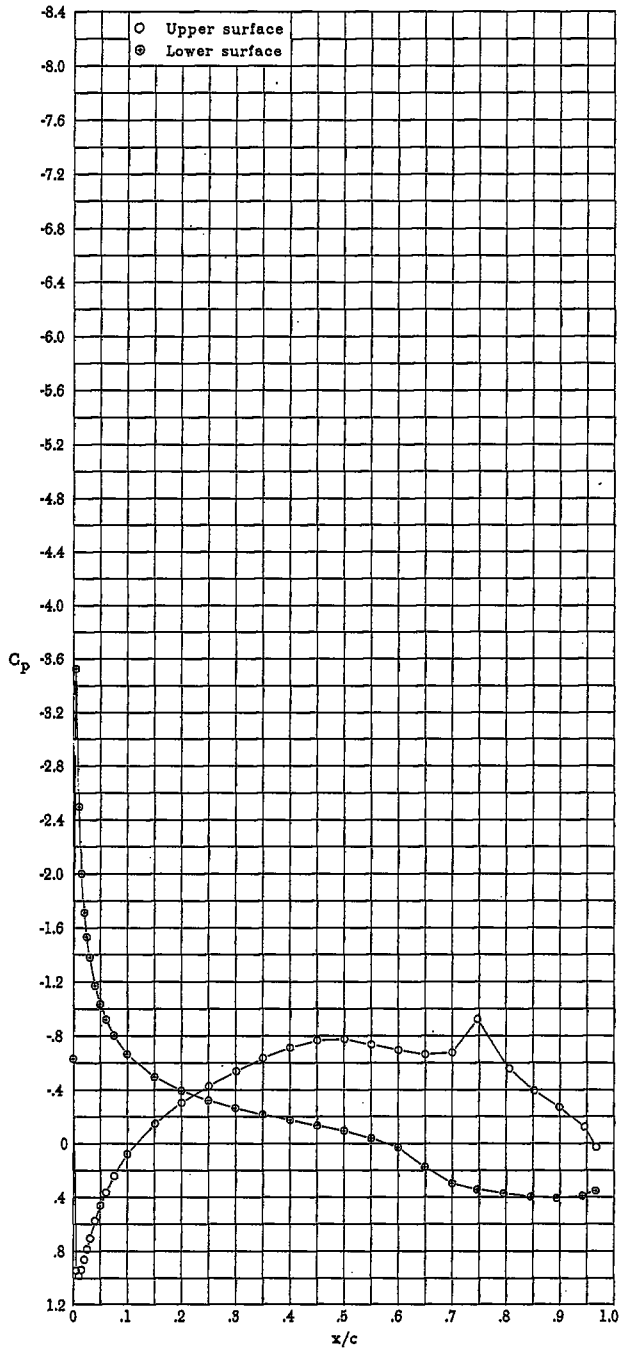

(c) $\alpha = -9.11^\circ$; $c_l = 0.284$; $c_d = 0.0077$; $c_m = -0.233$.

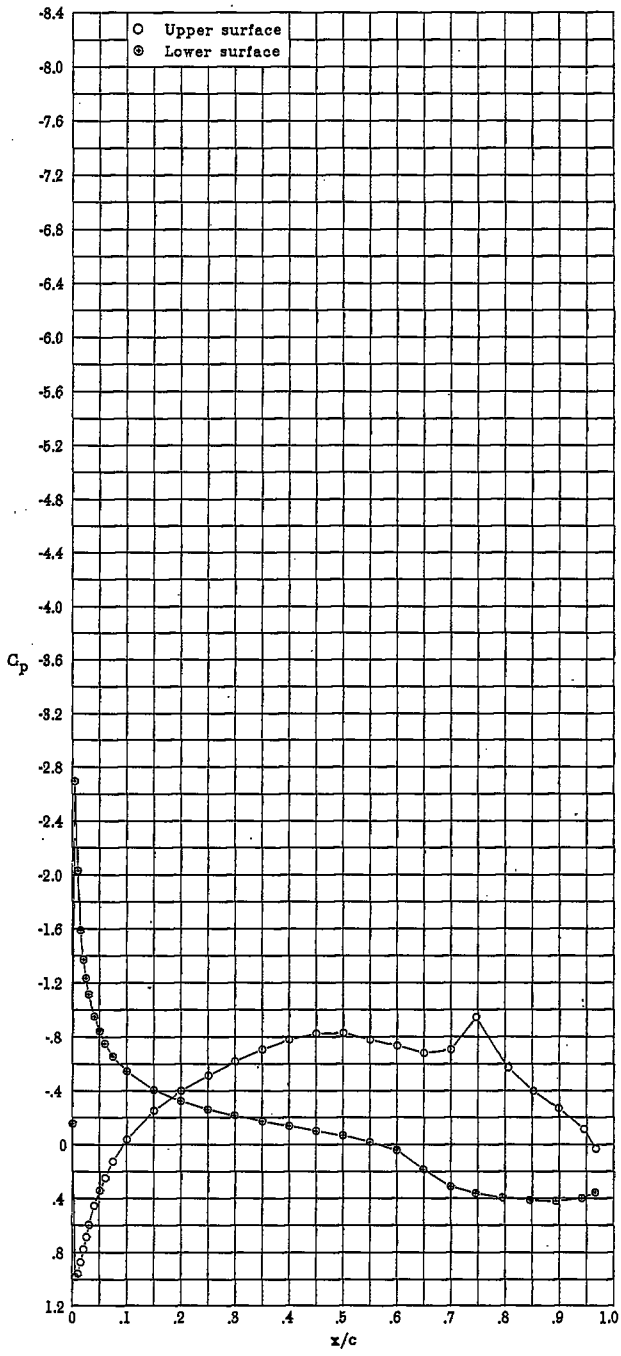

(d) $\alpha = -8.11^\circ$; $c_l = 0.387$; $c_d = 0.0080$; $c_m = -0.234$.

Figure 8.- Continued.

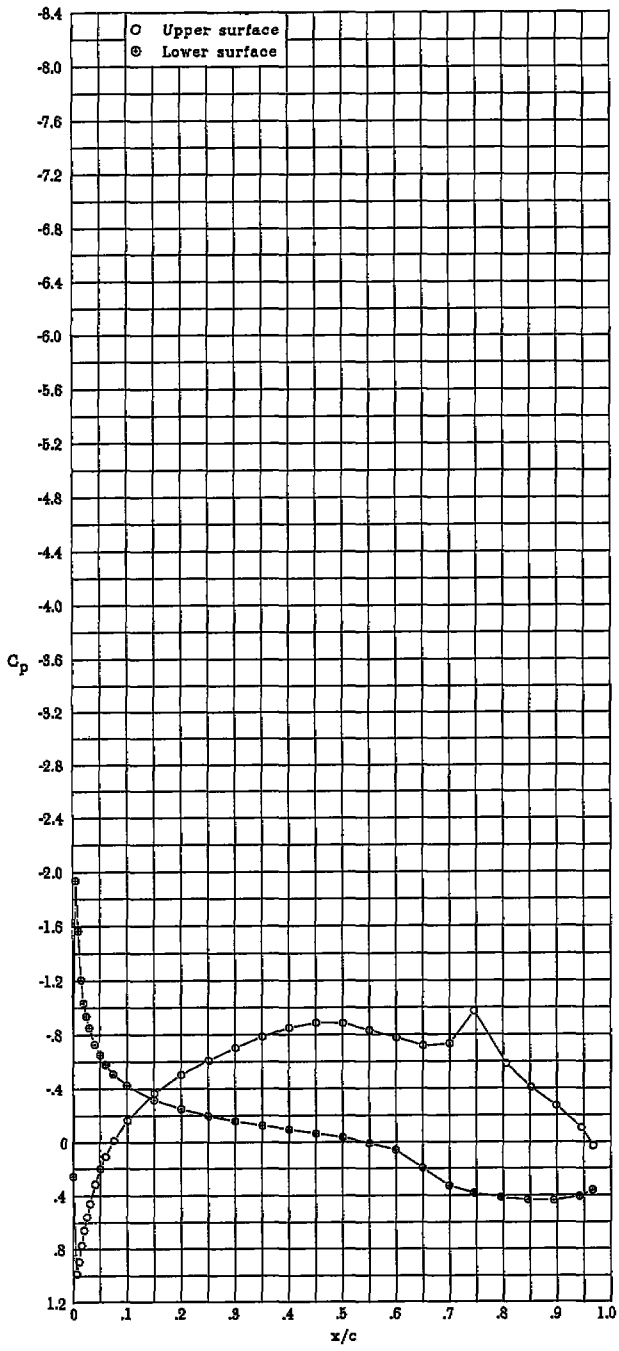

(e) $\alpha = -7.08^\circ$; $c_l = 0.500$; $c_d = 0.0075$; $c_m = -0.237$.

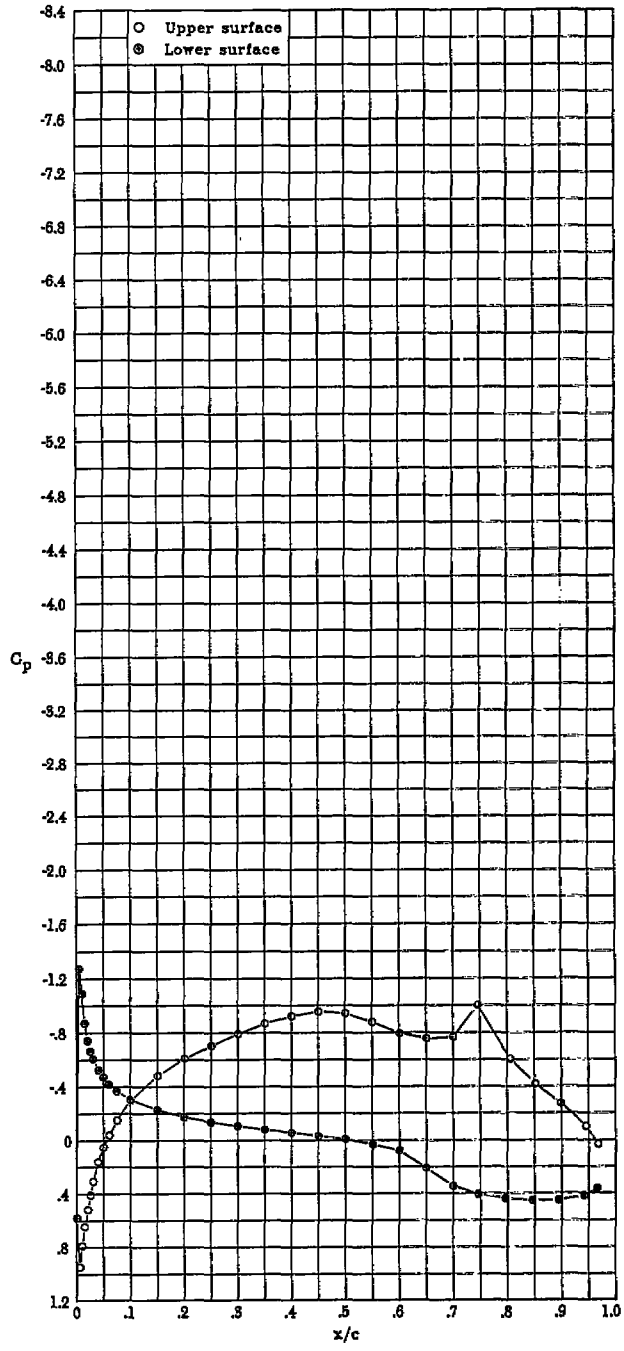

(f) $\alpha = -6.05^\circ$; $c_l = 0.609$; $c_d = 0.0073$; $c_m = -0.239$.

Figure 8.- Continued.

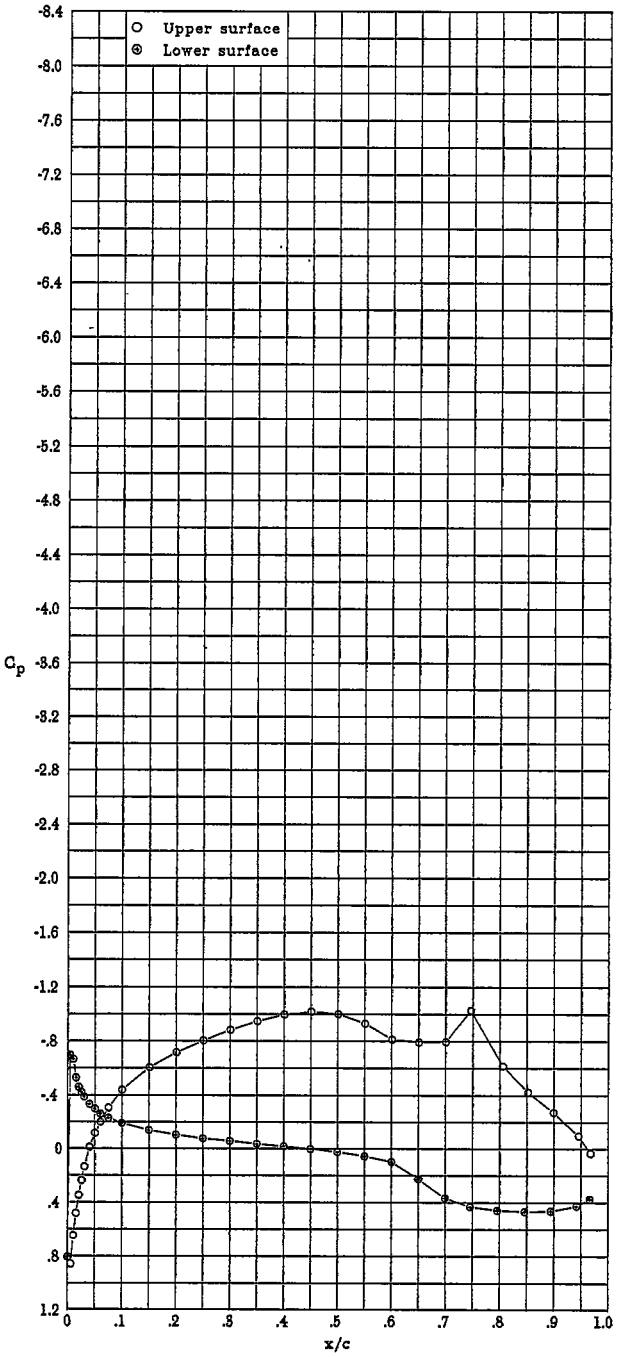

(g) $\alpha = -5.04°$; $c_l = 0.721$; $c_d = 0.0066$; $c_m = -0.240$.

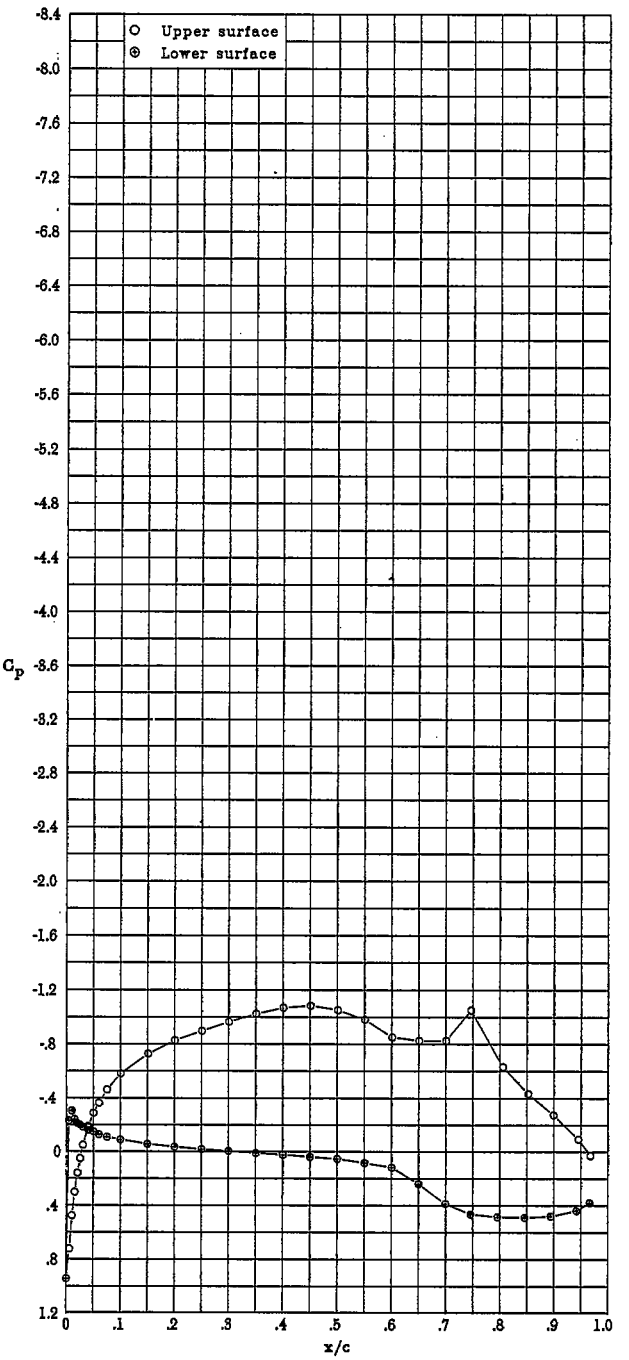

(h) $\alpha = -4.08°$; $c_l = 0.830$; $c_d = 0.0063$; $c_m = -0.243$.

Figure 8.- Continued.

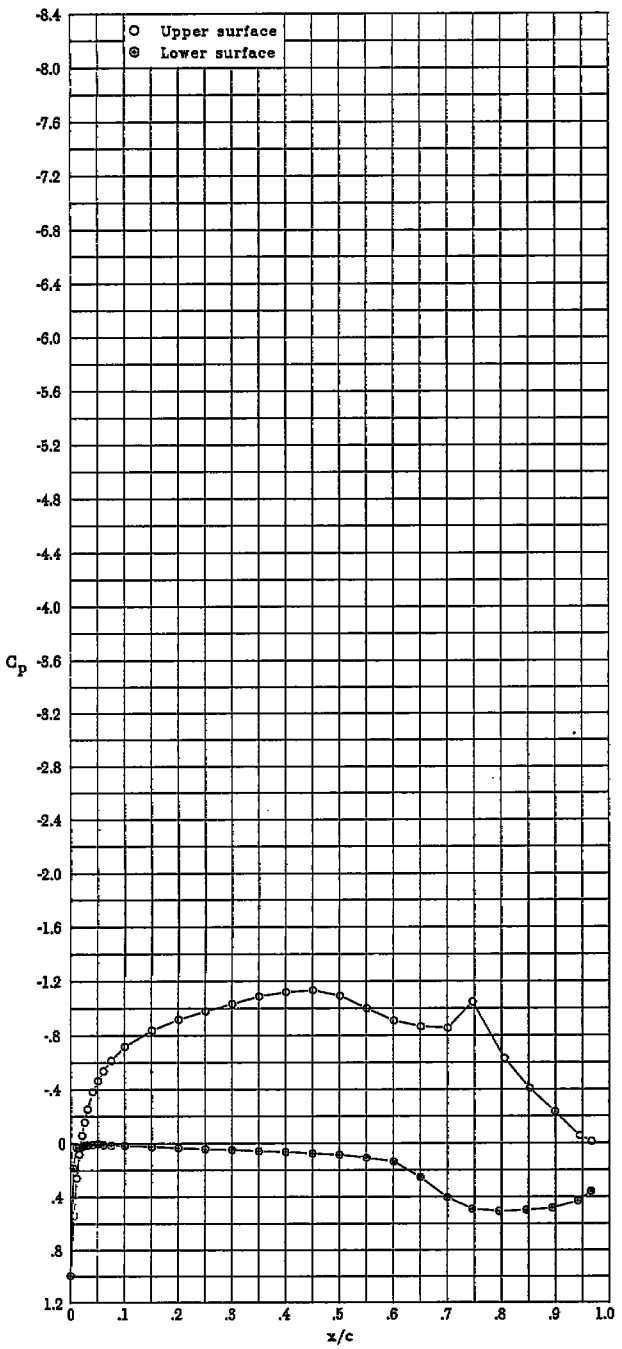

(i) $\alpha = -3.04^\circ$; $c_l = 0.925$; $c_d = 0.0057$; $c_m = -0.241$.

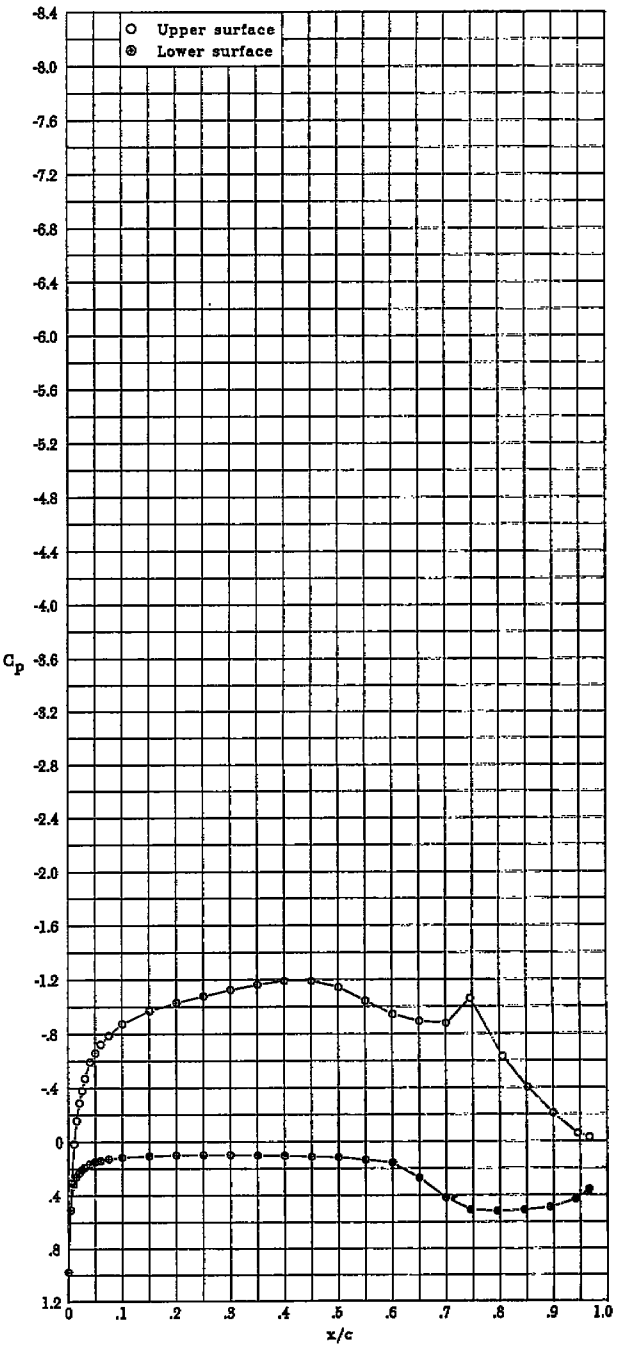

(j) $\alpha = -2.00^\circ$; $c_l = 1.030$; $c_d = 0.0058$; $c_m = -0.240$

Figure 8.- Continued.

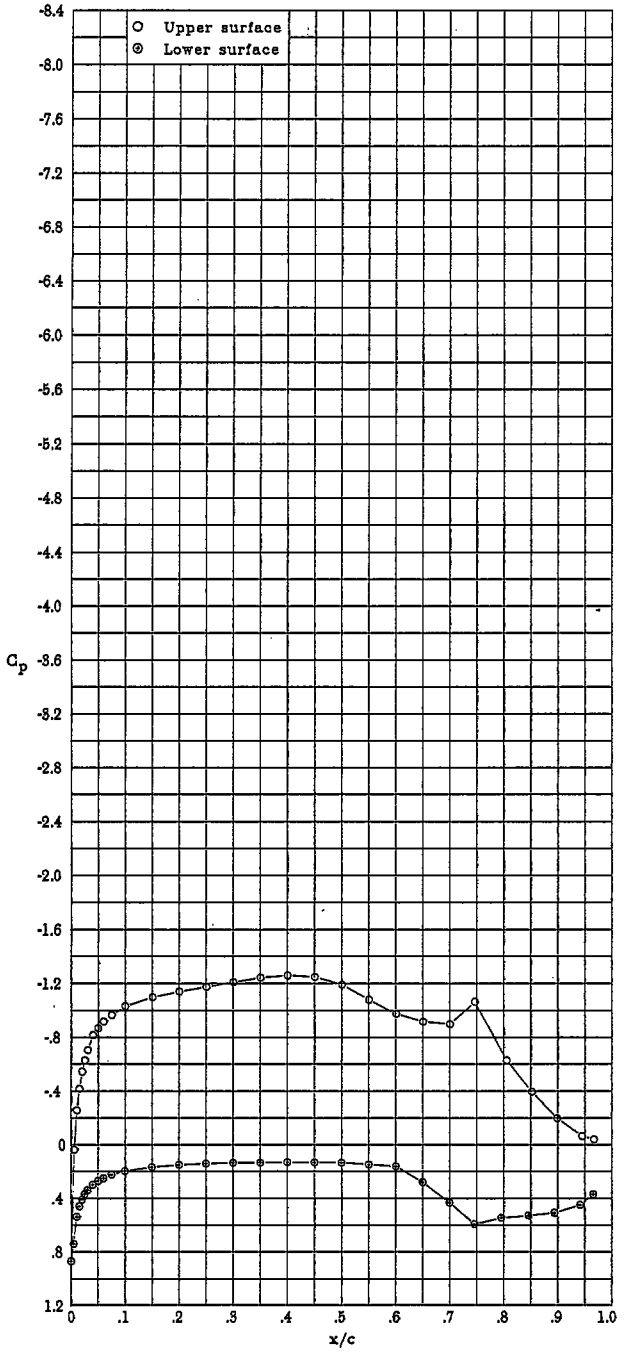

(k) $\alpha = -0.96^\circ$; $c_l = 1.129$; $c_d = 0.0059$; $c_m = -0.242$.

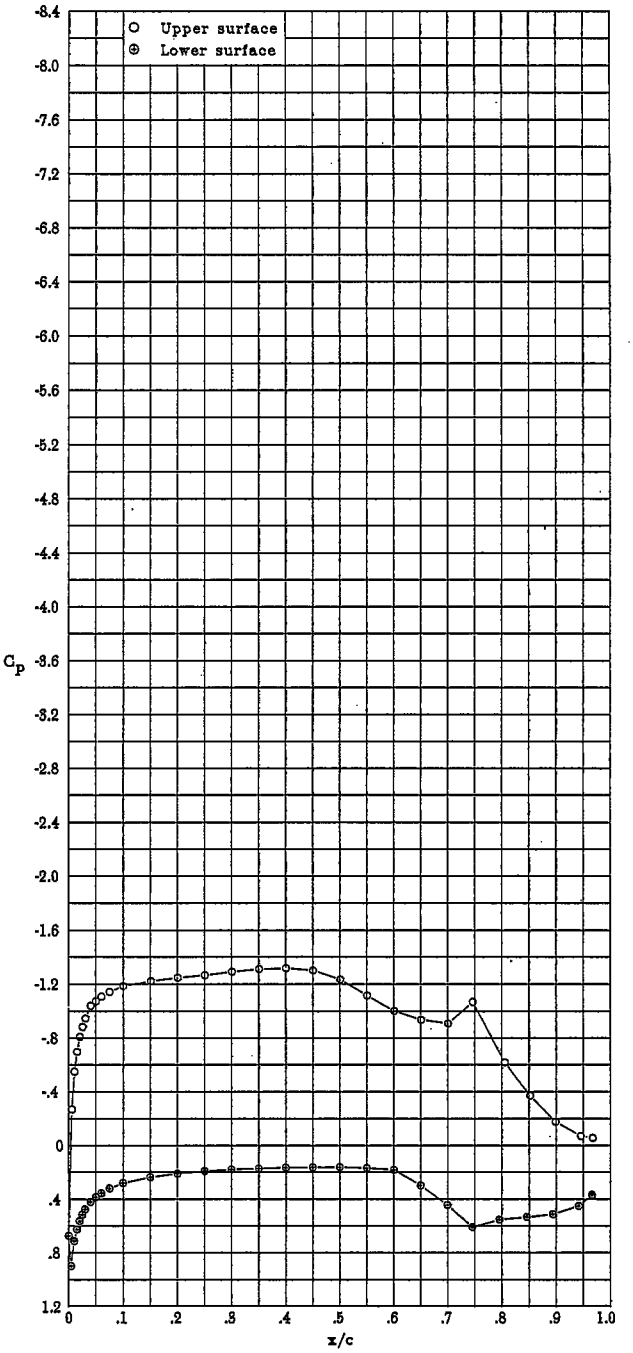

(l) $\alpha = 0.05^\circ$; $c_l = 1.223$; $c_d = 0.0061$; $c_m = -0.240$.

Figure 8.- Continued.

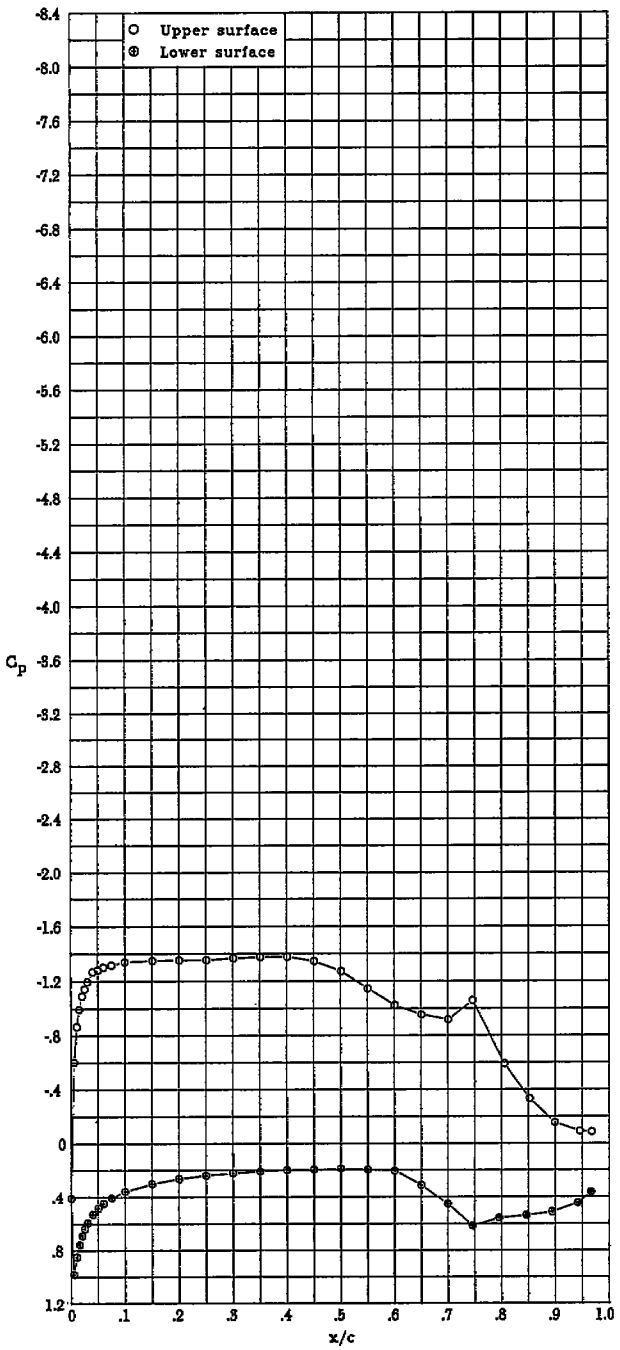

(m) $\alpha = 1.05°$; $c_l = 1.309$; $c_d = 0.0064$; $c_m = -0.236$.

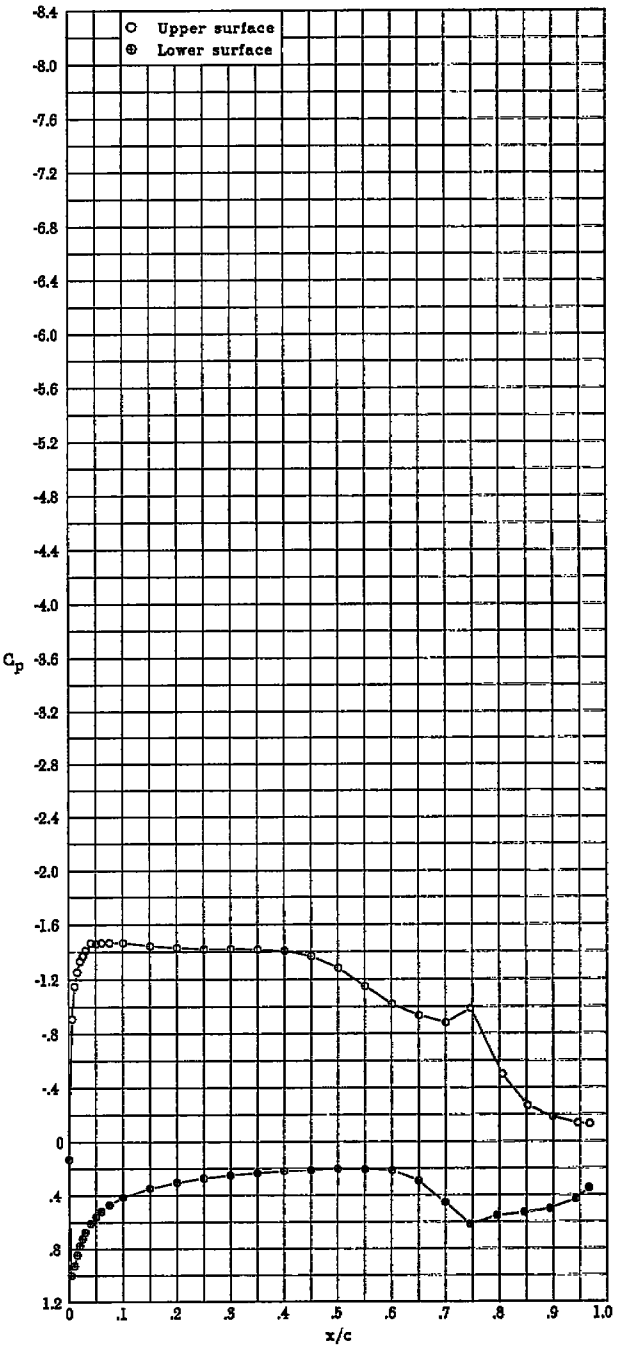

(n) $\alpha = 2.08°$; $c_l = 1.356$; $c_d = 0.0084$; $c_m = -0.226$.

Figure 8.- Continued.

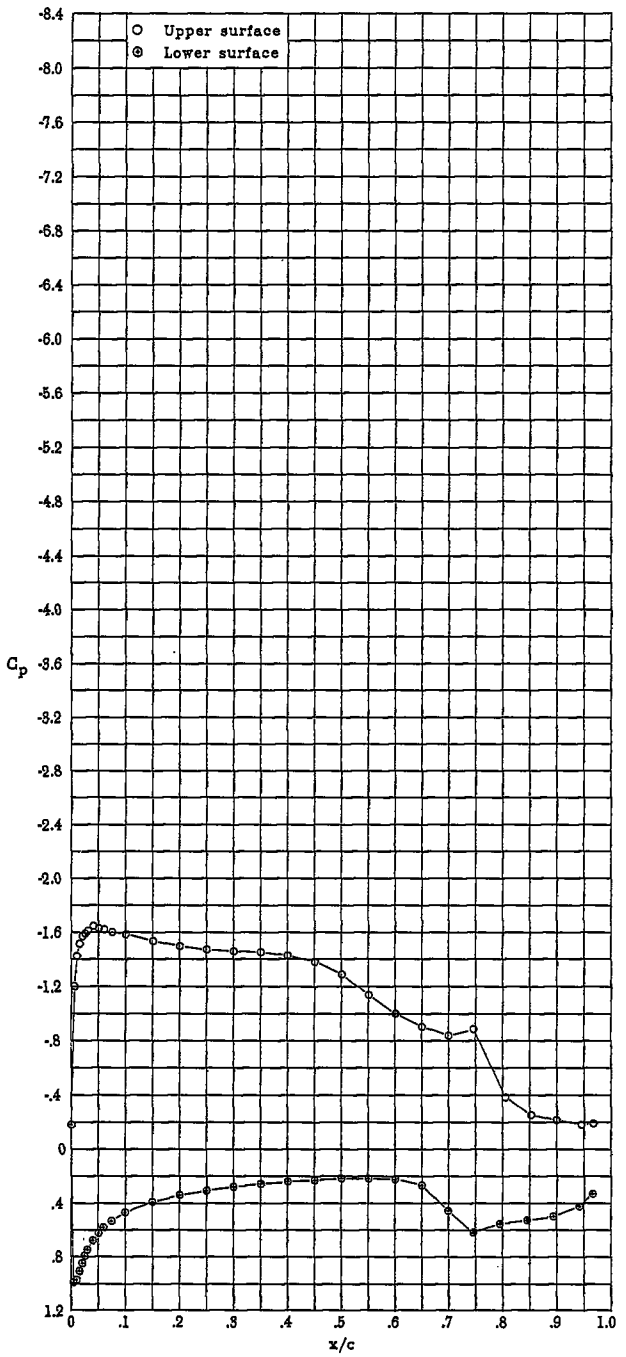

(o) $\alpha = 3.09^\circ$; $c_l = 1.395$; $c_d = 0.0114$; $c_m = -0.215$.

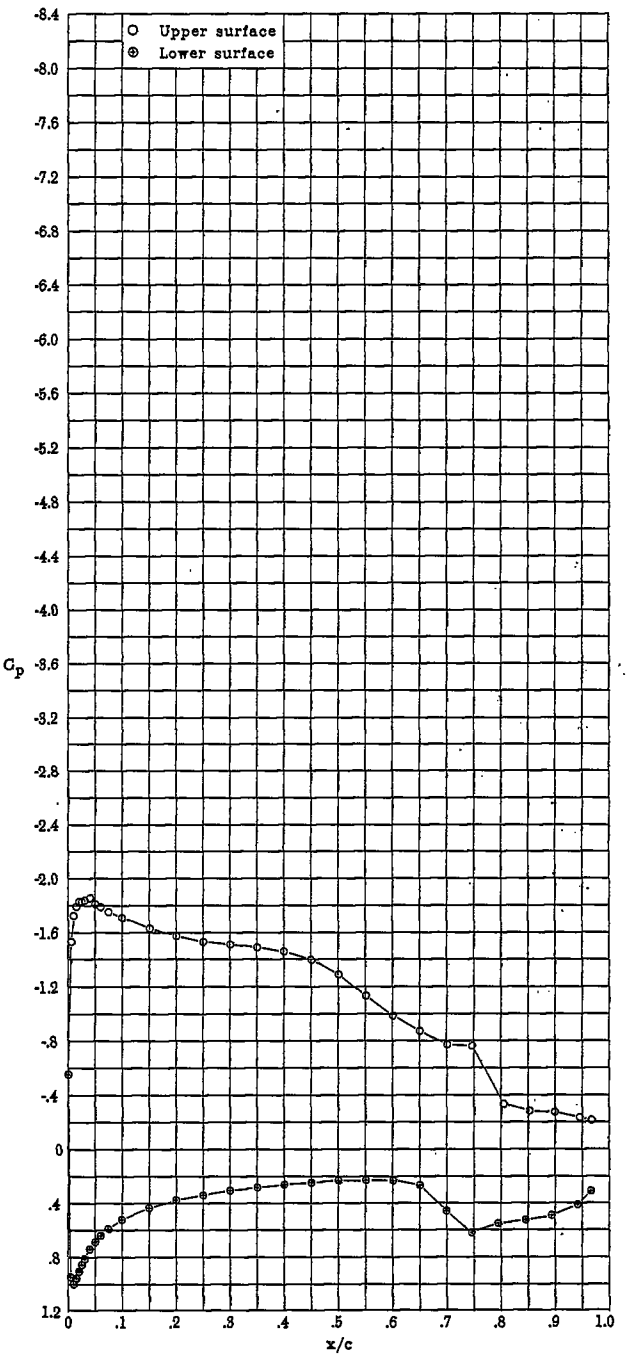

(p) $\alpha = 4.08^\circ$; $c_l = 1.443$; $c_d = 0.0145$; $c_m = -0.207$.

Figure 8.- Continued.

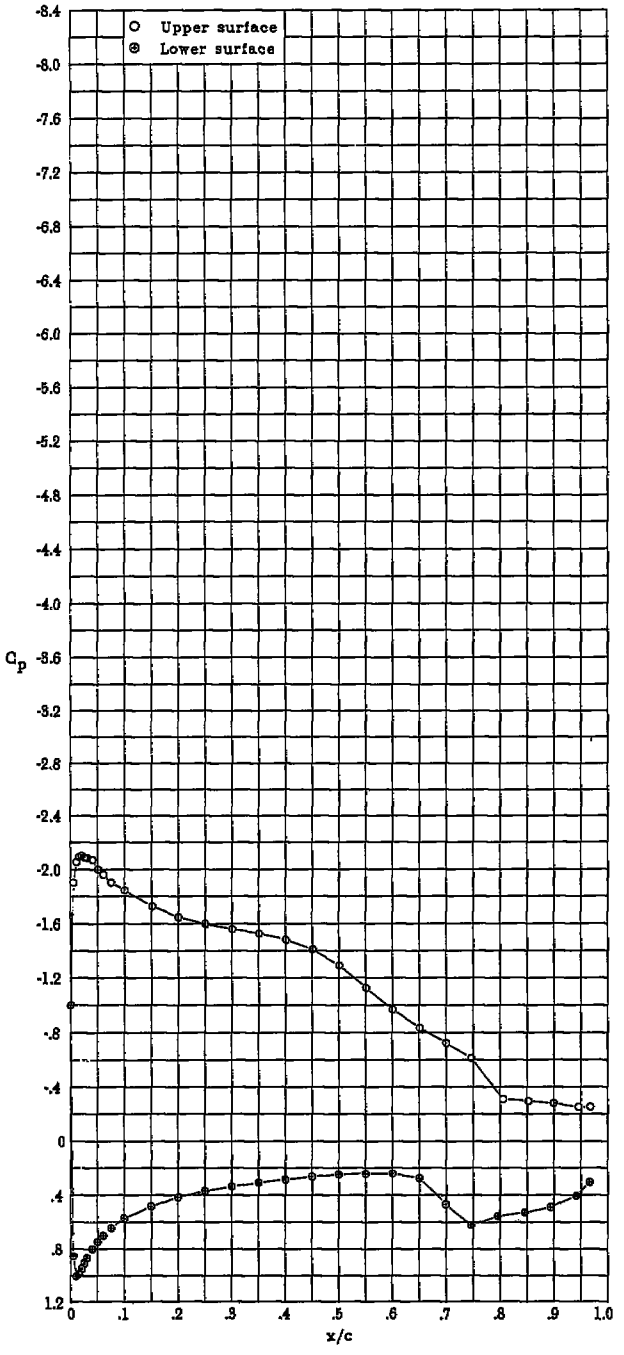

(q) $\alpha = 5.10^\circ$; $c_l = 1.489$; $c_d = 0.0239$; $c_m = -0.198$.

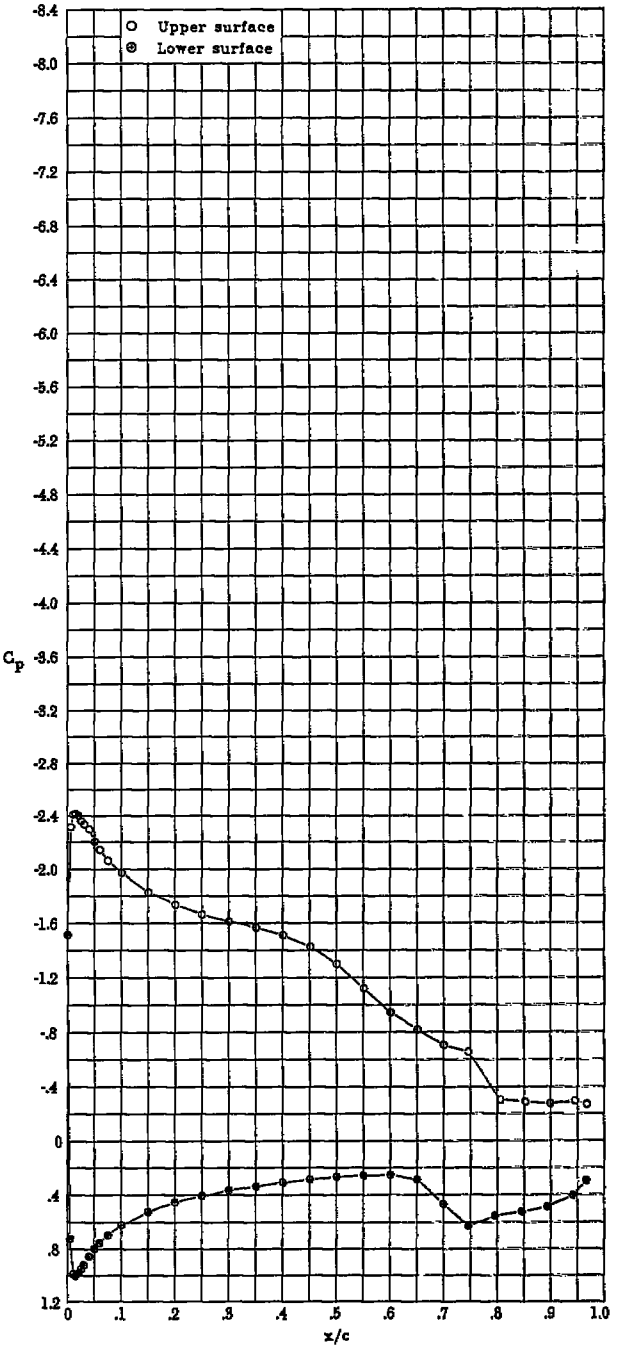

(r) $\alpha = 6.11^\circ$; $c_l = 1.561$; $c_d = 0.0309$; $c_m = -0.195$.

Figure 8.- Continued.

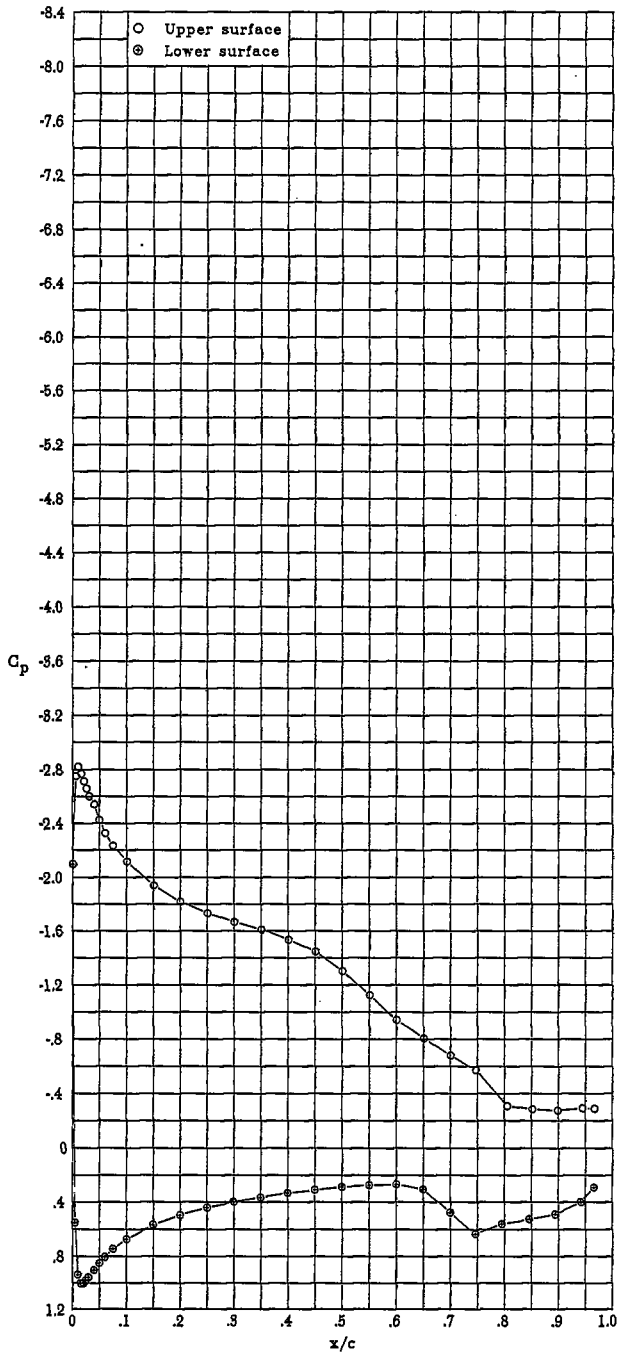

(s) $\alpha = 7.13°$; $c_l = 1.612$; $c_d = 0.0338$; $c_m = -0.189$.

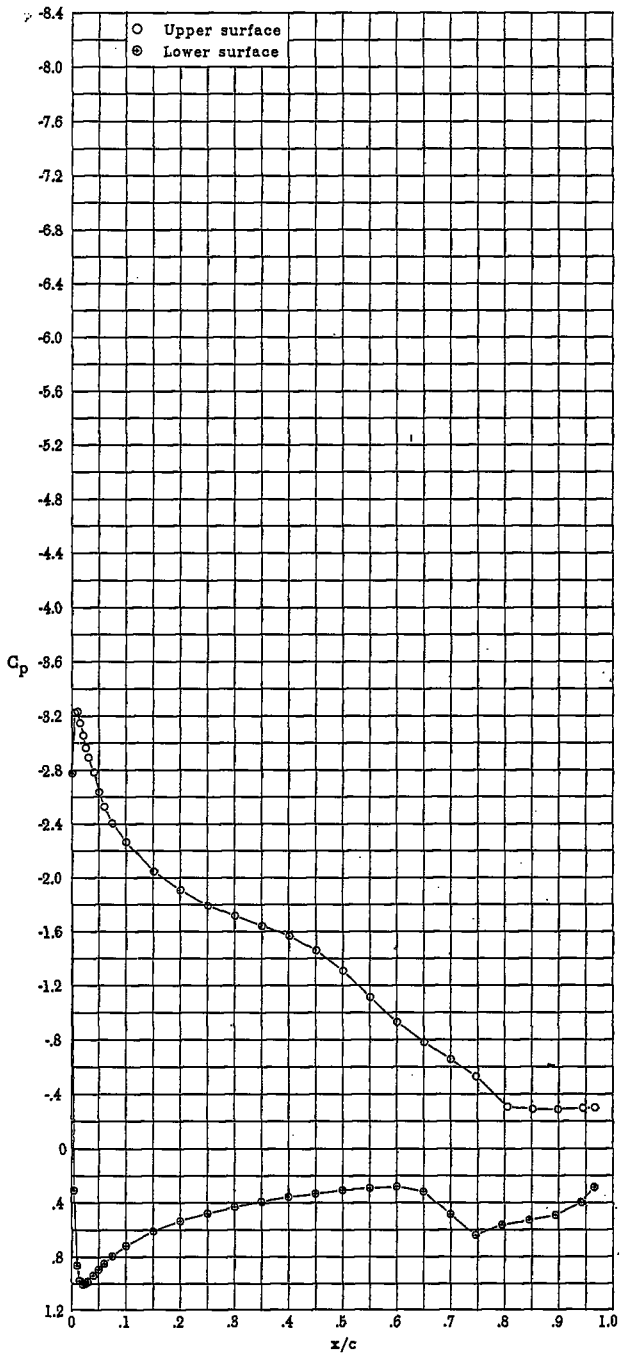

(t) $\alpha = 8.14°$; $c_l = 1.674$; $c_d = 0.0358$; $c_m = -0.184$.

Figure 8.- Continued.

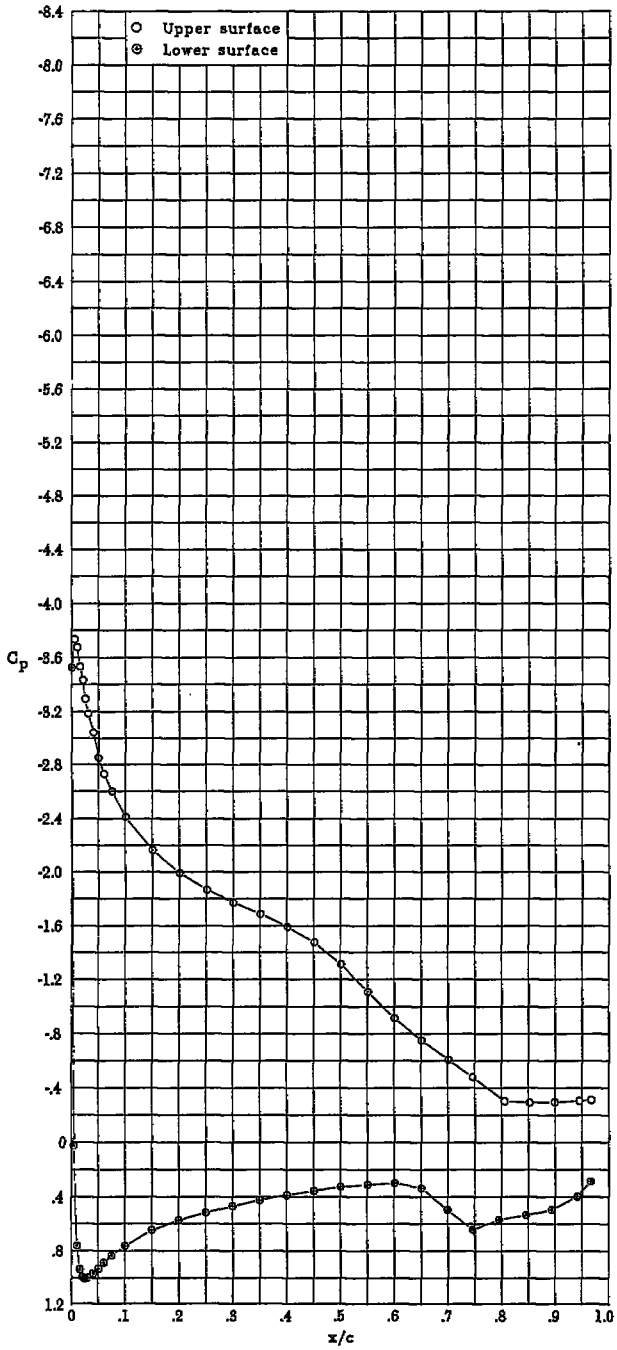

(u) $\alpha = 9.16^\circ$; $c_l = 1.736$; $c_d = 0.0418$; $c_m = -0.178$.

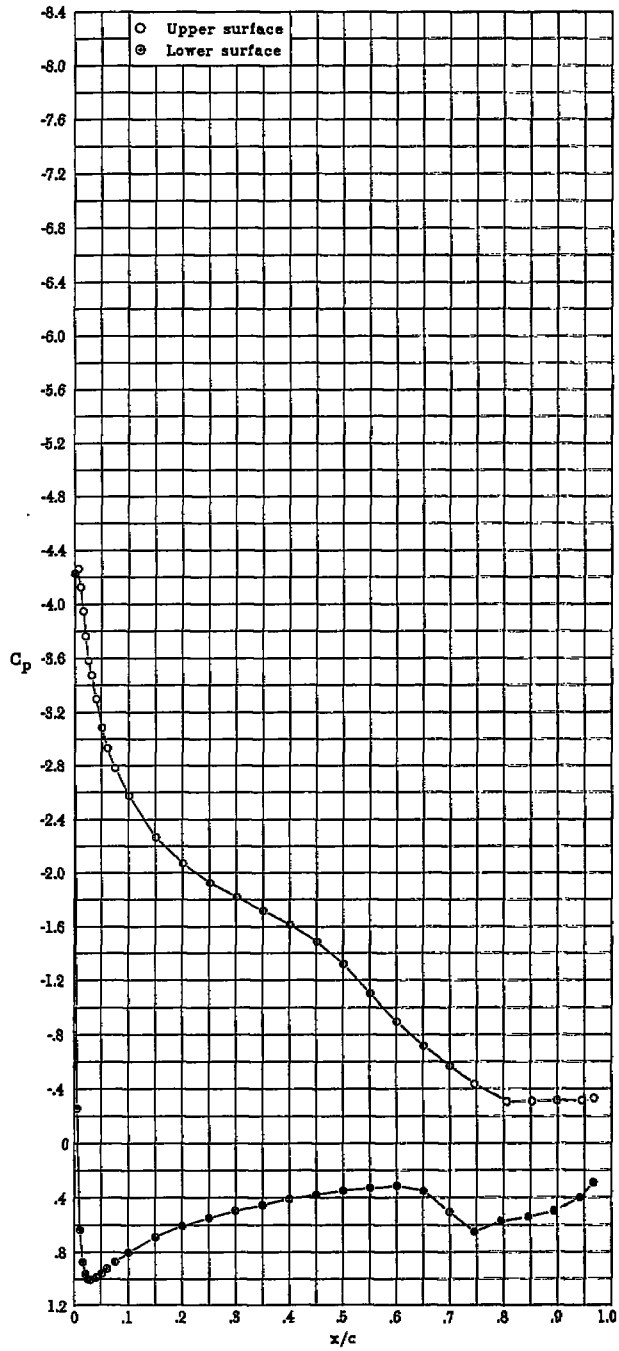

(v) $\alpha = 10.17^\circ$; $c_l = 1.796$; $c_d = 0.0429$; $c_m = -0.173$.

Figure 8.- Continued.

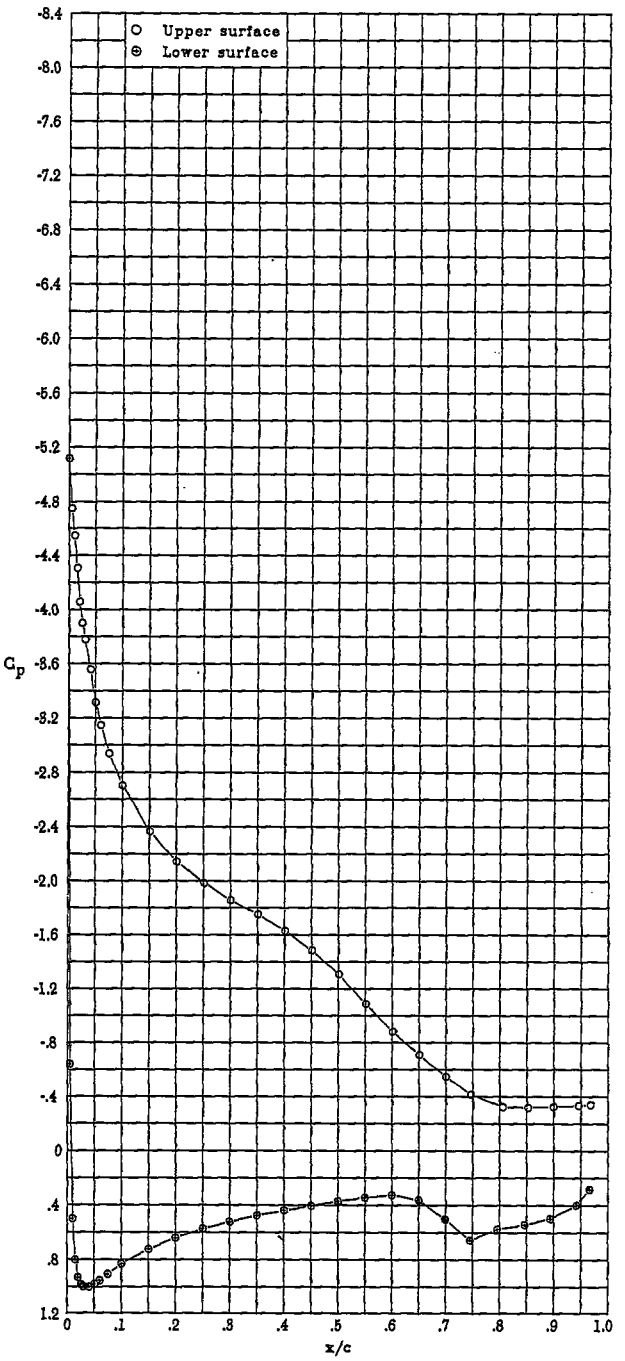

(w) α = 11.19°; c_l = 1.852; c_d = 0.0425; c_m = -0.170.

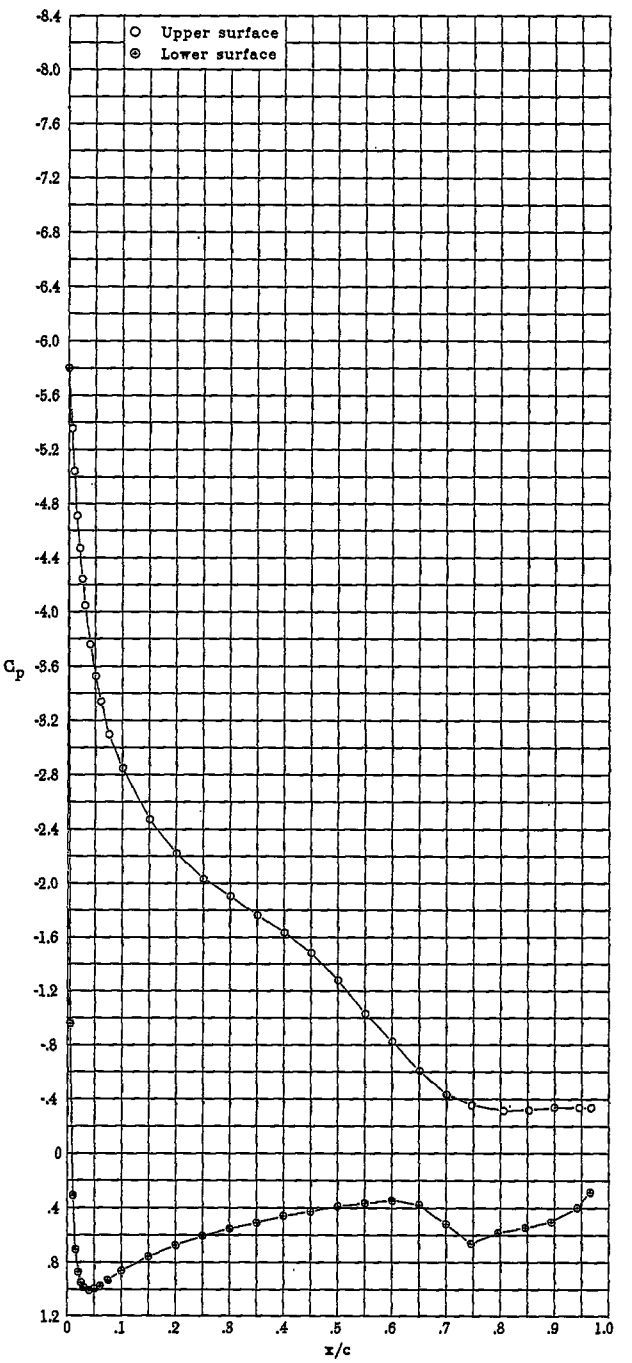

(x) α = 12.20°; c_l = 1.892; c_d = 0.0481; c_m = -0.160.

Figure 8.- Continued.

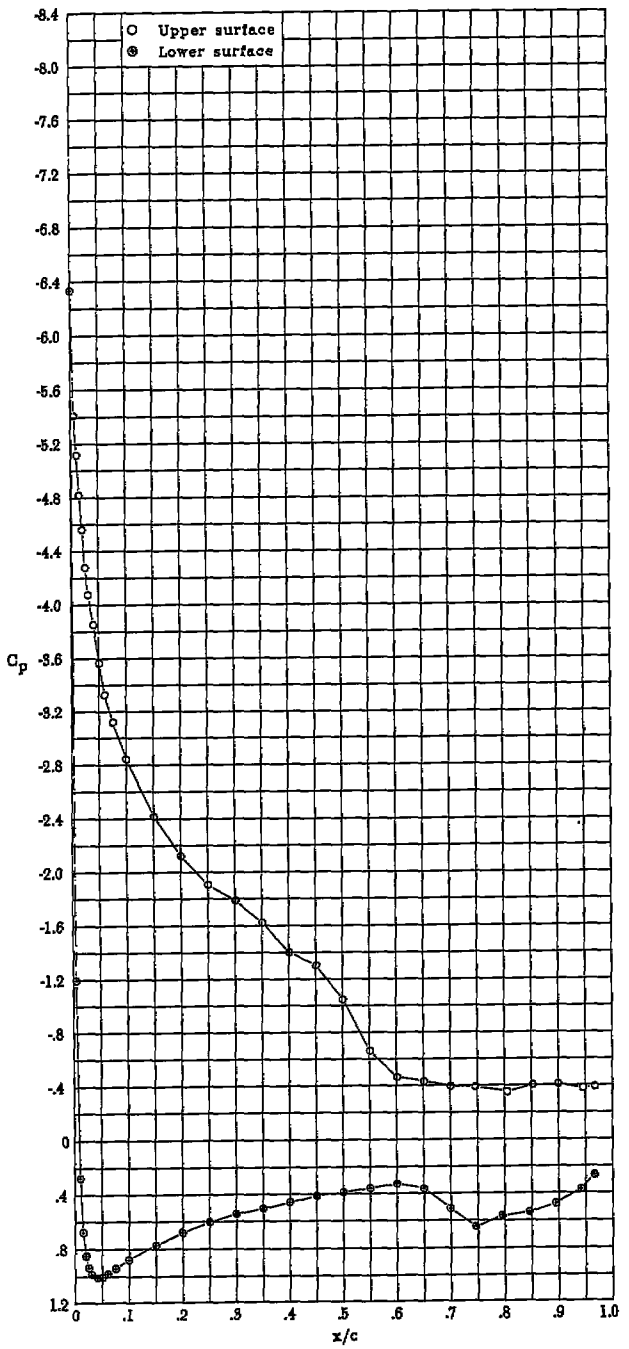

(y) $\alpha = 13.20^{\circ}$; $c_l = 1.786$; $c_d = 0.1039$; $c_m = -0.140$.

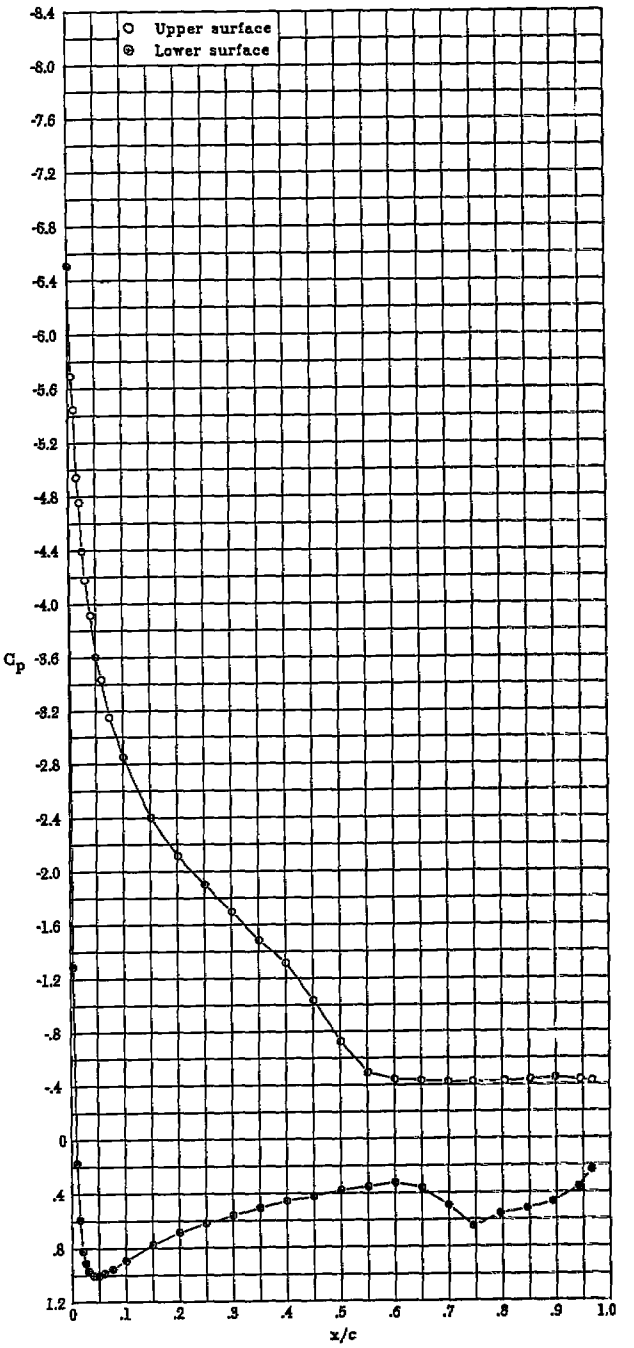

(z) $\alpha = 14.21^{\circ}$; $c_l = 1.745$; $c_d = 0.1312$; $c_m = -0.133$.

Figure 8.- Continued.

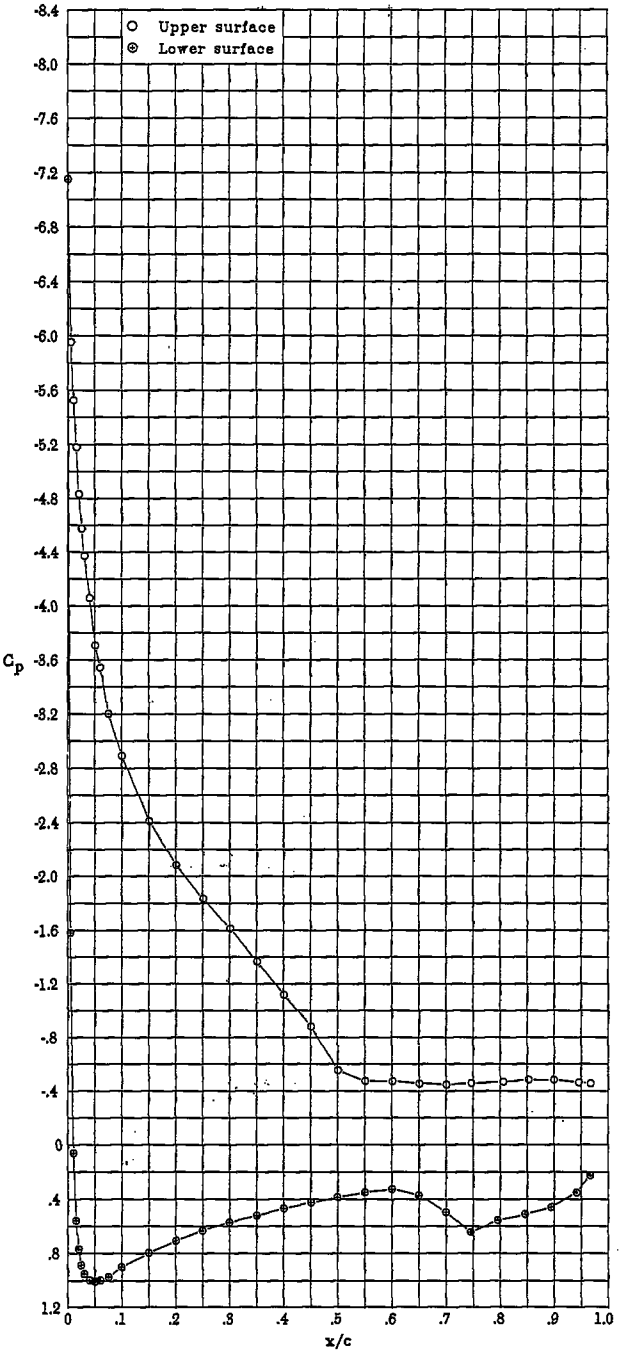

(aa) α = 15.21°; c_l = 1.726; c_d = 0.1529; c_m = −0.130.

Figure 8.- Concluded.

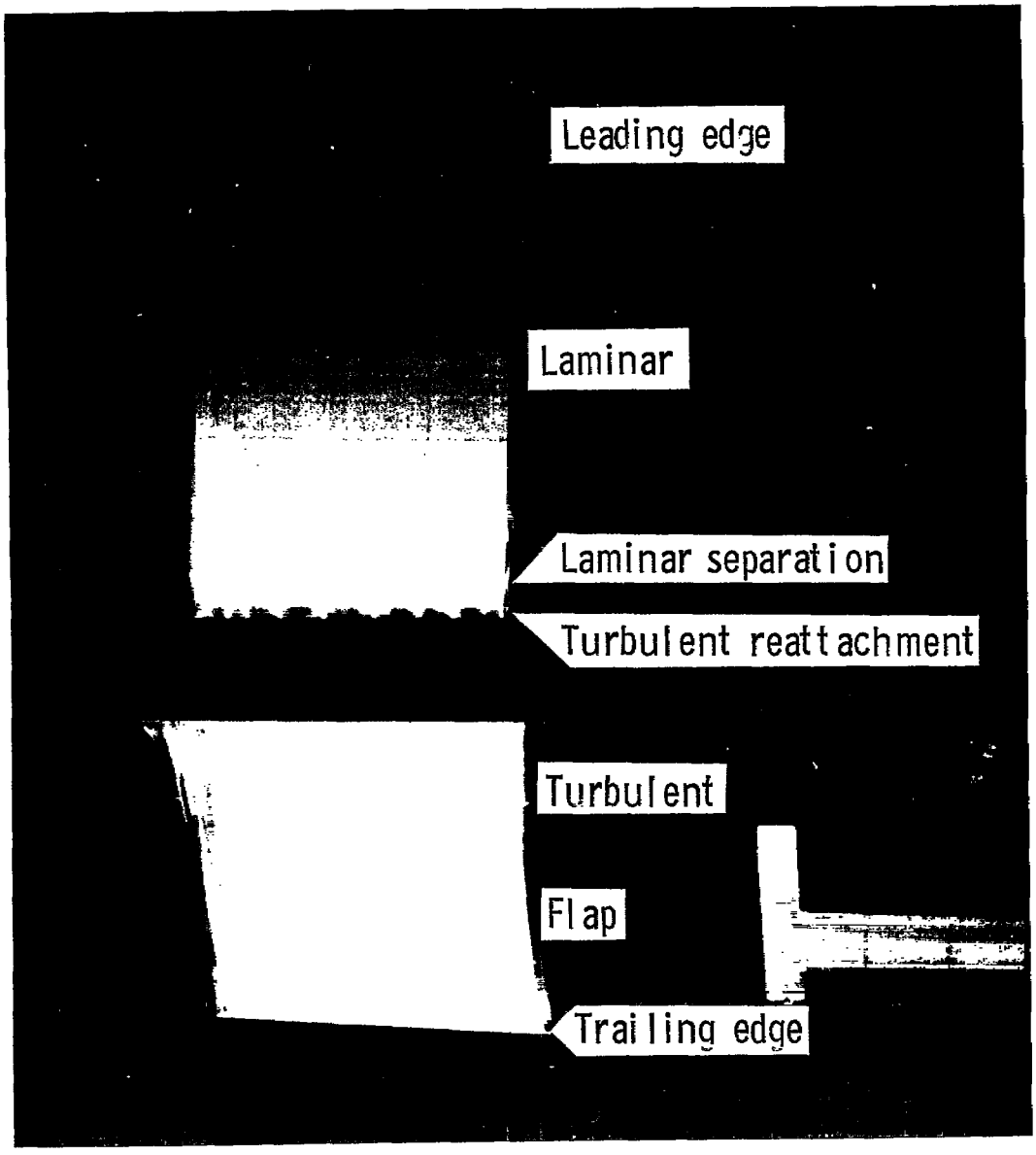

L-81-118

(a) $\alpha = 0.0^{\circ}$; $c_l = 0.7$.

Figure 9.- Oil-flow photographs of upper surface with $\delta_f = 0^{\circ}$ for $R = 3.0 \times 10^6$ and $M = 0.21$.

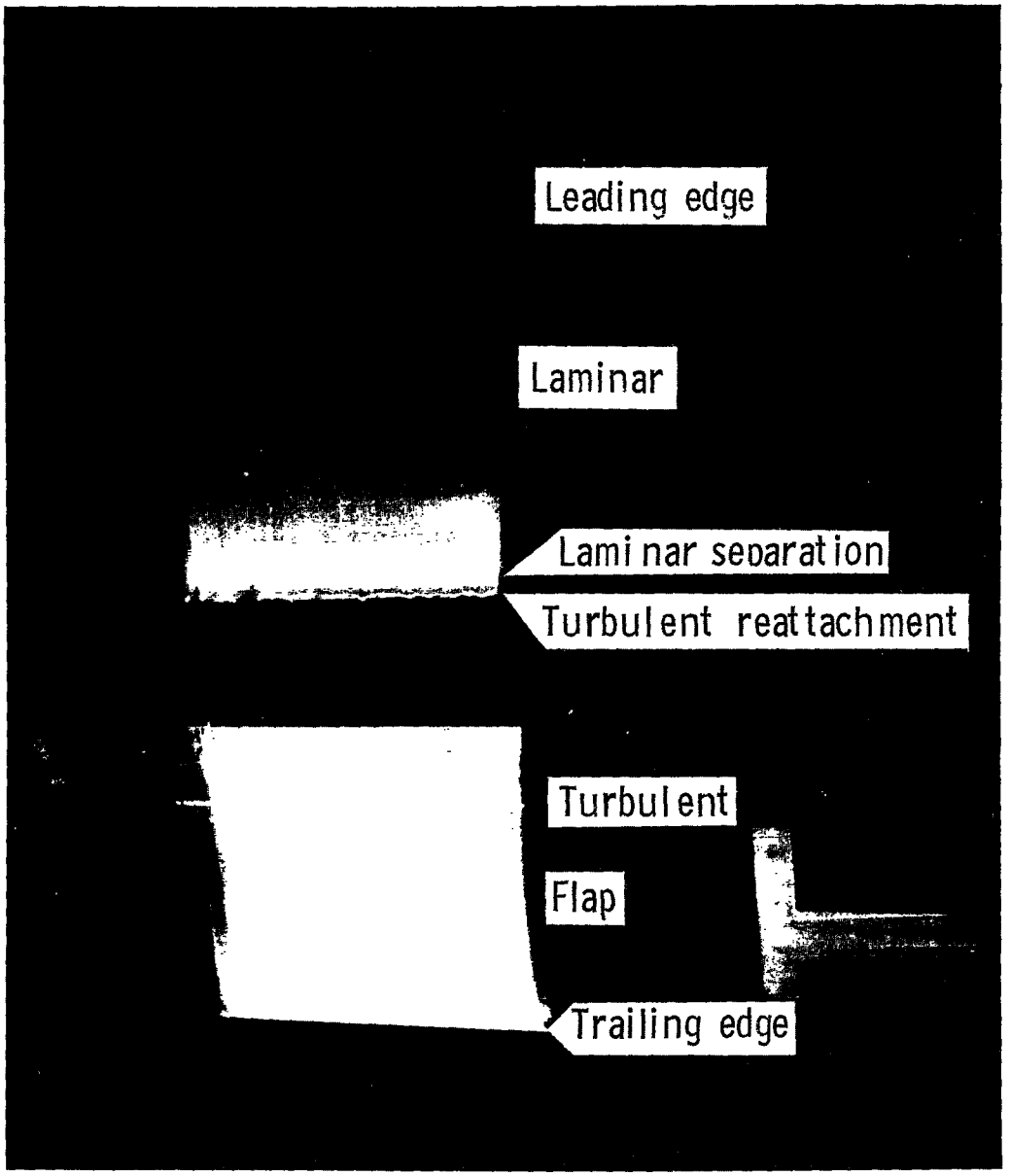

L-81-119

(b) $\alpha = 2.0^{\circ}$; $c_l = 0.9$.

Figure 9.- Continued.

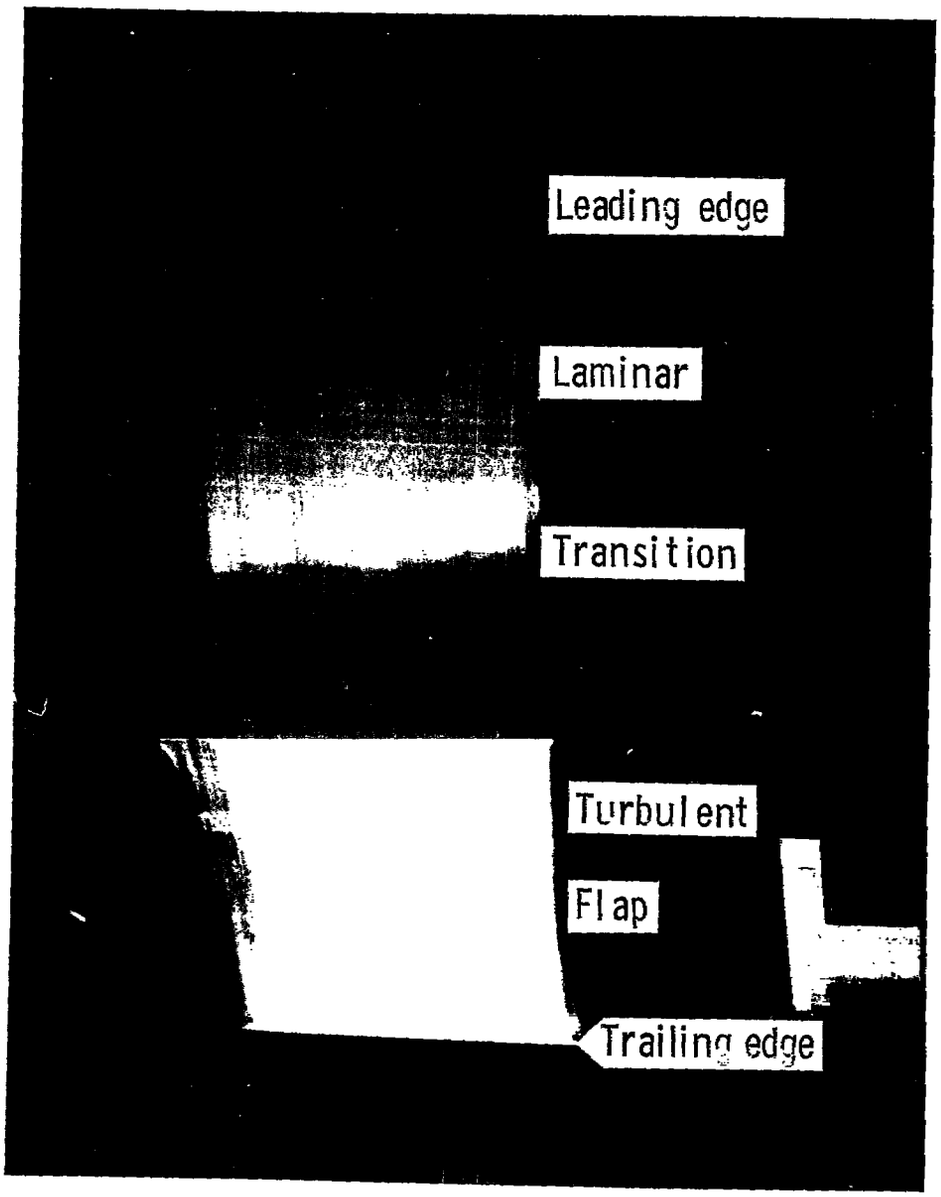

L-81-120

(c) $\alpha = 4.0^{\circ}$; $c_l = 1.1$.

Figure 9.- Concluded.

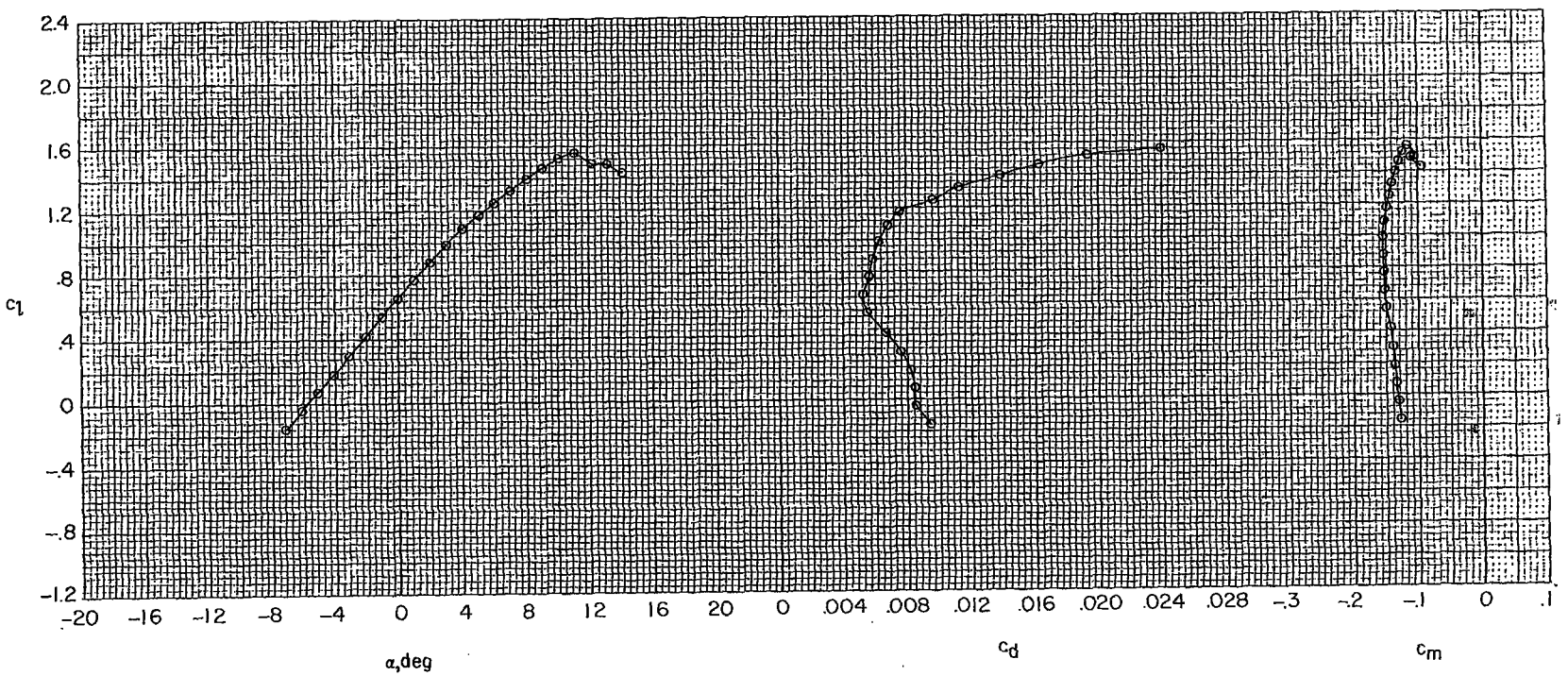

(a) $R = 3.0 \times 10^6$.

Figure 10.- Section characteristics with $\delta_f = 0^o$ at $M = 0.10$.

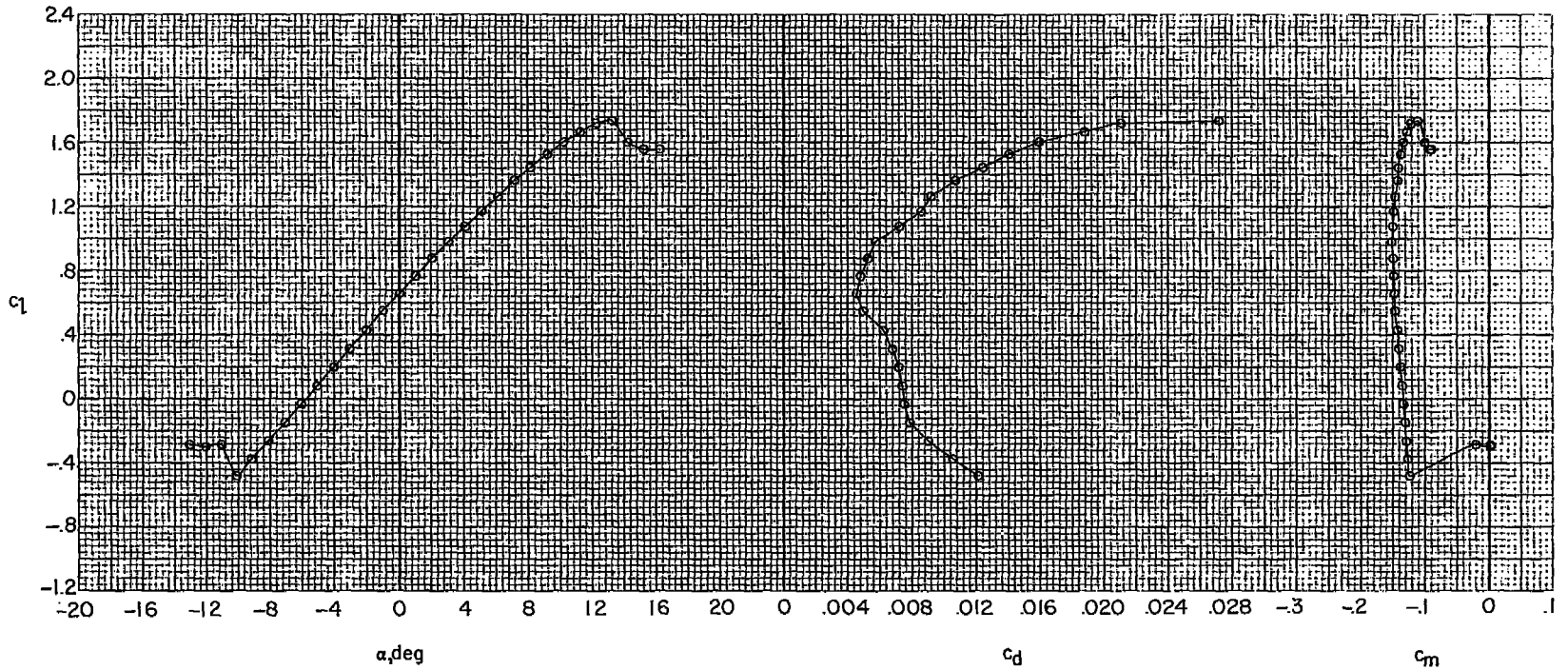

(b) $R = 6.0 \times 10^6$.

Figure 10.- Continued.

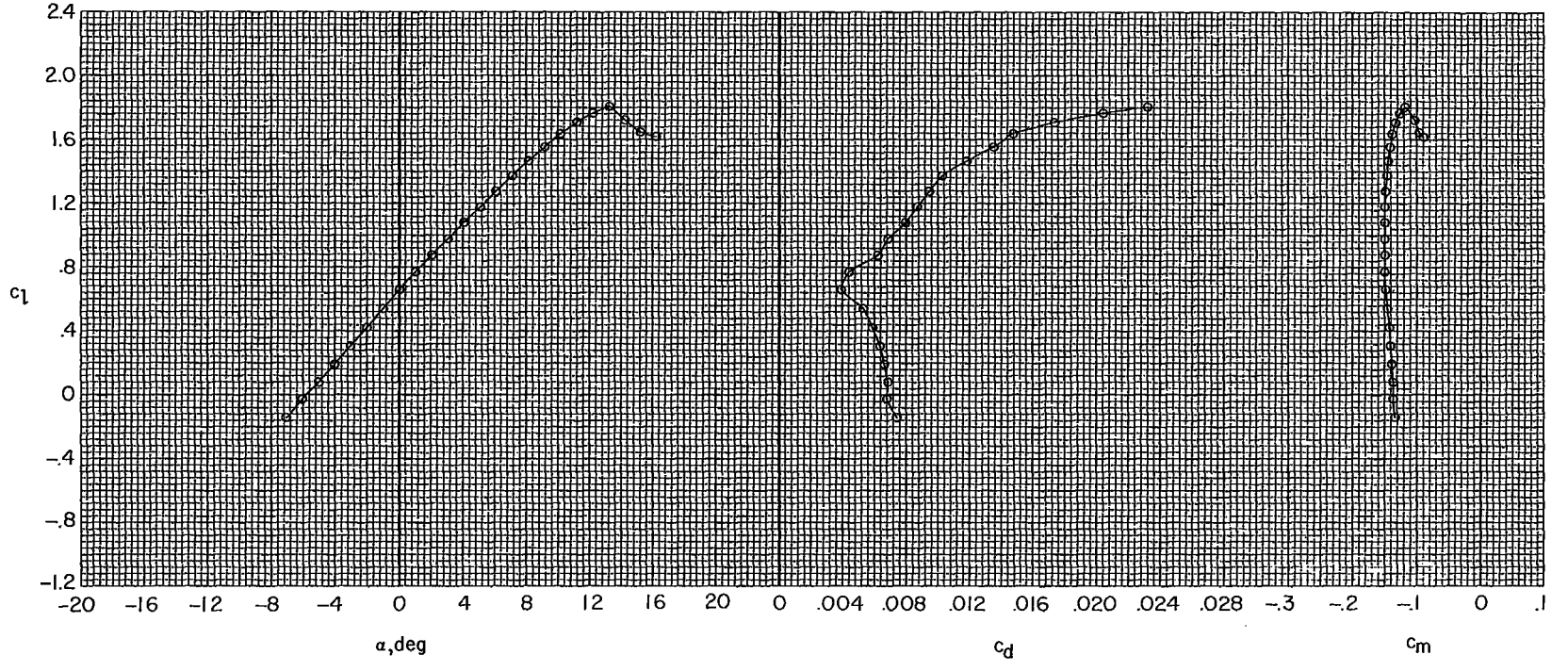

(c) R = 9.0 × 10^6.

Figure 10.- Concluded.

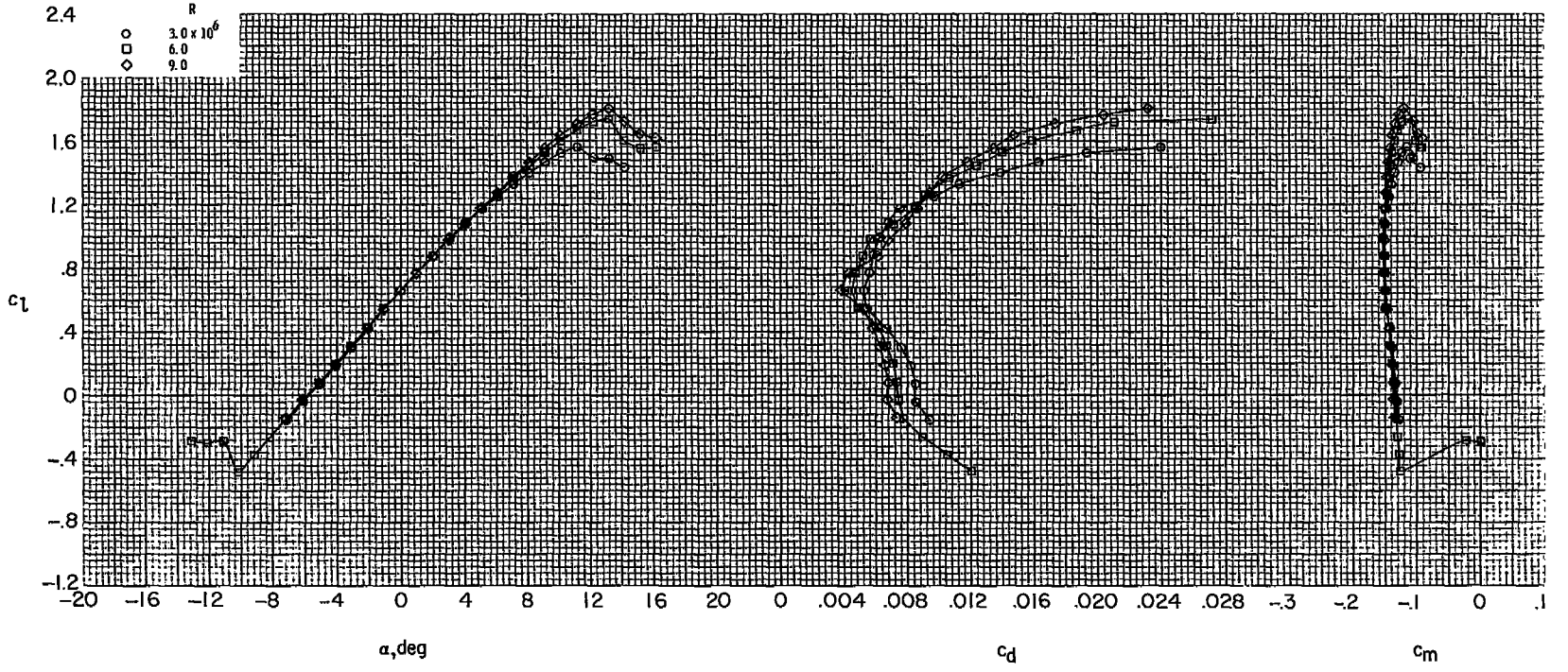

Figure 11.- Effects of Reynolds number on section characteristics with $\delta_f = 0^o$ at M = 0.10.

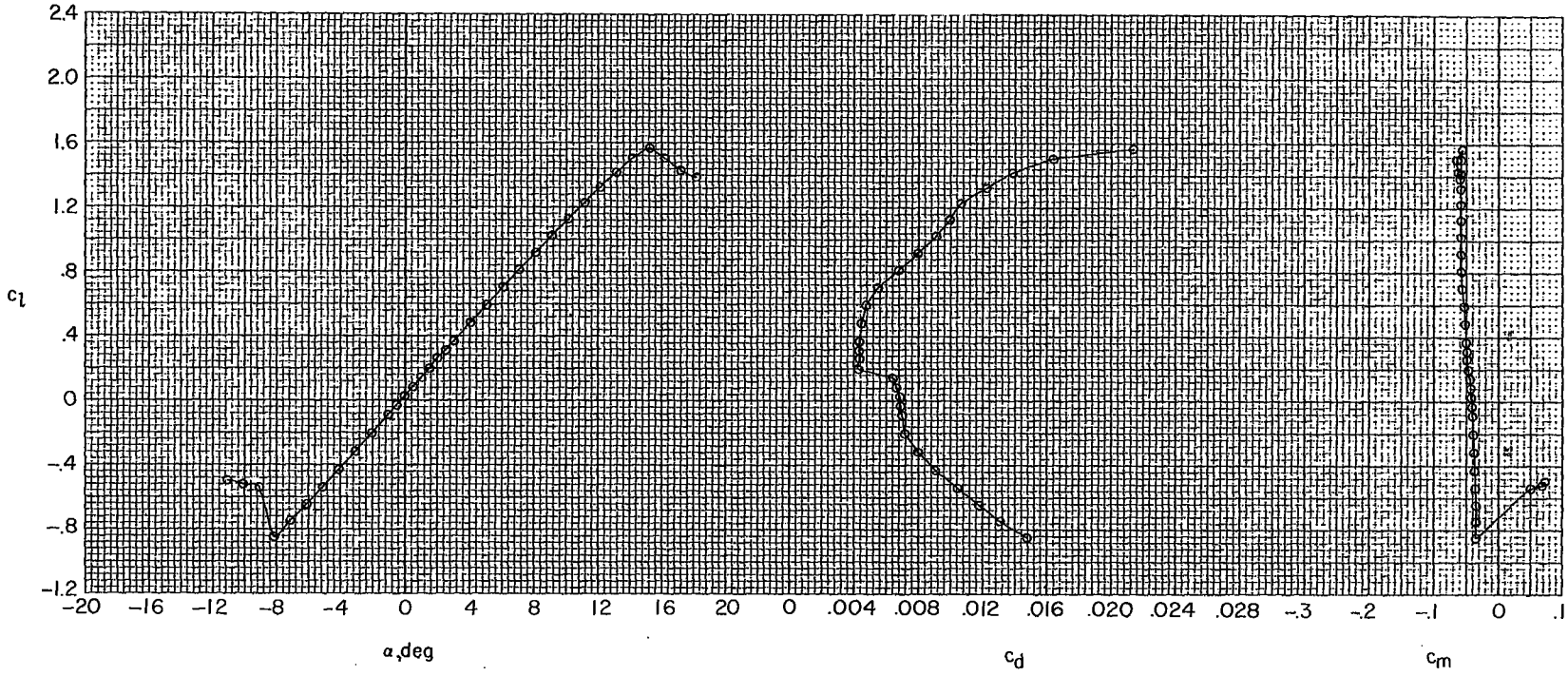

(a) $R = 6.0 \times 10^6$.

Figure 12.- Section characteristics with $\delta_f = -10^o$ at $M = 0.10$.

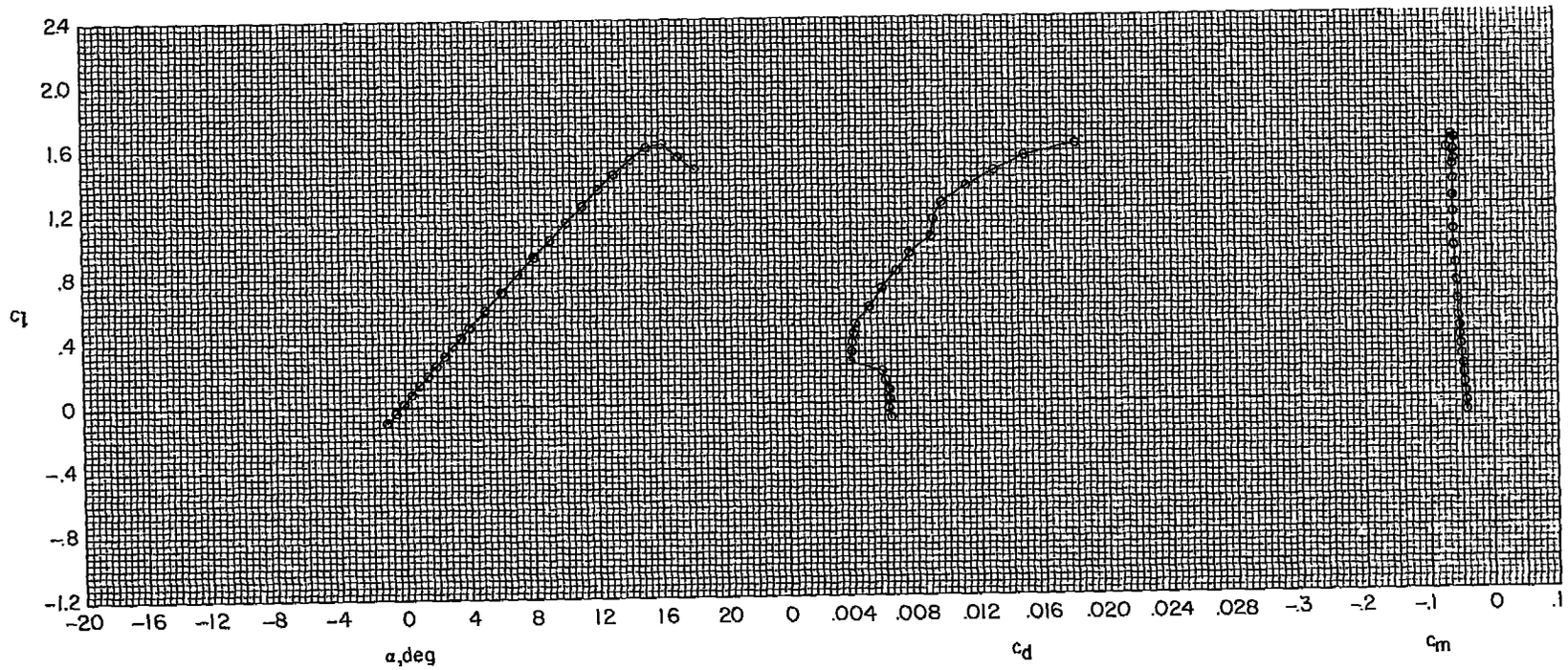

(b) $R = 9.0 \times 10^6$.

Figure 12.- Concluded.

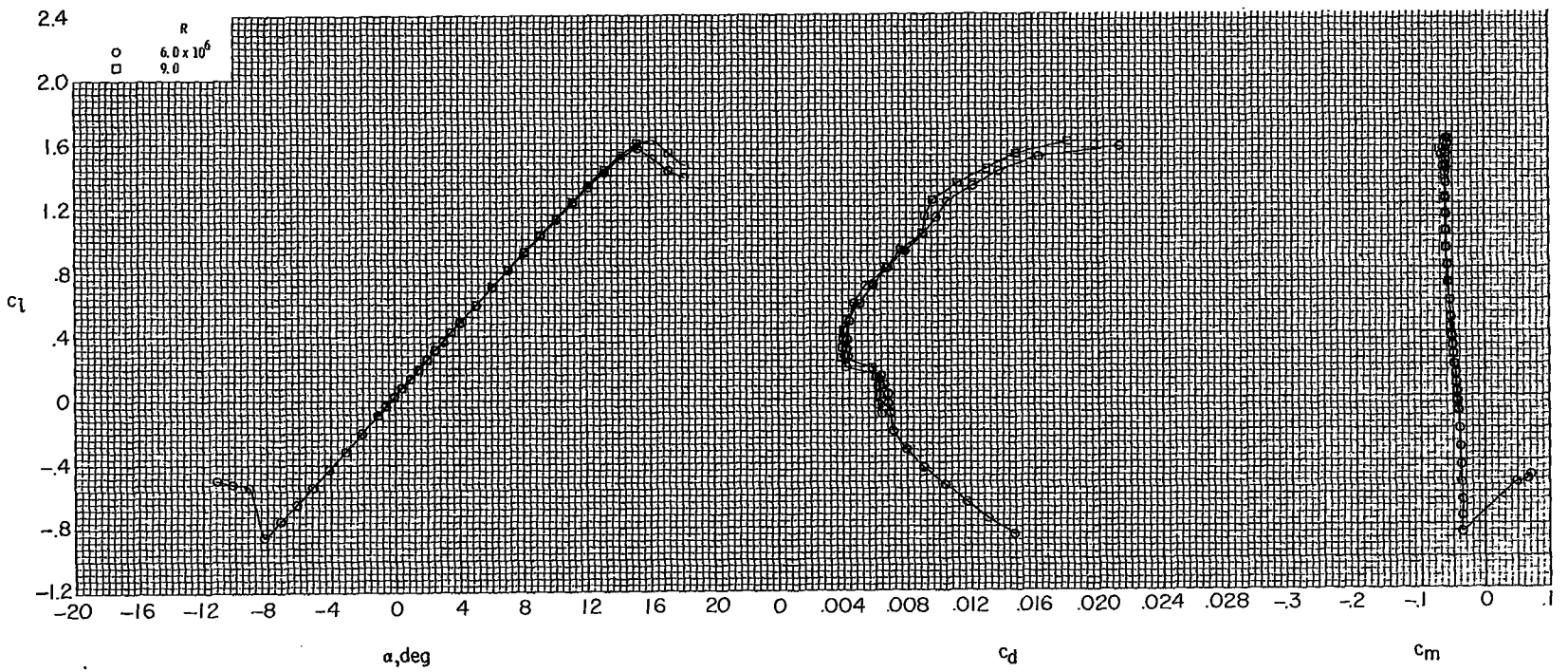

Figure 13.- Effects of Reynolds number on section characteristics with $\delta_f = -10^o$ at M = 0.10.

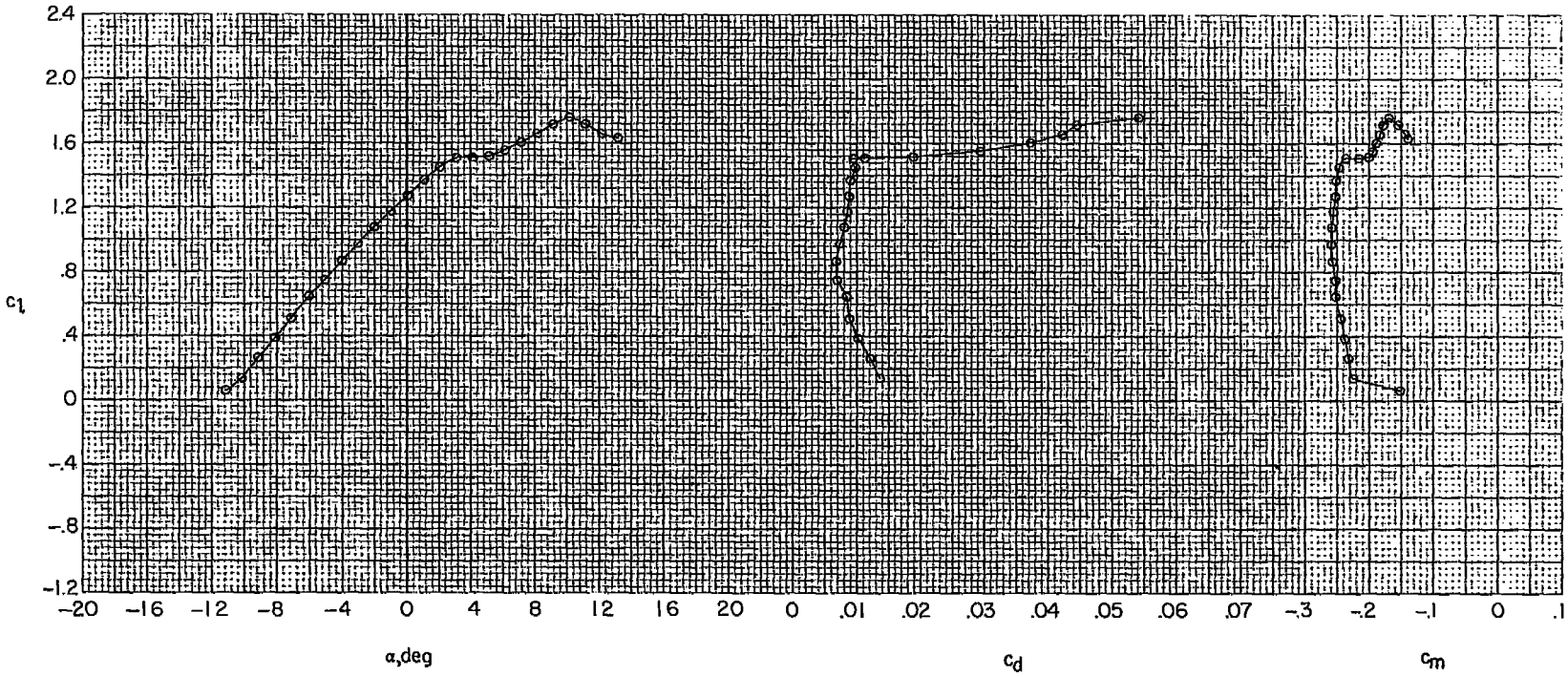

(a) $R = 2.0 \times 10^6$.

Figure 14.- Section characteristics with $\delta_f = 10^o$ at $M = 0.10$.

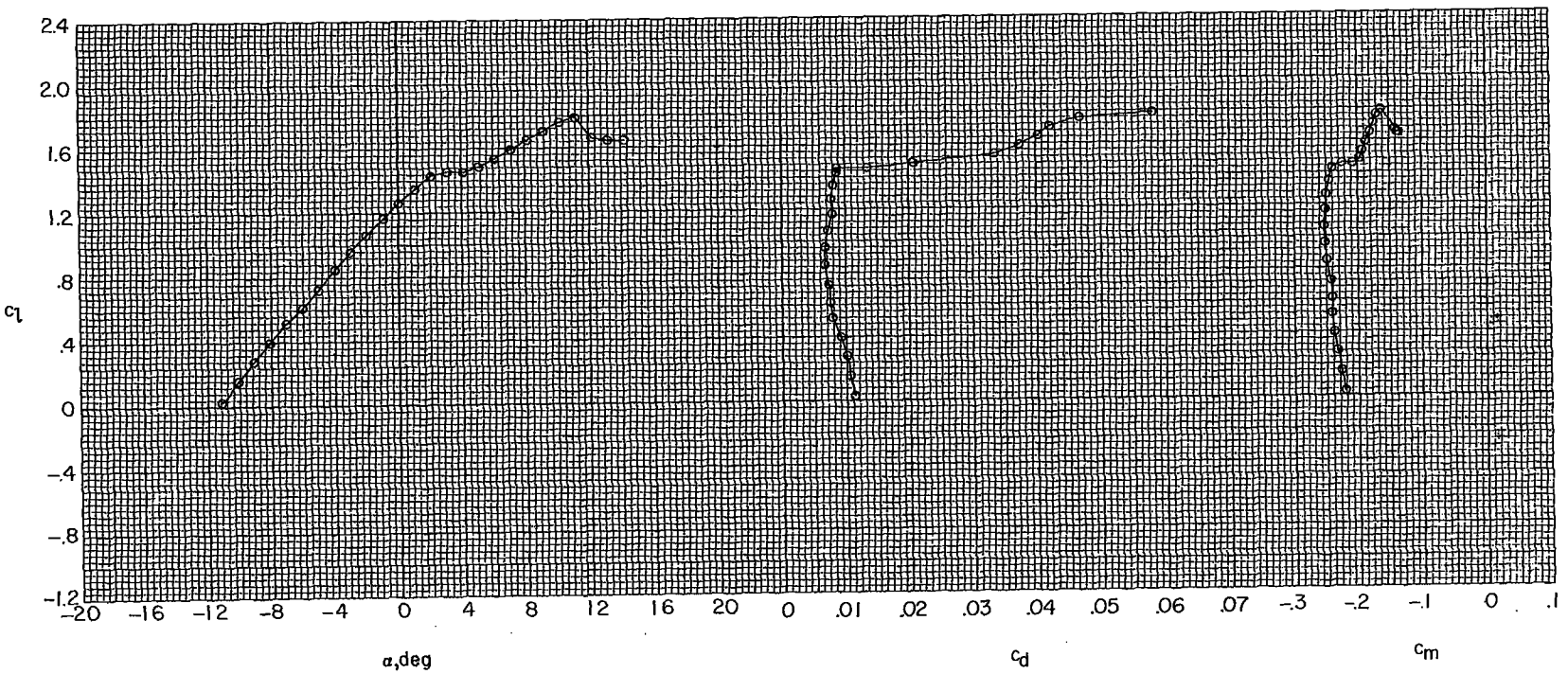

(b) $R = 3.0 \times 10^6$.

Figure 14.- Continued.

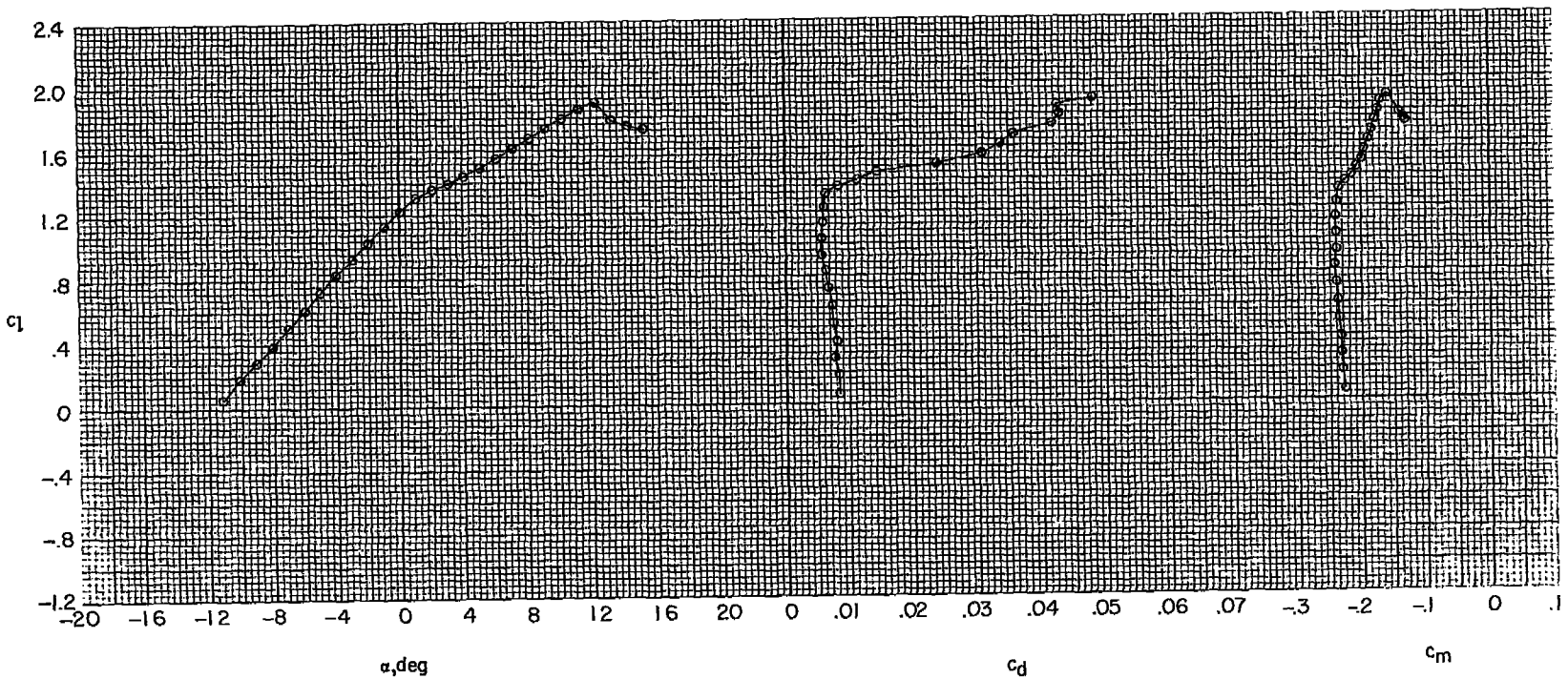

(c) $R = 6.0 \times 10^6$.

Figure 14.- Concluded.

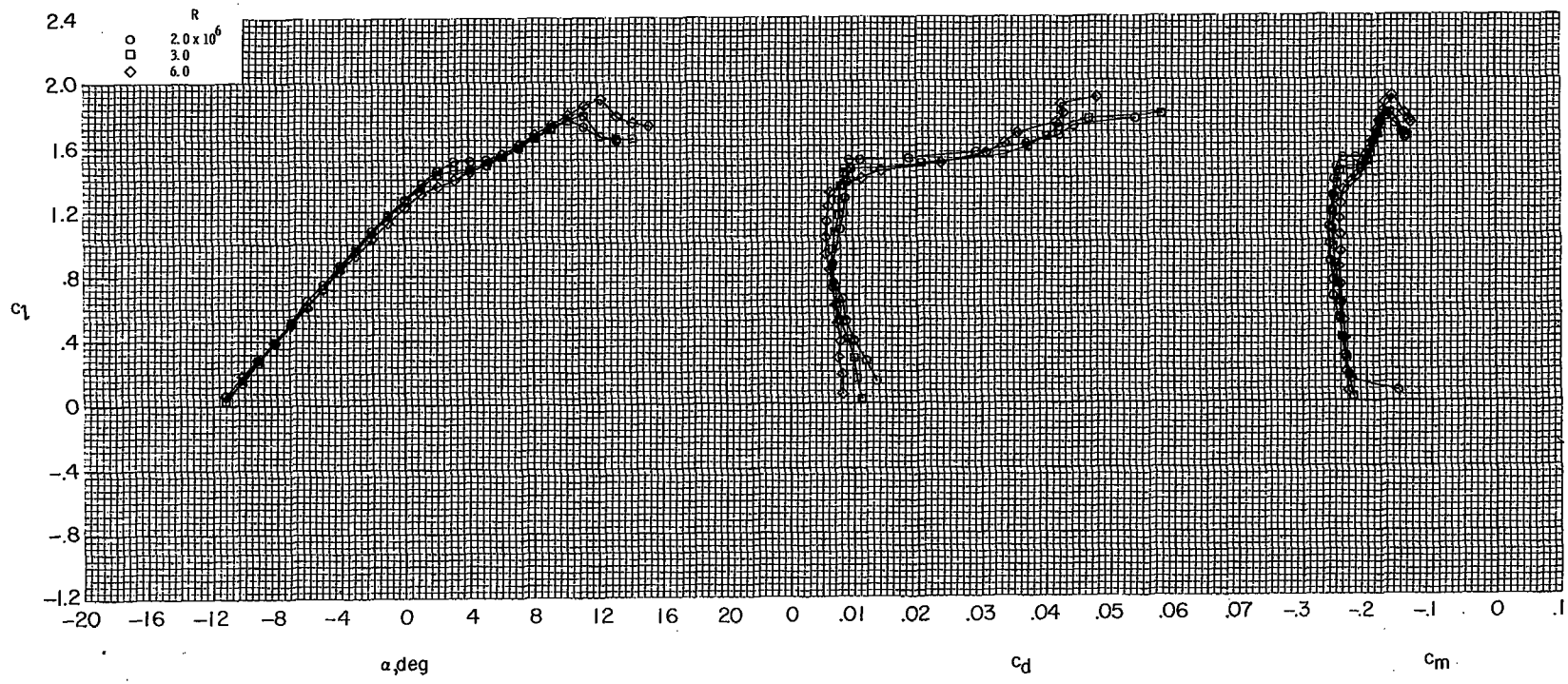

Figure 15.- Effects of Reynolds number on section characteristics with $\delta_f = 10^o$ at M = 0.10.

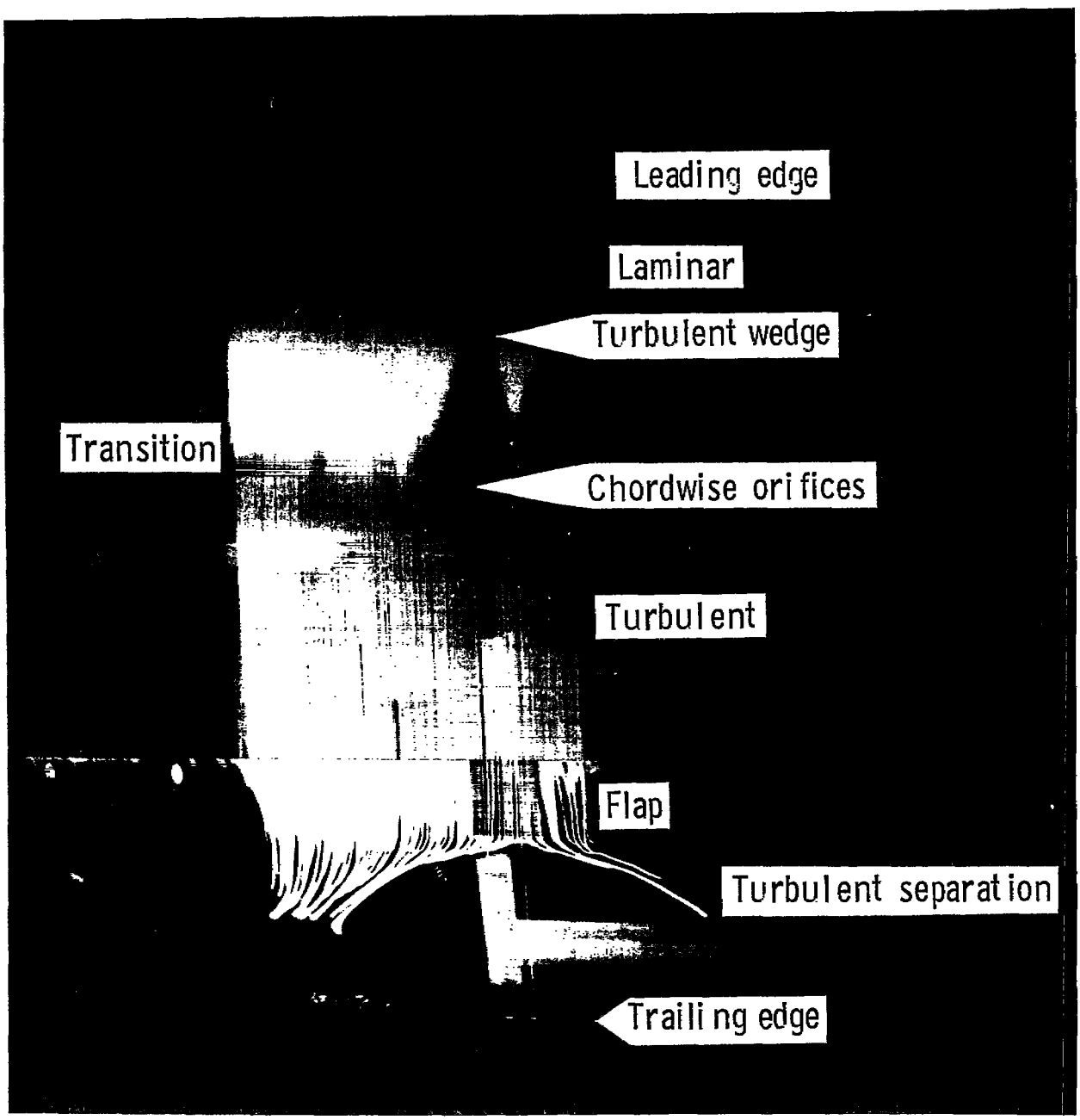

L-81-121

Figure 16.- Oil-flow photograph of upper surface with $\delta_f = 10^o$ for $R = 3.0 \times 10^6$, $M = 0.22$, $\alpha = 4.0^o$, and $c_l = 1.5$.

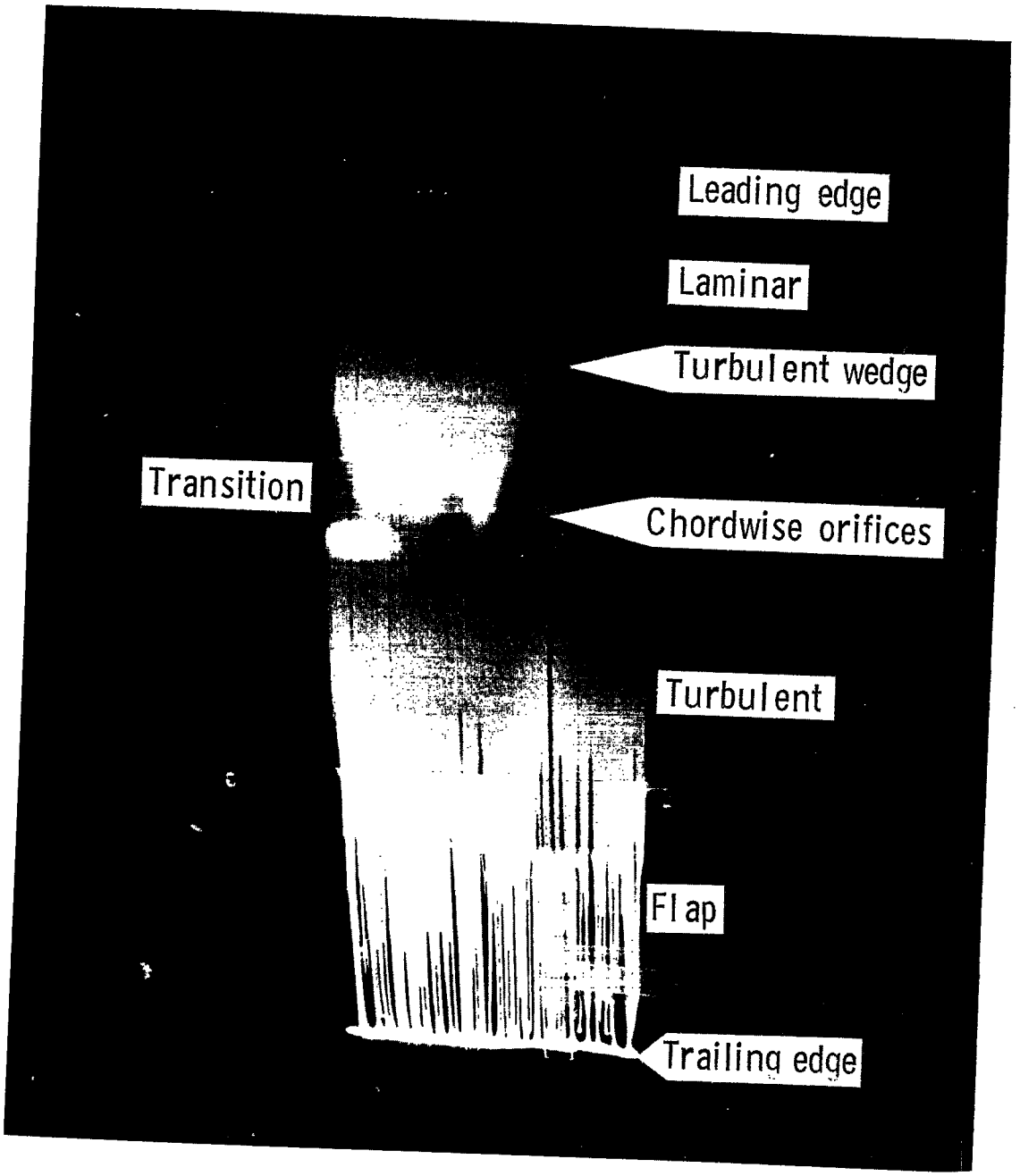

L-81-122

Figure 17.- Oil-flow photograph of upper surface with $\delta_f = 0^o$ for $R = 3.0 \times 10^6$, $M = 0.21$, $\alpha = 5.0^o$, and $c_l = 1.2$.

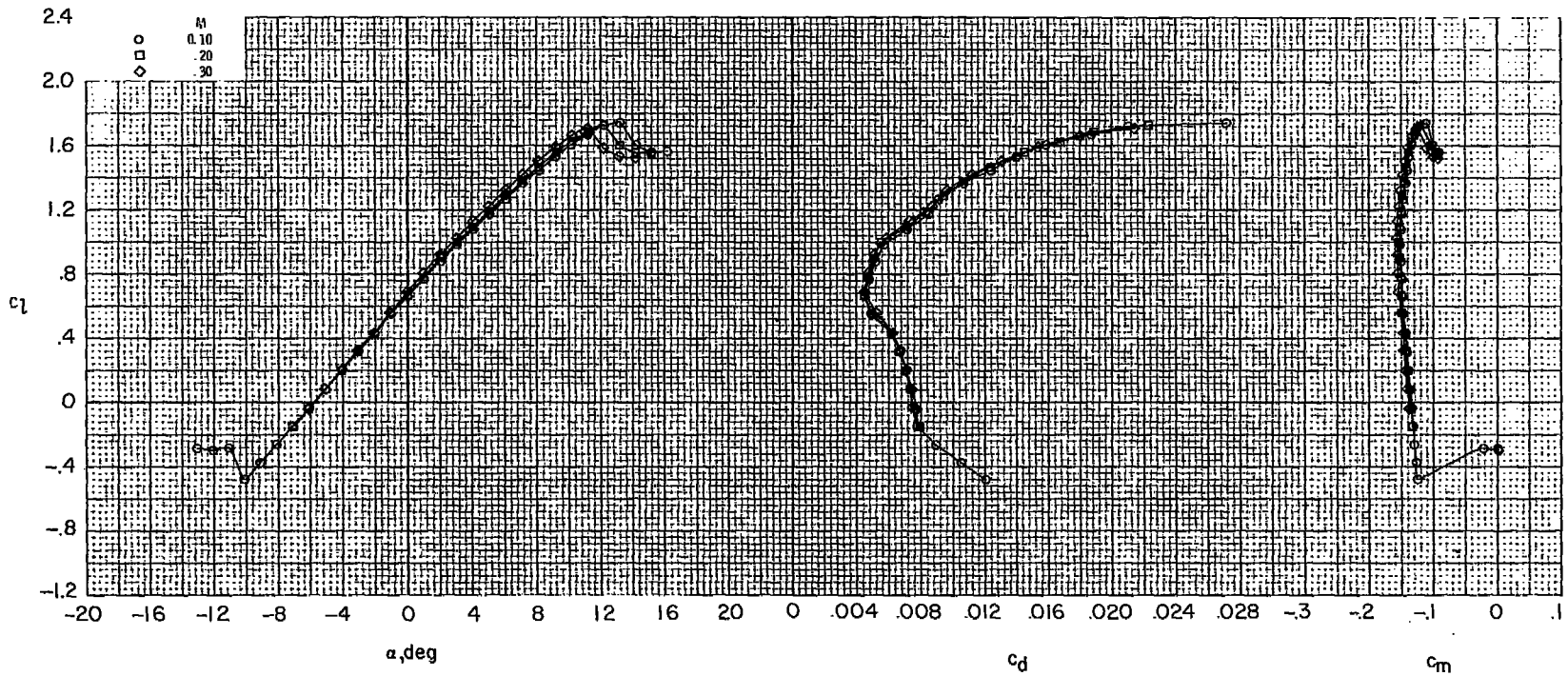

Figure 18.- Effects of Mach number on section characteristics with $\delta_f = 0^o$ for $R = 6.0 \times 10^6$.

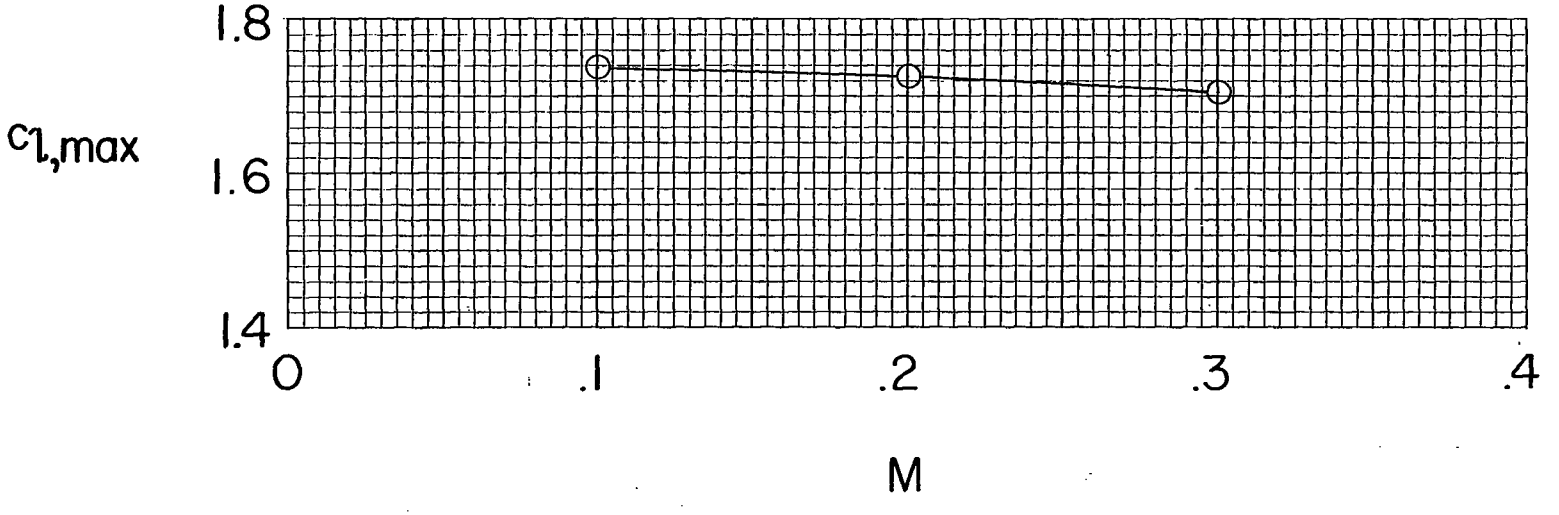

Figure 19.- Variation of maximum lift coefficient with Mach number with $\delta_f = 0^o$ for $R = 6.0 \times 10^6$.

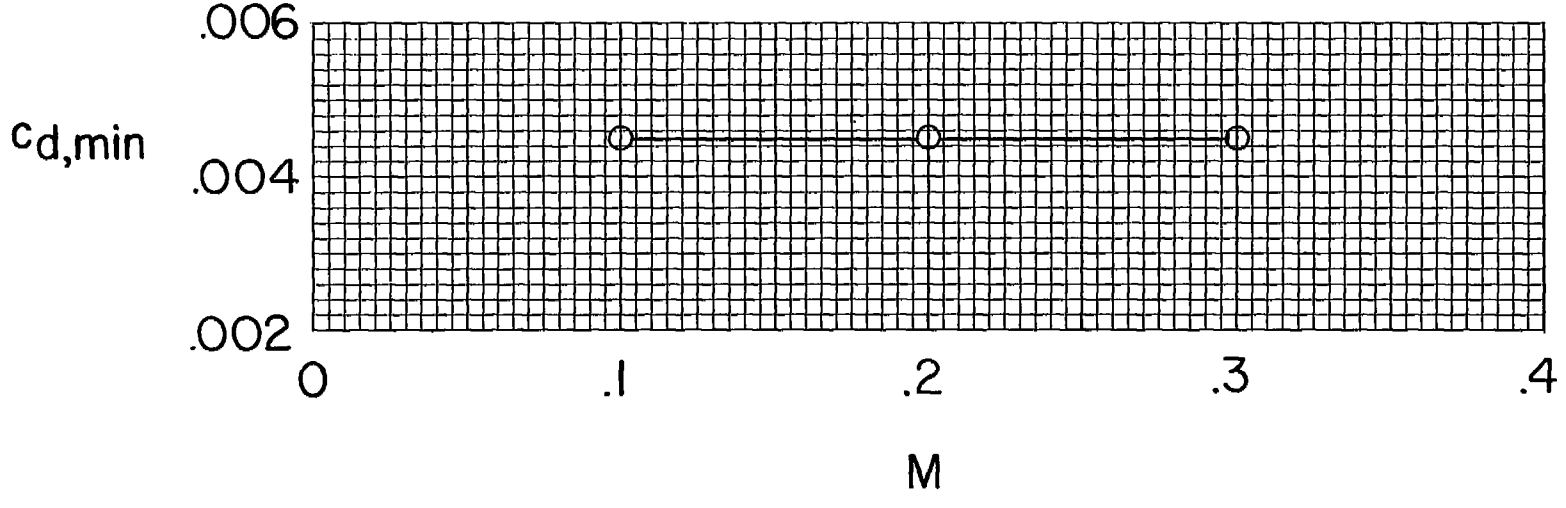

Figure 20.- Variation of minimum drag coefficient with Mach number with $\delta_f = 0^o$ for $R = 6.0 \times 10^6$.

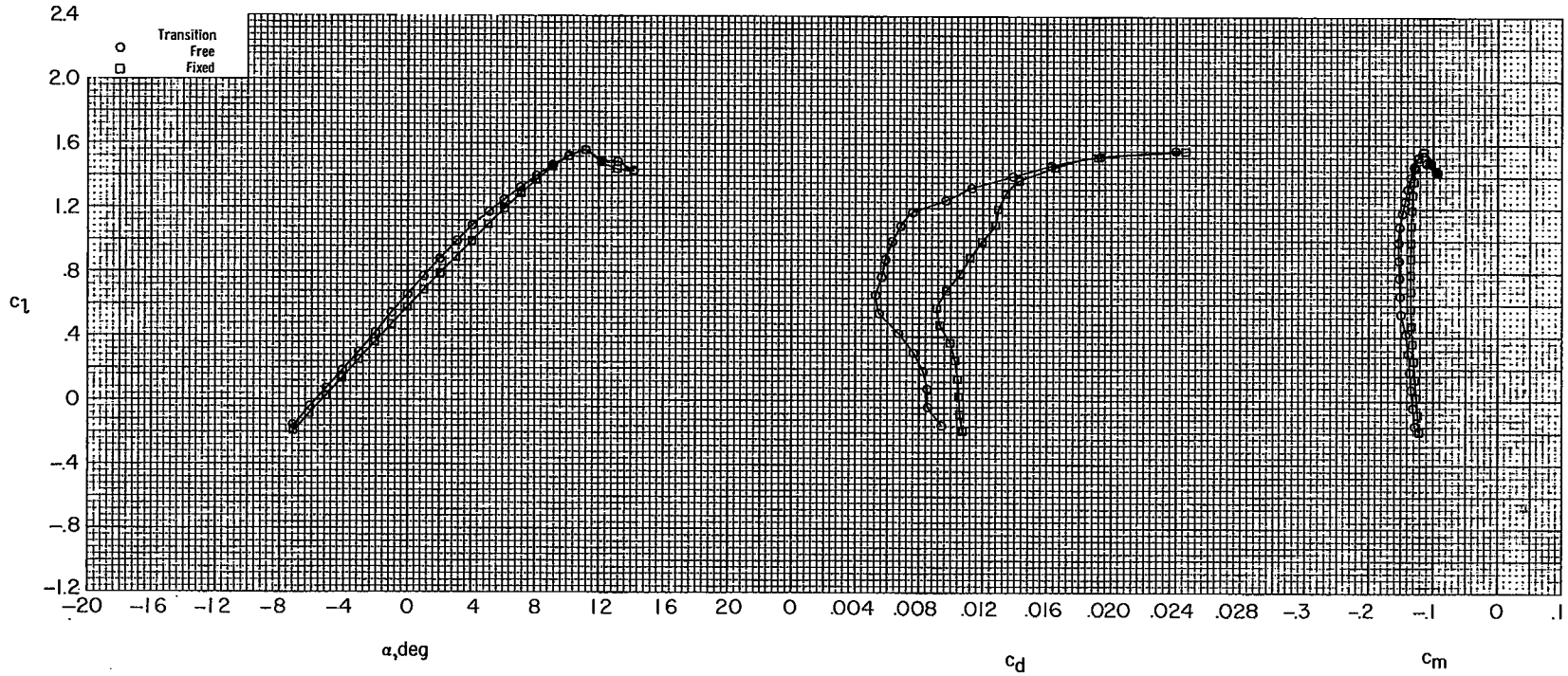

(a) $R = 3.0 \times 10^6$.

Figure 21.- Effect of roughness on section characteristics with $\delta_f = 0^o$ for various Reynolds numbers at $M = 0.10$.

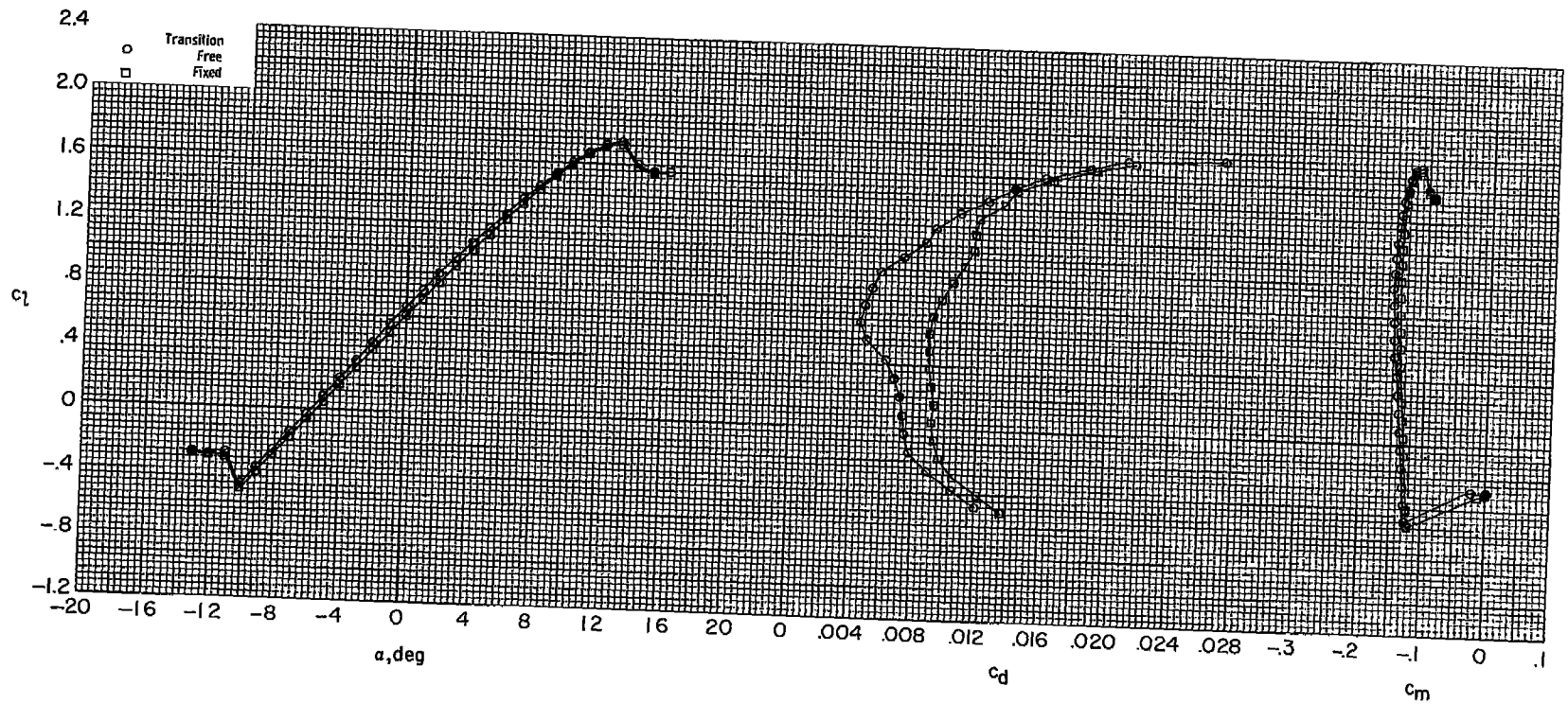

(b) $R = 6.0 \times 10^6$.

Figure 21.- Continued.

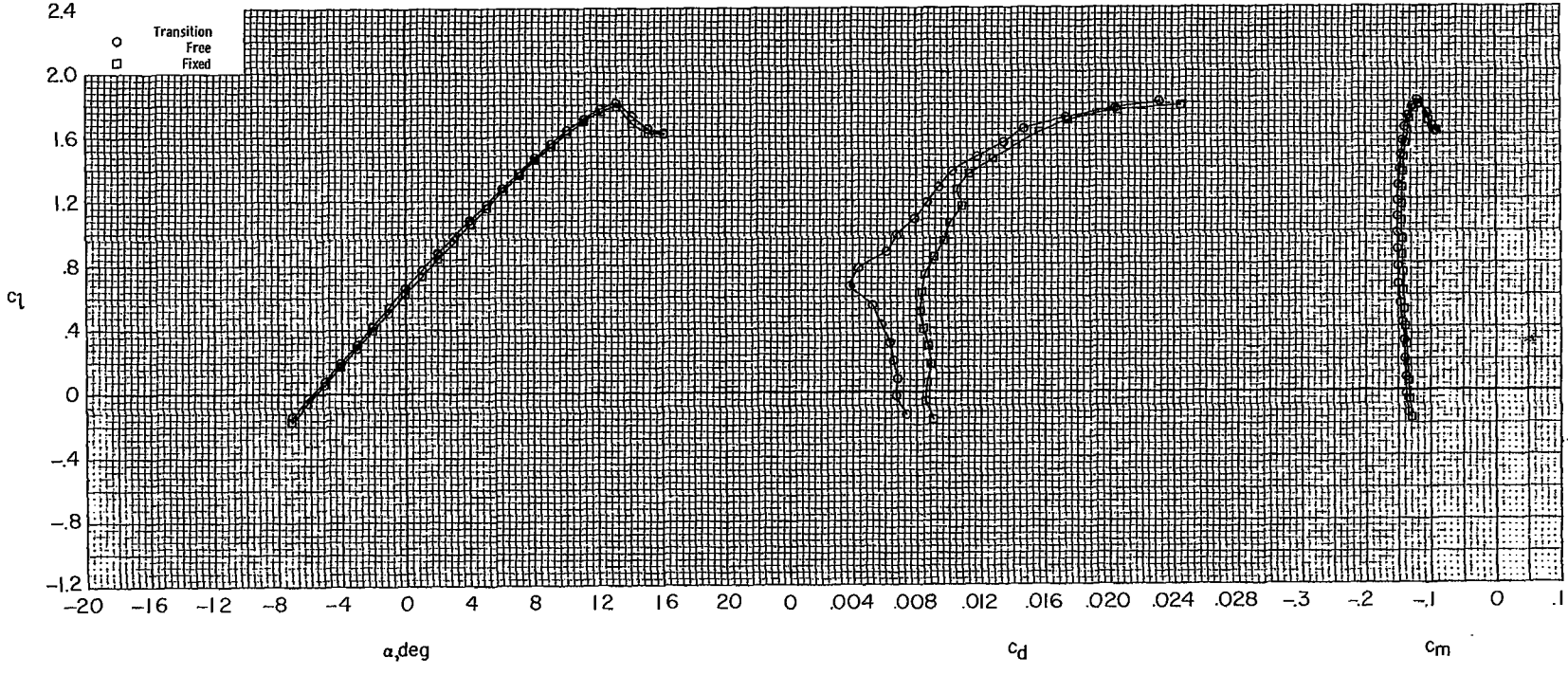

(c) $R = 9.0 \times 10^6$.

Figure 21.- Concluded.

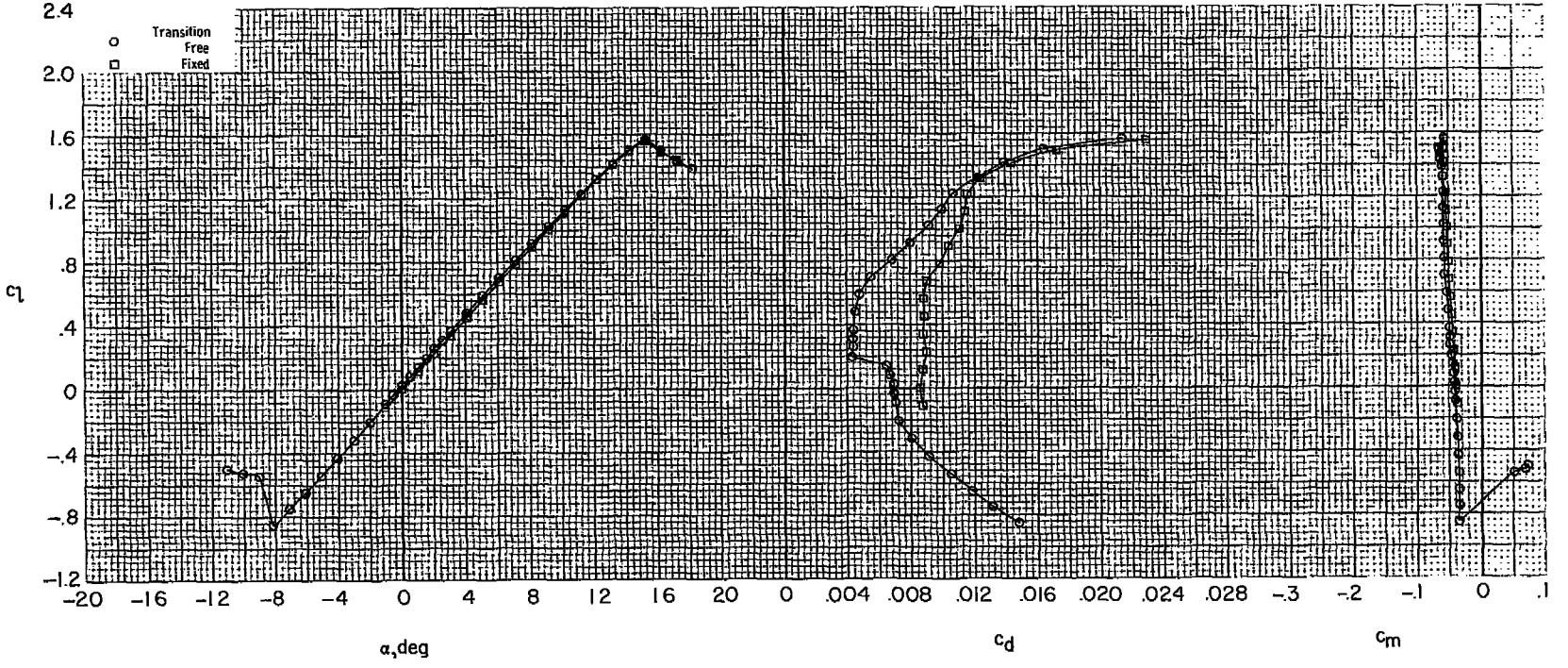

(a) $R = 6.0 \times 10^6$.

Figure 22.- Effect of roughness on section characteristics with $\delta_f = -10^o$ for various Reynolds numbers at $M = 0.10$.

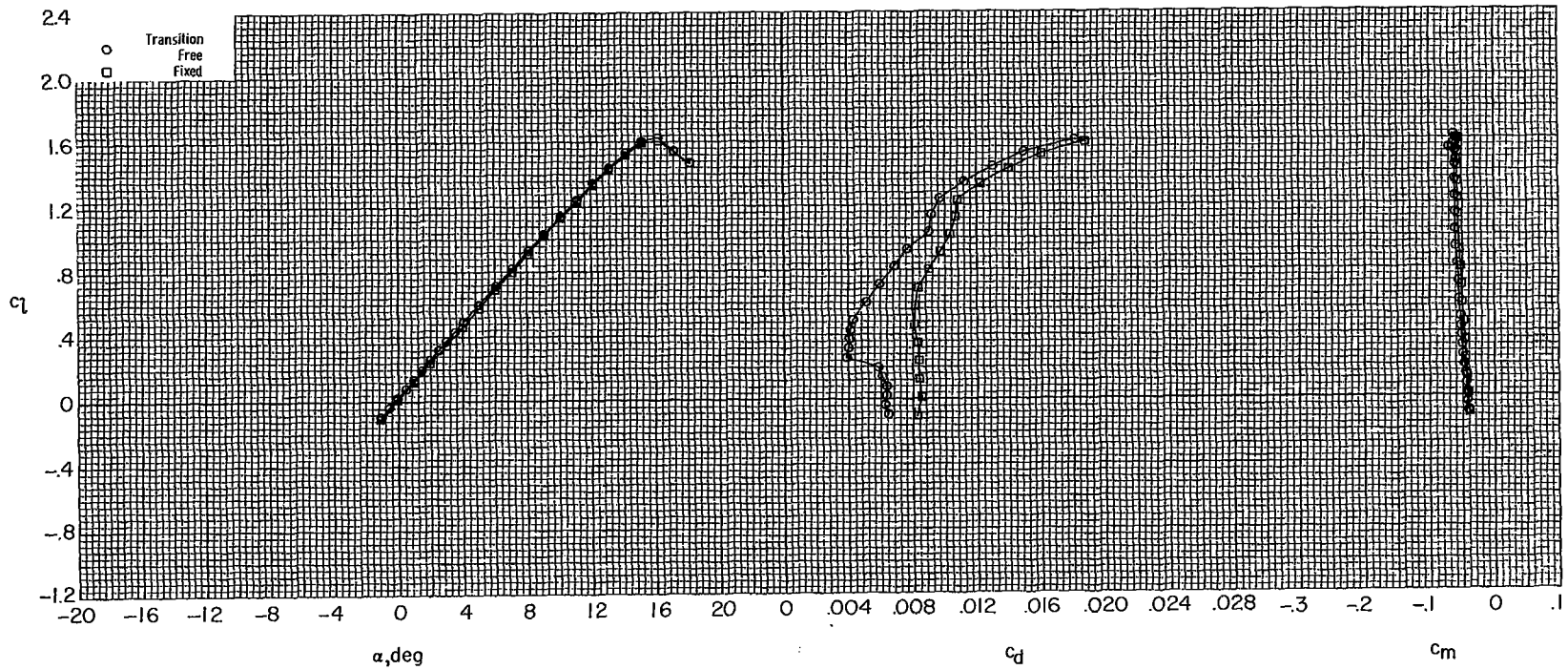

(b) $R = 9.0 \times 10^6$.

Figure 22.- Concluded.

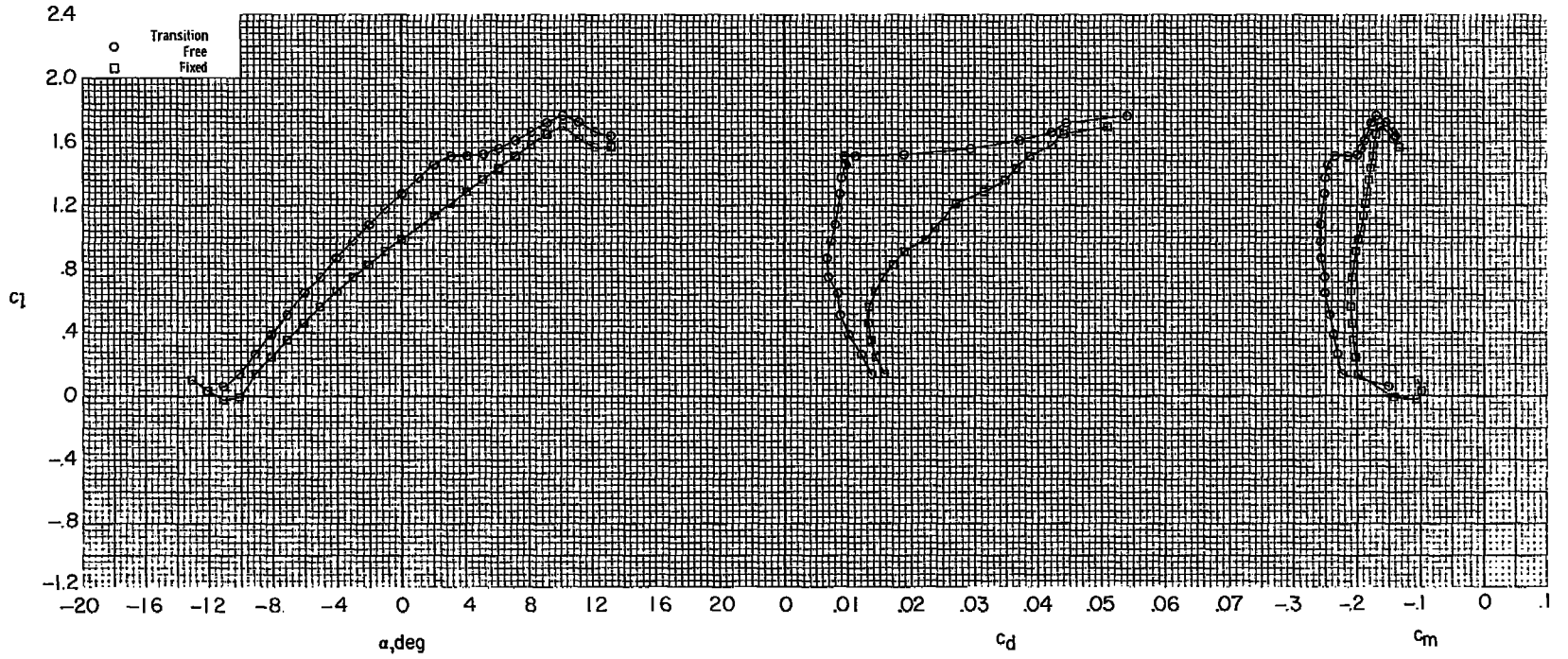

(a) $R = 2.0 \times 10^6$.

Figure 23.- Effect of roughness on section characteristics with $\delta_f = 10^o$ for various Reynolds numbers at $M = 0.10$.

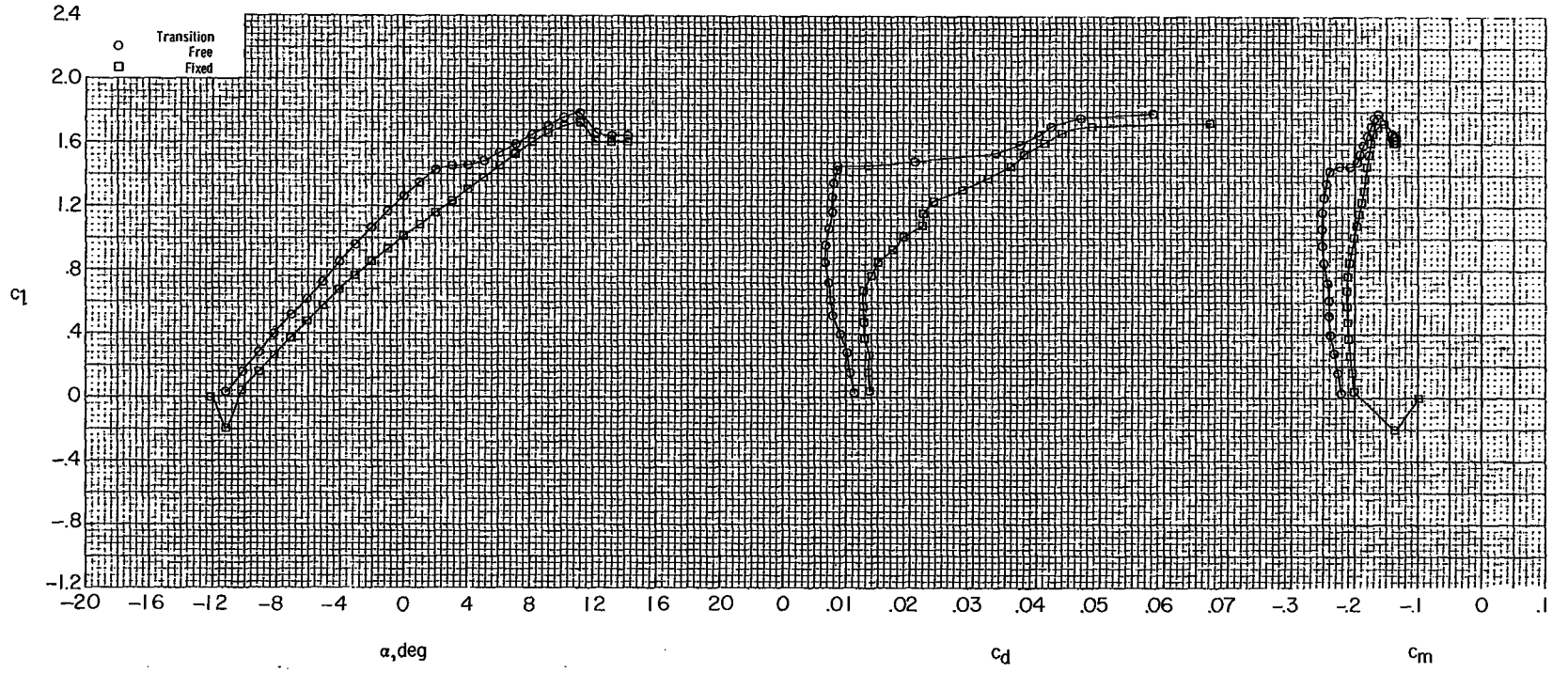

(b) $R = 3.0 \times 10^6$.

Figure 23.- Continued.

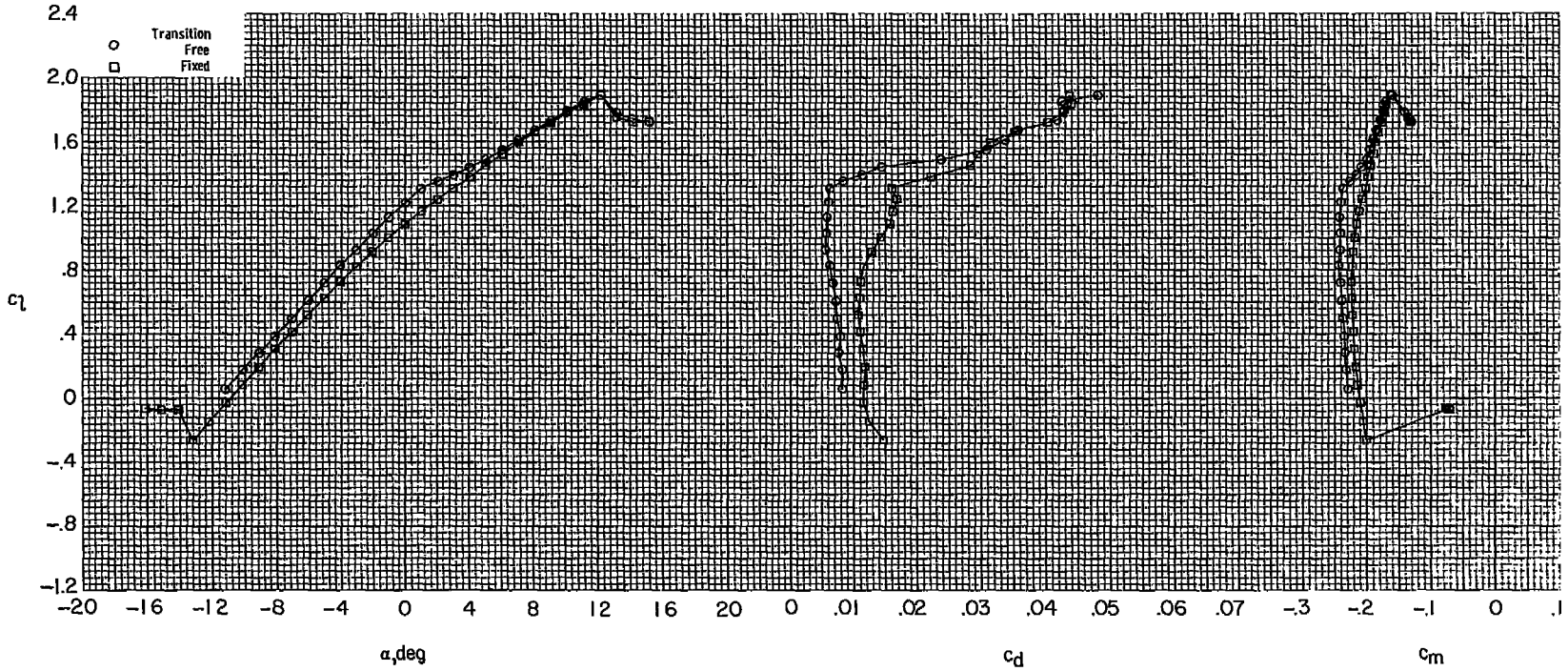

(c) $R = 6.0 \times 10^6$.

Figure 23.- Concluded.

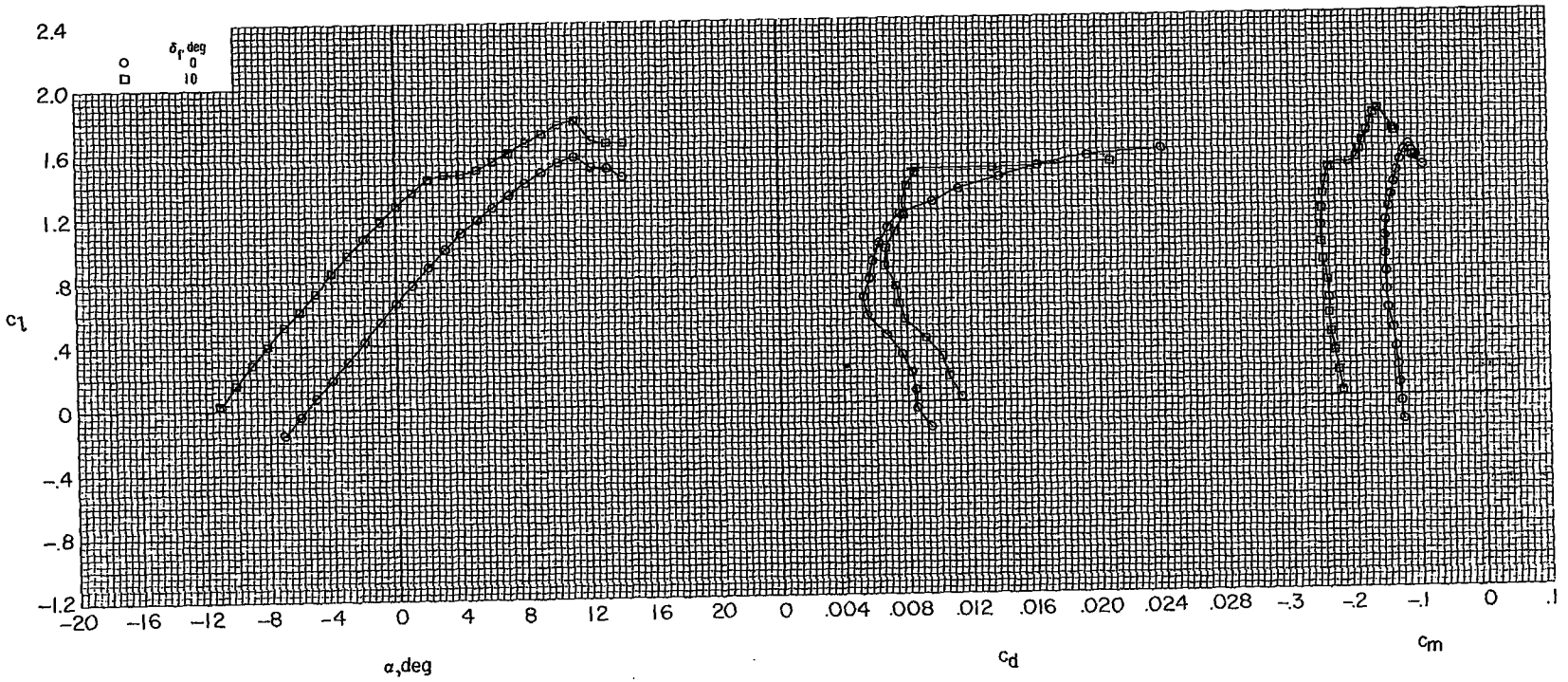

(a) $R = 3.0 \times 10^6$.

Figure 24.- Effect of flap deflection on section characteristics for various Reynolds numbers at $M = 0.10$.

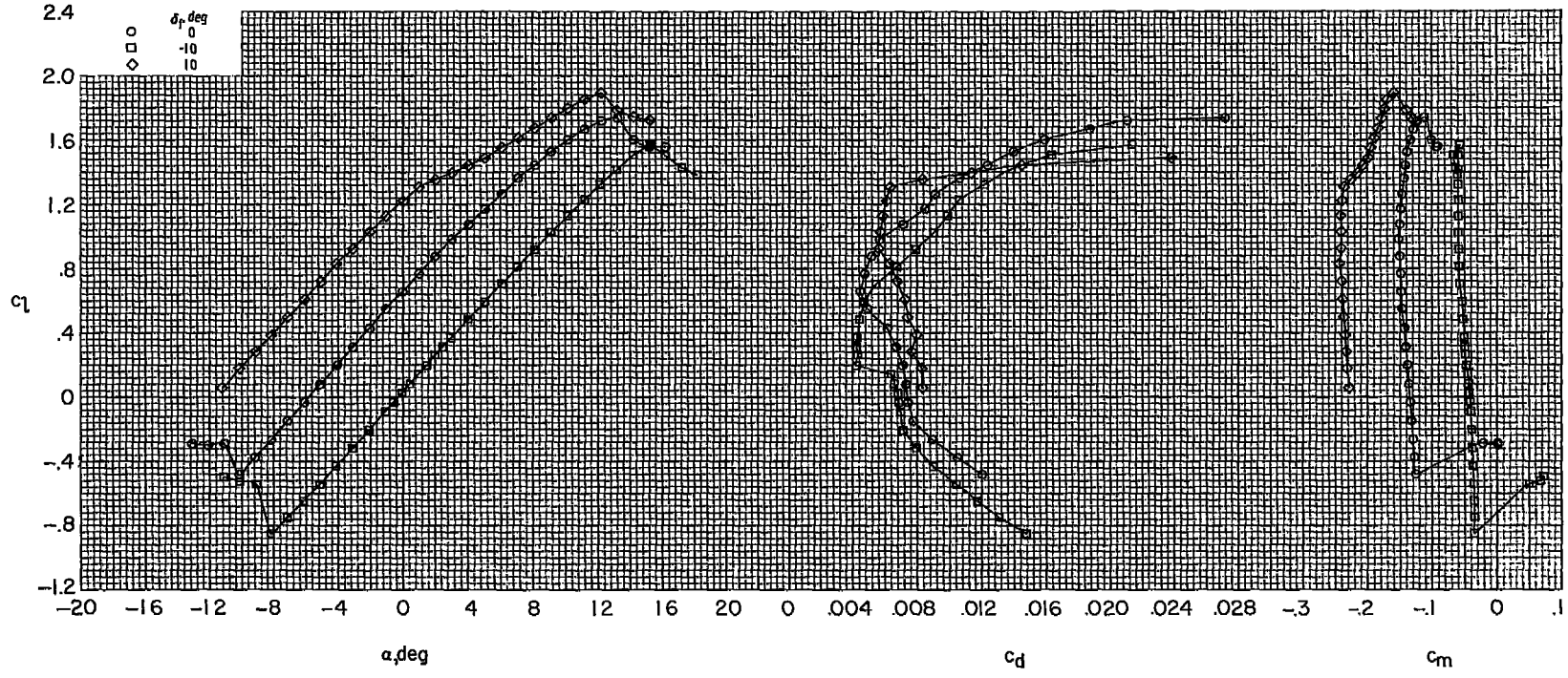

(b) $R = 6.0 \times 10^6$.

Figure 24.- Continued.

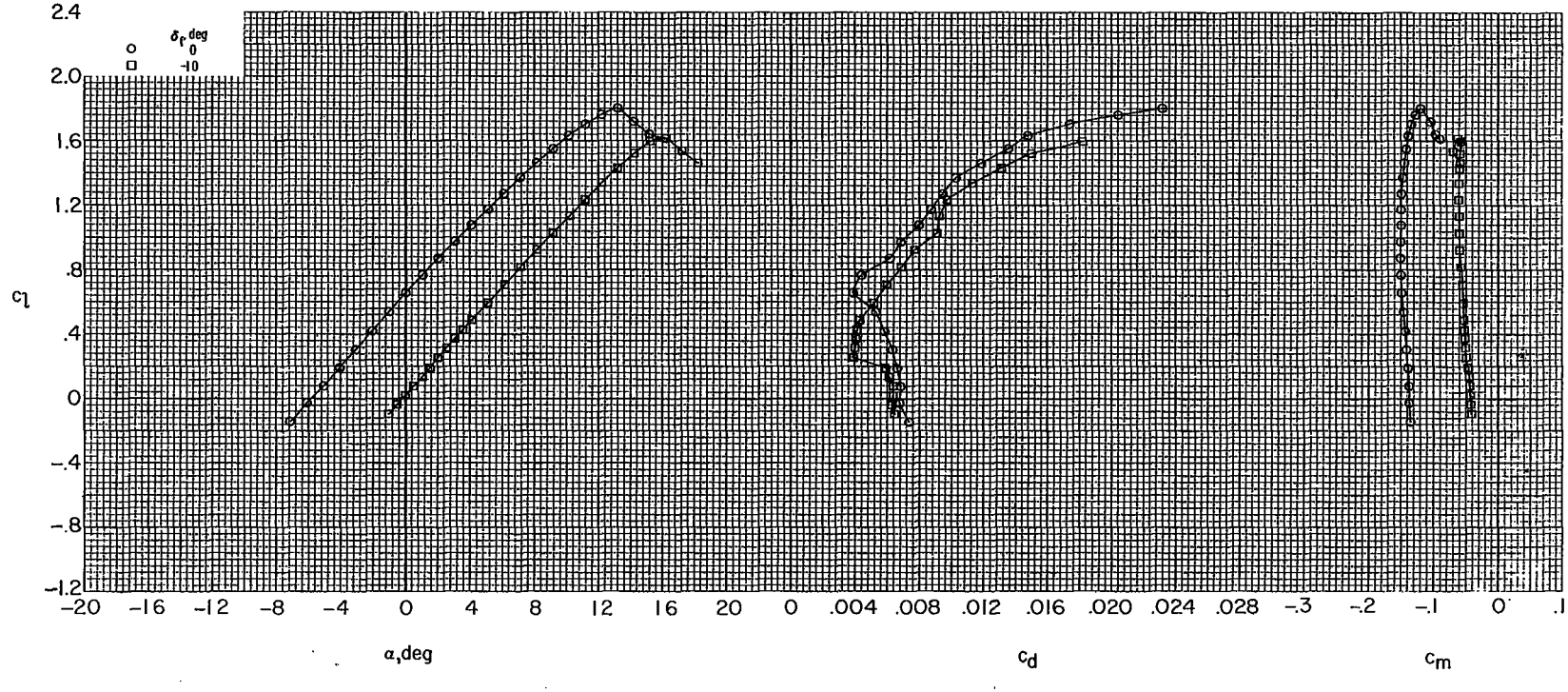

(c) $R = 9.0 \times 10^6$.

Figure 24.- Concluded.

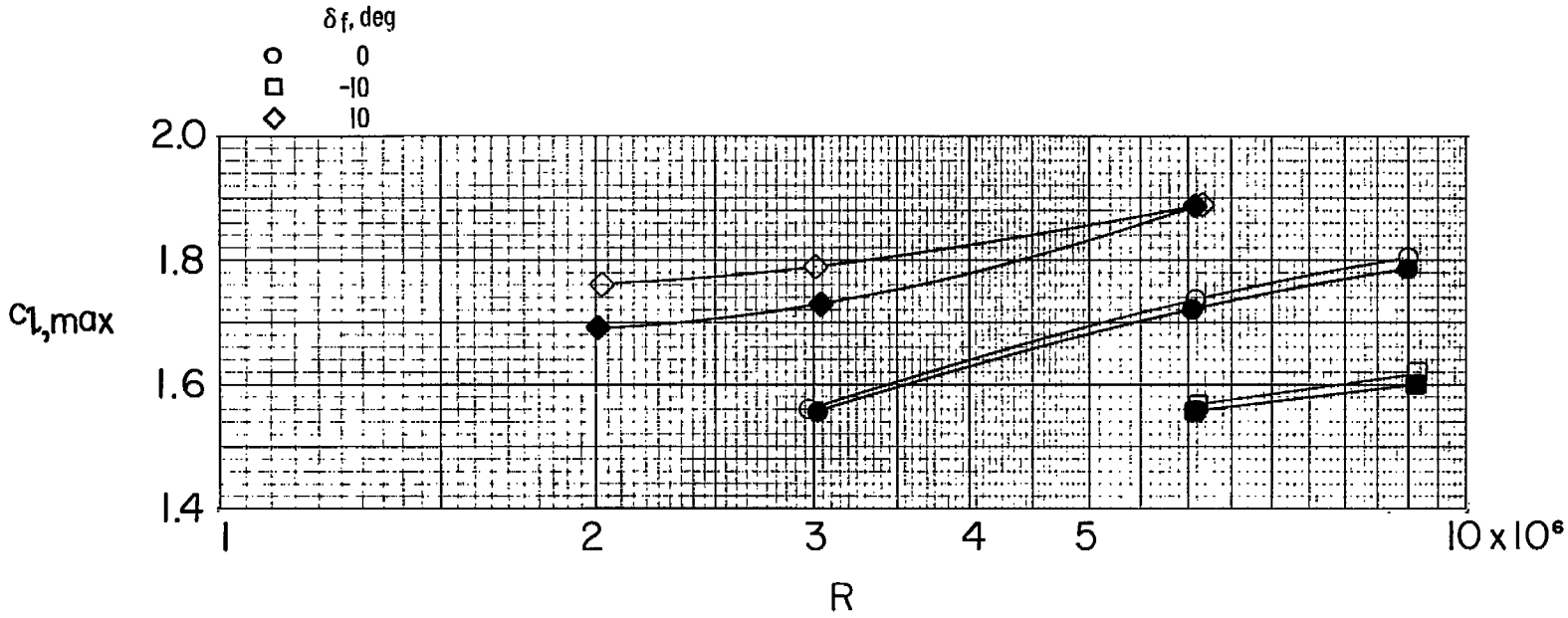

Figure 25.- Variation of maximum lift coefficient with Reynolds number for various flap deflections at M = 0.10. Open symbols represent data with transition free; solid symbols, data with transition fixed.

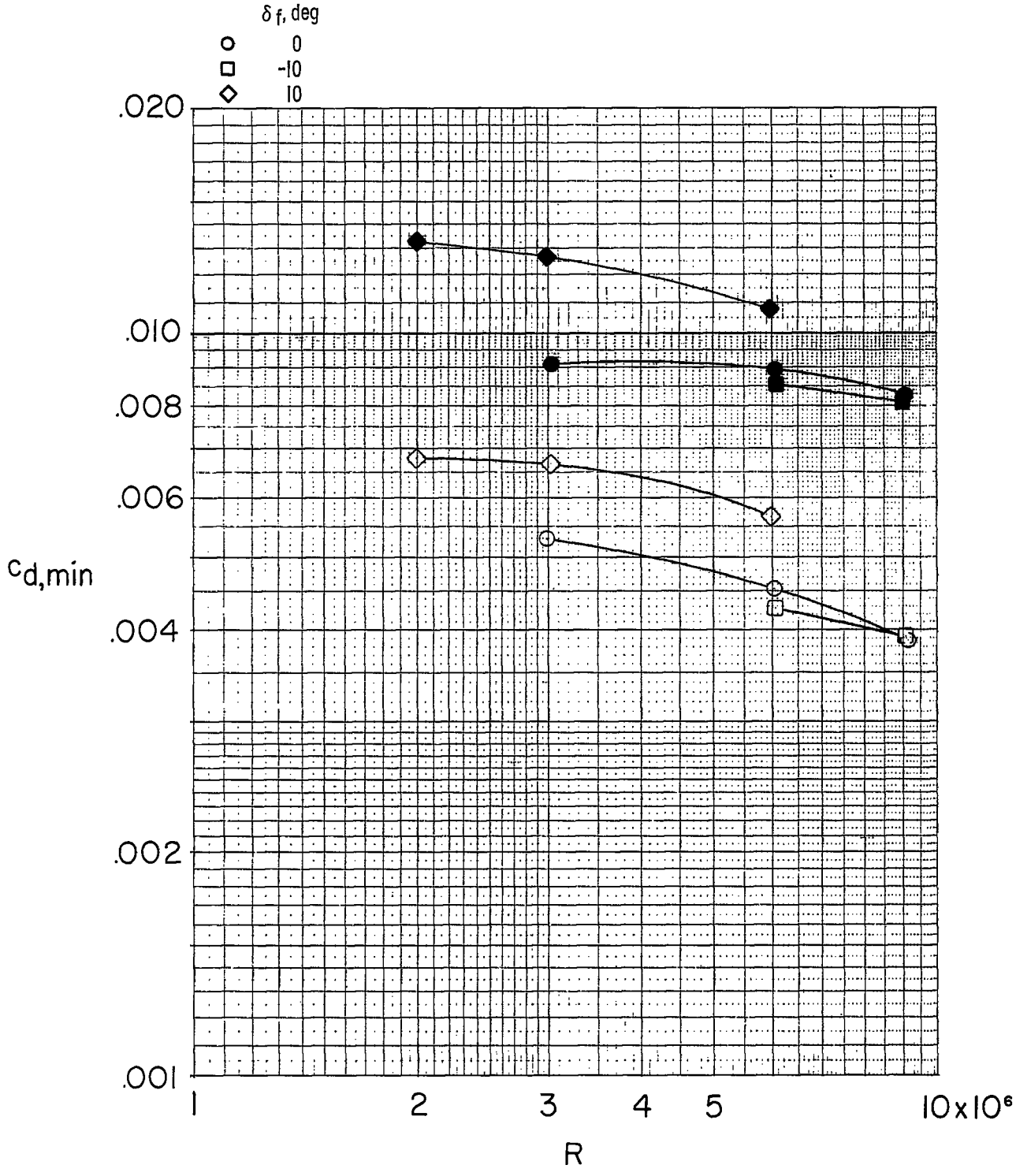

Figure 26.- Variation of minimum drag coefficient with Reynolds number for various flap deflections at M = 0.10. Open symbols represent data with transition free; solid symbols, data with transition fixed.

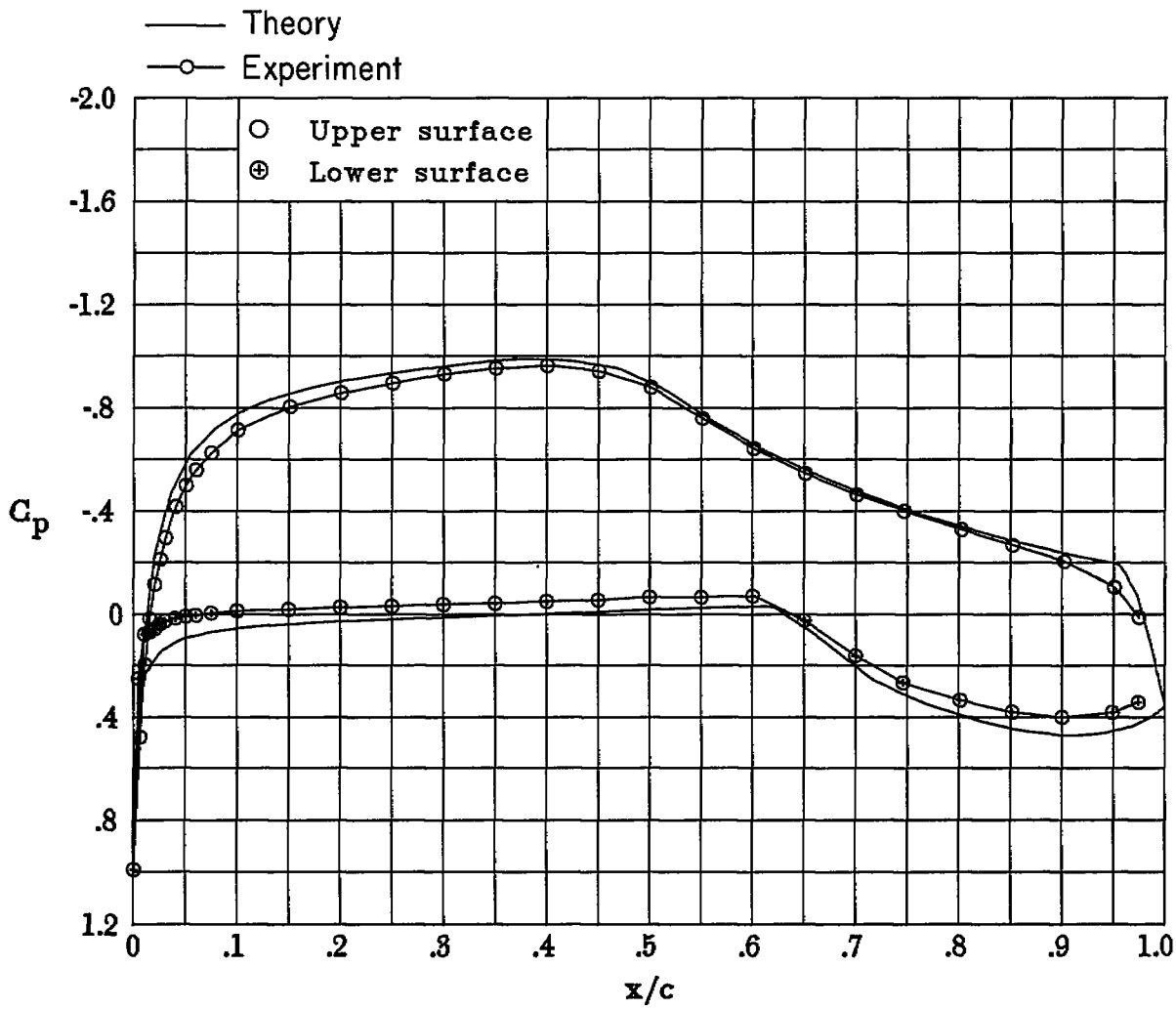

(a) $\delta_f = 0^o$; $\alpha = 0.01^o$.

Figure 27.- Comparison of theoretical and experimental pressure distributions.

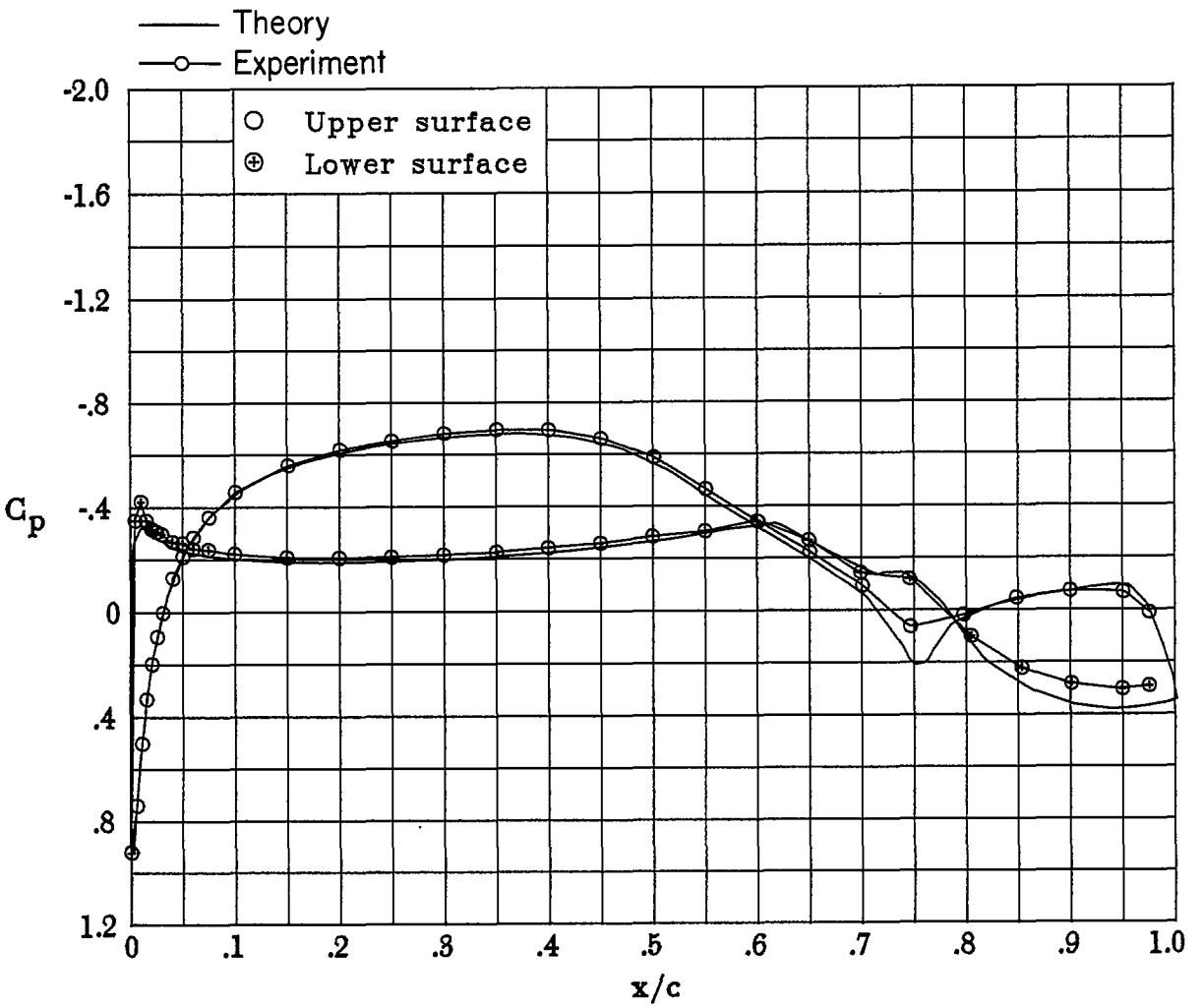

(b) $\delta_f = -10^\circ$; $\alpha = 1.52^\circ$.

Figure 27.- Continued.

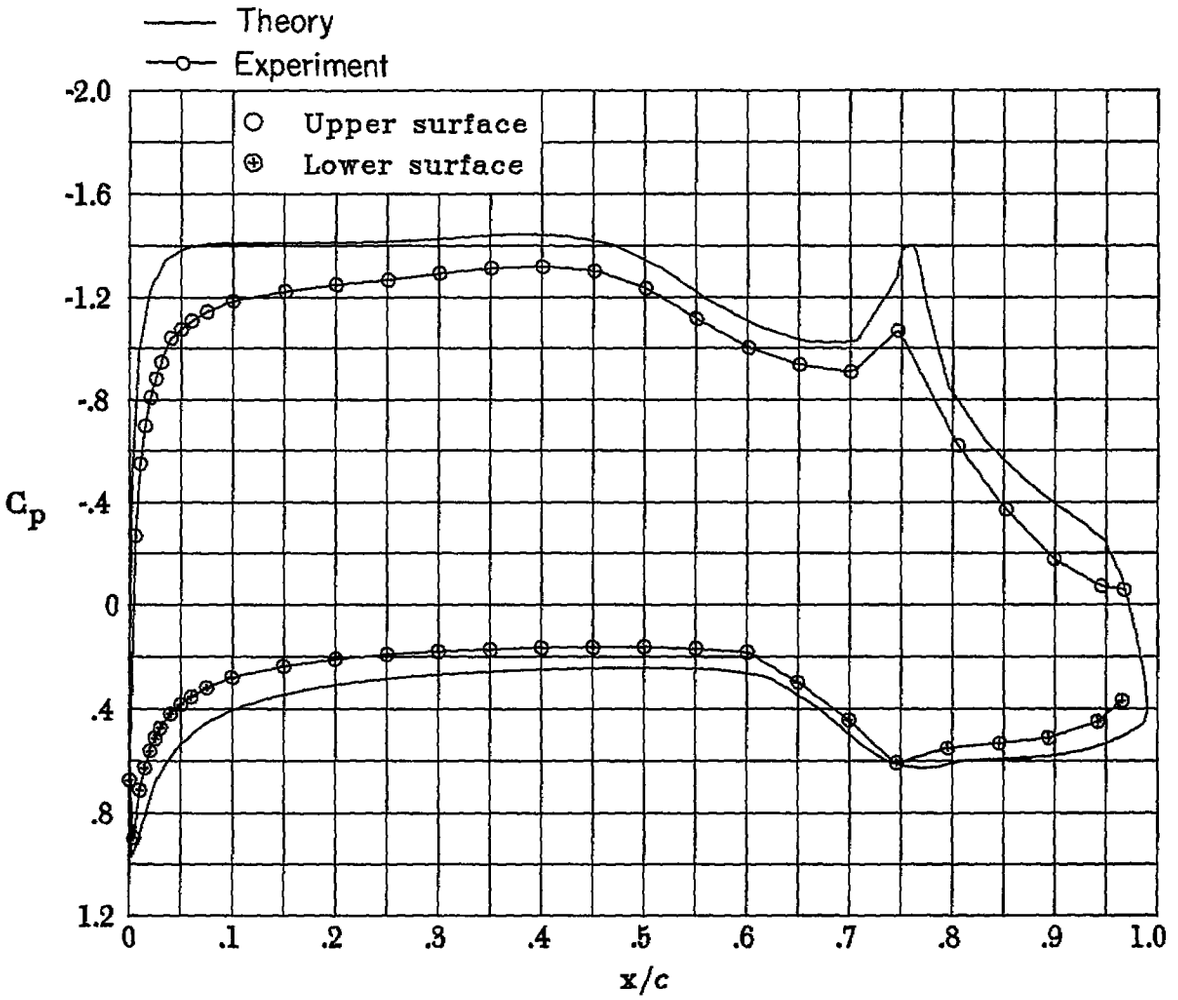

(c) $\delta_f = 10^o$; $\alpha = 0.05^o$.

Figure 27.- Concluded.

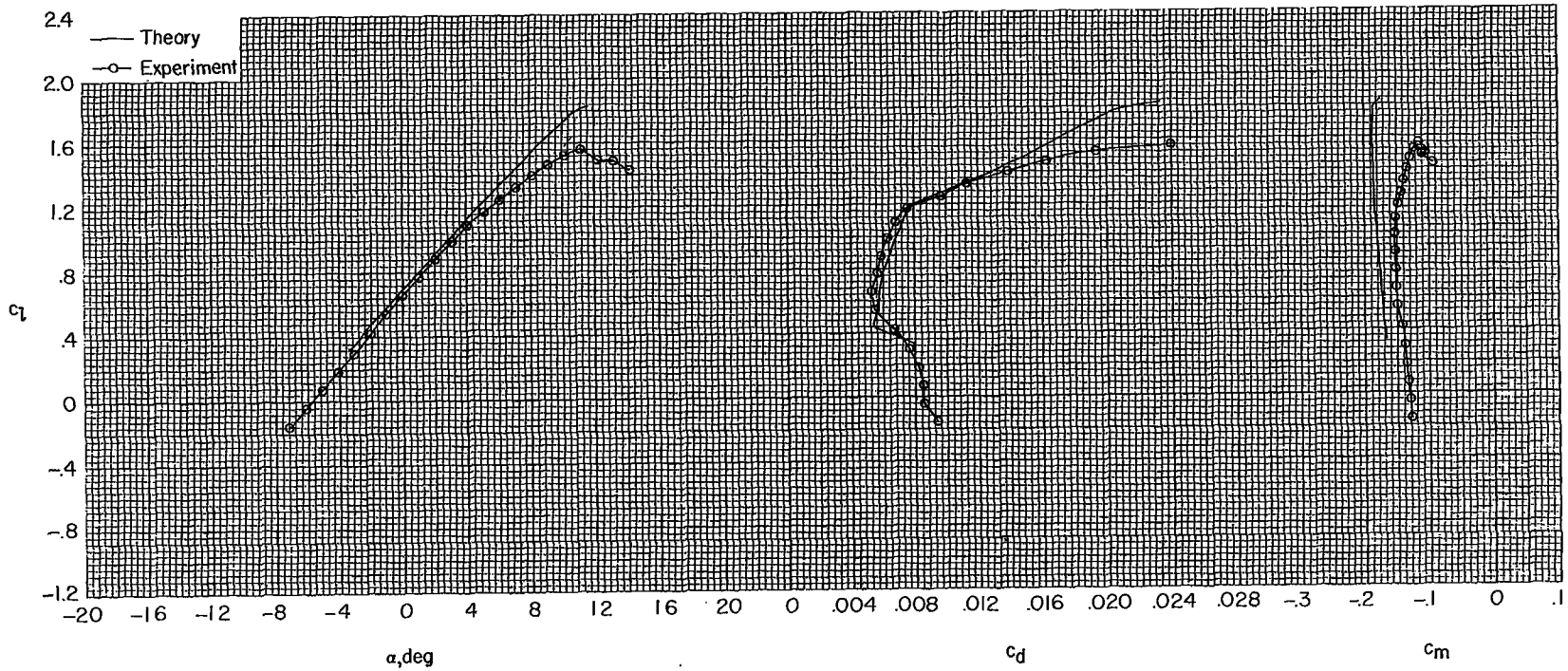

(a) $R = 3.0 \times 10^6$.

Figure 28.- Comparison of theoretical and experimental section characteristics with $\delta_f = 0^o$ and transition free.

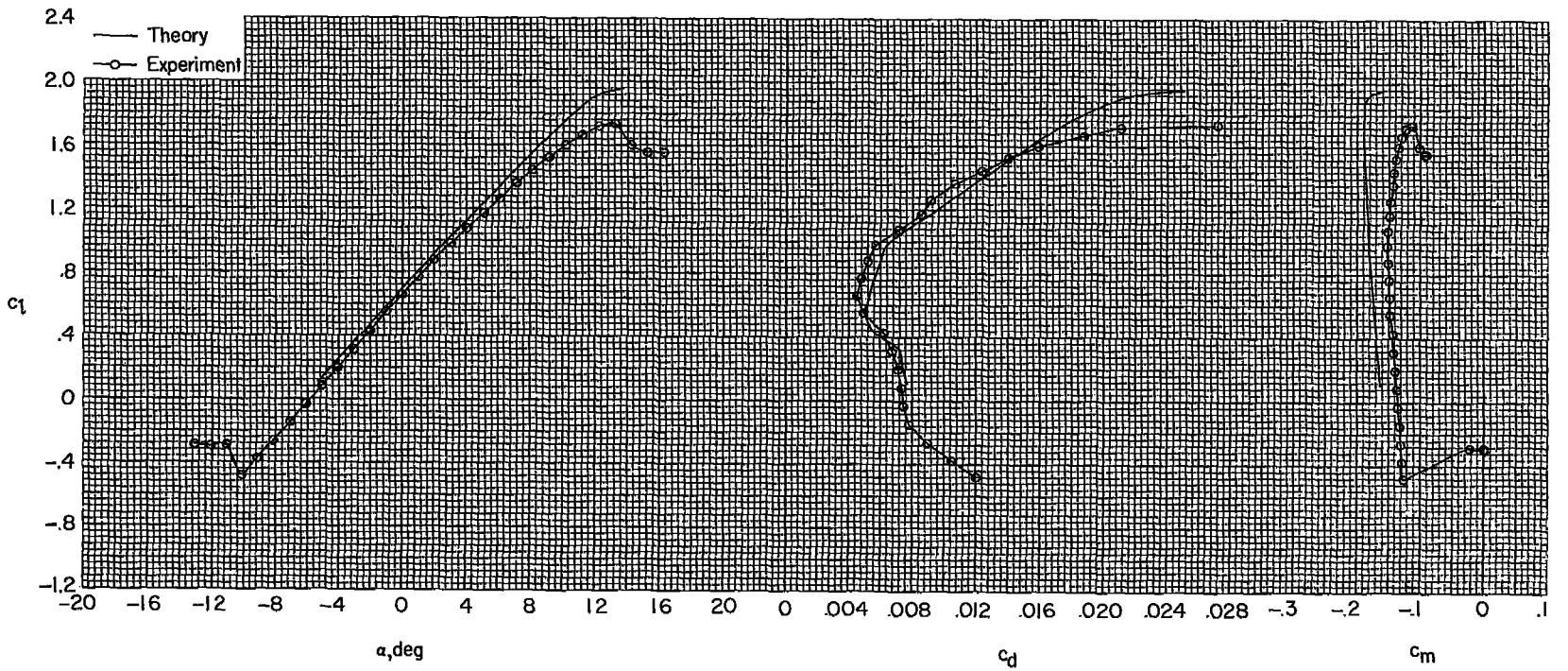

(b) $R = 6.0 \times 10^6$.

Figure 28.- Continued.

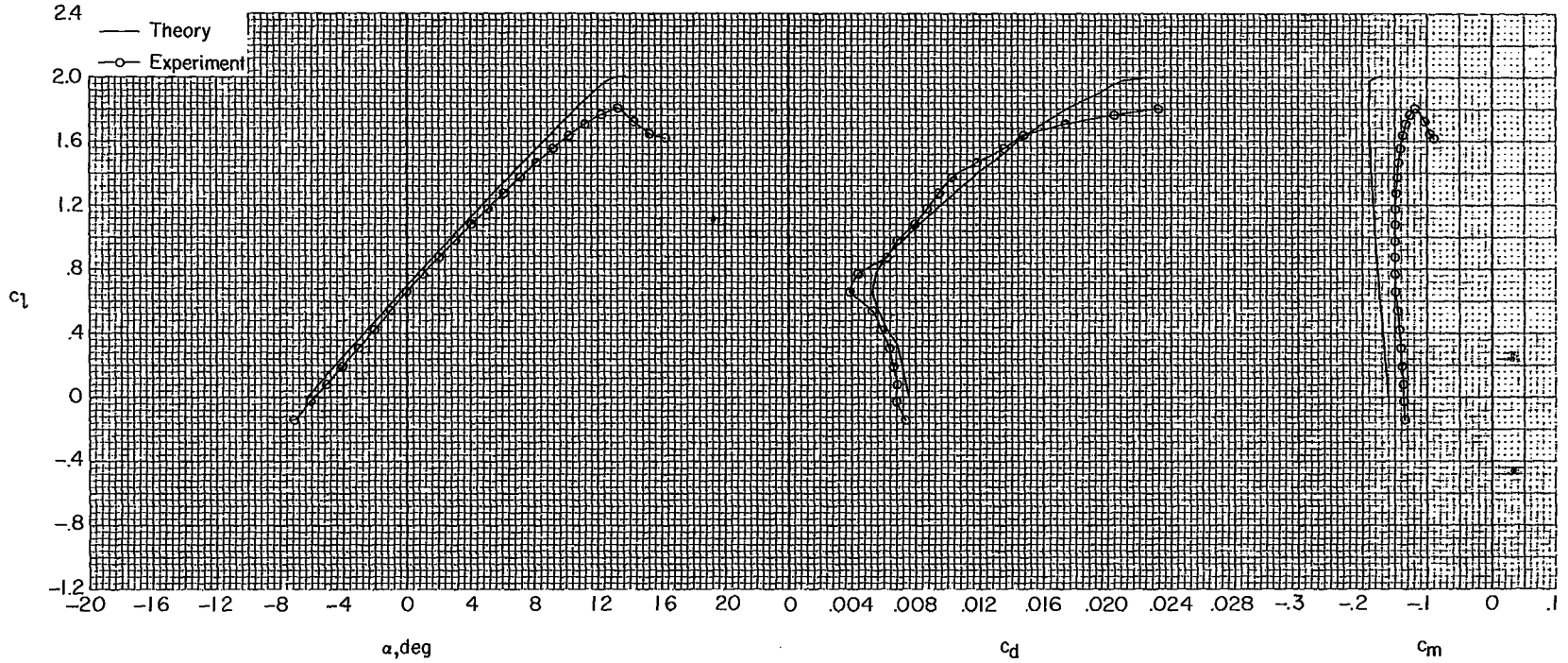

(c) $R = 9.0 \times 10^6$.

Figure 28.- Concluded.

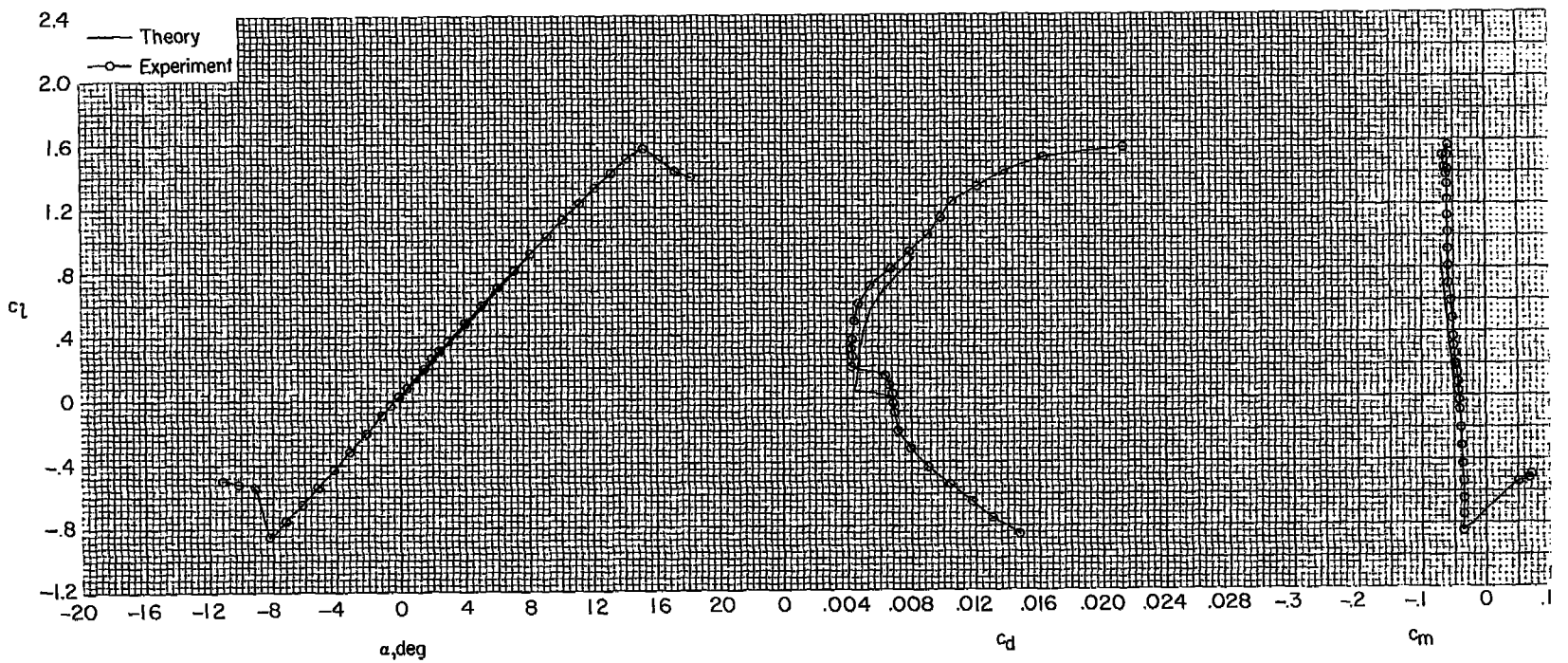

(a) $R = 6.0 \times 10^6$.

Figure 29.- Comparison of theoretical and experimental section characteristics with $\delta_f = -10^o$ and transition free.

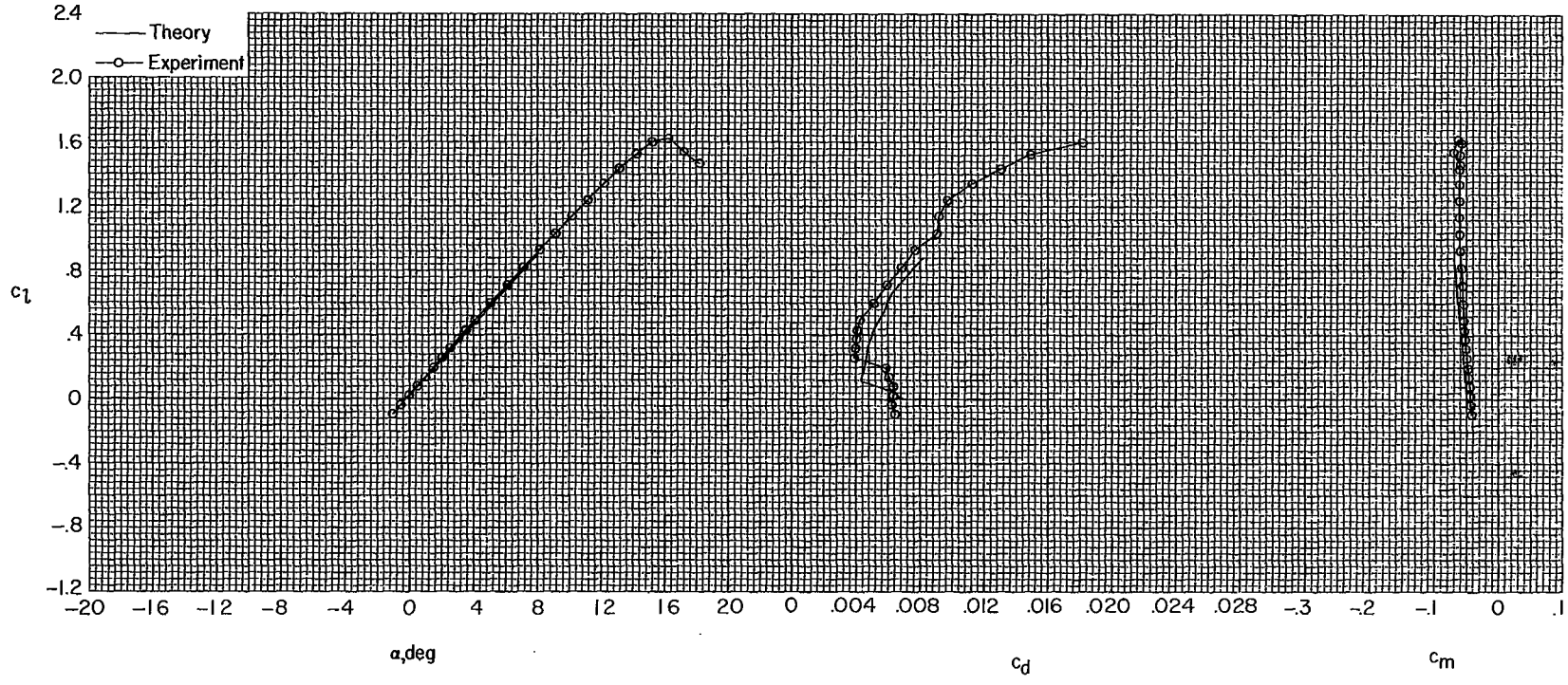

(b) $R = 9.0 \times 10^6$.

Figure 29.- Concluded.

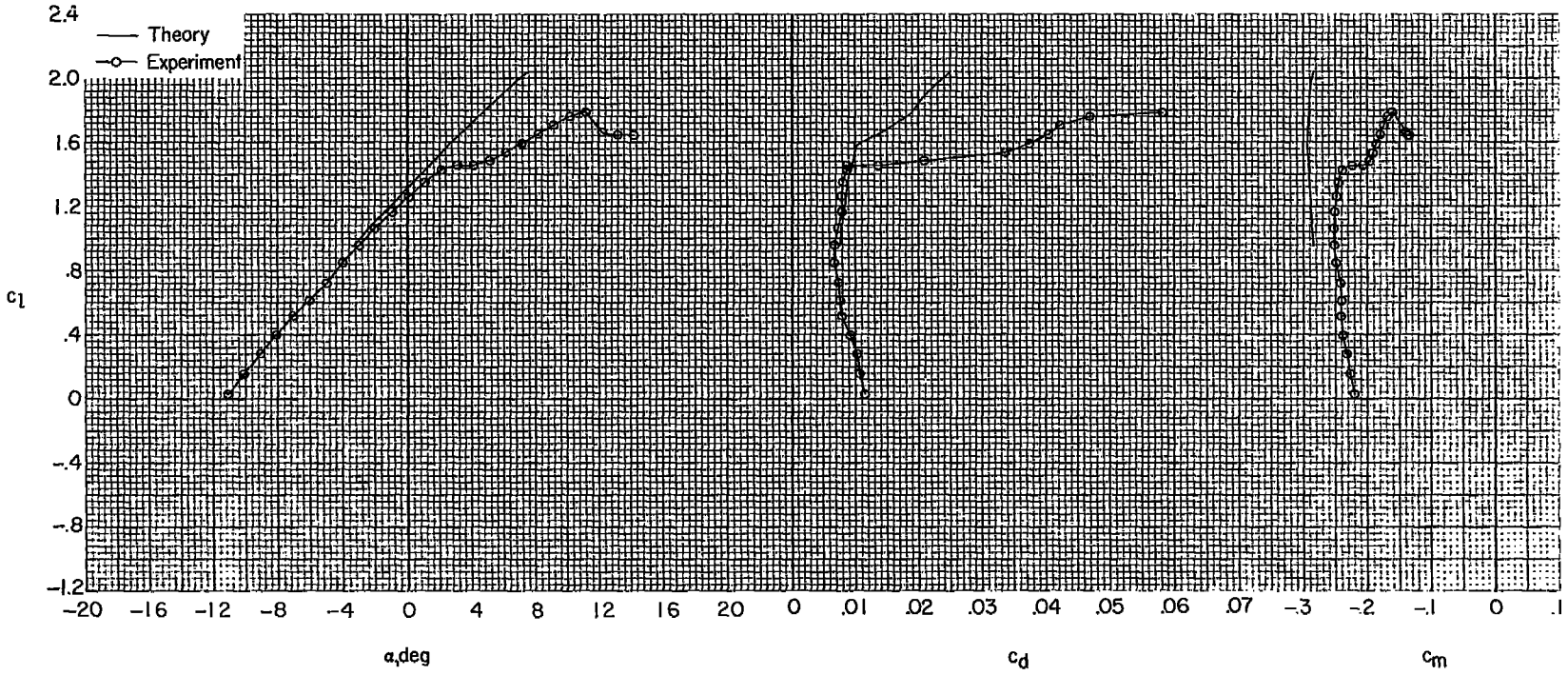

(a) $R = 3.0 \times 10^6$.

Figure 30.- Comparison of theoretical and experimental section characteristics with $\delta_f = 10^o$ and transition free.

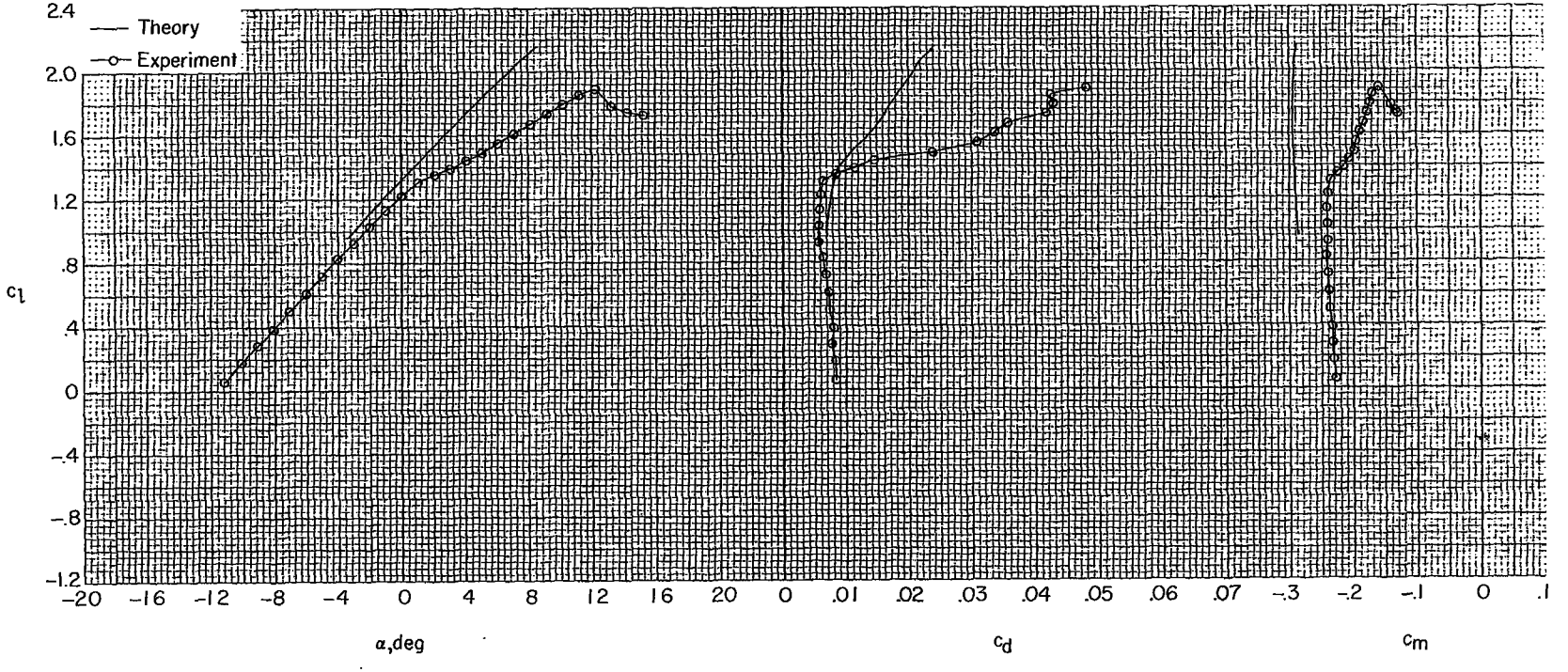

(b) $R = 6.0 \times 10^6$.

Figure 30.- Concluded.

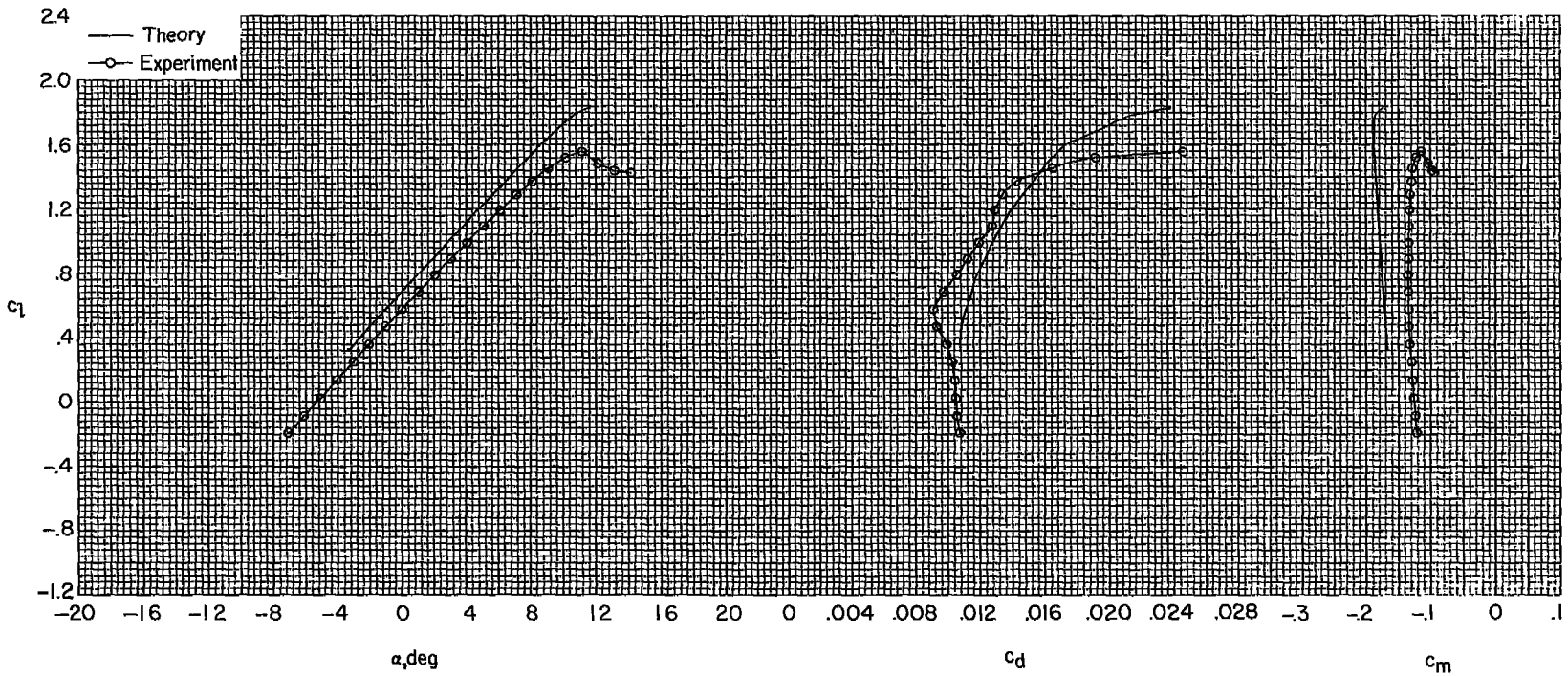

(a) $R = 3.0 \times 10^6$.

Figure 31.- Comparison of theoretical and experimental section characteristics with $\delta_f = 0^o$ and transition fixed.

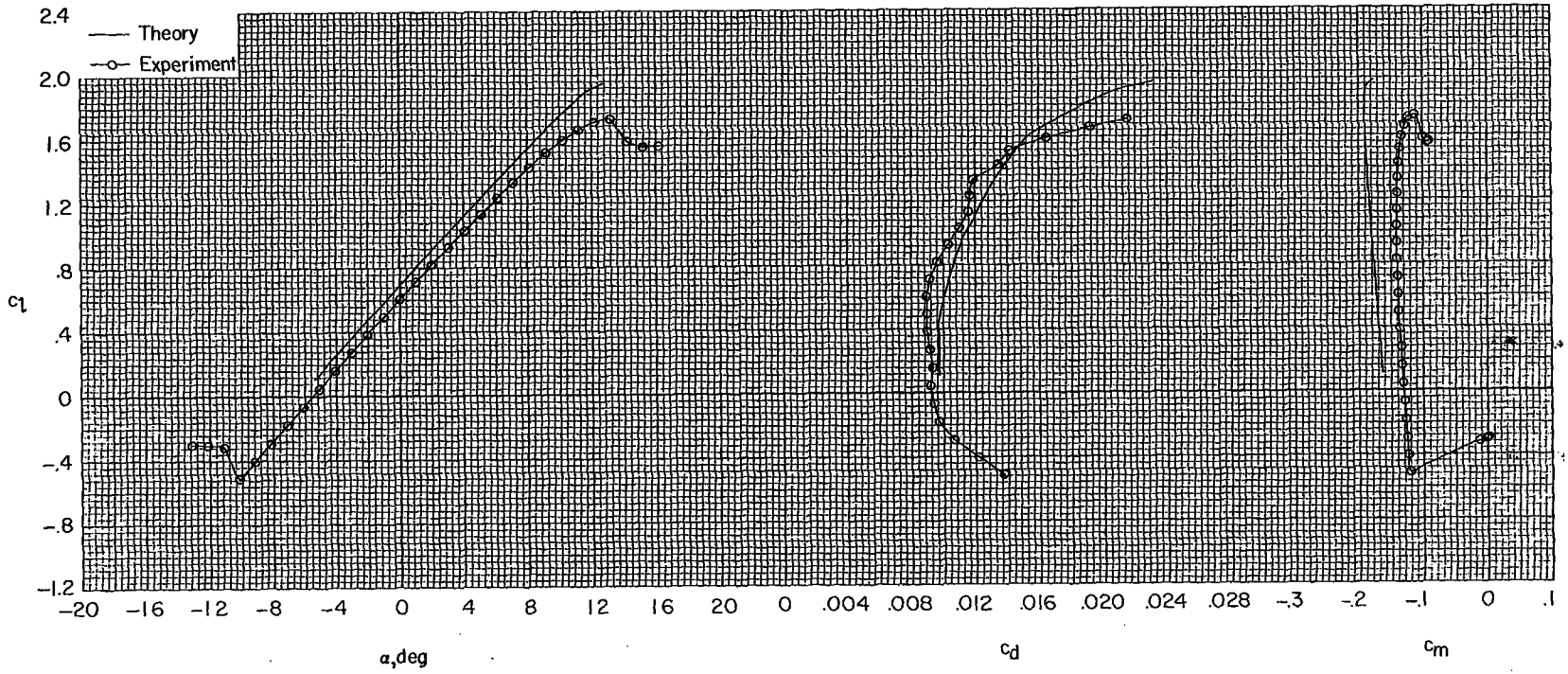

(b) $R = 6.0 \times 10^6$.

Figure 31.- Continued.

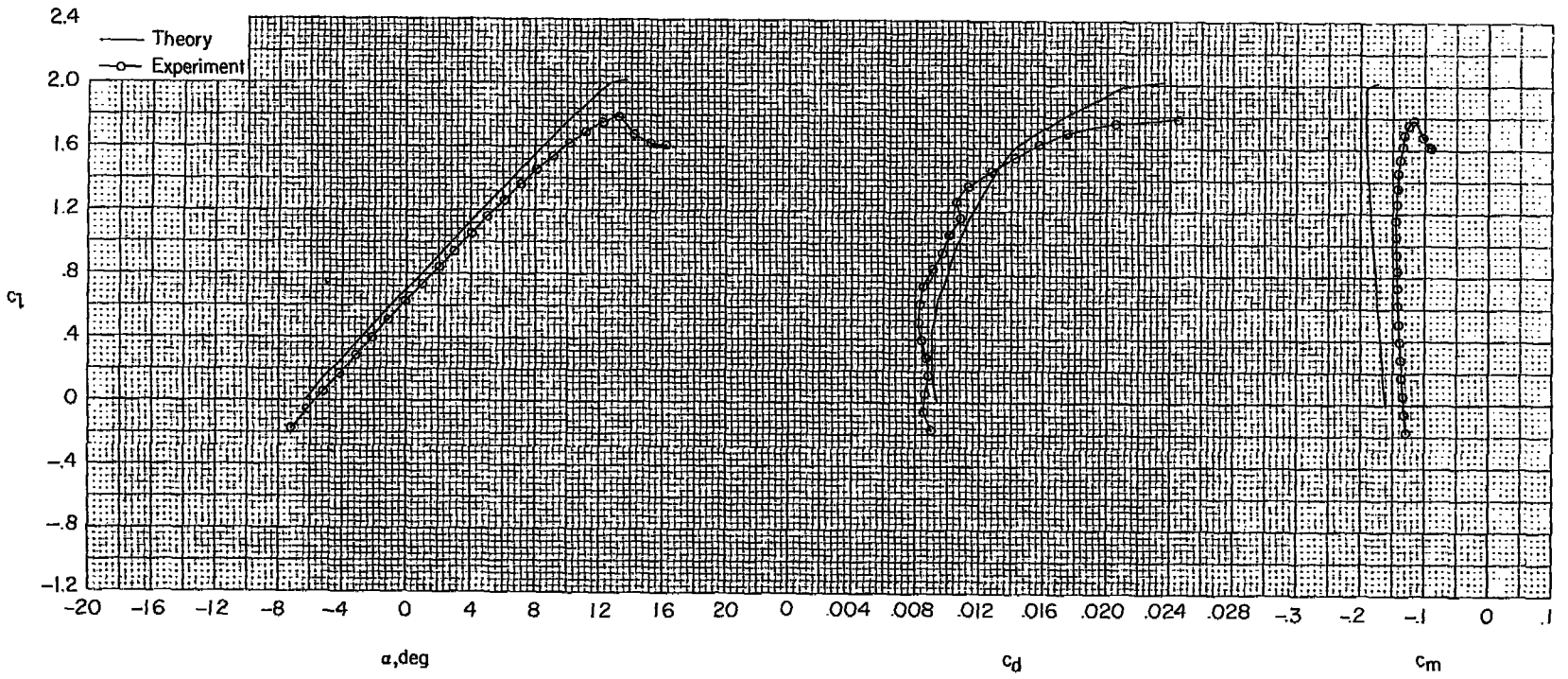

(c) $R = 9.0 \times 10^6$.

Figure 31.- Concluded.

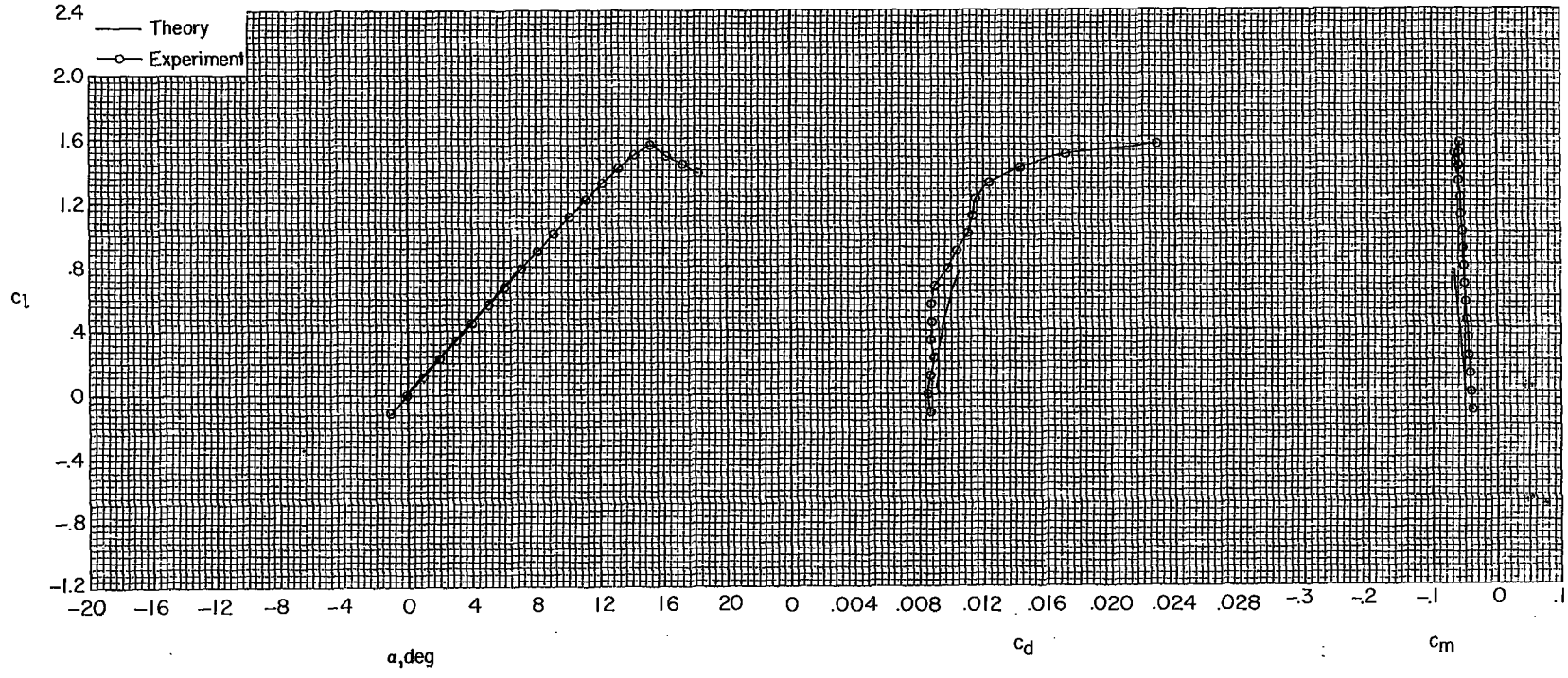

(a) $R = 6.0 \times 10^6$.

Figure 32.- Comparison of theoretical and experimental section characteristics with $\delta_f = -10^o$ and transition fixed.

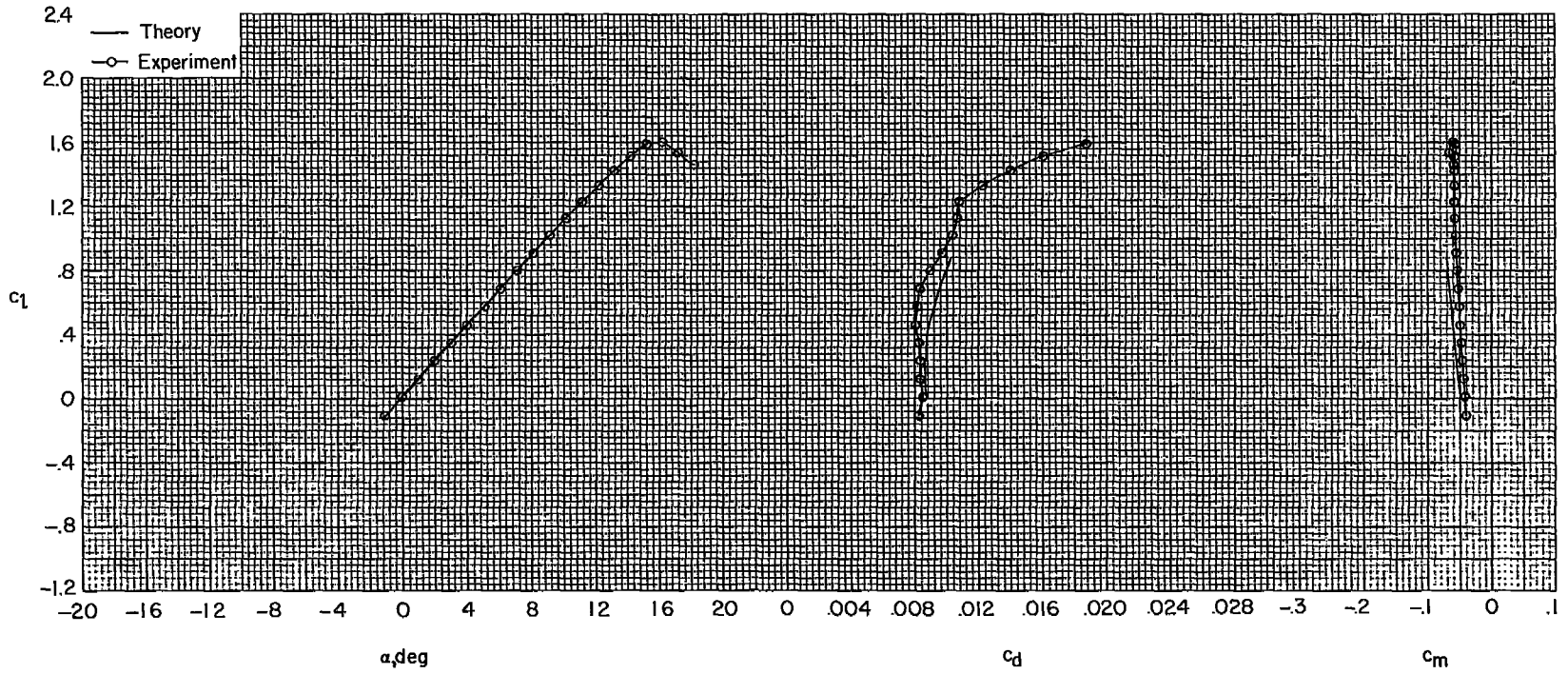

(b) $R = 9.0 \times 10^6$.

Figure 32.- Concluded.

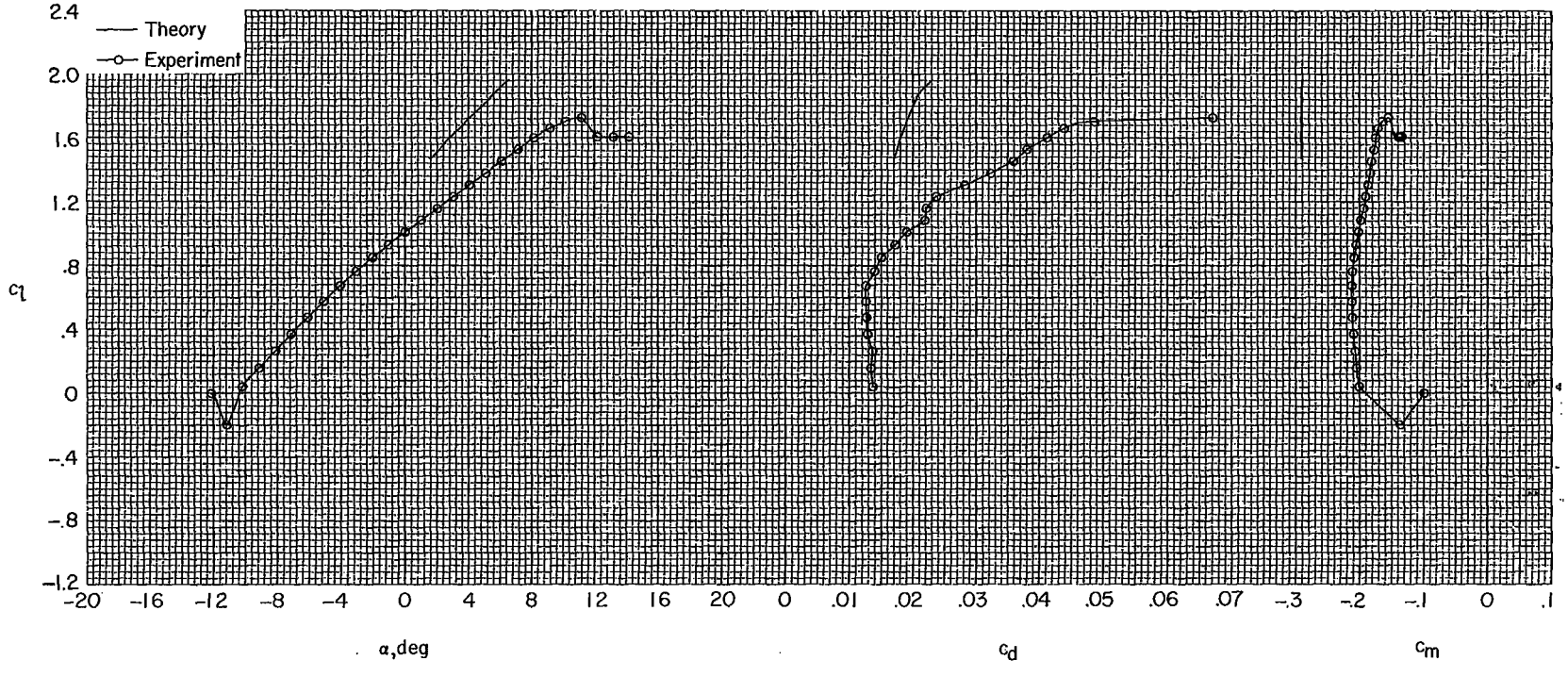

(a) $R = 3.0 \times 10^6$.

Figure 33.- Comparison of theoretical and experimental section characteristics with $\delta_f = 10^o$ and transition fixed.

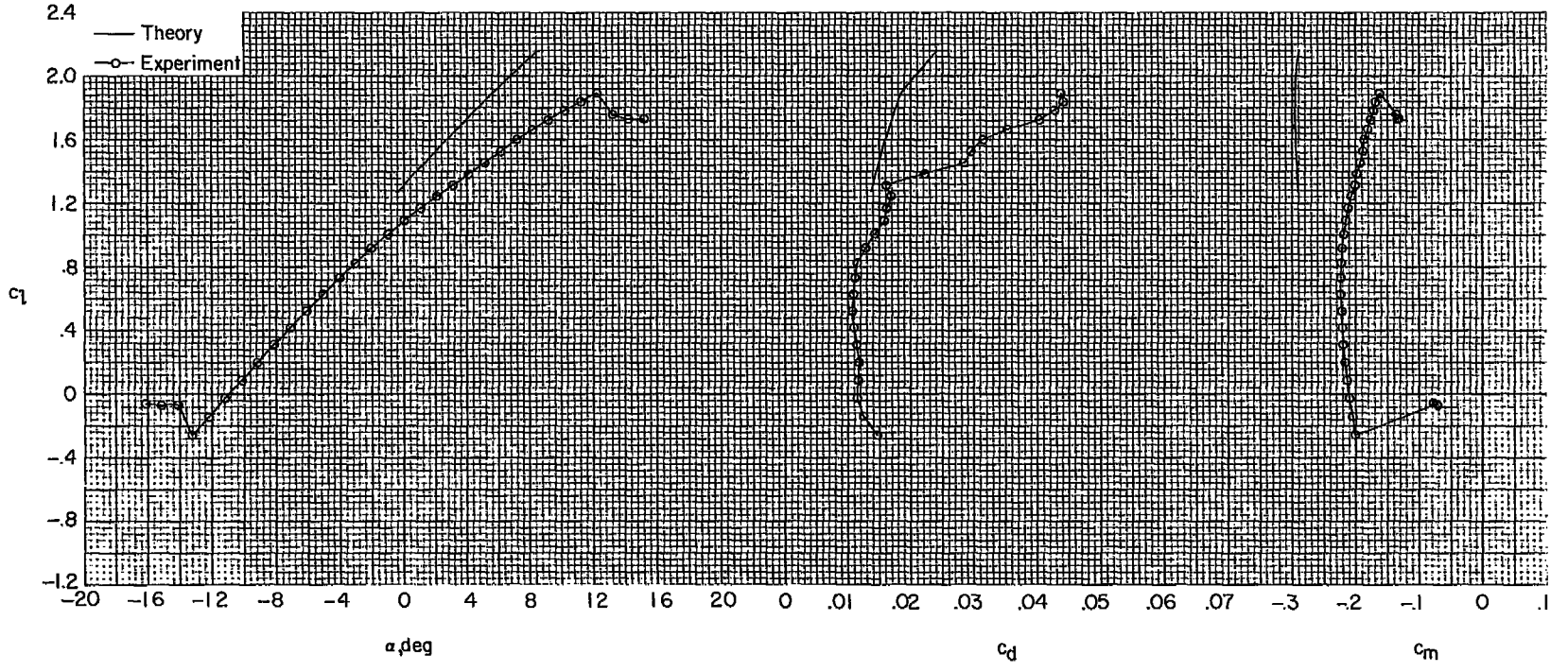

(b) $R = 6.0 \times 10^6$.

Figure 33.- Concluded.

1. Report No.	2. Government Accession No.	3. Recipient's Catalog No.
NASA TP-1865		

4. Title and Subtitle	5. Report Date
DESIGN AND EXPERIMENTAL RESULTS FOR A FLAPPED NATURAL-LAMINAR-FLOW AIRFOIL FOR GENERAL AVIATION APPLICATIONS	June 1981
	6. Performing Organization Code: 505-31-33-05
7. Author(s): Dan M. Somers	8. Performing Organization Report No.: L-14409
9. Performing Organization Name and Address: NASA Langley Research Center, Hampton, VA 23665	10. Work Unit No.
	11. Contract or Grant No.
12. Sponsoring Agency Name and Address: National Aeronautics and Space Administration, Washington, DC 20546	13. Type of Report and Period Covered: Technical Paper
	14. Sponsoring Agency Code

15. Supplementary Notes

16. Abstract

A flapped natural-laminar-flow airfoil for general aviation applications, the NLF(1)-0215F, has been designed and analyzed theoretically and verified experimentally in the Langley Low-Turbulence Pressure Tunnel. The basic objective of combining the high maximum lift of the NASA low-speed airfoils with the low cruise drag of the NACA 6-series airfoils has been achieved. The safety requirement that the maximum lift coefficient not be significantly affected with transition fixed near the leading edge has also been met. Comparisons of the theoretical and experimental results show generally good agreement.

17. Key Words (Suggested by Author(s))	18. Distribution Statement
NLF(1)-0215F Airfoils Low speed Laminar flow General aviation	[redacted] Unclassified - Unlimited Subject Category 02

19. Security Classif. (of this report)	20. Security Classif. (of this page)	21. No. of Pages	22. Price
Unclassified	Unclassified	122	

[redacted]

NASA-Langley, 1981